

List of Contributors

Rasmus Bro, *The Royal Veterinary and Agricultural University, Rolighedsvej 30, 1958 Frederiksberg C, Denmark*

Melinda J. Duer, *Department of Chemistry, University of Cambridge, Lensfield Road, Cambridge, CB2 1EW, UK*

Marianne Dyrby, *Umetrics AB, Stortorget 21, 211 34 Malmö, Sweden*

Søren B. Engelsen, *Quality and Technology, Department of Food Science, The Royal Veterinary and Agricultural University, Rolighedsvej 30, 1958 Frederiksberg C, Denmark*

Leslie D. Field, *School of Chemistry, University of New South Wales, Sydney NSW 2052, Australia*

C. Odin, *Groupe Matière, Condensée et Matériaux, UMR6626 au CNRS, Université Rennes I, Campus de Beaulieu, Bat11A, 35042 Rennes Cedex, France*

Henrik T. Pedersen, *Protein Structure and Biophysics, Novo Nordisk A/S, Novo Nordisk Park, 2760 Måløv, Denmark*

Hiroyuki Takashima, *Novartis Institutes for BioMedical Research, Ohkubo 8, Tsukuba, Ibaraki 300-2611, Japan*

Preface

Volume 59 of Annual Reports on NMR contains current accounts of some of the many active and exciting areas of scientific research, which have a crucial dependence on NMR measurements. I am very happy to take the opportunity of introducing the following contributions.

The volume opens with a report by L.D. Field on Multiple Quantum NMR of Partially Aligned Molecules; following this is an account on Solid-State NMR Studies of Molecular Motion by M.J. Duler; C. Odin reviews NMR Studies of Phase Transitions; Application of Multi-way Analysis to 2D NMR Data is covered by H.T. Pedersen, M. Dyrby, S.B. Engelsen and R. Bro; the final contribution is on High Resolution Protein Structure Determination by NMR and it is provided by H. Takashima. My sincere thanks go to all of these reporters and to the production staff at Elsevier for their assistance in the creation of this volume.

*Royal Society of Chemistry
Burlington House
Piccadilly
London, UK*

G. A. WEBB
February 2006

Multiple Quantum NMR of Partially Aligned Molecules

LESLIE D. FIELD

School of Chemistry, University of New South Wales, Sydney, NSW 2052, Australia

1. Introduction	2
2. NMR of partially aligned molecules	3
3. Multiple quantum NMR and spectral simplification	4
4. Excitation and detection of multiple quantum coherence	6
4.1. Non-selective excitation/detection of multiple quantum coherence	7
4.2. Selective excitation of multiple quantum coherence	9
4.3. Selective detection of MQC	10
4.4. Time proportional phase incrementation and order selective detection using 3D NMR	14
4.5. MQ filters to simplify 1Q spectra	15
5. Selective deuteration to simplify spectral analysis	17
6. The analysis and simulation of multiple quantum spectra	19
6.1. Chemical shift refocusing	20
6.2. Estimating order parameters by MQNMR	21
7. Heteronuclear MQNMR	24
8. Measuring diffusion in anisotropic media using MQNMR	25
9. Multiple quantum spectra of exchanging systems	28
10. MQ relaxation in anisotropic media	28
11. Counting spins in clusters	29
12. Studies of aligned molecules by MQNMR	30
References	37

The NMR spectra of solutes partially aligned in liquid crystalline solution are significantly more complex than the spectra obtained in isotropic solution because dipolar couplings and other spectral parameters are not averaged to zero by rapid isotropic tumbling. Whereas conventional single quantum NMR spectroscopy involves the excitation and detection of

individual spins embedded in a spin system, multiple quantum NMR (MQNMR) involves the excitation and detection of coherence in groups of coupled spins. MQNMR spectra contain fewer transitions than single quantum spectra and, in principle, MQNMR spectra are significantly easier to analyse than single quantum spectra. This chapter describes the methods available to excite multiple quantum coherence, both selectively and non-selectively and methods available to detect, extract and analyse multiple quantum spectra. The chapter also describes the use of selective and random deuteration, combined with multiple quantum spectroscopy, to analyse the complex spectra of larger spin systems as well as applications of multiple quantum spectra in: (i) obtaining dipolar coupling constants (and hence accessing information about the shape of the spin system); (ii) studying molecular diffusion; (iii) accessing relaxation parameters which then provide information about molecular motion and mobility; and (iv) counting spins in domains and clusters. The chapter concludes with a comprehensive review of molecules, aligned in liquid crystalline solution, where MQNMR spectra have been obtained and analysed to provide information about their spin systems.

1. INTRODUCTION

Since the first reports of the use of liquid crystalline materials as solvents for NMR spectroscopy, high-resolution NMR of partially aligned molecules has become an important area of NMR spectroscopy.¹ Liquid crystals are mesophases – their properties are intermediate between the liquid and solid phase. In the liquid crystalline phase, there is still molecular mobility (as in a liquid), but there is a degree of molecular alignment so the molecules are not oriented randomly with respect to each other and tend to align preferentially in some direction making the “liquid” anisotropic. Most compounds that form a liquid crystalline phase can act as solvents and can take up solutes without destroying the structure of the mesophase. The freedom of solute molecules to move and rotate in partially aligned solvents is restricted by the orientation of the mesophase, so the solute molecules themselves are partially oriented by the medium.

NMR spectroscopy in isotropic solution is characterised by the fact that free and random molecular reorientation averages many parameters that have a directional dependence, e.g. dipolar-coupling constants, chemical shifts, etc. Some parameters, such as dipolar-coupling constants, average to zero in isotropic solution; so once the ability of a molecule to rotate and move freely and isotropically is removed, its NMR spectra immediately become more complex.

2. NMR OF PARTIALLY ALIGNED MOLECULES

The NMR spectra of solutes oriented in mesophases are significantly more complex than the spectra obtained in isotropic solution because: (i) the non-zero averaging of dipolar couplings results in many more coupling constants (splittings) being expressed in the spectrum – there is a non-zero dipolar coupling constant for every pair of interacting nuclei and (ii) the magnitude of the dipole coupling constants (D_{ij}) between a pair of interacting nuclei is generally large (up to a few kilohertz) compared to the magnitude of indirect coupling constant (typically a few hertz).

One of the main uses of NMR of partially aligned molecules has been to gain access to the dipolar coupling constants (D_{ij}), because these can be related directly to the internuclear distances (r_{ij}) between each pair of interacting nuclei i and j . The D_{ij} values are obtained by spectral analysis, most usually by computer simulation of experimental spectra. The D_{ij} are inversely proportional to the cube of the internuclear distances (r_{ij}) (Eq. (1)). Providing sufficient independent D_{ij} values can be measured and the relative positions of the nuclei in the spin system can be determined then the shape of the molecule as well as its average orientation in the magnetic field can be deduced.

$$D_{ij} = -\left(\frac{h\gamma_H^2}{4\pi^2}\right) \frac{S_{ij}}{r_{ij}^3} \quad (1)$$

where γ_H is the proton magnetogyric ratio, r_{ij} the internuclear distance between protons i and j and S_{ij} the order of the internuclear vector between i and j .²

The order parameter S_{ij} derives from the Saupe order matrix S , which is a symmetric traceless 3×3 tensor where the diagonal order parameters (S_{xx} , S_{yy} and S_{zz}) can have values between -0.5 and 1.0 , and the off-diagonal order parameters (S_{xy} , S_{yz} and S_{xz}) vary between -0.75 and $+0.75$.³ The higher the symmetry of the molecule, the lower the number of independent non-zero-order parameters that are required to completely describe the orientation of the spin system. S_{ij} is 0 when the the i,j axis is completely non-aligned (as in an isotropic solution). S_{ij} is -0.5 , where the i,j axis is orthogonal to the magnetic field and S_{ij} is 1.0 where the i,j axis is aligned perfectly with the magnetic field. Room temperature S_{ij} values between 0.6 and 0.8 are typical for many liquid crystalline materials.

The induced alignment of solutes oriented in liquid crystalline solution is very sensitive to small variations in temperature. S_{ij} values are temperature sensitive and since D_{ij} is proportional to S_{ij} , care must be exercised if spectra

are to be compared directly since these must be recorded sequentially under identical conditions.

3. MULTIPLE QUANTUM NMR AND SPECTRAL SIMPLIFICATION

For a system of coupled $I = 1/2$ nuclei, the transition frequencies in the multiple quantum spectra are determined by the dipolar coupling constants, the scalar coupling constants and the chemical shifts of the nuclei. In theory, the spectra of order $N-1$ and $N-2$ contain sufficient transitions to measure all of the dipolar coupling constants and chemical shifts in an N -spin system. For additional accuracy and confidence, the $N-3$ quantum spectrum can also be analysed to provide redundancy and more reliable estimates of the D_{ij} .

The number of transitions in an NMR spectrum increases dramatically as the number of interacting nuclei in the spin system increases. The number of transitions appearing in a 1-quantum spectrum of a spin system (without any simplifying symmetry) partially oriented in a nematic phase is expressed by Eq. (2), with some examples shown in Table 1.

$$\text{Number of transitions} = \frac{(2N)!}{[(N-1)!(N+1)!]} \quad (2)$$

where N is the number of interacting spins in the spin system.

If there is some element of symmetry in the spin system, the number of transitions is reduced. For a 6-spin system with no simplifying symmetry, aligned in an anisotropic solution, there would be 792 transitions in an ^1H 1-quantum spectrum. However in the spectrum of benzene, C_6H_6 (a planar hexagonal 6-spin proton spin system) aligned in anisotropic solution there are only 72 transitions in the 1-quantum proton spectrum.

Severe overlap between transitions in spin systems containing more than about 7 or 8 spins (without simplifying symmetry) makes analysis of the 1-quantum spectra a virtually intractable problem. In larger spin systems, it becomes impossible to resolve or assign individual transitions for an iterative computer analysis.

Table 1. The number of transitions in a 1-quantum spectrum of a partially oriented spin system as a function of the number of spin $1/2$ nuclei

Number of spins	1	2	3	4	5	6	7	8	9	10
Transitions	1	4	15	56	210	792	3003	1.1×10^4	4.4×10^4	1.7×10^5

Where conventional single quantum NMR involves the excitation and detection of individual spins embedded in a spin system, multiple quantum NMR (MQNMR) involves the excitation and detection of coherence in groups of coupled spins. As a simplified example, in a coupled spin system with three nuclei ($I = 1/2$), there are 15 possible single quantum transitions (some of which are disallowed in practice). If we examine the coherence between spins in pairs (a 2-quantum experiment), there are only six transitions and there is only one transition resulting from the excitation of all three nuclei together in the spin system (a 3-quantum experiment). MQNMR⁴⁻¹⁰ reduces the complexity of the spectrum of a solute dissolved in a liquid crystalline solvent¹¹ and one of the main benefits of MQNMR is that there are fewer transitions in the high-order MQ spectra than in the 1-quantum or lower-order MQ spectra.

The number of M -quantum transitions in a system of N nuclei ($I = 1/2$) neglecting symmetry, is given by Eq. (3) and representative values are summarised in Table 2.

$$\text{Number of } M\text{-quantum transitions in an } N\text{-spin system} = \frac{(2N)!}{[(N - M)!(N + M)!]} \tag{3}$$

There is always only 1 transition in the N -quantum spectrum of an N -spin system. The frequency of the transition in the N -quantum spectrum will be the sum of the frequencies of the N nuclei in the spin system. The $(N-1)$ -quantum spectrum of an N -spin system ($I = 1/2$), with no simplifying symmetry, will

Table 2. The number of transitions in the M -quantum spectra as a function of the number (N) of interacting nuclei ($I = 1/2$)

	Number of interacting spins ($I = 1/2$)						
N	2	4	8	10	15	20	25
M							
1	4	56	1.1×10^4	1.7×10^6	1.5×10^8	1.3×10^{11}	1.3×10^{14}
2	1	28	8.0×10^3	1.3×10^5	1.2×10^8	1.1×10^{11}	1.1×10^{14}
4	—	1	1.8×10^3	3.9×10^4	4.5×10^7	6.3×10^{10}	6.7×10^{13}
8	—	—	1	1.9×10^2	2.0×10^6	5.6×10^9	9.5×10^{12}
10	—	—	—	1	1.4×10^5	8.5×10^8	2.3×10^{12}
15	—	—	—	—	1	6.6×10^5	1.0×10^{10}
20	—	—	—	—	—	1	2.1×10^6
25	—	—	—	—	—	—	1
$N-3$	—	56	560	1.1×10^3	4.1×10^3	9.9×10^3	2.0×10^4
$N-2$	—	28	120	190	435	780	1.2×10^3
$N-1$	4	8	16	20	30	40	50

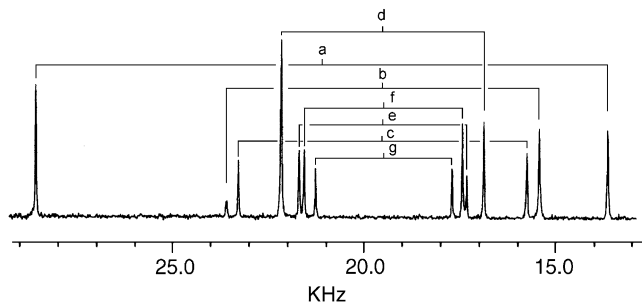
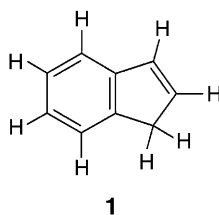


Fig. 1. 7Q ¹H NMR spectrum of indene (**1**) partially aligned in a nematic liquid crystalline solution. (Reproduced with permission from ref. 62.)

always consist of $(N-1)$ doublets, with each doublet centred on the sum of chemical shifts of the $N-1$ protons that contribute to the coherence.

Fig. 1 shows the ¹H 7Q spectrum of indene (**1**). This is an 8-proton spin system and the 7Q spectrum can be analysed as distinct seven doublets each centred at the sum of the chemical shifts of the nuclei, which contribute to the coherence.



The frequencies of transitions in the MQNMR spectra are determined by chemical shifts, scalar, dipolar and quadrupolar couplings (as are conventional single quantum NMR spectra). For large spin systems, the N , the $N-1$ and $N-2$ quantum spectra will contain only relatively few transitions, there will be significantly less overlap between transitions and the spectra are more easily analysed than the 1-quantum spectrum. In many spin systems, the analysis of the high-order MQNMR spectra has been used to provide spectral parameters that have then been used to analyse the more complex single quantum spectrum. The 1-quantum spectrum can typically be obtained with higher digitisation and resonances are typically sharper, providing a solution that is inherently more accurate if spectral overlap is not prohibitively severe.

4. EXCITATION AND DETECTION OF MULTIPLE QUANTUM COHERENCE

MQ coherences (MQCs) cannot be observed directly, however MQ coherences generated in a spin system, can be observed indirectly by their

modulation of observable single quantum coherences. MQNMR spectra can be readily obtained by using an appropriate two dimensional (2D) NMR experiment.

4.1. Non-selective excitation/detection of multiple quantum coherence

The most general method¹² for generating MQC in a homonuclear-coupled spin system by means of two non-selective $\pi/2$ pulses separated by a fixed time interval τ . The value of τ should be greater than (or of the same order as) the reciprocal of the dipolar couplings in the spin system and this simple 2-pulse sequence generates all order of MQC in the spin system. In this basic sequence (Fig. 2), t_1 , the time for which MQC are permitted to evolve, is incremented systematically in a 2D NMR experiment, 2D transformation against t_1 and t_2 gives rise to a 2D spectrum with single quantum transitions in f_2 and MQ spectra in f_1 .

Various orders of MQC can be separated by judicious choice of the transmitter offset. MQCs evolved at the sum of the chemical shifts of the nuclei contributing to the coherence spectra of order M are offset by approximately $M\Delta\omega$, where $\Delta\omega$ is the average chemical shift of nuclei in the spin system with respect to the transmitter offset. By carefully choosing the transmitter offset, the various orders of MQC can be separated with no overlap (Fig. 3). Useful MQNMR spectra are then typically extracted as f_1 projections (or as f_1 slices) from the 2D spectrum. If the phases of all three pulses in the simple sequence are maintained constant (Fig. 2) and the phase of the detector is kept constant, then the resulting MQ spectrum contains all orders of coherences (Fig. 4). Since most spectra of partially aligned solutes typically span tens of thousands of hertz, cleanly separating all orders of coherence requires a very large f_1 sweep width. While the offset method of separating MQ spectra is useful because it allows the spectra of all orders of coherence to be obtained simultaneously (in one experiment), in practice, the spectral width required to accommodate all MQ spectra without overlap is very large and this limits the digital resolution in the MQ (f_2) dimension of the 2D spectrum.

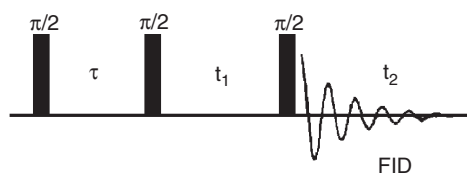


Fig. 2. Basic 3-pulse sequence for generating MQNMR spectra.

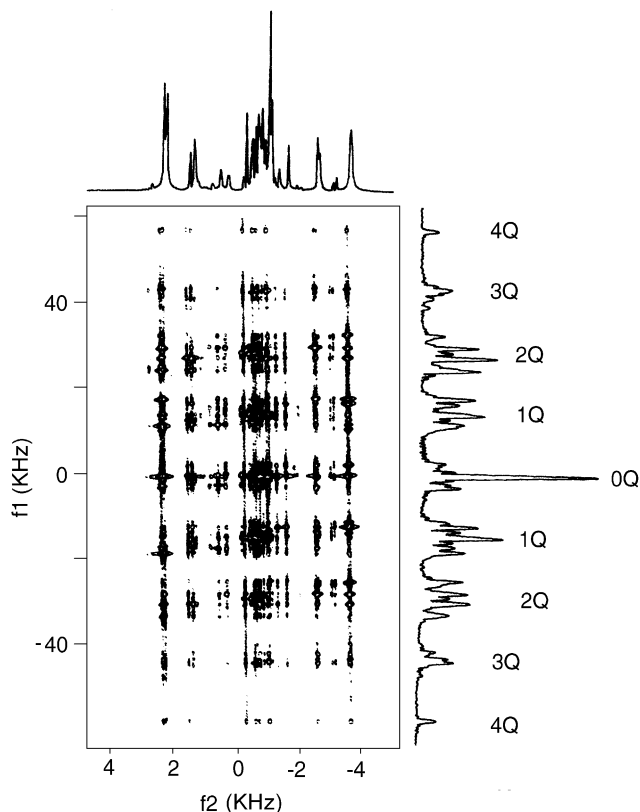


Fig. 3. Two-dimensional MQNMR spectrum of 3-chloriodobenzene (**2**) oriented in liquid crystalline solution with non-selective excitation and detection (Fig. 2). 1,024 increments in f_1 , 12 scans per increment, 48 kHz in f_2 , 160 kHz in f_1 , 400 MHz at 295 K, transmitter offset 18 kHz from the centre of the ^1H spectrum. The transmitter offset was set to provide dispersion between the various MQ spectra.

MQCs are not excited uniformly and the efficiency with which the various orders of MQC are excited depends specifically on the parameters of the spin system (dipolar couplings, scalar couplings, quadrupolar couplings, chemical shifts) in the spin system and the choice of the preparation time τ . Many researchers have co-added spectra acquired with different preparation times to ensure that all transitions are observed with reasonable intensity. A number of “broadband” excitation techniques have been developed,^{13–15} where the value of τ in the preparation sequence has been varied either in a pseudo-random or systematic fashion to achieve a more uniform excitation in the multiple quantum domain. An experimental search method has been used to optimise the delays in the preparation period of the MQ excitation sequence¹⁶ and Wimperis¹⁷ used average Hamiltonian theory to propose

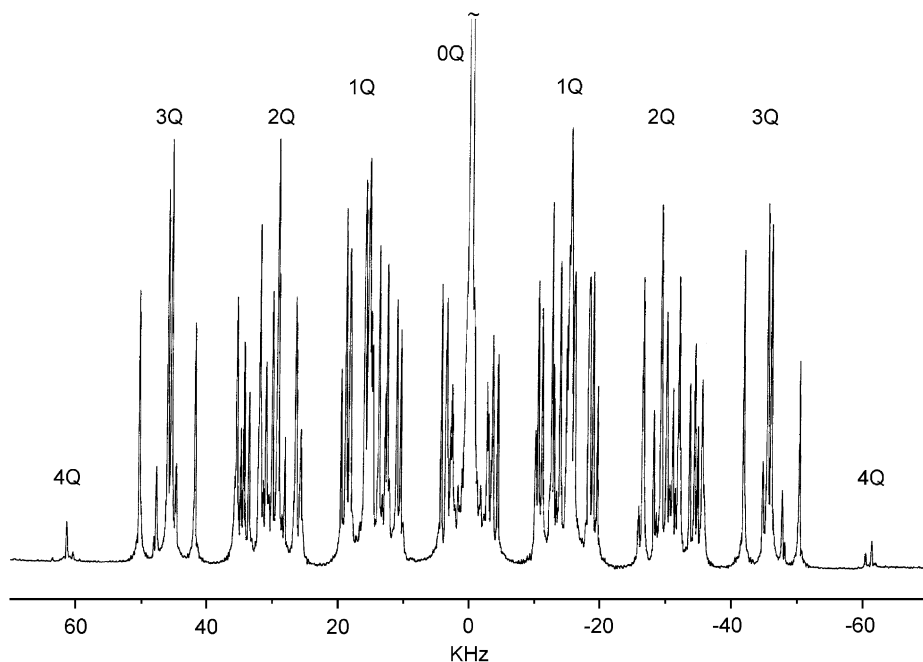
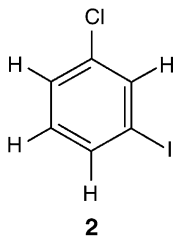


Fig. 4. MQNMR spectra of 3-chloriodobenzene (**2**) aligned in liquid crystalline solution, extracted as the f_1 projection from the 2D spectrum in Fig. 3. (Adapted with permission from ref. 40.)

broadband excitation sequences to achieve uniform excitation of MQC over a range of couplings in the spin system.



4.2. Selective excitation of multiple quantum coherence

Non-selective excitation excites all possible MQCs, however most of the spectral intensity remains in the single quantum and lower-order MQ spectra.¹⁸ There have been a number of methods employed to excite one order of coherence in a spin system or to selectively excite only a few orders of coherence. In principle, this more effectively focuses the available intensity into one order or a set of selected orders and should lead to improved quality of higher-order MQ spectra.

$$\begin{array}{cccc} \phi = 2\pi/N & \phi = 4\pi/N & \phi = 6\pi/N & \phi = 2\pi \\ \boxed{p_1 \dots p_q} & \boxed{p_1 \dots p_q} & \boxed{p_1 \dots p_q} & \dots \dots \boxed{p_1 \dots p_q} \end{array}$$

Fig. 5. General form of the pulse sequence employed for order-selective excitation.^{19,24}

Order selective excitation has been achieved by the use of phase-cycled sequences of Rf pulses^{19–24} and composite pulse trains.²⁵ Warren and Pines^{19–24} established that it was possible to construct Nk -quantum selective excitation sequences ($k = 0, \pm 1, \pm 2, \dots$) by systematically repeating an appropriate train of pulses with a phase increment $2\pi/N$ between repetitions (Fig. 5).

Specific pulse trains $[p_1 \dots p_q]$ employed in each section of the sequence are effective in generating selected orders of MQC and sequences involving several thousand-cycled pulses have been explored.^{19–24} Such extended repeating pulse sequences have a high transmitter duty cycle and may cause heating and temperature gradients in the sample. This has limited the application of these sequences in liquid crystalline solutions where temperature stability is critical. The length of the excitation sequence is also limited by relaxation in the spin system and the better phase-cycled excitation sequences compensate for cumulative errors that can arise through pulse imperfections.

Pulse sequences, which are selective for desired orders of coherence in spin systems of given topology and symmetry have also been developed.^{26,27}

DANTE-type frequency-selective pulses have also been used to selectively excite specific nuclei in the spin system and this has been employed to simplify MQ spectra. This approach is limited to relatively simple spin systems where the resonances of some nuclei are well separated from the normally overlapped signals in the spectrum.^{28,29}

4.3. Selective detection of MQC

A number of methods have been developed to enable MQ spectra of various orders to be observed selectively. Generally, a non-selective sequence (such as that in Fig. 2) is used to generate all orders of coherence in the spin system, then some type of filtering is used to remove or cancel unwanted coherence so that the detected signal reflects only the desired order(s) of coherence.

4.3.1. Phase cycling

The simplest approach to selective detection of MQ spectra involves phase-cycling in the basic 3–pulse sequence (in Fig. 2) to allow selection of the

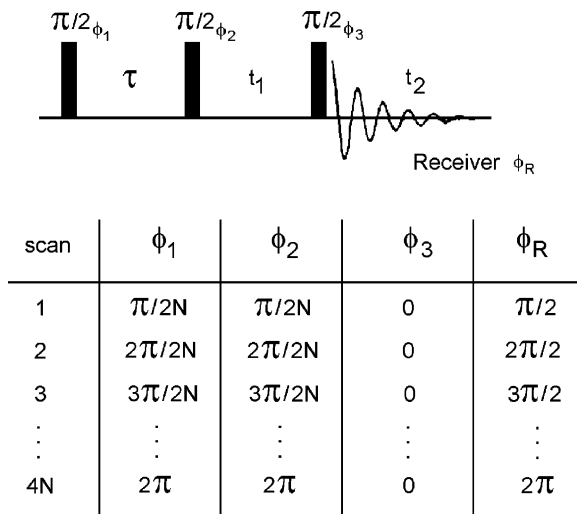


Fig. 6. Phase cycle required for selective detection of MQ spectra.

spectrum of a particular order of coherence. In any spin system, order selective detection of the spectrum of order N is achieved by coadding $4N$ FIDs at each value of t_1 with the phase of the first two pulses incremented from $2\pi/4N$ to 2π in steps of $2\pi/4N$ with the receiver phase incremented by $\pi/2$ at each step (Fig. 6).^{30–33} Fig. 7 provides an example of the selective detection of the 3-quantum spectrum of the 4-spin system of 3-chloriodobenzene (**2**) aligned in nematic liquid crystalline solution.

One limitation of the phase-cycling method of selective detection is the expanding length of the required phase cycle as the order N increases. The number of steps in the phase cycle is $4N$; so for large N , this dictates that the phase cycle becomes prohibitively long and, in practice, this limits the number of increments that can be obtained in f_1 and hence ultimately the digital resolution of the MQ spectra which can be obtained.

4.3.2. Magnetic field gradients

Order-selective detection of the spectrum of a desired order ' N ' can also be achieved using magnetic field gradients.³⁴ A field gradient pulse of amplitude g is applied at the end of the MQ evolution period, prior to the mixing pulse of the MQ pulse sequence (Fig. 8). The first gradient effectively labels all coherence in the spin system and a gradient of amplitude Ng immediately after the mixing pulse selects only coherences arising from the N -quantum domain.^{35–39} By changing the $g_1 : g_2$ ratio different orders of coherence can be selected. Fig. 9 shows the 2Q, 3Q and 4Q spectra of 3-chloriodobenzene (**2**), (a 4-proton spin system) obtained using the sequence in Fig. 5 changing

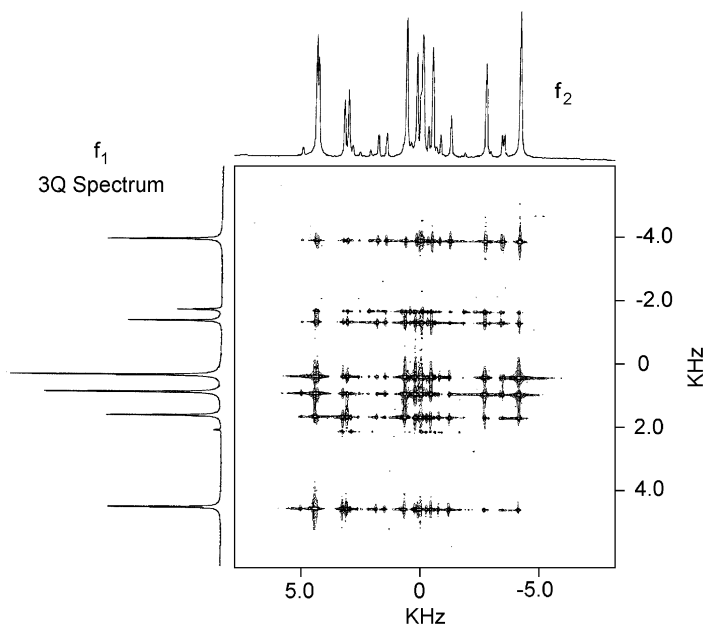


Fig. 7. 3Q ^1H NMR spectrum of 3-chloriodobenzene (**2**) aligned in liquid crystalline solution. The f_1 projection on the left is the MQ spectrum. (Adapted with permission from ref. 40.)

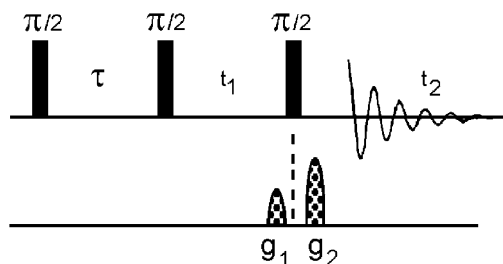


Fig. 8. Pulse sequence required for selective detection of coherence of order M using magnetic field gradients.

the $g_1:g_2$ ratio from 2.0 to 4.0.⁴⁰ Spectra are only obtained when the field gradients are precisely matched in the correct ratio to select the desired order of coherence.

Spectra obtained using magnetic field gradients to selectively filter the desired order of coherence are typically much cleaner than those obtained using phase cycling for MQ filtration, since the sequence does not rely on

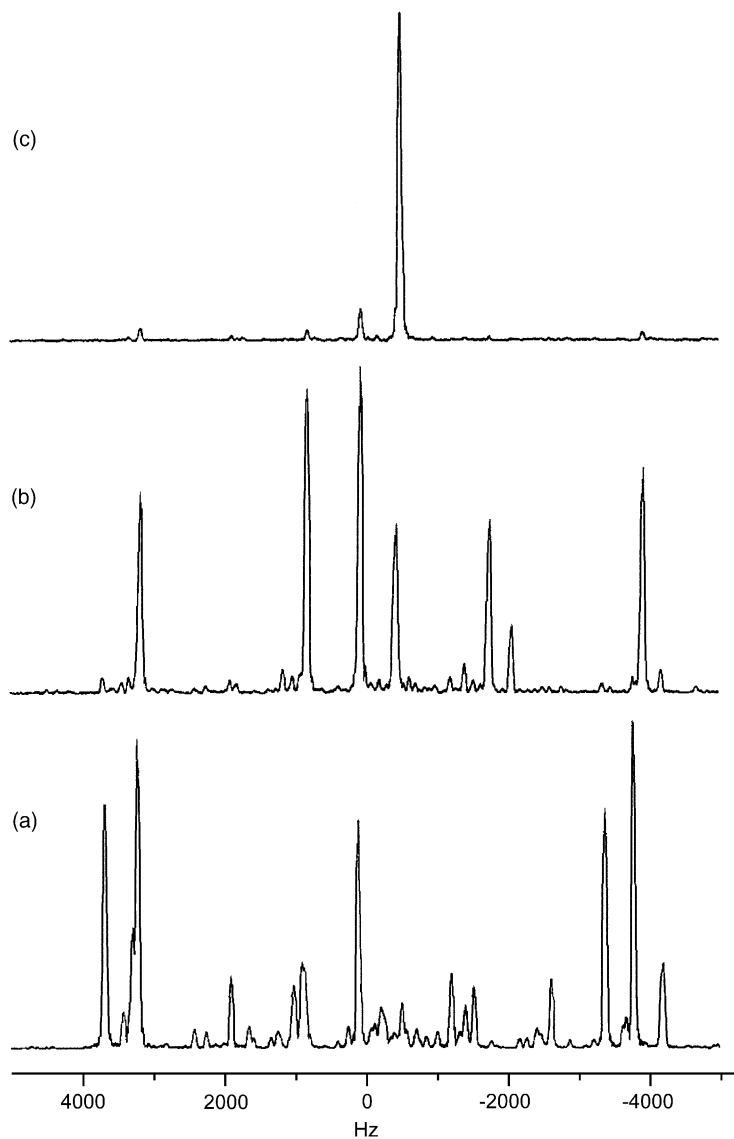


Fig. 9. ^1H multiple quantum spectra of 3-chloriodobenzene (2) obtained using the sequence in Fig. 8 as a function of the $g_1:g_2$ ratio. (a) The 2Q spectrum obtained when the ratio of $g_1:g_2$ is 2.0; (b) the 3Q spectrum obtained when the ratio of $g_1:g_2$ is 3.0; (c) the 4Q spectrum obtained when the ratio of $g_1:g_2$ is 4.0. (Adapted with permission from ref. 34.)

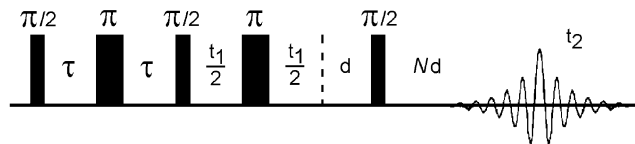


Fig. 10. Pulse sequence for selective detection of coherence of order N by capturing coherence transfer echoes.

perfect signal cancellation over a long cycle of FIDs. Spectra can also be obtained much more rapidly since there is no need to acquire multiple FIDs in an extended phase cycle to achieve selective detection.

4.3.3. Coherence transfer echos

The phase properties of MQC transfer echoes have also been employed to selectively detect desired orders of MQ spectra. Using the basic sequence (Fig. 2), an additional (fixed) period d is inserted in the MQ pulse sequence, prior to the mixing pulse of the MQ pulse sequence (Fig. 10). MQC evolves beyond the normal t_1 period and coherence transfer echoes of the N -quantum coherences maximise in the detection period at a time Nd .^{35,41,42} The echoes of different coherence orders maximise at different times in the detection period and the spectra of different orders of coherence can be obtained by sampling the FID in the appropriate window in the detection period.

4.4. Time proportional phase incrementation and order selective detection using 3D NMR

If the phase of the excitation radiation is incremented by $\Delta\phi = \Delta\omega\Delta t_1$ each time that t_1 is incremented by Δt_1 in the 2D NMR experiment i.e. time proportional phase incrementation (TPPI), the N -quantum spectrum is offset by a frequency $N\Delta\omega$ from the transmitter in the 2D NMR spectrum. MQ orders are separated in frequency by $\Delta\omega$ in the same fashion as if an offset had been employed.

Syvitski *et al.*⁴³ reported a 3D sequence which uses TPPI to separate the spectra of different coherence orders. The pulse sequence employs a non-selective 2D excitation sequence (as in Fig. 2) but also systematically increments the phase of the first two pulses in the excitation sequence by $\Delta\phi$ at each value of t_1 (Fig. 11). The number of phase increments ($\Delta\phi$) in the experiment is arbitrary but needs to be at least $2N + 1$, where N is the number of spins in the spin system. The 3D interferogram is then a function of t_1 , ϕ and t_2 and Fourier transformation over these dimensions^{6,30,44} affords MQ spectra of various orders cleanly separated in the “pseudo-frequency”

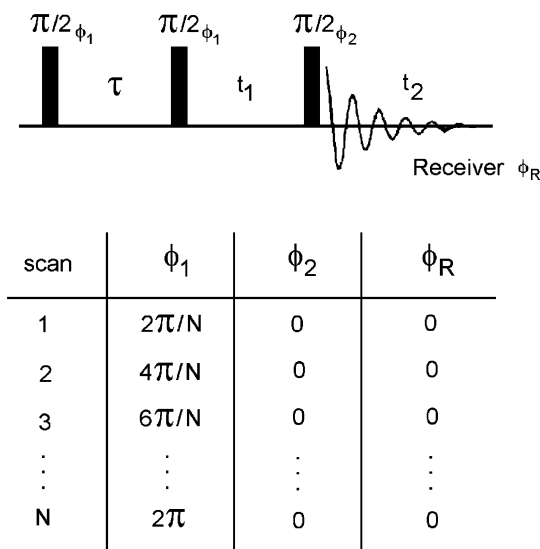
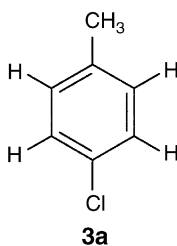


Fig. 11. Pulse sequence and phase-cycling scheme for the acquisition of a 3D data set, which separates the spectra of various MQ orders in one of the dimensions.

dimension resulting from transformation against ϕ . Fig. 12 shows the various MQ spectra for 4-chlorotoluene (**3a**) obtained as projections from a single 3D experiment. This spin system contains seven protons and there is considerable time saving in obtaining MQ spectra simultaneously in a single 3D acquisition compared to the time required to obtain individual MQ spectra selectively using phase cycling.



4.5. MQ filters to simplify 1Q spectra

The allowed transitions in the N and $(N-1)$ quantum spectra of an N -spin system must belong to the highest symmetry class of the spin permutation group. By creating N or $(N-1)$ quantum coherence and then converting this into an observable 1Q coherence, one obtains a symmetry-filtered 1Q-spectrum which contains only a subset of those transitions originating from the most symmetric class. The 1Q spectra of solutes aligned in liquid crystalline

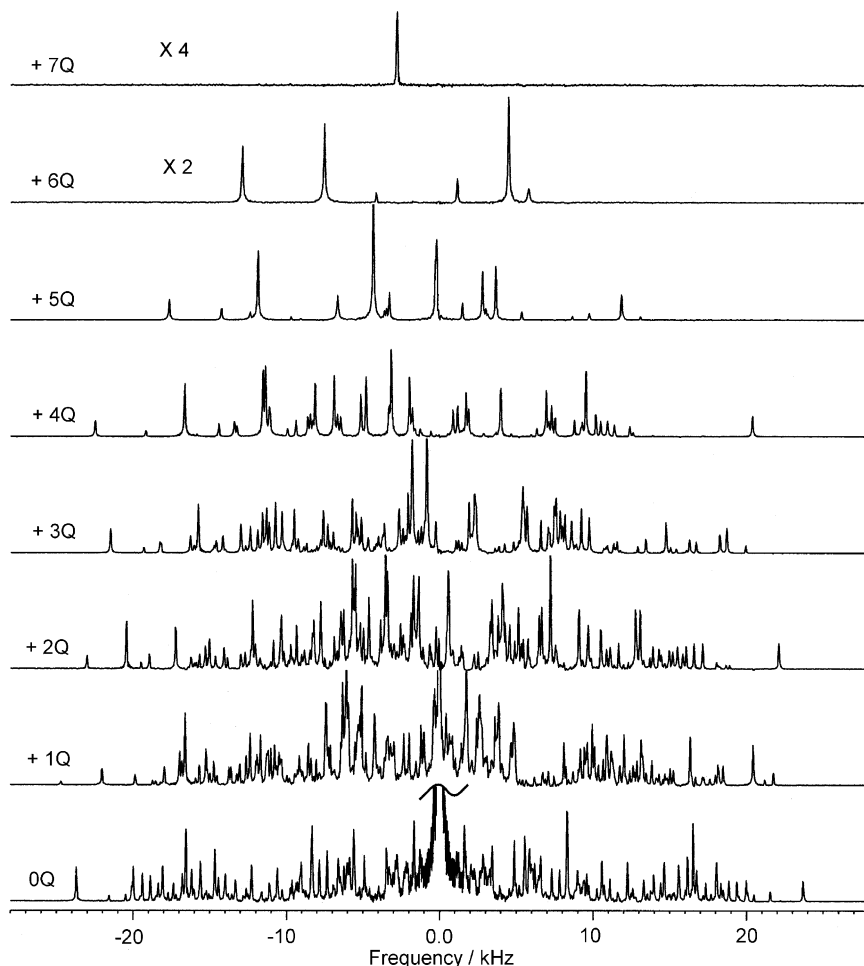


Fig. 12. Multiple quantum spectra of 4-chlorotoluene (**3a**) aligned in liquid crystalline solution obtained as projections from the 3D spectrum acquired using the pulse sequence in Fig. 11. (Reproduced with permission from ref. 43.)

solution are considerably simplified by selecting those transitions belonging to a given symmetry class⁴⁵ and these MQ-filtered spectra contain substantially fewer transitions than the non-filtered spectra, with significantly less spectral overlap and the spectra can be more readily analysed to give dipolar couplings and chemical shifts.

This concept was extended by Carravetta *et al.*⁴⁶ to larger spin systems. Iterative analysis of the symmetry-selected, MQ-filtered single quantum spectra of spin systems up to eight spins ($I = 1/2$) has been used to determine dipolar coupling constants of molecules aligned in liquid crystalline

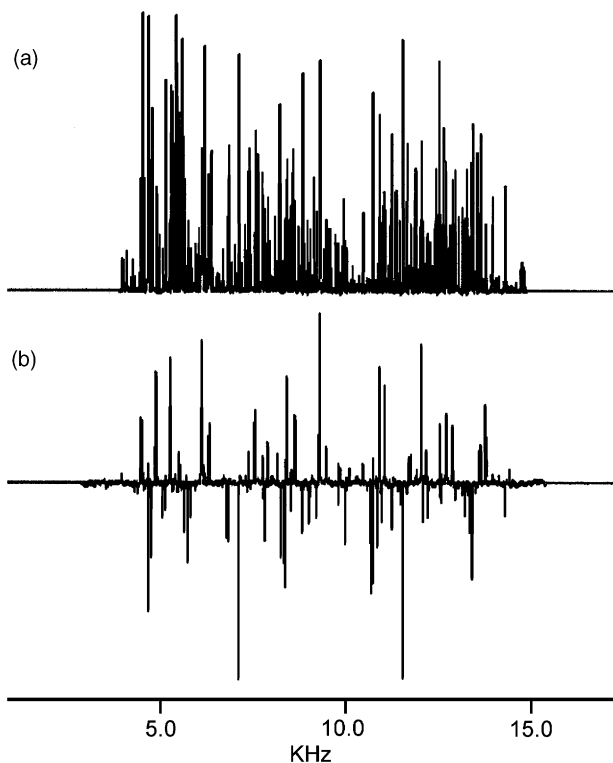
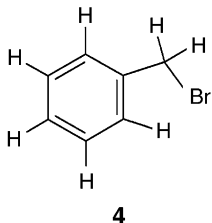


Fig. 13. (a) The 500 MHz 1Q spectrum of a sample of benzyl bromide (**4**) aligned in a nematic liquid crystalline solvent. (b) The 7Q-filtered 1Q spectrum of the same sample. (Adapted with permission from ref. 46.)

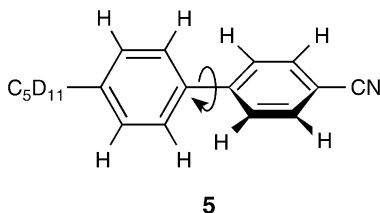
solution. Fig. 13 shows the 7Q-filtered 1Q spectrum of a sample of benzyl bromide (**4**) (a 7-spin system) aligned in a liquid crystalline phase.



5. SELECTIVE DEUTERATION TO SIMPLIFY SPECTRAL ANALYSIS

Another approach to the simplification of proton NMR spectra of solutes dissolved in liquid crystalline solvents is by selective, partial deuteration

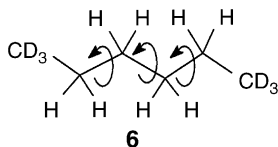
followed by deuterium decoupling.^{47,48} In the early 1980s, Sinton and Pines⁴⁹ and Sinton *et al.*⁵⁰ first demonstrated that MQNMR spectra could be used to simplify the complex NMR spectra arising from complex spin systems derived from oriented molecules. Using the side-chain deuterated liquid crystal, 4-cyano-4'-pentylbiphenyl (5CB-*d*₁₁) (**5**), Sinton and Pines⁴⁹ reported excellent 5Q, 6Q and 7Q spectra on the 8-proton spin system and successfully simulated and analysed the MQ spectra to extract dipolar couplings. The molecule is strongly aligned and the intramolecular dipolar couplings were used to model the structure and conformation of the biphenyl subunit including an estimate of the torsional angle between the phenyl rings.



Deuteration is generally synthetically challenging and, in many cases, simply not possible. In addition, deuterium substitution is known to cause small but significant changes to orientation and structure⁵¹ so it is not always easy to mount the argument that deuteration has no (or little) effect on molecular structure or alignment. Broadband heteronuclear ²H decoupling can also cause sample heating which makes spectral acquisition more challenging, since the molecular alignment in liquid crystalline solution is very temperature sensitive.

A combination of both selective deuteration as well as MQNMR has been used to determine the dipolar coupling constants in larger spin systems. In a mixture of randomly deuterated benzenes, Gochin *et al.*⁵² extracted all of the coupling constants by analyzing the sub-spectra containing 2, 3, 4 and 5 protons. This principle was extended to the study of randomly deuterated alkanes,^{52–56} where the analysis of double quantum-filtered COSY spectra, INADEQUATE spectra and MQ spectra permitted the measurement of all of the interproton dipolar couplings. A detailed analysis of dipolar couplings obtained for alkanes from C6 to C10⁵⁶ indicated a *trans-gauche* energy difference of 2.1–2.7 kJ/mol that was consistent with other measurements of alkane conformation in the condensed phase. Gochin *et al.*⁵³ reported the spectrum of heavily deuterated hexane (81% deuterium exchanged), aligned in liquid crystalline solution. Deuteration was to the extent that, on average, only two protons remain in each molecule and the double-quantum spectrum and the double-quantum-filtered COSY spectrum (with ²H decoupling) were used to derive all 16 *D_{ij}*s in the spin system.

Fully protonated hexane (C_6H_{14}) has 14 protons in the spin system and Drobny⁹ reported the MQ spectra of *n*-hexane- d_6 (deuterated in the terminal methyl groups) dissolved in a nematic solvent. Analysis of the 6Q and 7Q spectra of hexane- d_6 , (**6**) was used to establish the relative signs of the dipolar couplings. The 6-quantum proton spectrum contains 36 transitions and the 7-quantum spectrum contains 4 transitions, as expected for an 8-proton spin system with C_{2h} symmetry. The best fit of theoretically generated MQNMR spectra to the experimental spectra were obtained with a model where only the all-trans conformations of the alkane chain were appreciably populated.



6. THE ANALYSIS AND SIMULATION OF MULTIPLE QUANTUM SPECTRA

The energy levels in a given spin system can be calculated from a knowledge of the dipolar coupling constants (D_{ij}), scalar coupling constants (J_{ij}), chemical shifts (ν_i) and quadrupolar coupling constants (q_{ij}). The energy levels fall into manifolds according to their Zeeman quantum number (M) and irreducible symmetry representations. N -quantum transitions occur between energy levels of the same symmetry where the difference in the Zeeman quantum number (ΔM) between levels is equal to N . The frequencies of MQ transitions can be calculated from energy levels in the spin system. A number of groups have devised algorithms, which enable the frequencies in experimental MQ spectra to be fitted iteratively to calculated frequencies using modifications of LAOCOON-type^{57,58} or LEQUOR⁵⁹ computer programs.

Note that these approaches calculate the frequencies of the MQ transitions without attempting to predict transition intensities and for the purposes of spectral analysis this is usually adequate. In most MQNMR experiments, the transition intensities depend on the spin system itself and on the specific pulse sequence used to generate the spectrum. There are now a number of effective and increasingly sophisticated simulation programs, which mimic the entire NMR experiment, i.e. the spectral output expected when a spin system is subjected to a given pulse sequence. These programs can give a good approximation of the intensities of MQ transitions on a given spin system; however, this approach has yet to be used in the complete analysis of MQNMR spectra (Fig. 14).

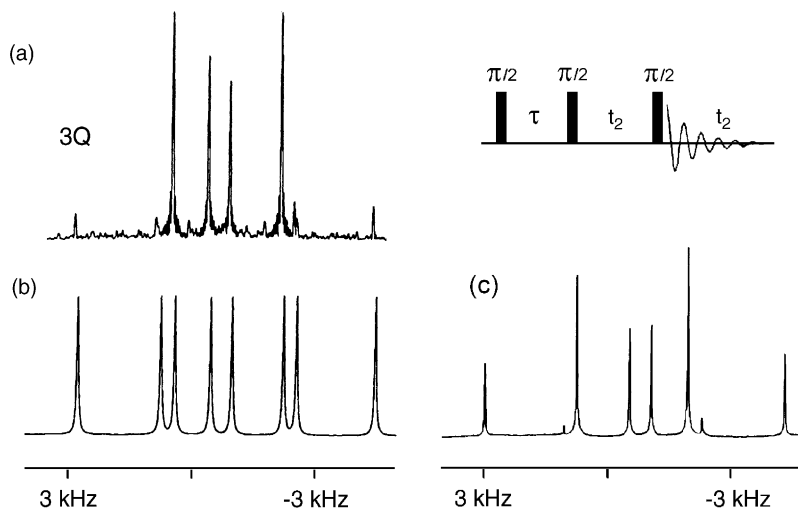


Fig. 14. 3-quantum spectra of 3-chloriodobenzene (**2**) aligned in liquid crystal-line solution. (a) Experimental spectrum obtained with the pulse sequence and phase cycling in Fig. 6 to selectively give the 3Q spectrum; (b) iterative best fit-simulated spectrum based only on the observed transition frequencies – no calculation of transition intensities; and (c) complete spectrum simulated from the pulse sequence using the best-fit parameters obtained as in (b).

The transition intensities in MQ spectra derived from the simple 3-pulse sequence (Fig. 2) have also been estimated using a statistical approach where all symmetry allowed transitions were assumed to be excited equally. Averaging over a range of τ values, the integrated intensity per order decreases as the observed order of coherence increases, but since the number of transitions decreases, the average intensity per transition increases as the observed order of coherence increases.¹⁸ Estimating the transition intensities in MQ spectra has also been extended to excitation sequences involving order-selective composite pulse excitation and these calculations provide a means for theoretically optimising the efficiency of the excitation sequence.⁶⁰

An automated protocol for sequentially analysing MQ spectra to obtain reasonable estimates of spectral parameters then analysing 1Q spectra has been developed.⁶¹ The analysis of MQNMR spectra has frequently been used to provide good initial estimates of parameters to permit the analysis of 1Q spectra where these are well resolved.

6.1. Chemical shift refocusing

If the aim of the spectral analysis is to extract dipolar couplings, D_{ij} (and hence structural information), then information about the chemical shifts of

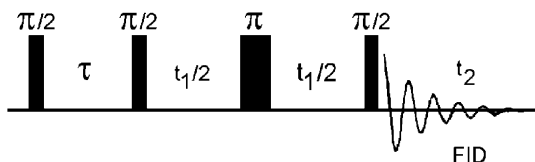


Fig. 15. Basic pulse sequence for the acquisition of MQ spectra with chemical shift refocusing.

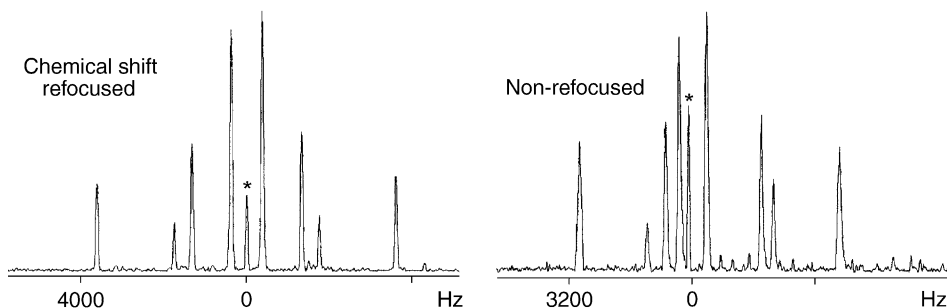


Fig. 16. 6Q spectrum of 4-chlorotoluene (3) aligned in nematic liquid crystalline solution (a) with chemical shift refocusing and (b) with no chemical shift refocusing. Signals marked (*) arise from the use of imperfect pulses. (Adapted with permission from ref. 83.)

the nuclei in the spin system is not actually required. There are fewer parameters to fit in the analysis of MQ spectra if the spectra are acquired with chemical shift refocusing. Shift refocusing is typically achieved by inserting a π pulse at the mid point of the MQ evolution period (Fig. 15). MQ spectra acquired with this sequence are always symmetrical about the offset frequency and the spectra obtained contain no information about the chemical shifts of spins in the spin system. Fig. 16 shows the 6Q spectra of 4-chlorotoluene (3) acquired with and without chemical shift refocusing. The 6Q spectrum with chemical shifts refocused consists of four doublets symmetrically disposed about the transmitter offset.

6.2. Estimating order parameters by MQNMR

The total spectral width of any MQ spectrum is dominated by the values of the dipolar couplings in the spin system. The dipolar couplings in turn are a function of the order parameters and the internuclear distances (Eq. (3)). The iterative analysis of most spectra of aligned molecules typically begins with a trial geometry then by trial and error assessing possible molecular ordering to provide a visual match to spectral features. Model compounds

or molecular modelling can be used to provide a reasonable molecular geometry. It is, however, much more difficult to obtain reasonable estimates of the orientation parameters.

Field *et al.*⁶² developed a general procedure to estimate the Saupe order parameters for spin systems aligned in liquid crystal media by iteratively fitting the experimental and simulated spectral widths of the high-order multiple quantum spectra.

For the 8-spin system of indene (**1'**), aligned in liquid crystalline solution, the observed spectral widths of the 5Q, 6Q and 7Q spectra were measured at 30428, 23185 and 14940 Hz, respectively (Fig. 17).

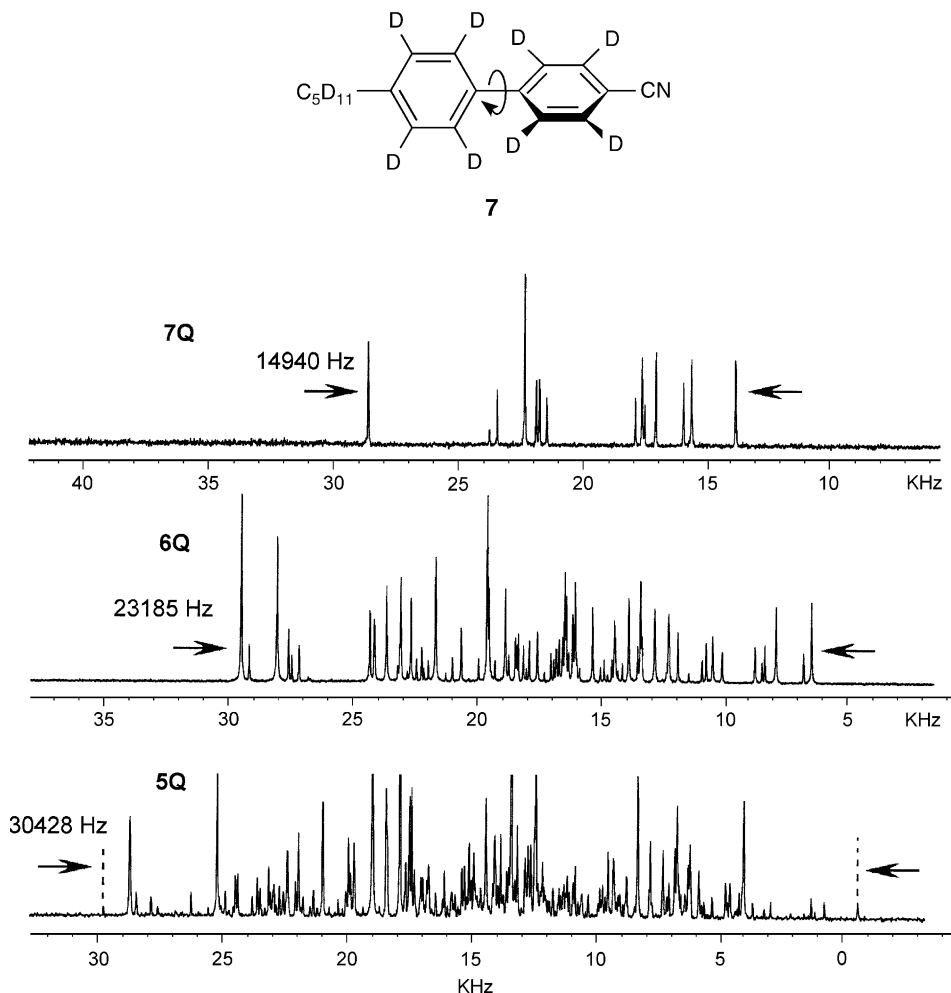
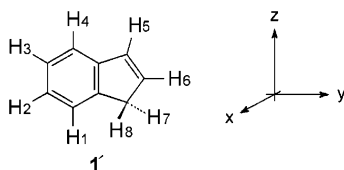


Fig. 17. 5Q, 6Q and 7Q spectra of indene (**1**) partially oriented in liquid crystalline solution. (Reproduced with permission from ref. 62.)



The proton spin system of indene has C_s symmetry and H_7 and H_8 are out of the aromatic plane. Three non-zero independent order parameters (S_{yy} , S_{zz} and S_{yz}) are required to define the molecular orientation. The spectral widths of simulated MQ spectra were obtained varying the order parameters S_{yy} and S_{zz} through all possible values (with S_{yz} fixed arbitrarily at 0) using estimates of the atomic coordinates for the protons of the spin system obtained from a molecular modelling programme.⁶³ There is an infinite number of combinations of S_{yy} and S_{zz} that can give a 6Q spectrum whose width is 23185 Hz (Fig. 18A); and likewise there is an infinite number of combinations of S_{yy} and S_{zz} that can give a 7Q spectrum whose width is 14,940 Hz (Fig. 18B). However, there are only very few combinations of S_{yy} and S_{zz} , which can simultaneously fit both the observed spectral widths of both the 6Q and 7Q spectra (Fig. 19). This analysis immediately gives reasonable estimates of the possible order parameters that can provide a match to the experimental data and the points marked A–D in Fig. 19, indicate sets of orientation parameters which simultaneously satisfy the observed experimental spectral widths of the 6Q and 7Q spectra. The process was automated such that a computer algorithm could search for suitable estimates of the orientation parameters based on the spectral widths of the MQ spectra.

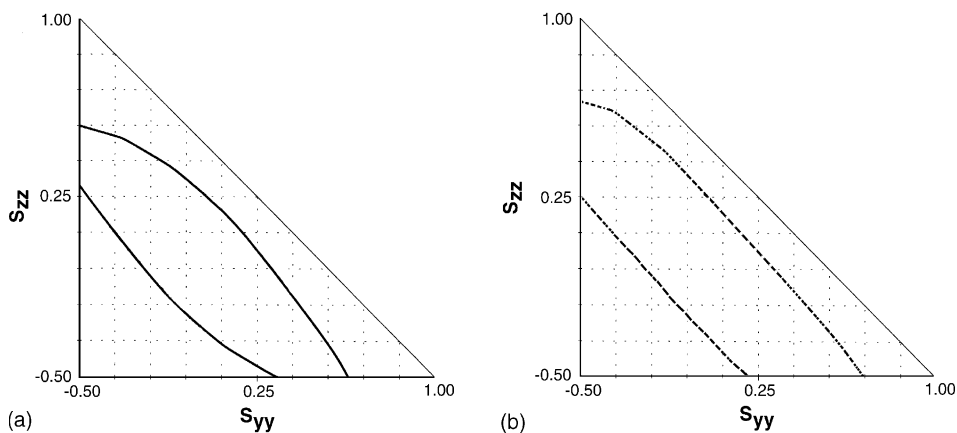


Fig. 18. Simulated spectral width as a function of molecular orientation for the 6Q (A), and 7Q (B) spectra of indene (**1**) partially oriented in liquid crystalline solution. (Reproduced with permission from ref. 62.)

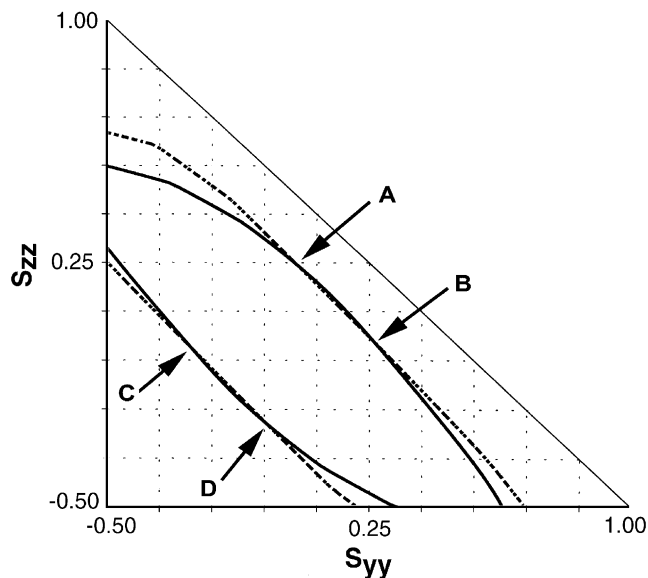
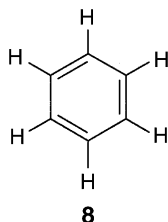


Fig. 19. Simultaneous simulated spectral widths as a function of molecular orientation for the 6Q, and 7Q spectra of indene (**1**) partially oriented in liquid crystalline solution. (Reproduced with permission from ref. 62.) Points marked A–D indicate sets of orientation parameters, which simultaneously satisfy the observed experimental spectral widths of both the 6Q and 7Q spectra.

7. HETERONUCLEAR MQNMR

Heteronuclear multiple quantum coherence (HMQC) is MQ coherence involving spins of different types, eg. $^1\text{H}/^2\text{H}$, $^1\text{H}/^{13}\text{C}$, $^2\text{H}/^{13}\text{C}$, $^1\text{H}/^{15}\text{N}$. Mi-norette *et al.*⁶⁴ demonstrated that there is a significant sensitivity advantage when the MQ coherences of a relatively insensitive nucleus such as ^2H can be detected indirectly by observing ^1H nuclei coupled to the heteronuclear spin system and Castiglione *et al.*⁶⁵ have used HMQC as an aid to the automatic analysis of spectra from molecules aligned in liquid crystalline solution.



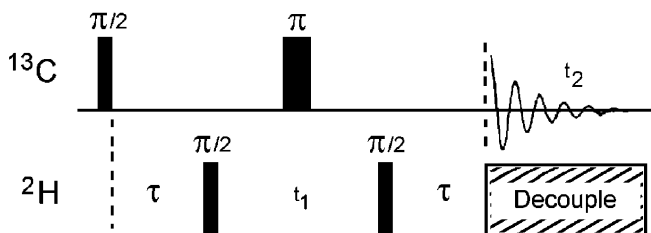


Fig. 20. Heteronuclear multiple quantum pulse sequence used for ^2H – ^{13}C correlation.

Sandröm and Zimmerman⁶⁶ have used heteronuclear MQC, using the heteronuclear pulse sequence in Fig. 20, to correlate shifts in ^{13}C and ^2H spectra of fully deuterated liquid crystal 4-cyano-4'-pentylbiphenyl (5CB- d_{19}) (7) aligned in a magnetic field (Fig. 21). The carbon–deuterium correlation permitted the assignment of the ^2H spectrum and deuterium quadrupole splittings were then used to estimate the molecular alignment. ^2H – ^{13}C correlation of fully deuterated 5CB (7) has also been studied by HMQC under off-magic-angle-spinning conditions.⁶⁷

8. MEASURING DIFFUSION IN ANISOTROPIC MEDIA USING MQNMR

The well-established NMR spin-echo measurement of diffusion can be extended by using MQNMR. N -quantum coherences dephase N -times more quickly than do single quantum coherences in an inhomogeneous magnetic field; so higher quantum coherences are more sensitive to molecular diffusion. In typical spin-echo experiments, molecules are position-labelled in a magnetic field gradient after an initial Rf pulse and diffusion is monitored by measuring the amplitude of the spin echo following a second pulse.

Martin *et al.*³⁸ measured the diffusion of methylene chloride (CH_2Cl_2) in liquid crystalline solvents by following the decay of the double quantum coherence. Zax and Pines³⁹ measured diffusion of benzene in a nematic liquid crystalline solution using a pulse sequence (Fig. 22) which non-selectively excites MQC, permits this to evolve in the presence of a magnetic field gradient, then uses a series of N identical gradient-delay periods to selectively provide an echo which arises solely from the N -quantum coherence in the evolution period t_1 .

The amplitude of echo decay for each order of coherence was fitted to a modified Stejskal–Tanner equation⁶⁸ (Eq. (4)) verifying that the rate of echo

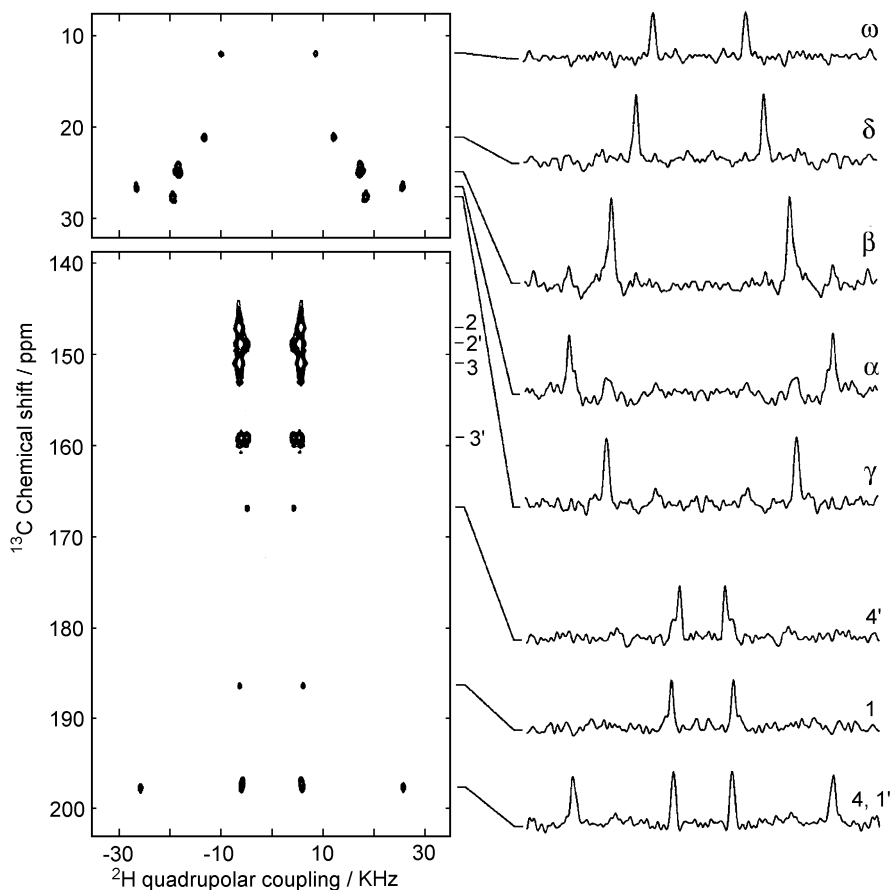


Fig. 21. Two-dimensional ^2H - ^{13}C correlation spectrum of 5CB- d_{19} (**7**) obtained with the pulse sequence in Fig. 20. (Reproduced with permission from ref. 66.)

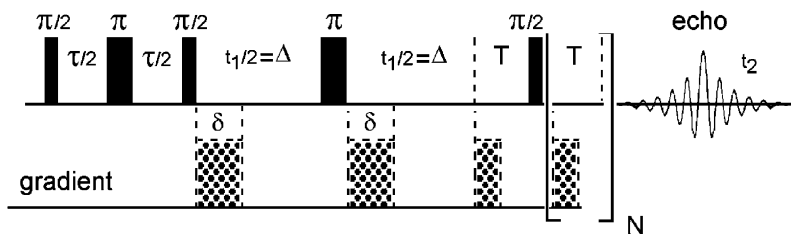
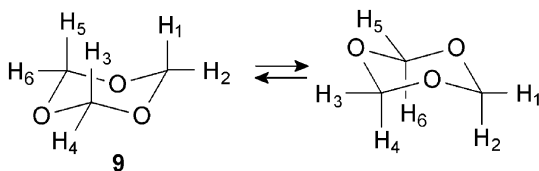


Fig. 22. Multiple quantum pulsed-field gradient sequence. The experiment is typically performed with Δ fixed, the value of δ incremented systematically.³⁹

decay is proportional to N^2 .

$$\ln \left[\frac{A(t_1)}{A_0(t_1)} \right] = -\gamma N^2 g^2 D \left[\delta^2 \left(\Delta - \frac{\delta}{3} \right) \right] \quad (4)$$

where $A(t_1)$ is the observed echo amplitude, $A_0(t_1)$ the amplitude in the absence of a gradient, γ the magnetogyric ratio of the observed nucleus, N the multiple quantum order being observed, D the diffusion coefficient, and Δ and δ are defined as in the pulse sequence (Fig. 22). The diffusion coefficient can be extracted from the slope of the plot of $\ln[A(t_1)/A_0(t_1)]$ against $[\delta^2(\Delta - \delta/3)]$. Fig. 23 depicts diffusion measurements on six different orders of coherence for benzene C_6H_6 (**8**) aligned in liquid crystalline solution, clearly indicating that the slopes of the lines vary as N^2 .



The decay of N -quantum coherences are much more sensitive to diffusion than conventional single quantum methods and this makes the use of MQ diffusion measurements attractive in viscous media (or for measuring relatively slow diffusion rates) where diffusion measurements by single quantum methods would require prohibitively large field gradients.

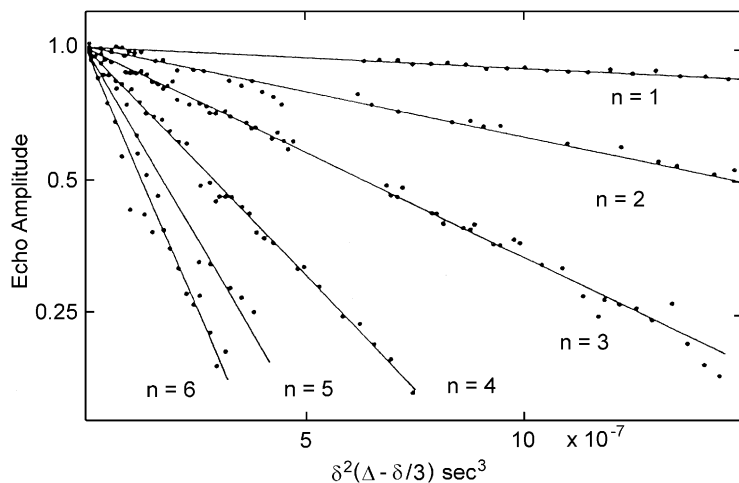
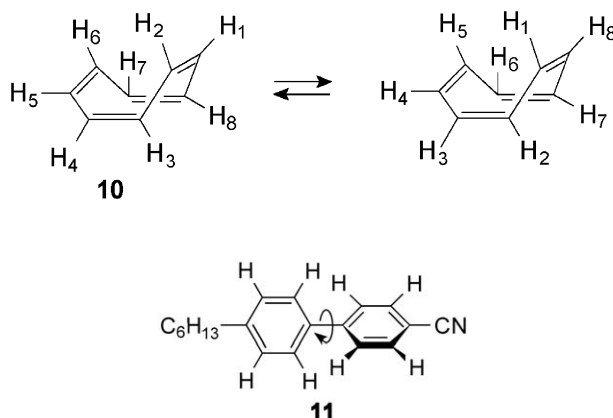


Fig. 23. NMR diffusion experiments for all six orders of coherence for benzene (**8**) aligned in nematic liquid crystalline solution. The straight lines are linear least squares fits to the accumulated data according to Eq. (4). (Adapted with permission from ref. 39.)

9. MULTIPLE QUANTUM SPECTRA OF EXCHANGING SYSTEMS

Aligned spin systems, which undergo exchange, have been investigated by MQNMR techniques. Like single quantum NMR spectra, the lineshapes of MQ spectra are averaged by chemical exchange and the lineshape of the high-quantum spectra of an exchanging spin system is considerably simpler than the complex lineshape of the single quantum spectra. Gamliel *et al.*⁶⁹ reported the theoretical treatment of MQNMR spectra in exchanging systems and matched this to experimental spectra for experimental MQ spectra of trioxane (**9**) and cyclooctatetraene (**10**). Fig. 24 shows the simulated 5Q spectra of the 6-proton spin system which undergoes rapid ring-flip while aligned in liquid crystalline solution.



10. MQ RELAXATION IN ANISOTROPIC MEDIA

Molecular reorientation in anisotropic media such as liquid crystals, described by the spectral densities of the motion of a molecule, $J_q(\omega)$, are usually estimated from a range of relaxation measurements. In quadrupolar systems, the relaxation of zero-, double-, triple- and higher-order coherences have been used to estimate the spectral densities of motion for small deuterated organic molecules (including CDCl_3 ,⁷⁰ $\text{D-C}\equiv\text{C-C}\equiv\text{N}$,⁷¹ CD_2Cl_2 ,⁷²⁻⁷⁴ and $\text{CD}_3\text{-C}\equiv\text{N}$,⁷⁵⁻⁷⁷) dissolved in liquid crystalline solution. The relaxation of the 2Q and 3Q resonances of ^{23}Na ($I = 3/2$) and the 4Q and 5Q resonances of ^{17}O ($I = 5/2$) have also been measured in lyotropic liquid crystals.⁷⁸

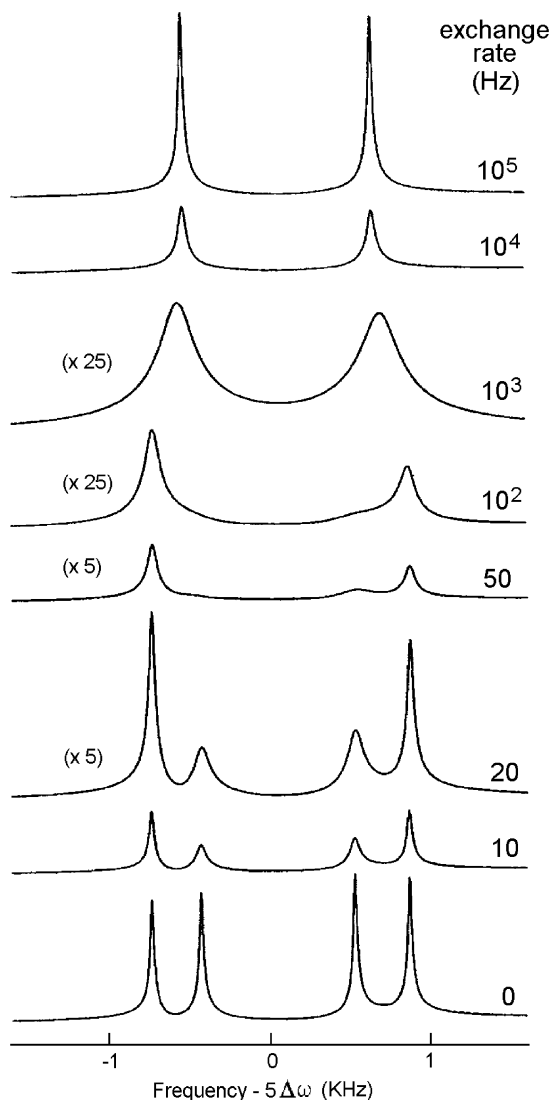


Fig. 24. Simulated 5-quantum NMR spectra of the 6-spin system of trioxane (**9**) undergoing ring inversion in a liquid crystalline solvent. (Reproduced with permission from ref. 69.)

11. COUNTING SPINS IN CLUSTERS

In MQNMR, individual spins become correlated with each other over time by interaction through their dipolar couplings. The rate at which MQ coherences develop is a complex function of the coupling constants present in the spin system. In solids, where the network of dipole-coupled spins is

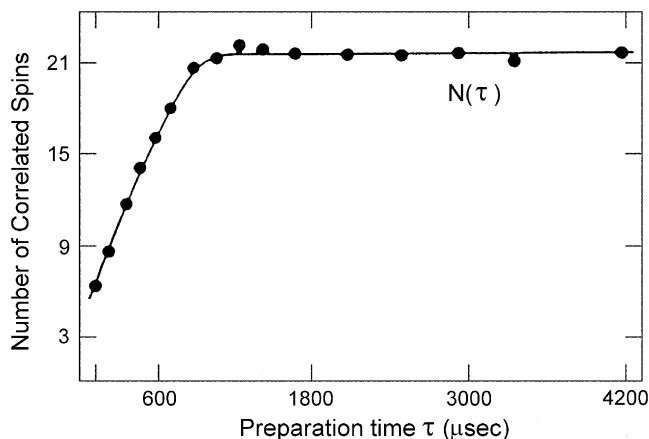


Fig. 25. The effective spin-system size, $N(\tau)$, as a function of the preparation time, τ , for the liquid crystal 4-cyano-4'-hexylbiphenyl (**11**). After an induction period of approximately 1 ms, $N(\tau)$ plateaus out at a value of 21, reflecting the total number of spins in the isolated molecular cluster. (Reproduced with permission from ref. 79.)

effectively infinite, the correlations between spins develop in a monotonic fashion. As time progresses, more spins can absorb more quanta and high-order MQC can be generated.⁷⁹ In systems where there are effectively isolated clusters of spins (e.g. liquid crystals, molecules dissolved in liquid crystalline phases, polycrystalline solids, molecules constrained in discrete compartments), the time-development of MQC is interrupted and the system can only support MQC up to the size of coupled spin clusters. In this application, the aim is to determine the largest order of coherence that can be readily supported by the sample and this gives an indication of the maximum number of spins that can support MQC in the sample. In the 21-spin system of the liquid crystal 4-cyano-4'-hexylbiphenyl (**11**), the effective spin system size increases to a maximum of 21 spins as the preparation time for MQC increases (Fig. 25).

Distinct subsections of the molecules comprising liquid crystals have also been observed using the rate of MQC development in a mixture of liquid crystalline materials. Separate MQ signals were observed for effectively isolated spin systems (phenyl rings) and weakly coupled multi-spin clusters (alkyl tails)⁸⁰ in a mixture of 4-cyanophenyl 4'-butylbenzoate and 4-cyanophenyl 4'-heptylbenzoate.

12. STUDIES OF ALIGNED MOLECULES BY MQNMR

Table 3 summarises the partially aligned molecules and proton spin systems that have been studied and analysed by MQNMR techniques.

Table 3. Spin 1/2 spin systems that have been studied and analysed by MQNMR techniques

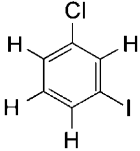
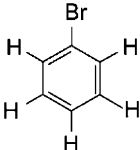
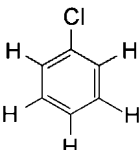
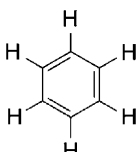
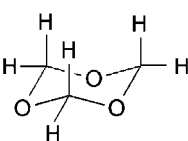
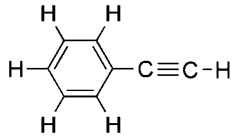
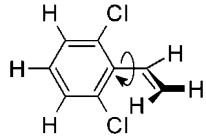
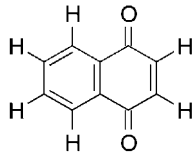
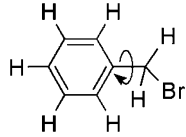
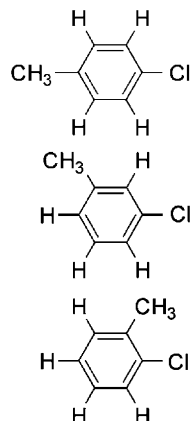
Compound	Structure	Formula	Spins		Reference
2		C_6H_4ClI	4	3-Chloriodobenzene (2). A rigid 4-spin aromatic system. The 2-, 3-, and 4Q spectra have been obtained and analysed. The spin system has been used extensively as a model system in developing pulse sequences and procedures for MQNMR.	34, 40, 85
12		C_6H_5Br	5	Bromobenzene (12). A rigid 5-spin aromatic system. The 4Q spectrum was obtained and analysed to provide spectral parameters that were used as starting parameters for an automated analysis of the 1Q spectrum. Structural information was derived.	61
13		C_6H_5Cl	5	Chlorobenzene (13). A rigid 5-spin aromatic system. The high-order MQ spectra were analysed to provide spectral parameters that were used as starting parameters for the analysis of the 1Q spectrum. The spectrum was analysed as a sub-spectrum of a 3-component mixture.	81
8		C_6H_6	6	Benzene (8). A rigid aromatic 6-spin system with high symmetry. 0Q–6Q spectra have been examined extensively as a model system in developing pulse sequences and procedures for MQNMR.	86, 31, 82, 23, 24
9		$C_3H_6O_3$	6	Trioxane (9). A fluxional 6-spin system where the high-order MQ spectra were analysed to investigate the lineshape of MQ spectra under exchange.	69

Table 3. (continued)

Compound	Structure	Formula	Spins	Reference
14		C_8H_6	6	Phenylacetylene (14). A rigid 6-spin aromatic system. The 5Q spectrum was obtained and analysed to provide spectral parameters that were used as starting parameters for an automated analysis of the 1Q spectrum. Structural information was derived. 61
15		$C_8H_6Cl_2$	6	1,3-Dichloro-2-ethenylbenzene (15). A 6-spin system in an aromatic molecule with an unsaturated 2-carbon side chain where there is restricted rotation between the aryl and the olefinic groups. The high-order MQ spectra were obtained and analysed to provide spectral parameters that were used as starting parameters for the analysis of the 1Q spectrum. The structure was refined with a model incorporating torsional motion between the three planes of the aromatic and olefinic groups and which provided a best-fit solution with a dihedral angle of $\sim 45^\circ$. 28
16		$C_{10}H_6O_2$	6	Naphthoquinone (16). A 6-spin rigid aromatic spin system. The 5Q spectrum was obtained and analysed to provide spectral parameters that were used as starting parameters for an automated analysis of the 1Q spectrum. 61
4		C_7H_7Br	7	Benzyl bromide (4). A 7-spin system in an aromatic molecule with a 1-carbon side chain. There is a low barrier of rotation of the CH_2Br group with respect to the 5-spin, rigid aromatic ring. The 5- and 6-quantum spectra were analysed to provide spectral parameters that were used as starting parameters for an automated analysis of the 1Q spectrum. 83

3a, 3b, 3c



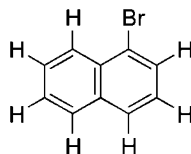
C₇H₇Cl

7

4-Chlorotoluene (**3a**), 3-Chlorotoluene (**3b**), 2-Chlorotoluene (**3c**). These are all 7-spin systems in aromatic molecules with 1-carbon side chains. The high-order MQ spectra were analysed to provide spectral parameters that were used as starting parameters for the analysis of the 1Q spectrum. There is a low barrier of rotation of the CH₃ group with respect to the 5-spin, rigid aromatic spin system. A complete set of 0Q–7Q spectra for 4-chlorotoluene was obtained using a 3D NMR experiment.

81, 84, 43

17



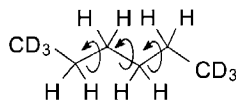
C₁₀H₇Br

7

1-Bromonaphthalene (**17**). A 7-proton, rigid aromatic spin system. The 5Q and 6Q spectra were obtained and analysed simultaneously to give all dipolar couplings and these were used directly to estimate molecular geometry.

33, 85

6



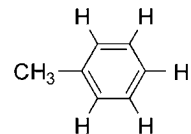
C₆H₈D₆

8

1,1,1,6,6,6-Hexadeuteriohexane (**6**). An 8-proton non-rigid spin system. The 6Q- and 7Q-spectra were analysed to give dipolar couplings that were fitted to structural models. Best fit was obtained when the *trans* conformations of the flexible backbone were appreciably populated.

9

18



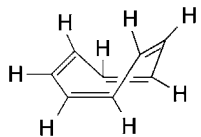
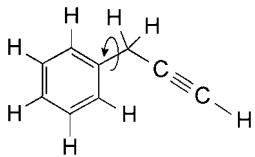
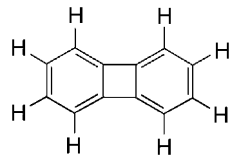
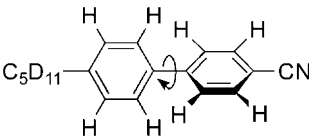
C₇H₈

8

Toluene (**18**). An 8-spin system in an aromatic molecule with a 1-carbon side chain. The high-order MQ spectra were analysed to provide spectral parameters that were used as starting parameters for the analysis of the 1Q spectrum. There is a low barrier of rotation of the CH₃ group with respect to the 5-spin, rigid aromatic spin system.

81

Table 3. (continued)

Compound	Structure	Formula	Spins	Reference
10		C ₈ H ₈	8	Cyclooctatetraene (10). An 8-spin fluxional molecule where the high-order MQ spectra were analysed to investigate the lineshape of MQ spectra under exchange. 69, 86
19		C ₉ H ₈	8	3-Phenyl-1-propyne (19). This is an 8-spin system in an aromatic molecule with a 3-carbon side chain. The 4-, 5-, 6- and 7-quantum spectra were obtained and analysed to provide spectral parameters that were used as starting parameters for an automated analysis of the 1Q spectrum. 65
20		C ₁₂ H ₈	8	Biphenylene (20). A rigid 8-spin aromatic spin system. The 6Q and 7Q spectra were analysed to provide spectral parameters that were used as starting parameters for an analysis of the 1Q spectrum. Structural information was derived. 87
5		C ₁₈ H ₈ D ₁₁ N	8	4-Cyano-4'-pentylbiphenyl (5CB- <i>d</i> ₁₁) (5). An 8-proton aromatic spin system where there is restricted rotation between the aryl rings. The 5-, 6- and 7-quantum spectra were obtained and analysed to provide spectral dipolar couplings that were used directly to estimate molecular geometry. The structure of the molecule was modelled to give an estimate of the torsional angle (30 ± 2°). 49, 50

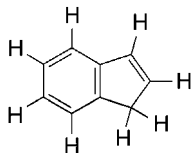
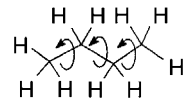
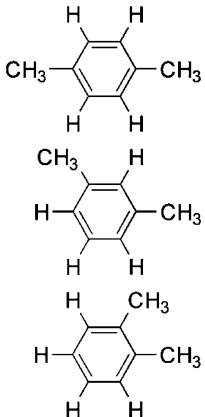
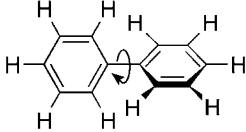
1		C_9H_8	9	Indene (1). An 8-spin system comprising an aromatic ring with a fused 5-membered ring. The spin system has C_s symmetry with a plane of symmetry that goes through plane of the aromatic ring. The system is essentially rigid. MQ coherence was generated non-selectively then MQ spectra were detected selectively using magnetic field gradients for MQ selection. The 6-, 7- and 8-quantum spectra were analysed to provide spectral dipolar couplings that were used directly to estimate molecular geometry.	62
21		C_4H_{10}	10	Butane (21). A 10-proton non-rigid spin system. The analysis of the 7- and 8-quantum spectra provided spectral parameters, which were used as starting parameters for the analysis of the 1Q spectrum. There is a low barrier to rotation about each of the C-C bonds and the structure of the molecule was modelled to give an estimate of the <i>trans-gauche</i> energy difference in the range 2.1–3.0 kJ/mol.	88
22a, 22b, 22c		C_8H_{10}	10	<i>p</i> -Xylene (22a), <i>m</i> -Xylene (22b), <i>o</i> -Xylene (22c). All 10-spin systems in aromatic molecules each with two 1-carbon side chains. The high-order MQ spectra were analysed to provide spectral parameters that were used as starting parameters for the analysis of the 1Q spectrum. There is a low barrier of rotation of the CH_3 groups with respect to the 4-spin, rigid aromatic spin system.	81, 84

Table 3. (*continued*)

Compound	Structure	Formula	Spins	Reference
23		C ₁₂ H ₁₀	10	<p>Biphenyl (23). A 10-spin aromatic spin system with C_2 symmetry where there is restricted rotation between the aryl rings. The 8-quantum ^1H NMR spectrum was solved, with some assumptions, to provide dipolar coupling constants and chemical shifts and these were then used as starting parameters for the analysis of the 1Q spectrum. The geometry was solved using vibrationally corrected geometric parameters to obtain the shape of the molecule. The structure was best modelled with an equilibrium dihedral angle of $\sim 37^\circ$ between the phenyl rings.</p>

REFERENCES

1. For leading references on NMR in liquid crystalline solvents see: (a) J. W. Emsley and J. C. Lindon, *NMR Spectroscopy Using Liquid Crystal Solvents*, Pergamon Press, Oxford, UK, 1975; (b) J. W. Emsley, ed., *Nuclear Magnetic Resonance of Liquid Crystals*, D. Riedel Publishing Co., Dordrecht, The Netherlands, 1985; (c) E. E. Burnell and C. A. de Lange, eds., *NMR of Orientationally Ordered Liquids*, Kluwer Academic Press, Dordrecht, The Netherlands, 2003.
2. See, for example, P. Diehl and C. L. Khetrapal, NMR studies of molecules aligned in liquid crystalline solution, *NMR, Basic Principles and Progress*, Vol. 1, P. Diehl, E. Fluck and R. Kosfeld, eds., Springer, New York, USA, 1969, 1.
3. E. E. Burnell and C. A. De Lange, *Chem. Rev.*, 1998, **98**, 2359.
4. R. R. Ernst and A. Wokaun, *Principles of Magnetic Resonance in One and Two Dimensions*, Oxford University Press, London, 1980.
5. G. Bodenhausen, *Prog. NMR Spectrosc.*, 1981, **14**, 137.
6. D. P. Weitekamp, *Adv. Magn. Reson.*, 1983, **11**, 111.
7. M. Munowitz and A. Pines, Principles and applications of multiple quantum NMR, *Advances in Chemical Physics*. Vol. LXVI, I. Prigogine and S. A. Rice, eds., Wiley, New York, USA, 1987, 1–153.
8. C. P. Slichter, *Principles of Magnetic Resonance*, 3rd edition, Springer, Berlin, 1990.
9. G. P. Drobny, *Ann. Rev. Phys. Chem.*, 1985, **36**, 451.
10. R. Freeman, *Concepts Magn. Reson.*, 1998, **10**, 63.
11. (a) L. D. Field, Multiple quantum spectroscopy in liquid crystalline solvents, *Encyclopedia of NMR*, D. M. Grant and R. K. Harris, eds., Wiley, Chichester, UK, 1996, 3172; (b) L. D. Field, Multiple quantum NMR spectroscopy in orientationally ordered fluids, *NMR of Orientationally Ordered Liquids*, E. E. Burnell and C. A. de Lange, eds., Kluwer Academic Press, Dordrecht, The Netherlands, 2003, Ch 4, 67–88.
12. W. P. Aue, E. Bartholdi and R. R. Ernst, *J. Chem. Phys.*, 1976, **64**, 2229.
13. G. Drobny, A. Pines, S. Sinton, D. P. Weitekamp and D. Wemmer, *Faraday Div. Chem. Symp.*, 1979, **13**, 49.
14. L. Braunschweiler, G. Bodenhausen and R. R. Ernst, *Mol. Phys.*, 1983, **48**, 535.
15. O. W. Sorenson, M. Levitt and R. R. Ernst, *J. Magn. Res.*, 1983, **55**, 104.
16. D. P. Weitekamp, J. R. Garbow and A. Pines, *J. Magn. Res.*, 1982, **46**, 529.
17. S. Wimperis, *J. Magn. Res.*, 1993, **102**, 302.
18. J. B. Murdoch, W. S. Warren, D. P. Weitekamp and A. Pines, *J. Magn. Res.*, 1984, **60**, 205.
19. W. S. Warren, S. Sinton, D. P. Weitekamp and A. Pines, *Phys. Rev. Lett.*, 1979, **43**, 1791.
20. W. S. Warren, D. P. Weitekamp and A. Pines, *J. Chem. Phys.*, 1980, **73**, 2084.
21. W. S. Warren, D. P. Weitekamp and A. Pines, *J. Magn. Res.*, 1980, **40**, 581.
22. G. Drobny, A. Pines, S. Sinton, W. S. Warren and D. P. Weitekamp, *Philos. Trans. Royal Soc. London A*, 1981, **299**, 585.
23. W. S. Warren and A. Pines, *J. Chem. Phys.*, 1981, **74**, 2808.
24. W. S. Warren and A. Pines, *Chem. Phys. Lett.*, 1982, **88**, 441.
25. T. M. Barbara, R. Tycho and D. P. Weitekamp, *J. Magn. Res.*, 1985, **62**, 54.

26. M. H. Levitt and R. R. Ernst, *Chem. Phys. Lett.*, 1983, **100**, 119.
27. M. H. Levitt and R. R. Ernst, *J. Chem. Phys.*, 1985, **83**, 3297.
28. J. C. T. Rendell and E. E. Burnell, *Mol. Phys.*, 1997, **90**, 541.
29. J. C. T. Rendell and E. E. Burnell, *J. Magn. Res. Ser. A*, 1995, **112**, 1.
30. A. Wokaun and R. R. Ernst, *Chem. Phys. Lett.*, 1977, **52**, 407.
31. G. Drobny, *Chem. Phys. Lett.*, 1984, **109**, 132.
32. L. D. Field and M. L. Terry, *J. Magn. Res.*, 1986, **69**, 176.
33. L. D. Field, G. K. Pierens, K. J. Cross and M. L. Terry, *J. Magn. Res.*, 1992, **97**, 451.
34. G. K. Pierens, T. A. Carpenter, L. D. Colebrook, L. D. Field and L. D. Hall, *J. Magn. Res.*, 1992, **99**, 398.
35. A. Bax, P. G. DeJong, A. F. Mehlkopf and J. Schmidt, *Chem. Phys. Lett.*, 1980, **69**, 568.
36. A. A. Maudsley, A. Wokaun and R. R. Ernst, *Chem. Phys. Lett.*, 1978, **55**, 9.
37. R. L. Vold, J. S. Waugh, M. P. Klein and D. E. Phelps, *J. Chem. Phys.*, 1982, **48**, 3831.
38. J. F. Martin, L. S. Selwyn, R. R. Vold and R. L. Vold, *J. Chem. Phys.*, 1982, **76**, 2632.
39. D. Zax and A. Pines, *J. Chem. Phys.*, 1983, **78**, 6333.
40. S. Ramadan, Ph.D. Dissertation, University of Sydney, 2000.
41. Y. S. Yen and D. P. Weitekamp, *J. Magn. Res.*, 1982, **47**, 476.
42. D. P. Weitekamp, J. R. Garbow and A. Pines, *J. Chem. Phys.*, 1982, **77**, 2870.
43. R. T. Syvitski, N. Burlinson, E. E. Burnell and J. Jeener, *J. Magn. Res.*, 2002, **155**, 251.
44. D. N. Shykind, J. Baum, S. -B. Liu and A. Pines, *J. Magn. Res.*, 1988, **76**, 149.
45. A. G. Avent, *J. Magn. Res.*, 1983, **53**, 513.
46. M. Carravetta, F. Castiglione, G. De Luca, M. Edgar, J. W. Emsley, R. D. Farrant, E. K. Foord, J. C. Lindon, M. Longeri, W. E. Palke and D. L. Turner, *J. Magn. Res.*, 1998, **135**, 298.
47. J. W. Emsley, J. C. Lindon, J. M. Tabony and T. H. Wilmshurst, *J. Chem. Soc. Commun.*, 1971, **19**, 1277.
48. E. Ciampi, G. De Luca and J. W. Emsley, *J. Magn. Res.*, 1997, **129**, 207.
49. S. W. Sinton and A. Pines, *Chem. Phys. Lett.*, 1980, **76**, 263.
50. S. W. Sinton, Z. B. Zax, J. B. Murdoch and A. Pines, *Mol. Phys.*, 1984, **53**, 333.
51. P. Diehl and C. L. Khetrapal, *Can. J. Chem.*, 1969, **47**, 1411.
52. M. Gochin, D. Hugi-Cleary, H. Zimmermann and A. Pines, *Mol. Phys.*, 1987, **60**, 205.
53. M. Gochin, K. V. Schenker, H. Zimmermann and A. Pines, *J. Am. Chem. Soc.*, 1986, **108**, 6813.
54. M. Gochin, H. Zimmermann and A. Pines, *Chem. Phys. Lett.*, 1987, **137**, 51.
55. M. Gochin, A. Pines, M. E. Rosen, S. P. Rucker and C. Schmidt, *Mol. Phys.*, 1990, **69**, 671.
56. M. E. Rosen, S. P. Rucker, C. Schmidt and A. Pines, *J. Phys. Chem.*, 1993, **97**, 3858.
57. S. Castellano and A. A. Bothner-By, *J. Chem. Phys.*, 1964, **41**, 3863.
58. J. A. Ferretti, R. K. Harris and R. B. Johannesen, *J. Magn. Res.*, 1970, **84**, 3.
59. P. Diehl, H. P. Kellerhals and W. Niederberger, *J. Magn. Res.*, 1971, **4**, 352.
60. W. S. Warren, J. B. Murdoch and A. Pines, *J. Magn. Res.*, 1984, **60**, 236.
61. G. Celebre, F. Castiglione, M. Longerie and J. W. Emsley, *J. Magn. Res. Ser. A*, 1996, **121**, 139.

62. L. D. Field, G. K. Pierens and S. Ramadan, *J. Magn. Res.*, 2002, **156**, 64.
63. HyperChemTM Release 4.5 for SGI, *Molecular Modeling System*, Hypercube, Inc., Gainsville, FL, USA.
64. A. Minoretti, W. P. Aue, M. Reinhold and R. R. Ernst, *J. Magn. Res.*, 1980, **40**, 175.
65. F. Castiglione, G. Celebre, G. De Luca and M. Longeri, *Liquid Cryst.*, 2001, **28**, 1403.
66. D. Sandström and H. Zimmerman, *J. Phys. Chem. B.*, 2000, **104**, 1490.
67. D. Sandström and H. Zimmerman, *Mol. Phys.*, 2002, **100**, 1935.
68. E. O. Stejskal and J. E. Tanner, *J. Chem. Phys.*, 1965, **42**, 288.
69. D. Gamliel, Z. Luz and S. Vega, *J. Chem. Phys.*, 1988, **88**, 25.
70. R. R. Vold and R. L. Vold, *J. Chem. Phys.*, 1977, **66**, 1418.
71. R. R. Vold, R. L. Vold and N. Szerverenyi, *J. Phys. Chem.*, 1981, **85**, 1934.
72. R. Poupko, R. R. Vold and R. L. Vold, *J. Magn. Res.*, 1979, **34**, 67.
73. G. Bodenhausen, R. R. Vold and R. L. Vold, *J. Magn. Res.*, 1980, **37**, 93.
74. R. R. Vold, R. L. Vold, R. Poupko and G. Bodenhausen, *J. Magn. Res.*, 1980, **38**, 141.
75. D. Jaffe, R. R. Vold and R. L. Vold, *J. Magn. Res.*, 1982, **46**, 475.
76. D. Jaffe, R. R. Vold and R. L. Vold, *J. Magn. Res.*, 1982, **46**, 496.
77. D. Jaffe, R. R. Vold and R. L. Vold, *J. Chem. Phys.*, 1983, **78**, 4852.
78. I. Furo and B. Halle, *Mol. Phys.*, 1992, **76**, 1169.
79. J. Baum and A. Pines, *J. Am. Chem. Soc.*, 1986, **108**, 7447.
80. W. V Gerasimowicz, A. N. Garroway and J. B. Miller, *J. Am. Chem. Soc.*, 1990, **112**, 3726.
81. R. T. Syvitsky and E. E. Burnell, *Can. J. Chem.*, 1999, **77**, 1761.
82. G. Drobny Ph.D., *Dissertation*, University of California, Berkeley, 1982.
83. F. Castiglione, G. Celebre, G. De Luca and M. Longerie, *J. Magn. Res.*, 2000, **142**, 216.
84. R. T. Syvitsky and E. E. Burnell, *J. Magn. Res.*, 2000, **144**, 58.
85. G. K. Pierens, Ph.D. Dissertation, University of Sydney, 1990.
86. W. S. Warren, Ph.D. Dissertation, University of California, Berkeley, 1981.
87. J. M. Polson and E. E. Burnell, *J. Magn. Res. Ser. A*, 1994, **106**, 223.
88. J. M. Polson and E. E. Burnell, *J. Chem. Phys.*, 1995, **103**, 6891.
89. T. Chandrakumar, J. M. Polson and E. Burnell, *J. Magn. Res. Ser. A*, 1996, **118**, 264.

Solid-State NMR Studies of Molecular Motion

MELINDA J. DUER

*Department of Chemistry, University of Cambridge, Lensfield Road,
Cambridge CB2 1EW, UK*

1. Introduction	42
2. Lineshape analysis and measurement of motionally averaged interactions	44
2.1. Basics	44
2.2. Resolving powder lineshapes	45
2.3. Chemical shift anisotropy lineshapes	53
2.4. Dipolar coupling lineshapes	57
2.5. Quadrupole coupling lineshapes	70
3. Relaxation time measurements	81
3.1. Basics – theory	81
3.2. Basics – experiments	87
3.3. Examples	90
4. Exchange experiments	98
4.1. Basics	98
4.2. One-dimensional experiments	101
4.3. Pure-exchange spectra	106
4.4. Other methods	111
References	114

Solid-state NMR is an excellent method by which to study molecular motion and molecular degrees of freedom in solid materials. This critical review examines the literature for the period 2000–2005 in this context and discusses the developments in methodology during that period. The review is divided into three sections: (i) powder lineshape analysis, which generally examines motions with inverse correlation times τ_c^{-1} of the order of the width of the powder lineshape ($\tau_c = 10^{-3}$ – 10^{-6} s, depending on the particular interaction causing the powder lineshape); (ii) relaxation time measurements, which may be used to study motions with shorter correlation times ($\tau_c = 10^{-6}$ – 10^{-9} s); and (iii) exchange methods which may be used to study much slower motions ($\tau_c < 10^{-3}$ s). Each section is introduced with a brief resume of the basic underlying theory and practise

pertaining to that area. New techniques and approaches in the review period are then discussed and the utility of each assessed.

1. INTRODUCTION

Nuclear magnetic resonance (NMR) continues to be used enthusiastically to study molecular degrees of freedom and the correlation times of motional processes in a wide variety of solids. Indeed, in the period of this review (2000–2005), the range of materials studied has increased hugely compared to the previous review period (1994–1999). In particular, there has been much interest in biological materials, such that this now forms the largest single area of interest, with the number of publications in this area far exceeding those with a primary focus on polymers, the largest area of molecular motion studies by NMR prior to 2000. The importance of characterizing molecular motion in the condensed state is becoming increasingly evident as more detailed models of solid materials are being developed. An important objective of modern materials science is to understand the properties of materials at a molecular level. A knowledge of the molecular structure and intermolecular relationships is a prerequisite for this, of course, but it has long been recognized that a description of a static or snapshot structure is incomplete and that a knowledge of the molecular degrees of freedom is fundamental to understanding material properties, including mechanical and thermodynamic properties, electric and magnetic characteristics and catalytic activity.

This review surveys the studies of molecular motion, dynamics and exchange in solids in the period 2000–2005. It is not intended to be exhaustive, but rather to show the principal methods currently being applied to commonly examined situations, to assess the efficacy of these and the recent useful developments.

NMR is an excellent method for studying dynamics of molecules in solids; all nuclear spin interactions, such as chemical shielding, dipole–dipole coupling and quadrupole coupling, are in general anisotropic, that is to say, their strength depends on the orientation of the molecule containing the nuclear spin, and in particular, on its orientation with respect to the applied magnetic field of the NMR experiment. Thus, a change of molecular orientation due to motion is accompanied by a change in the strength of the nuclear spin interaction.

Very slow motions (correlation times, $\tau_c > 10^3$ s) may be studied via *exchange methods*. Such techniques are often two (or higher) dimensional. The strength of a particular nuclear spin interaction is monitored during the t_1 period of the experiment, usually by allowing transverse nuclear spin

magnetization to evolve under the influence of the chosen interaction, so that the transverse magnetization acquires a phase by the end of t_1 , which is determined by the strength of the interaction. A mixing period for a time τ_m then follows, where the magnetization is stored along the direction of the applied magnetic field (the direction in which its decay is least rapid, in general) while molecular motion and/or exchange occurs. Finally, the new strength of the nuclear spin interaction after molecular motion and/or exchange has occurred is monitored in the t_2 period of the experiment in an FID, during which transverse magnetization once again evolves under the influence of the interaction. The final two-dimensional experiment correlates the strengths of the interactions during t_1 and t_2 , and from this, the angular reorientation involved in the motion can be inferred. Repeating the experiment for different mixing times τ_m allows the correlation time for the motion to be determined. Clearly, a two-dimensional experiment can be lengthy to record, especially if it is to be repeated for several correlation times. For this reason and others, one-dimensional exchange methods have been developed and are proving popular. These are discussed further in Section 4.

Motions with τ_c^{-1} of the order of the strength of a nuclear spin interaction can be readily assessed by analyzing the lineshape arising from that interaction. These are generally motions of intermediate rates, $10^{-6} \text{ s} < \tau_c < 10^{-3} \text{ s}$, with the lower end of the range being more appropriate for quadrupolar spins suffering large quadrupole coupling interactions and the higher end of the range generally appropriate for chemical shift and dipolar interactions. If the correlation time for the motion is sufficiently short that the interaction is rapidly averaged in comparison to the magnitude of its strength, then a *fast-motion limit motionally averaged lineshape* will result. The lineshape will correspond to that arising from the motionally averaged interaction tensor and its associated anisotropy and asymmetry. The averaged anisotropy and asymmetry so arising are dependent on the angular reorientation involved in the motional process (though not on its correlation time, provided the correlation time is shorter than the fast-motion limit), and hence these parameters are worth measuring to gain information on the motional process. Such measurements are now commonplace with the required tensorial parameters often being derived from lineshape analysis, but now increasingly from other sources, in particular from experiments that allow high resolution of signals arising from different chemical sites. The current options for such experiments are discussed in Section 2.

Finally, shorter correlation time motions ($10^{-9} \text{ s} < \tau_c < 10^{-6} \text{ s}$) can be examined via spin-lattice relaxation time studies. Spin-lattice relaxation (as other relaxation processes) relies on fluctuations in nuclear spin interactions induced by molecular motion. Thus, in cases where relaxation is dominated by one particular nuclear spin interaction, the spin-lattice relaxation time

constants can be calculated for different molecular motions and compared with experiment. Spin–lattice relaxation is not the only relaxation process in a nuclear spin system. Transverse relaxation and spin–lattice relaxation in the rotating frame also depend on molecular motion and are both also extensively used to study motion. The dependence of these latter processes on motions with longer correlation times than spin–lattice relaxation means that they are used to study quite different motional regimes.

The basic methods for studying molecular motions are well understood and well documented elsewhere.^{1–3} Therefore, it is not the intention of this review to discuss the underlying principles of these experiments in detail, except where they impinge on some new development.

2. LINESHAPE ANALYSIS AND MEASUREMENT OF MOTIONALLY AVERAGED INTERACTIONS

2.1. Basics

The samples we examine in solid-state NMR are generally powders, consisting of many crystallites with random orientation, such that all possible molecular orientations are present with a statistical distribution (although oriented samples, e.g. in membranes are increasingly popular). The orientation dependence of each nuclear spin interaction means that, for a static powder sample, the NMR spectrum consists of a broad powder lineshape for each distinct chemical site. This lineshape can be considered as being made up of a very large number (equal to the number of crystallites present in the sample) of infinitely sharp lines, one from each different molecular orientation presents the sample, the frequency of each line being determined by the molecular orientation itself. The lines from the different orientations inevitably overlap and result in a broad, but not featureless, line. The intensity at any point in the powder lineshape reflects the population of the corresponding molecular orientation. Any molecular motion that changes molecular orientation within a crystallite in the sample changes the spectral frequency associated with the crystallite, so that the resonance line for that crystallite now moves to some other part of the powder lineshape. If the motion has a correlation time τ_c such that τ_c^{-1} is similar to the width of the powder lineshape, then coalescence occurs between the lines corresponding to the different molecular orientations that arise during the course of the motion. This in turn causes distinctive distortions of the powder lineshapes, the distortions being dependent on both the correlation time and geometry of the motion. Powder lineshapes can be simulated for likely models of the molecular motion and compared with experiment to reveal details of the dynamics.

If the motion involved has a correlation time such that τ_c^{-1} is much smaller than the width of the powder lineshape, then no effect is observed on the lineshape. Conversely, if the motion has a correlation time such that τ_c^{-1} is much larger than the width of the powder lineshape, then the motion is in the *fast-motion limit*, and while the powder lineshape is averaged by the motion in a manner that is dependent on the geometry of the motion, it is no longer dependent on the correlation time for the motion; the interaction producing the lineshape is being averaged rapidly and the lineshape resulting from the motionally averaged interaction tensor is observed, i.e. the tensor arising from the average of the interaction tensor in all the molecular orientations visited in the course of the molecular motion.

Lineshape analyses are straightforward, provided it is known what nuclear spin interactions are acting and provided the lineshapes from different chemical sites are resolved in some way. This latter point is crucial and much effort has been dedicated to deriving the methods, which allow the information from lineshape analysis to be obtained while also achieving resolution.

An online package now exists to assist in the simulation of lineshapes arising from molecular motion. The NMR WEBLAB prepared by the Spiess group in Mainz, <http://www.mpip-mainz.mpg.de/weblab40/> contains programmes for the simulation of lineshapes due to motion on a cone (including complex motions involving motion about more than one axis) and for calculating exchange spectra for the case of jumps between discrete sites. Details and examples are given in ref. ⁴

2.2. Resolving powder lineshapes

Most efforts at resolving powder lineshapes involve magic-angle spinning (MAS) to remove the effects of the anisotropic nuclear spin interactions from one dimension of a multi-dimensional experiment.² In the review period, one nice development in this area is the use of magic-angle turning (MAT) to resolve powder lineshapes arising from chemical shift anisotropy.⁵ The MAT experiment was developed by Gan⁶ and is a two-dimensional experiment, which resolves chemical shift anisotropy powder patterns in f_2 according to their isotropic chemical shifts in f_1 . The whole experiment is conducted under very slow MAS. Under very slow MAS, the spectrum approximates to that of a static (non-spinning) experiment, and it is this feature that produces static-like powder patterns in the f_2 dimension of the MAT experiment.

The isotropic spectrum in the other dimension of the experiment is produced as follows. MAS averages the anisotropic parts of the chemical shift anisotropy to zero by continuous rotation about a vector oriented at the magic angle with respect to the applied magnetic field, \mathbf{B}_0 . In fact, however,

we do not need to use continuous rotation; we could use discrete hopping instead. Provided we hop the sample between a minimum of three equally spaced angles about the magic angle, we achieve the same averaging of the anisotropic parts of the interaction. This is shown schematically in Fig. 1(a). In the MAT experiment, it is assumed that the MAS rate is sufficiently slow compared with the precession of transverse magnetization under the chemical shift anisotropy that the sample is effectively stationary during any reasonably short time delay. The radio frequency (rf) pulse sequence used in the MAT experiment is shown in Fig. 1(a). In the experiment, after initial excitation of transverse magnetization, the magnetization is allowed to evolve for a period $t_1/3$. During this period, the rotor is assumed static, at (say) position **1** in Fig. 1(a). The magnetization is then moved (by a 90° rf pulse) to z to be stored parallel to \mathbf{B}_0 until the rotor reaches position **2**. At this point, another 90° pulse moves the stored magnetization back to the transverse plane where it is allowed to evolve for a further $t_1/3$. It is then stored along z/\mathbf{B}_0 again until the rotor reaches position **3**, where the same process is repeated. Finally after the last $t_1/3$ period at position **3**, an FID is recorded (as a function of t_2). This whole experiment is repeated for many t_1 increments in the usual manner for a two-dimensional experiment; note, however, that the condition $t_1 \ll \tau_R$, where τ_R is the rotor period, must exist for all t_1 values. Fourier transformation in t_2 gives a static-like powder pattern (due to the ultraslow spinning). Fourier transformation with respect to t_1 produces an isotropic spectrum, as the net evolution during t_1 depends only on the isotropic chemical shift, the anisotropic parts averaging to zero between the three rotor orientations used in t_1 .

Some of the results obtained by Kaji *et al.*⁵ using the MAT experiment to study motion in poly(2-hydroxypropyl ether of bisphenol A) are shown in Fig. 2. The projection in f_2 of the full two-dimensional spectrum in Fig. 2(a) is effectively the lineshape that would be recorded for a powder sample. As this spectrum clearly shows, the chemical shift anisotropy powder patterns from the nine ^{13}C sites in this polymer are extensively overlapped and would not be resolved without the aid of this MAT experiment. The powder lineshapes for each ^{13}C site taken from the two-dimensional spectrum in Fig. 2(a) are shown in Fig. 2(b). Those for carbons **4** and **5** show distortions of the lineshape shoulders typical of motional averaging, in this case from 180° phenyl ring flips in the fast-motion limit. These were compared with simulations of the lineshapes assuming a distribution of flip angles (as would be appropriate for a non-crystalline polymer), the simulations themselves taking the same form as for a simple one-dimensional static powder lineshape.² As their results in Fig. 3 show, good agreement is obtained for reasonable distributions of flip angles. This motion is associated with the γ -relaxation process in this material and has previously been studied by ^2H NMR lineshape analysis.⁷

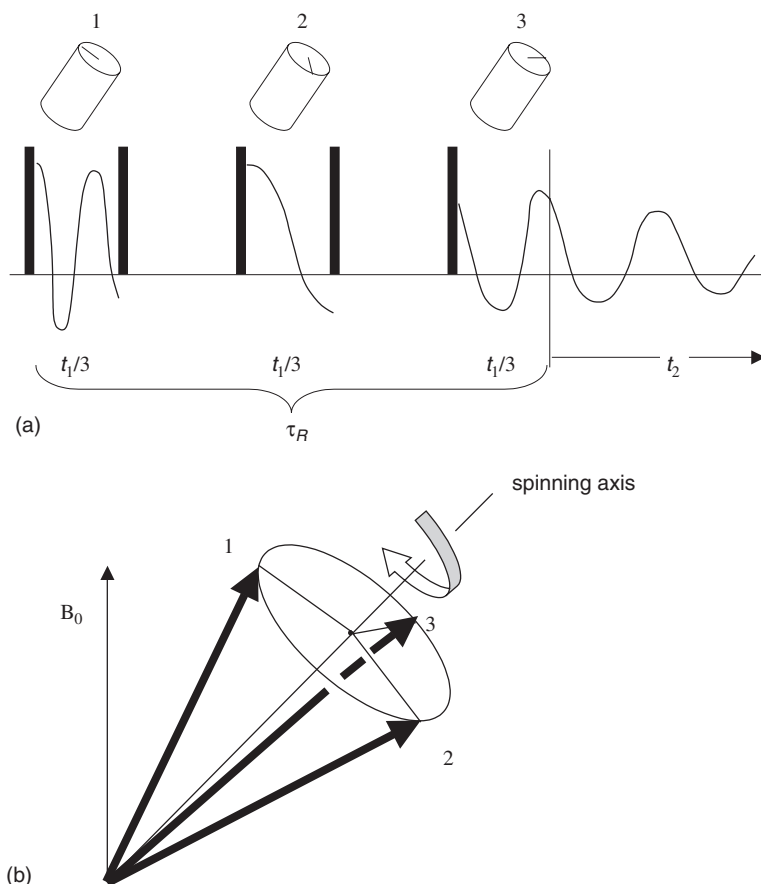
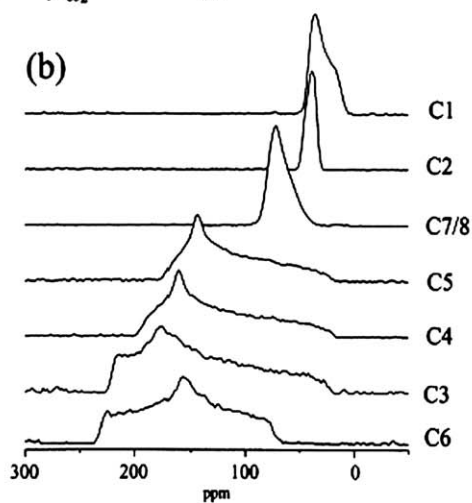
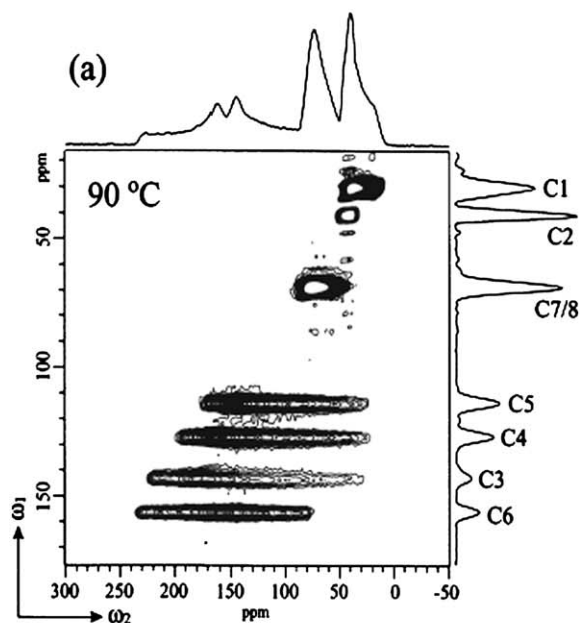
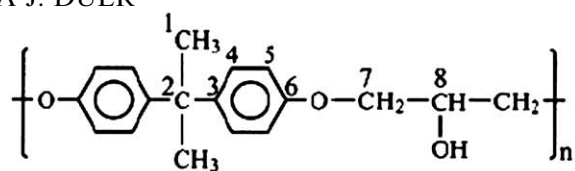


Fig. 1. The MAT experiment.⁶ The experiment takes place under very slow MAS, so that during the periods in which the t_1 magnetization is sampled, the rotor appears stationary at the positions 1, 2 and 3 labelled in (a). The pulse sequence used is also shown in (a). All pulses are 90° pulses. After each $t_1/3$ period, the magnetization is rotated to $z(\mathbf{B}_0)$ by a 90° pulse of suitable phase and is stored while the sample rotates to the next position. The net evolution during the whole t_1 period is as if the spins suffered their isotropic chemical shift only; all anisotropic parts cancel identically. During t_2 , the spinning is so slow that the spectrum recorded is as if the sample is static. (b) shows the position of the shielding tensor principal-axis frame z -axis for one molecular/crystallite orientation at the three rotor positions shown in (a). The average orientation for this axis is the sample-spinning axis, which in turn, is oriented at the magic angle. For this average orientation, the anisotropic chemical shift contribution to the chemical shift frequency is zero. Thus, the net evolution of the transverse magnetization in t_1 is governed by the isotropic chemical shift frequency only.



The quality of the results in the work just described is excellent. It should perhaps be pointed out that such results do not come without some effort and that the MAT experiment is not to be recommended for novices. One problem with the experiment is that it requires stable spinning at very low spinning rates, 125 Hz in the case cited above, when the vast majority of modern solid-state NMR systems are optimized for spinning as fast as possible, and usually well in excess of 5 kHz. This makes for some difficulties in achieving stable spinning, and often some modification to the spinning equipment is required, i.e. an extra valve or regulator to decrease the gas pressures driving and supporting the sample spinning. Furthermore, such slow spinning rates will not remove the effects of homonuclear or heteronuclear dipolar coupling in the f_1 dimension, should this be necessary. One will be entirely dependent on the application of rf pulses for decoupling ^1H for instance, from the observed ^{13}C spins in an organic solid, and this may mean high-rf amplitudes are needed to obtain sufficiently good decoupling. In turn, such high-rf amplitudes are not healthy for the probehead. For homonuclear dipolar coupling, there is no solution using MAT, and so MAT cannot be considered useful when dealing with extensively ^{13}C -labelled systems, for instance. The second problem with the experiment is that the high-resolution dimension is the indirectly observed one. The high-resolution dimension necessarily needs many points in order to achieve the required resolution and for the time domain data in t_1 not to be truncated (and so introduce spectral distortions). The broader lines associated with the disordered sites in this polymer sample meant that the workers in this case could obtain good results with just 64 t_1 slices; but in many cases, this number will need to be increased, resulting in long experiment times. For this sample, however, it has meant that an accurate assessment of the molecular dynamics in the sample, relating to the various motional relaxation processes, was able to be made without recourse to lengthy, and possibly expensive, selective deuteration, as was required for the ^2H study.⁷

The MAT experiment utilizes very slow spinning to prevent the averaging of Chemical shift anisotropy (CSA) by MAS. A more common procedure in

Fig. 2. The MAT experiment applied to poly(2-hydroxypropyl ether of bisphenol A)⁵ (top) to examine the 180° ring flips affecting ^{13}C **4** and **5**. (a) The complete two-dimensional MAT spectrum.⁵ The projection in f_2 is effectively the lineshape that would be recorded for a powder sample. As this spectrum clearly shows, the chemical shift anisotropy powder patterns from the nine ^{13}C sites in this polymer are extensively overlapped and would not be resolved without the aid of this MAT experiment. (b) The powder lineshapes for each ^{13}C site taken from the two-dimensional spectrum in (a).⁵ Those for carbons **4** and **5** show distortions of the lineshape shoulders typical of motional averaging, in this case from 180° phenyl ring flips.

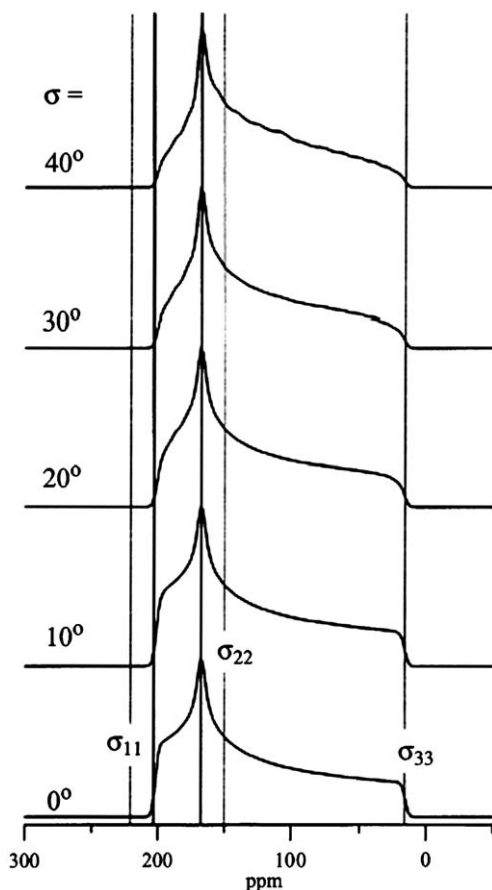


Fig. 3. Simulations of the lineshape expected for carbon **4** in Fig. 2 assuming phenyl ring flips in the fast-motion limit and a Gaussian distribution of flip angles centred at 180° with standard deviation σ .⁷

solid-state NMR is to use much higher spinning rates and to recouple the interaction of interest, which is otherwise averaged to zero by MAS, in one dimension of a multi-dimensional experiment. There are many pulse sequences available for recoupling chemical shift anisotropy and dipolar couplings. In a paper, which considers the effect of intermediate rate motions on the outcome of such pulse sequences, Saalwächter and Fischbach⁸ effectively provide a new method by which to study such motions. They consider the REDOR pulse sequence (Fig. 4), which recouples any nuclear spin interaction that is linear in I_z , where I is the observed spin. It does this by a sequence of 180° I spin pulses placed at the midpoint and end of every rotor period. A 180° pulse has the effect of inverting the I spins and hence changes the sign of the spin part of the interaction Hamiltonian. This sequence of

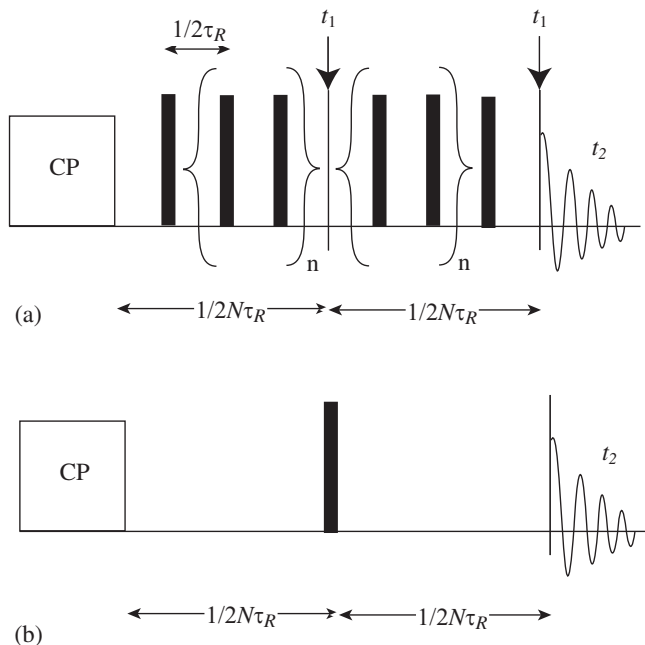


Fig. 4. (a) The pulse sequence that recouples under MAS any interaction which is linear in I_z the observed spin, i.e. chemical shift anisotropy and heteronuclear dipolar coupling between a pair of spins IS . (b) Reference pulse sequence. The sequences shown are appropriate for recoupling chemical shift anisotropy. If the interaction to be recoupled is heteronuclear dipolar coupling, the sequence in (a) is applied to the dipolar coupling partner S , while (a) is applied to the observed spin I . In the reference experiment, sequence (b) only is applied to I .

180° pulses thus exactly compensates for the change in the sign of the space part of the Hamiltonian as it oscillates due to MAS. Thus at the end of N rotor periods, the net effect of the interaction Hamiltonian on the I spin is non-zero, i.e. there is evolution under the interaction during the N rotor periods.

Saalswächter and Fischbach⁸ give a theoretical analysis of this pulse sequence for the case of intermediate rate molecular motion, which changes the orientation of a ^{13}C CSA tensor and shows that the effect of the motion is to reduce the signal intensity at the end of the N rotor periods of recoupling compared to the intensity expected if there is no motion. As the length of time $N\tau_R$ (τ_R = rotor period) for which recoupling is applied is increased, the signal intensity decays, with the decay being described by an apparent transverse relaxation time T_2^{rcpl} . For the two-site exchange process considered in the work, T_2^{rcpl} has a very simple dependence on the rate constant, $k = \tau_c^{-1}$ for the motion. Fig. 5 shows how the decay curve varies with rate constant and how T_2^{rcpl} depends on k . The example used in this work is the

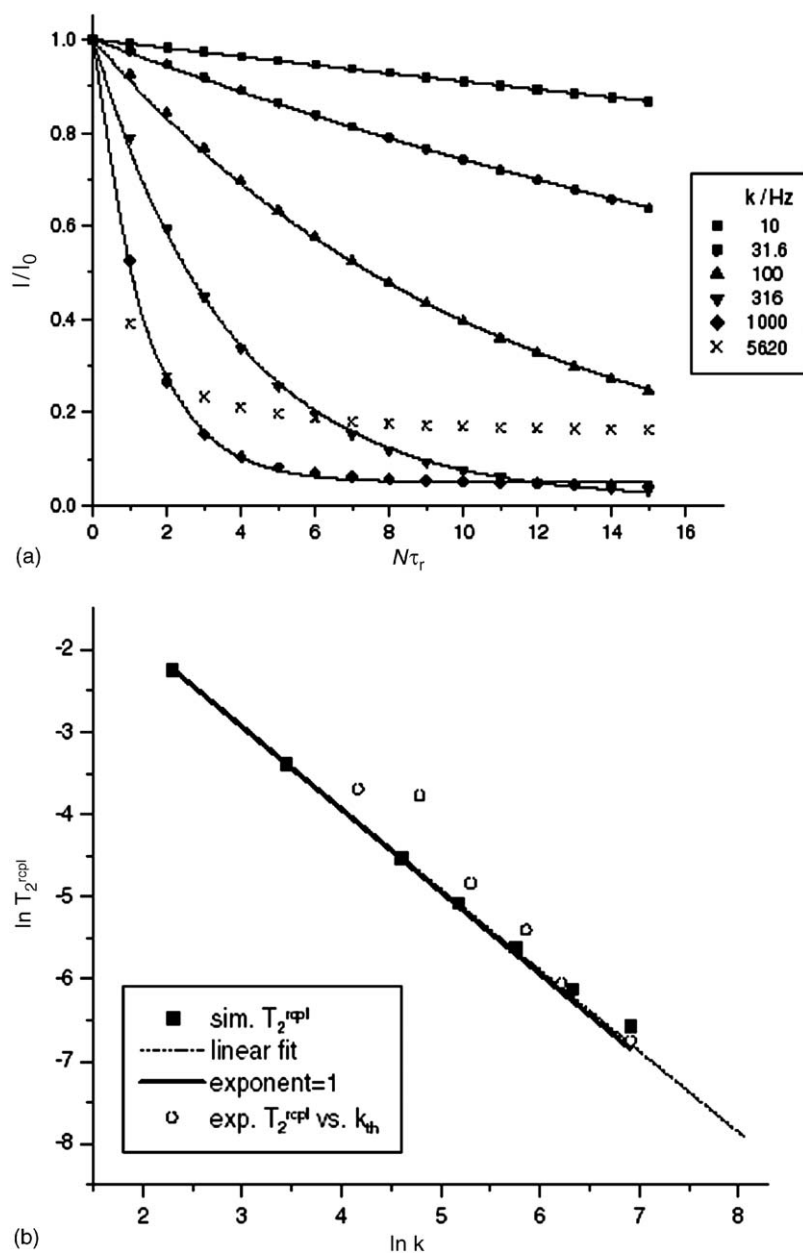


Fig. 5. (a) The intensity of the recoupled signal from the pulse sequence in Fig. 4(a) divided by that of the reference experiment (Fig. 4(b)) as a function of the motional exchange rate k for a two-site jump process for the ^{13}C chemical shift tensors of DMS.⁸ (b) The effective decay constant of the recoupled signal T_2^{rcpl} determined from the simulations in (a), plotted as a function of rate constant k .

^{13}C CSA tensor of dimethylsulphone (DMS). Obviously in this sample, there is only a single ^{13}C site, so there is no need of MAS here, except to demonstrate the effect. However, this experiment could be used with good effect in more complicated systems, as the curves in Fig. 5 may be produced for each signal that is resolved in the MAS spectrum.

Recoupling strategies are considered further in the work by Spiess *et al.*⁹ Here, the emphasis is on orientation, rather than powder samples and how to determine whether an NMR signal arises from molecular orientation or molecular dynamics. The approach is to recognize that MAS modulates nuclear spin interactions according to both ω_{R} and $2\omega_{\text{R}}$ and that the averaging because of either modulation may be interrupted by recoupling pulse sequences. By comparing the results from ω_{R} and $2\omega_{\text{R}}$ recoupling, details of molecular orientation and dynamics may be extracted. While for a powder sample, the details of molecular orientation are not relevant, the principles expounded in this work still apply.

2.3. Chemical shift anisotropy lineshapes

One potential problem with chemical shift anisotropy lineshape analysis (or indeed analysis of lineshapes arising from any nuclear spin interaction) is that the analysis results in a description of the angular reorientation of the *chemical-shielding tensor* during the motion, not the *molecule*. To convert this information into details of how the molecule moves, we need to know how the chemical-shielding tensor (or other interaction tensor) is oriented in the molecular frame. A further possible complication with the analysis is that it may not be possible to achieve an experiment temperature at which the motion is completely quenched, and thus it may not be possible to directly measure the principal values of the interaction tensor, i.e. anisotropy, asymmetry and isotropic component. If the motion is complex, lack of certainty about the input tensor parameters leads to an ambiguous lineshape analysis, with several (or even many) possible fits to the experimental data.

With the development of much faster computers and more reliable, more efficient computer codes for electronic structure calculations, a solution to both the above problems is to calculate both the orientation and principal values of the required interaction tensor from first principles, from an input molecular or (preferably) crystal structure.

One very promising approach to this is the work of Pickard and Mauri,¹⁰ which uses density functional theory with a plane wave basis set (which means that the basis set can be very large, as plane waves are computationally very efficient) and pseudocore potentials to describe the core electrons. The advantage of this approach is that it uses periodic boundary conditions, which is ideal for calculations involving solids. In effect, the

structure of one unit cell (or supercell) is input, and the calculation assumes that the structure is repeated *ad infinitum* in three dimensions. The alternative is to use a cluster approach, where the structure of the solid is approximated by a “cluster” of atoms and/or molecules. Such an approach must be used with caution; decisions have to be made about how the cluster is terminated so that bonds are not left dangling and so that the cluster is not conferred with a symmetry that does not exist in the real structure.

The approach of Pickard and Mauri allows the calculation of both chemical shift tensors and quadrupole coupling tensors and is available through the CASTEP code.¹¹

An interesting example of the use of *ab initio* calculation of chemical shift tensor orientation and principal values for use in a molecular motion study concerns the metallocene, $[\text{AlCp}^*_2]^+$.¹² The structure of this ion in the $[\text{AlCl}_4]^- [\text{AlCp}^*_2]^+$ salt is shown in Fig. 6. The authors of this work¹² use a hybrid density functional approach to calculate the ^{13}C -shielding tensor (and ^{27}Al shielding and quadrupole coupling tensors) for the ring carbons in the metallocene unit. Using the shielding tensor derived from this, they were then able to calculate the powder lineshapes they expect from the ^{13}C CSA as a function of the frequency k of ring hopping between chemically equivalent sites, i.e. adjacent carbon sites in the cyclopentadienyl ring. These are shown in Fig. 7 and led to the unequivocal conclusion that the

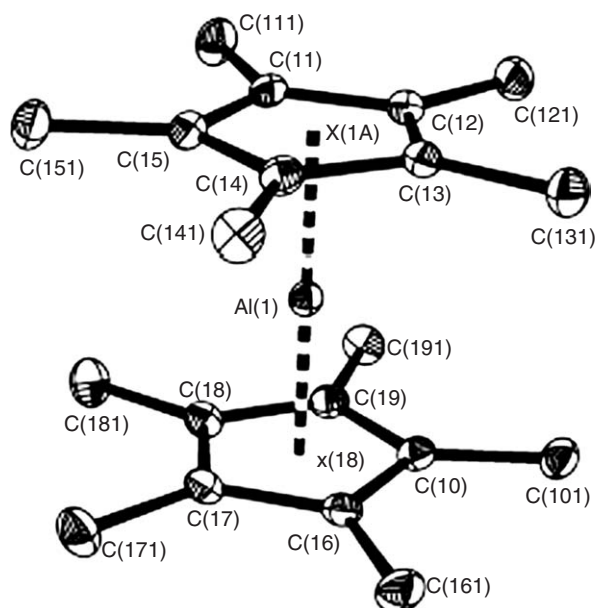


Fig. 6. The structure of the $[\text{AlCp}^*_2]^+$ metallocene in $[\text{AlCl}_4]^- [\text{AlCp}^*_2]^+$.¹²

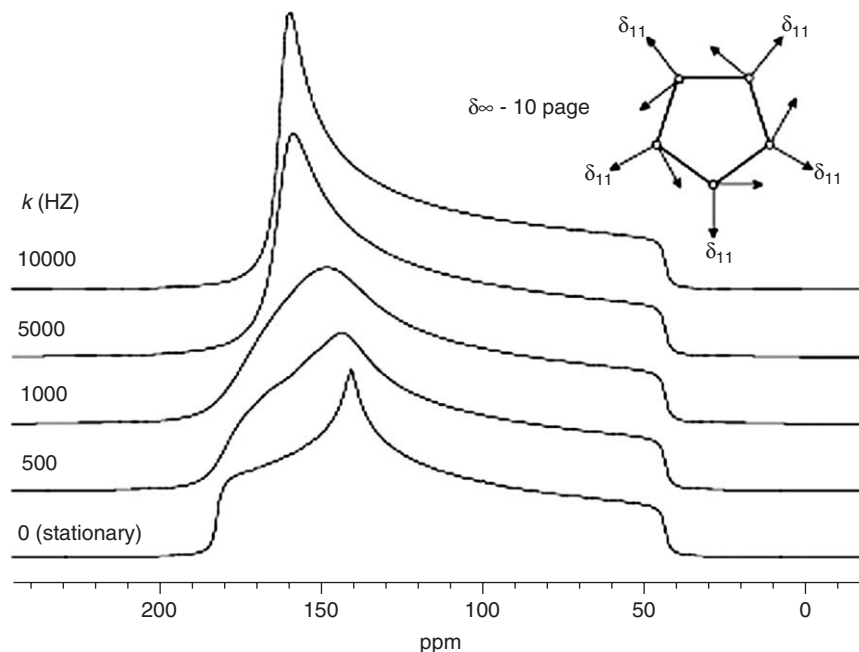


Fig. 7. The ^{13}C powder lineshape calculated for the Cp^* ring hopping between chemically equivalent sites in $[\text{AlCl}_4]^- [\text{AlCp}^*_2]^+$ using the ^{13}C -shielding tensor determined from *ab initio* electronic structure calculations.¹² The figure illustrates how the lineshape varies with the ring hopping rate k . The orientation of the principal axes of the ^{13}C -shielding tensor determined from the *ab initio* calculations is shown in the inset.

cyclopentadienyl rings are in the fast-exchange limit at room temperature. Their electronic structure calculation was repeated for different relative orientations of the two cyclopentadienyl rings in the metallocene unit between the limiting cases of staggered and eclipsed, so that the energy barrier to rotation of the rings could be determined. Their analysis led to a rotational energy barrier of 4.15 kJ mol^{-1} , which would indeed lead to motion in the fast limit at room temperature.

The energy barriers to motion were also calculated for naphthylphenylsulphoxide¹³ using an X-ray crystal structure and the MM3 code, adapted to deal with crystal lattices.¹⁴ In this case, it was the energy barrier to the restricted rotation about the S–Ph bond, which was calculated. The resulting value for ΔG^\ddagger of $(14.7 \pm 0.4) \text{ kcal mol}^{-1}$ leads to rate constants for the motion that agree well with those derived from simulating the ^{13}C CP–MAS spectrum, which shows exchange broadening because of the motion (Fig. 8).

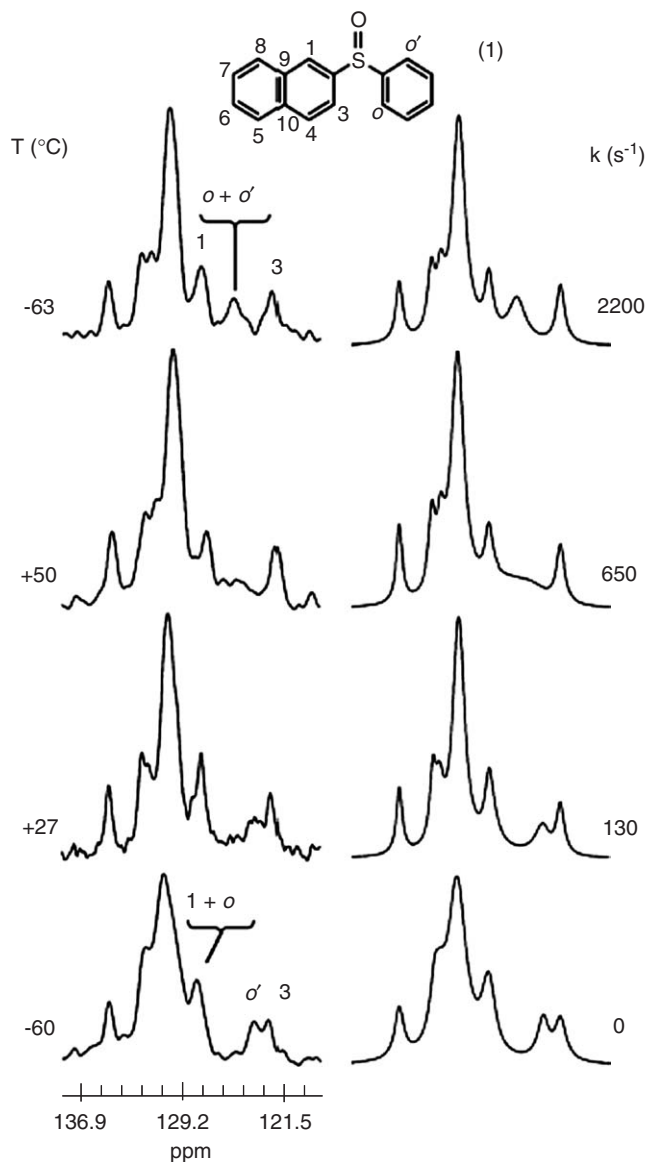


Fig. 8. The ^{13}C CP-MAS spectrum of naphthylphenylsulphoxide, showing the region containing the phenyl resonances, as a function of temperature (left) and the simulations of these experimental lineshapes (right) assuming restricted rotation of the phenyl ring about the S-Ph bond with rate constant k .¹³

2.4. Dipolar coupling lineshapes

In the past, dipolar coupling has probably been the least used nuclear spin interaction as far as molecular motions studies are concerned, except in work involving relaxation time measurements (where dipolar coupling is frequently a major, if not dominant relaxation mechanism). However, in the last few years there have been a number of studies, which utilize dipolar coupling, particularly for studying motions in the fast limit.

One nice demonstration is the work by Hong *et al.*¹⁵ where a two-dimensional experiment performed under rapid MAS is used to separate lineshapes arising from heteronuclear dipolar coupling according to isotropic chemical shift of a suitable spin species. The experiment uses the pulse sequence in Fig. 9(a) (or the modified one in Fig. 9(b), which achieves the same result, but with a sensitivity increase of up to a factor of 2, by inserting a Hartman–Hahn crosspolarization (CP) step before the main part of the pulse sequence). The experiment proceeds by creating ^1H – I Lee–Goldburg CP (LG-CP) after an initial ^1H 90° pulse. LG-CP is established by creating an effective ^1H spin-lock field in the ^1H -rotating frame, which is oriented at 54.74° , i.e. the magic angle, to the applied magnetic field of the NMR experiment. This is done in practise by applying an rf field with an offset $\Delta\omega_{\text{H}}$ to the ^1H resonance frequency and amplitude $\omega_{1\text{H}}$ such that $\Delta\omega_{\text{H}}/\omega_{1\text{H}} = \tan 54.74^\circ$, which creates the effective field shown in Fig. 9(c). When the ^1H magnetization is spin locked in this orientation, the ^1H – ^1H dipolar coupling is effectively suppressed. If the I spins are then irradiated with an rf field of amplitude $\omega_{1\text{H}} = \omega_{1I}$, i.e. the Hartman–Hahn matching condition, then the ^1H – I heteronuclear dipolar coupling is maintained, albeit scaled by a factor of $\sin 54.74^\circ$, i.e. the projection of the ^1H magnetization in the direction of the I -magnetization spin-lock field (the effective quantization axis for the I spins in their rotating frame) is $\sin 54.74^\circ M_{\text{H}}$, where M_{H} is the magnitude of the ^1H spin Zeeman magnetization. In the experiment, the LG-CP contact time is incremented (t_1) in successive experiments, so that the ^1H – I dipolar coupling evolves during this t_1 period of the experiment. The I spin signal is then recorded in t_2 in the normal way. Fourier transformation in both dimensions of the time-domain dataset yields an isotropic I spin spectrum in f_2 and a powder pattern in f_1 corresponding to the dipolar evolution in t_1 . One advantage of the experiment compared with experiments that record a chemical shift anisotropy or quadrupole coupling lineshape in f_1 is that only cosine-modulated data needs to be recorded in t_1 , as the dipolar lineshapes in f_1 are necessarily symmetric about zero frequency (and the dipolar evolution has no isotropic component, so the patterns are also necessarily centred at zero frequency).

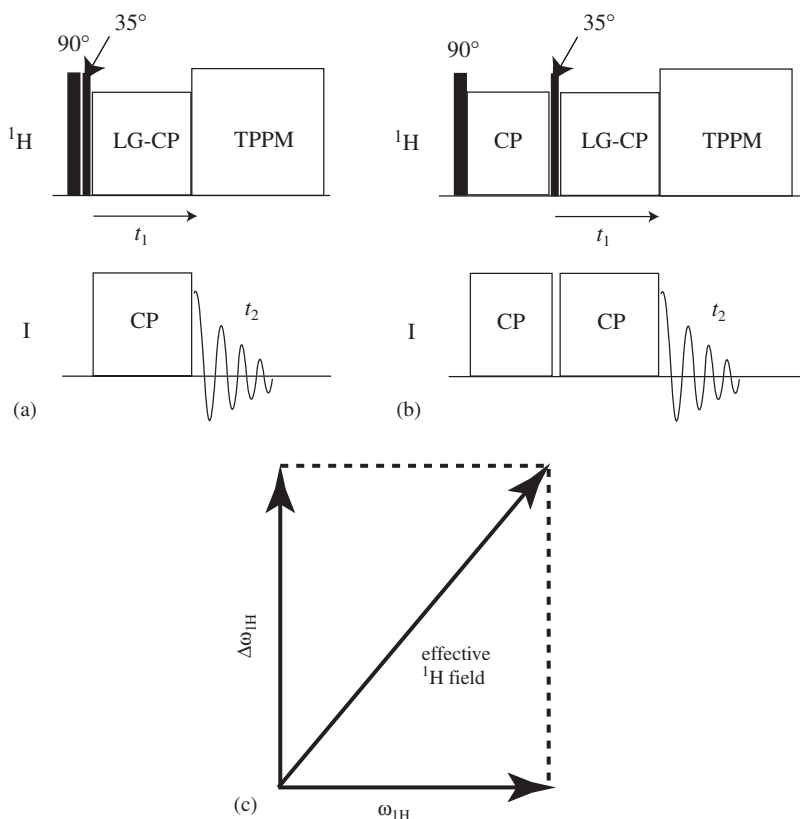


Fig. 9. (a) The LG-CP pulse sequence used in a two-dimensional experiment, which separates lineshapes due to heteronuclear dipolar coupling according to the isotropic chemical shift of the X nucleus.¹⁵ (b) The modified pulse sequence (named PILGRIM), which gives an increase in sensitivity of up to a factor of 2.¹⁵ (c) The effective field for the ^1H spins arising from LG-CP, created with rf irradiation of amplitude $\omega_{1\text{H}}$ and offset $\Delta\omega_{1\text{H}}$ from the ^1H resonance frequency.

The work of Hong *et al.*¹⁵ discusses the theoretical analysis of the dipolar lineshapes in the limit of rapid, anisotropic motion. The analysis assumes a motionally averaged dipolar coupling tensor, i.e. the average of the tensor over all the sites/orientations visited during the course of the motion, which has an effective anisotropy Δ_D and asymmetry η_D .

¹Fig. 10 shows some of the simulations from the work for motions with different effective asymmetries. The experiment was applied to ^1H – ^{13}C dipolar couplings in phenylalanine, and a polymer (polycarbonate) as shown in Fig. 11 and was also demonstrated for a membrane peptide using ^{15}N – ^1H dipolar couplings.

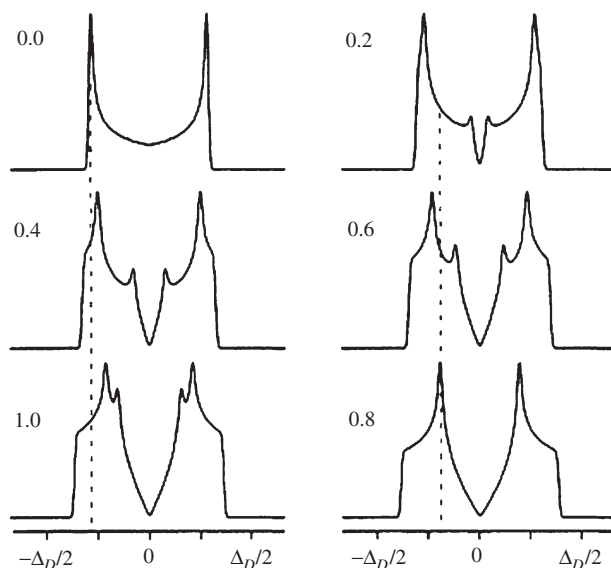


Fig. 10. Simulated LG-CP dipolar powder lineshapes for motions with different effective asymmetry, as labelled, and effective anisotropy Δ_D .¹⁵

Another development has been an extension of the WISE^{16,17} experiment, the so-called J-WISE experiment.¹⁸ The basic WISE experiment is shown in Fig. 12. In the particular case shown in Fig. 12, broad line ^1H signals are resolved according to isotropic ^{13}C chemical shifts. This is achieved by an initial ^1H 90° pulse, which creates ^1H transverse magnetization which is then allowed to evolve in t_1 . The experiment is conducted under MAS, but provided the spinning rate is not too high, the spinning has little effect on the ^1H lineshape for a strongly dipolar-coupled ^1H network. At the end of the t_1 period, the remaining ^1H magnetization is transferred to ^{13}C via CP, and the high-resolution ^{13}C spectrum recorded. The aim is to identify sites according to their ^{13}C isotropic chemical shifts and then to assess the mobility of the site by examining the correlated ^1H lineshape. The ^1H lineshape is dominated under usual conditions by the ^1H - ^1H dipolar coupling, which under molecular motion of sufficient amplitude and short enough correlation time is averaged so that narrower ^1H lines result. The problem is that when the ^1H are strongly dipolar coupled to each other, all ^1H in the network contribute to the CP process, and hence it is difficult to assess the motion associated with individual ^{13}C sites. The experiment was originally used, not

¹The dipole coupling tensor itself necessarily has zero asymmetry of course, but the motionally averaged tensor will only have zero asymmetry for motions that preserve the symmetry of the dipole coupling tensor, i.e. axial motions.

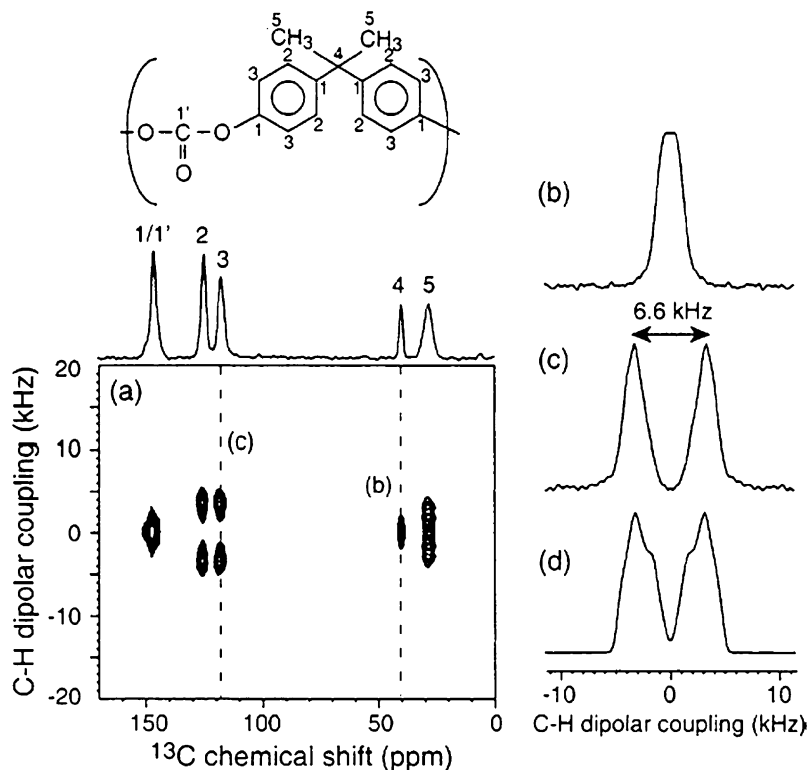


Fig. 11. The LG-CP experiment of Fig. 9(a) applied to ^1H - ^{13}C dipolar couplings in polycarbonate.¹⁵ (a) The full two-dimensional spectrum. (b) The LG-CP dipolar lineshape for the quaternary ^{13}C (carbon 4), which as expected shows only very small ^1H - ^{13}C dipolar couplings (as evidenced by the lack of observable splitting of the lineshape). (c) The LG-CP dipolar lineshape for carbon 3. (d) The best-fit simulation to the lineshape in (c). The motion used in this simulation (fast limit) assumes that the phenyl ring containing the carbon reorients about the local two-fold axis of the ring through an angle of 120° , with the reorientation axis wobbling with an amplitude of 20° .

to assess the motion in individual sites, but the different mobilities of molecules in different regions or domains of a sample. For instance, the relative mobilities of parts of molecules in the crystalline and amorphous domains of a polymer material are easily assessed by this method.

However, for many applications, the requirement is to assess the motion of individual sites within a molecule, and for this one requires greater selectivity in the ^1H - ^{13}C transfer step. One could of course use a very short contact time in the CP step to ensure that each ^{13}C spin acquires magnetization from only the closest ^1H spins. Under these conditions, it has been shown that the ^1H lineshapes in the f_1 dimension are dominated by the

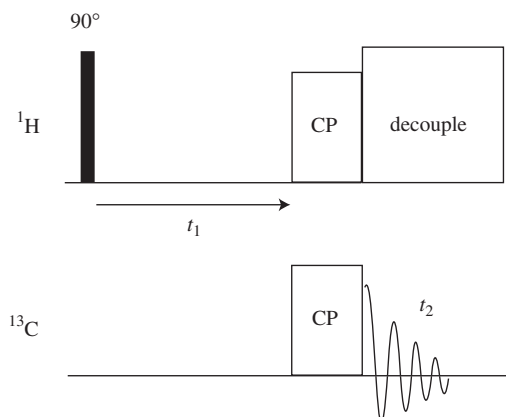


Fig. 12. The WISE experiment^{16,17} pulse sequence as applied to organic solids, i.e. ^1H and ^{13}C . See text for details.

heteronuclear ^1H – ^{13}C dipolar coupling, rather than the ^1H – ^1H homonuclear dipolar coupling.¹⁹ The lineshapes are still useful indicators of molecular motion, but must be compared to the lineshape expected for a static system for the effects of motion to be seen.²⁰

The J-WISE experiment¹⁸ is shown in Fig. 13(a). After initial CP to ^{13}C from ^1H (to enhance the ^{13}C transverse magnetization), the ^{13}C transverse magnetization is transferred to ^1H via the ^{13}C – ^1H J coupling (the period labelled τ , Fig. 13(a)). The resulting anti-phase ^1H transverse magnetization is then allowed to evolve in t_1 as for the usual WISE experiment. At the end of t_1 , the remaining ^1H magnetization is again transferred to ^{13}C as in the usual WISE experiment, except that in J-WISE, the transfer is via the agency of the ^1H – ^{13}C J coupling once more (the second τ period in Fig. 13(a)).

The whole experiment is reminiscent of the MAS-J-HSQC experiment.²¹ In cases where spinning sidebands appear in f_1 of the resulting two-dimensional experiment and are very well resolved, it may be necessary to use the constant time version of the J-WISE experiment, shown in Fig. 13(b). In order to achieve in-phase detection of the sidebands in f_1 , the rotor phase must be synchronized at the beginning and end of each t_1 period²², and this is achieved in the constant time version of the J-WISE experiment by replacing t_1 with a constant time T , which contains the usual t_1 evolution period with the remaining time $T-t_1$ being occupied by a spin lock pulse which stores one component of the remaining ^1H magnetization until the end of the T period. Clearly, this version of the experiment will lack sensitivity compared with the J-WISE experiment in Fig. 13(a), so should only be used where really necessary. The results from the work of ref. 18 on L-alanine are shown in Fig. 14.

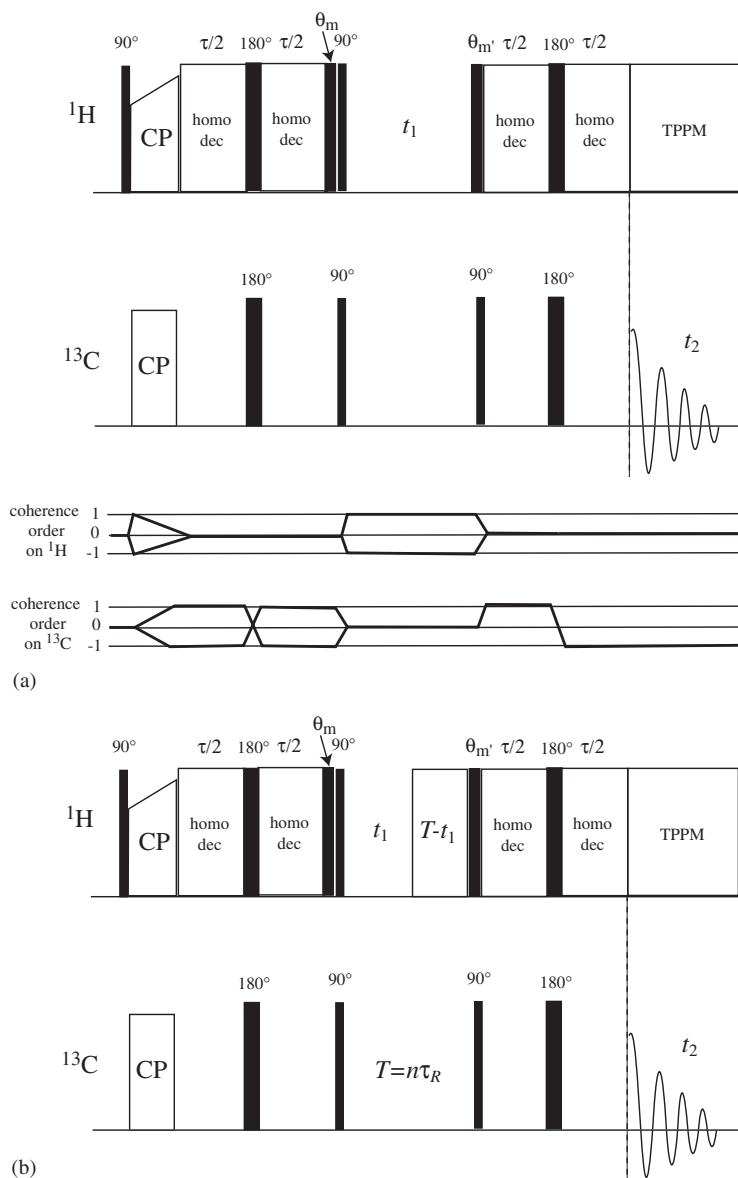


Fig. 13. (a) The J-WISE pulse sequence.¹⁸ (b) The constant time J-WISE pulse sequence.¹⁸ The θ_m pulse angle is the angle between the applied magnetic field of the NMR experiment and the direction of the effective ^1H field in the homonuclear decoupling sequence applied to the ^1H . $\theta_{m'} = 90^\circ - \theta_m$.

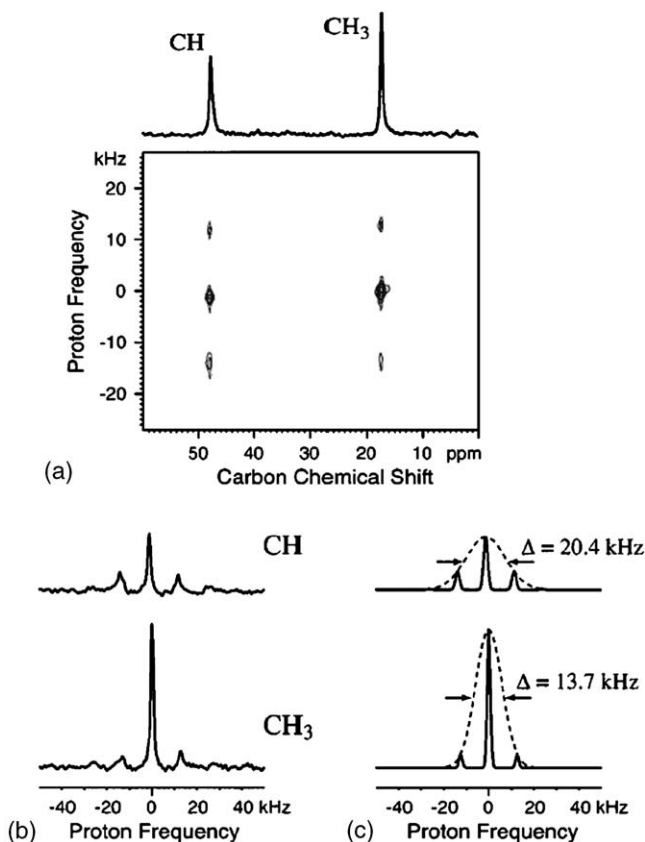


Fig. 14. The results of the constant time J-WISE experiment of Fig. 13(b) applied to L-alanine.¹⁸ (a) The full two-dimensional spectrum showing ^1H lineshapes (with sidebands due to ^1H - ^1H dipolar coupling). (b) Slices through the f_1 dimension corresponding to the CH ^{13}C and the CH_3 ^{13}C . (c) Simulations of the sideband patterns in (b) according to Δ , the linewidth (full width at half height) of the Gaussian line, which reflects the motionally averaged ^1H line (in a static sample).

Rapid anisotropic motion may be assessed by the reduction in the apparent dipolar coupling (because of averaging of the interaction by the motion) between two nuclei involved in the motion. ^1H is a convenient nucleus to monitor motion with due to their abundance in many materials. However, that very abundance leads to a lack of resolution in the ^1H spectrum under many conditions, due to the strong homonuclear dipolar coupling between the ^1H . This strong dipolar coupling can be exploited and high-resolution spectra achieved by ^1H multiple-quantum experiments under rapid MAS. A comprehensive review of ^1H multiple-quantum spectroscopy by Schnell and Spiess²³ contains all the information one could want on how to set up suitable experiments, their underlying theory and analysis. To

a first approximation, under very rapid MAS (e.g. 35 kHz for strongly dipolar-coupled ^1H systems), the extensively dipolar-coupled spin system can be treated as a sum of spin pairs. Thus, a double-quantum (DQ) coherence excited in the spin system may be regarded as having contributions very largely from spin pairs only, provided the DQ excitation time is kept short, as shown in Fig. 15. It is possible to create DQ coherences involving more than two spins, of course, and the amplitude of these increases as the DQ excitation time increases. For this reason, in a multiple-spin system, it is not practical to measure a spin pair dipolar coupling by following the amplitude of DQ coherence created with the length of the double-quantum excitation time, as one would do for an isolated spin pair system. Instead, one may use short DQ excitation times, so as to ensure contributions very largely from spin pairs only in the resulting DQ coherence, in a DQ–single-quantum (SQ) correlation experiment and rely on the *rotor-encoding* effect in such an experiment. Rotor encoding occurs as follows. The amount of DQ coherence excited during the excitation period depends (strongly) on the strength of the dipolar coupling during that period. This varies through the excitation period for a particular crystallite due to the MAS. Each crystallite will go through a well-defined, cyclic series of dipolar couplings during the

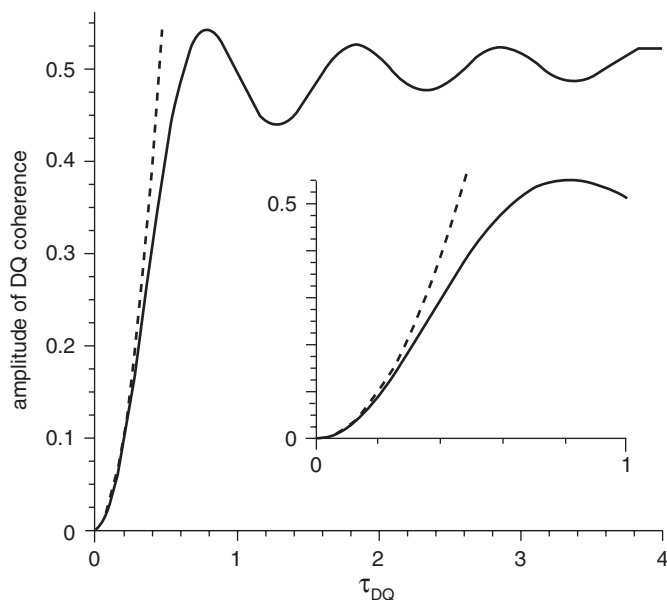


Fig. 15. Comparison of the DQ build-up curve with DQ excitation time τ_{DQ} for a spin pair system (solid line) and the leading spin pair term arising from a multi-spin system (dotted line).²³ For short excitation times, the two curves are approximately coincident. The inset shows this in more detail.

excitation period. Exactly the same feature is true for the reconversion step. Now if the intervening t_1 period is not an integral number of rotor periods, but some arbitrary time, then in general the series of dipolar couplings that are sampled during excitation will be different to those sampled during conversion by a phase factor, $\exp(i\Delta(d, \omega_R) t_1)$, where Δ depends on the dipolar coupling constant, d , and the sample-spinning rate, ω_R .

Thus, subsequent Fourier transformation in t_1 yields a spinning sideband pattern, with sidebands separated by ω_R and intensity distribution determined by d . Simulation of the sideband pattern then yields d , the dipolar coupling constant, or in a mobile system undergoing rapid uniaxial motion, d_{eff} , where d_{eff} is the motionally averaged dipolar coupling parameter, given for uniaxial motion by

$$d_{\text{eff}} = \frac{1}{2}d(3\cos^2\theta - 1), \quad (1)$$

where θ is the angle between the axis of motion and the internuclear axis corresponding to the particular dipolar coupling. Fig. 16 shows an example for a hexabenzocoronene.

Another very interesting example of the use of ^1H multiple-quantum spectroscopy under rapid MAS for the purpose of investigating rapid molecular motion concerns the motion of ethanol adsorbed on a silica surface.²⁴ The DQ sideband patterns obtained from DQ–SQ correlation experiments using different DQ excitation times are shown in Fig. 17, along with their simulation according to the motion of the OCH_2 group of the adsorbed ethanol.

Other examples include the use of rotor-encoded spinning sidebands resulting from heteronuclear dipolar couplings. Fig. 18(a) shows the rotor-encoded REDOR (REREDOR) pulse sequence²⁵, which uses the REDOR sequence²⁶ to recouple the ^1H – ^{13}C heteronuclear dipolar coupling. By making the t_1 period asynchronous with the sample spinning, the second period of REDOR recoupling begins with a different rotor phase to the first REDOR period and hence the signal resulting from the final t_1 period acquires a phase shift, which depends on t_1 and the ^1H – ^{13}C dipolar coupling. Hence, Fourier transformation of the t_1 time domain yields a series of spinning sidebands, analogous to those in the ^1H DQ experiments, whose intensities depend upon the ^1H – ^{13}C dipolar coupling.

An alternative to the REREDOR experiment is the REcoupled polarization transfer–heteronuclear dipolar order (REPT–HDOR),²⁷ shown in Fig. 18(b). This experiment uses initial ^1H transverse magnetization, rather than ^{13}C as in the REREDOR experiment, to create a heteronuclear ^1H – ^{13}C coherence (corresponding to dipolar order, described by a term $3I_zS_z - IS$ in the density operator, where $I = ^1\text{H}$ and $S = ^{13}\text{C}$) in t_1 after dipolar

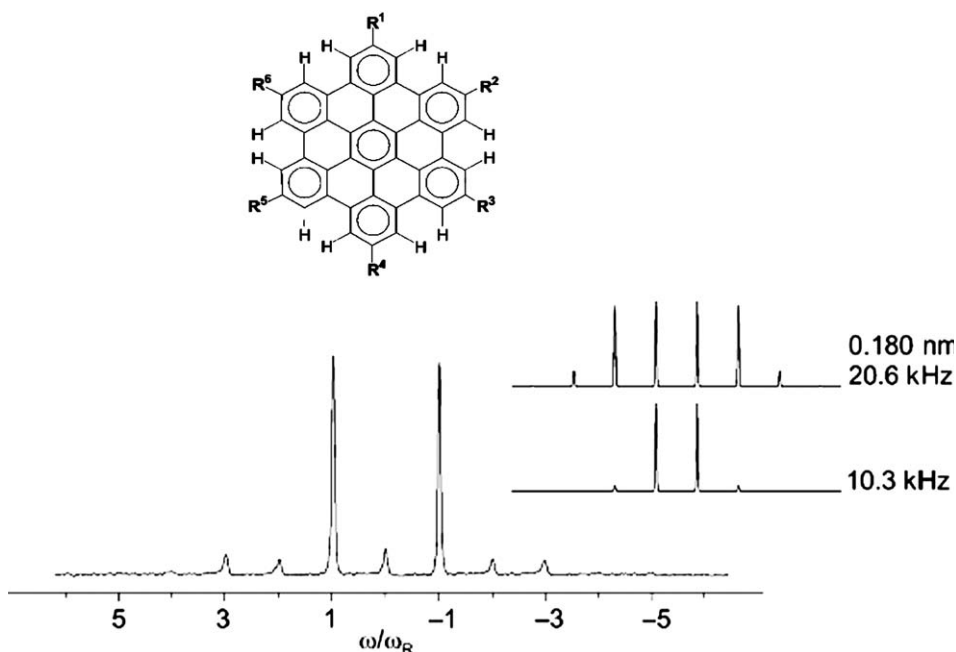


Fig. 16. The ^1H DQ sideband patterns arising from RE in a DQ–SQ correlation experiment for the aliphatic CH_2 ^1H in the hexabenzocoronene shown ($\text{R} = \text{CD}_2(\text{CH}_2)_{10}\text{CH}_3$).²³ Shown alongside are the simulated sideband patterns assuming a static system (top) and half the dipolar coupling strength of the static system (bottom). Note that the simulated sideband patterns only show odd-order sidebands, which is expected from theory.²³ That the experimental sideband pattern also contains weak even-order sideband patterns is a sign of the breakdown of the spin pair approximation.

recoupling via a classic REDOR sequence. The t_1 coherence is then transferred to anti-phase ^{13}C SQ coherence, via a ^{13}C 90° pulse (which creates an $I_z S_x$ term in the density operator) before a further REDOR period. The second REDOR period (in which the refocussing 180° pulses are applied to ^1H) begins at a different rotor phase to the first REDOR period, resulting in rotor-encoded spinning sidebands in the f_1 dimension of the final two-dimensional spectrum. The advantage of this experiment is that the ^1H to ^{13}C transfer is highly efficient.

Both REREDOR and REPT–HDOR experiments are used in an assessment of segmental dynamics in a dendritic polymer²⁸ by examining the residual dipolar couplings through simulation of the f_1 sideband patterns arising from the two types of experiment. Fig. 19 shows the results for the phenyl rings in the polymer.

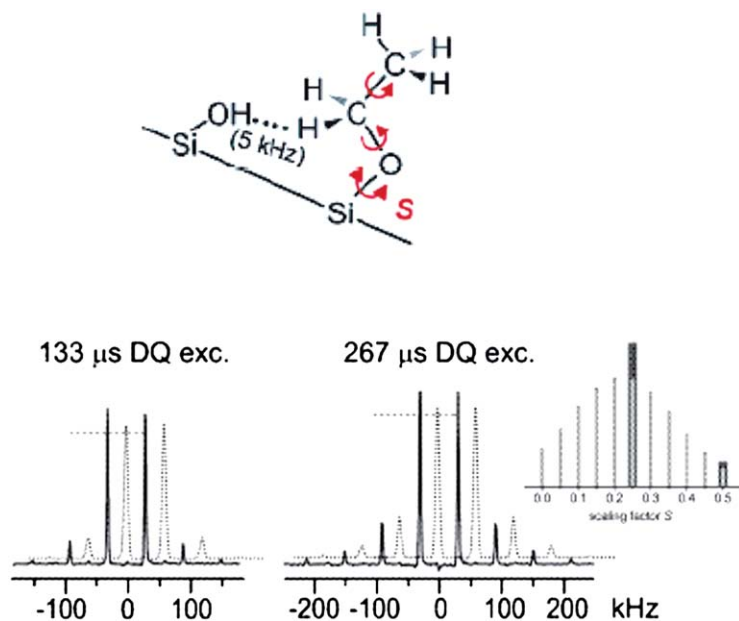


Fig. 17. The ^1H DQ sideband patterns arising from DQ–SQ correlation experiments on the OCH_2 group of ethanol bound to amorphous silica surfaces.²⁴ The sideband patterns are shown for two different DQ excitation times, as indicated. The solid lines are the experimental results; the dotted lines are simulations assuming the motion indicated at the top of the figure and a distribution of effective dipolar coupling constants for the ^1H – ^1H dipolar coupling within the OCH_2 group. The dashed lines indicate the expected contribution from the underlying water signal. The effective dipolar coupling constants are given by the dipolar coupling constant expected for the rigid system multiplied by a scaling factor, S , which accounts for the conformational freedom about the Si–O bond. Rapid motion about this bond will scale the dipolar coupling constant as described in Eq. (1). The distribution of scaling factors used in the simulation is shown in the inset figure.

As well as the use of new experiments, there have been a number of interesting examples of utilizing dipolar couplings via well-known experiments in order to assess motion during the review period.

In one study, a model for elastin, the main protein that confers elasticity on solid structures in mammals, had its mobility investigated by examining ^1H – ^{13}C and ^1H – ^1H dipolar couplings extracted from isotropic–anisotropic correlation experiments.²⁹ The elastic properties of elastin are almost certainly conferred by molecular degrees of freedom, so such studies are important in understanding how this material works in Nature. The motional amplitudes determined from these experiments were found to depend upon the degree of hydration, with the mean square fluctuation angles found to be 11 – 18° in the dry protein and 16 – 21° in the 20% hydrated protein.

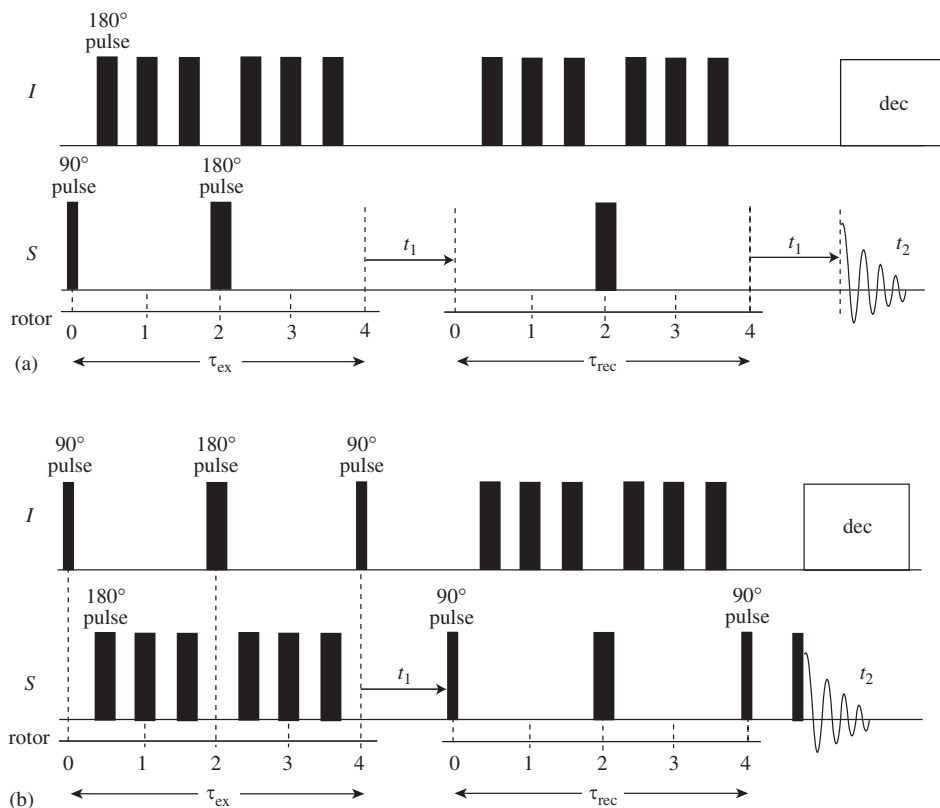


Fig. 18. (a) The REREDOR pulse sequence.²⁵ (b) The REPT-HDOR pulse sequence.²⁷

In another study of highly mobile elastomers, where the dipolar couplings are drastically reduced by molecular motion, REDOR²⁶ was found to be a reliable method of establishing the residual dipolar couplings and so assessing the molecular mobility.³⁰ The elastomers in question are vulcanized natural rubbers, predominantly *cis*-polyisoprene. Fig. 20 shows the REDOR difference curves for the ^{13}CH resonance from different samples, which had different lengths of vulcanization time. There are clear differences between the curves for different samples, which are interpreted in terms of the distribution of motional amplitudes in the samples, which in turn are related to the cross-link density arising from the vulcanization process.³⁰

Finally, in this section, the simple Hartmann-Hahn cross polarization experiment, and in particular, the ^1H - ^{19}F CP build up curve was used to determine the residual ^1H - ^{19}F dipolar coupling constant due to motion in an ethylene/tetrafluoroethylene co-polymer.³¹ This curve for the crystalline

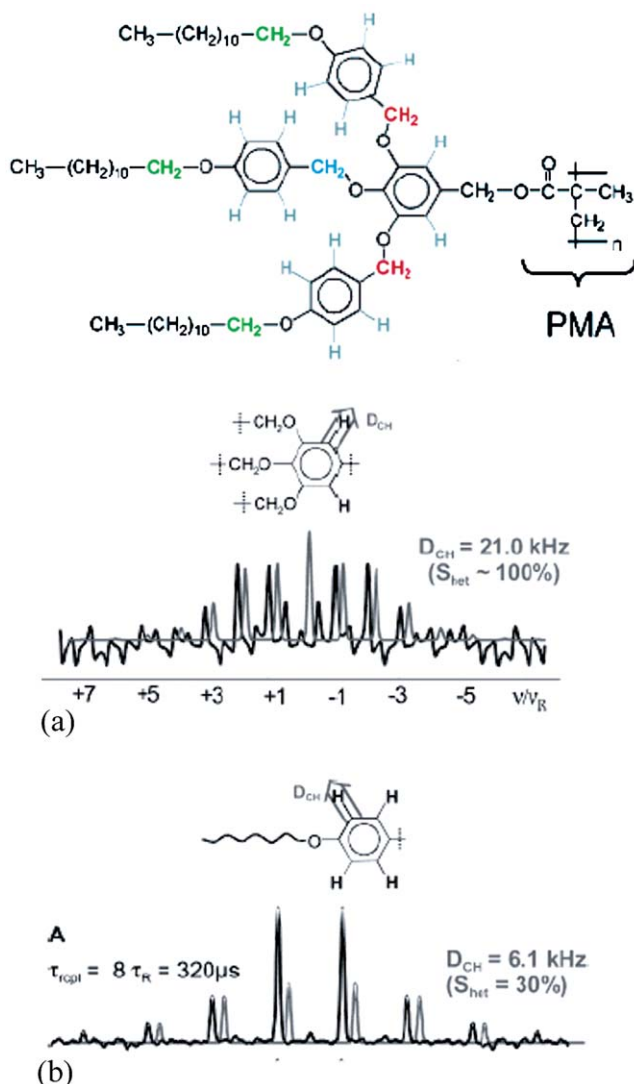


Fig. 19. Assessment of the residual dipolar couplings arising from motion of the phenyl rings in the dendritic polymer shown.²⁸ (a) Results from a REREDOR experiment on the inner phenyl rings. The black line is the experimental result, the grey one a simulation assuming a $^{13}\text{C}-^1\text{H}$ dipolar coupling constant of 21 kHz, which is that expected for a static $^{13}\text{C}-^1\text{H}$ bond. The direction of the unique axis of the $^{13}\text{C}-^1\text{H}$ dipolar coupling tensor used in the simulation is shown with an arrow on the inset above the spectrum. (b) Results from the REPT-HDOR experiment on the outer phenyl rings. The black line is again the experimental result; the grey one the simulation, this time assuming a residual $^{13}\text{C}-^1\text{H}$ dipolar coupling constant of 6.1 kHz, which is 30% of that expected for a rigid $^{13}\text{C}-^1\text{H}$ bond.

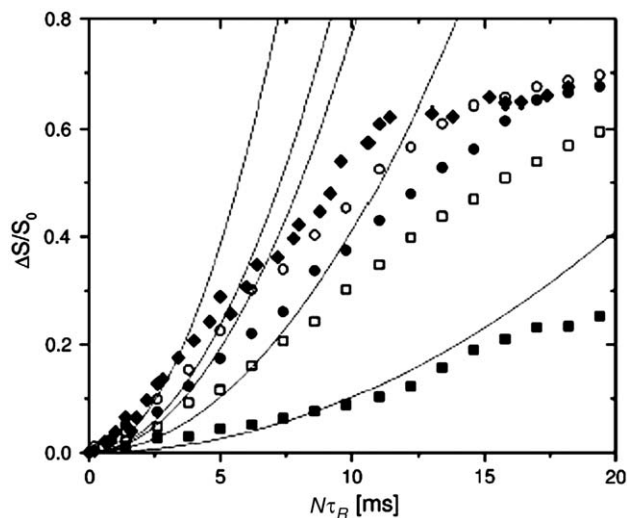


Fig. 20. $^{13}\text{C}\{-^1\text{H}\}$ REDOR difference curves for the ^{13}CH resonance in different samples of vulcanized natural rubber.³⁰ The samples differ in the length of time for which vulcanization was allowed to proceed: solid squares, 14 min; open squares, 12 min; solid circles, 10.5 min; open circles, 8 min; solid diamonds, 7 min. The solid lines are best fits to the initial slopes of each curve.

regions of the material shows distinct dipolar oscillations whose frequency indicates that the $^1\text{H}\text{--}^{19}\text{F}$ dipolar coupling is significantly reduced as the temperature is increased from 42°C to 145°C . Thus, a relatively simple experiment can be utilized to yield high-quality information on molecular motion.

2.5. Quadrupole coupling lineshapes

2.5.1. Deuterium spectroscopy

^2H has always been a popular nucleus for studying molecular motion. This spin-1 nucleus gives rise to quadrupole coupling constants in the range 160–220 kHz in most organic compounds. Thus, the effects of quadrupole coupling are moderate and need only to be considered to first order. Its static quadrupolar-broadened powder patterns are sensitive to motions with correlation times in the range 10^{-7} – 10^{-4} s, which makes such powder patterns ideal for studying a large range of reorientational motions in solids.

^2H quadrupole powder patterns are generally fairly straightforward to record. Usually, a solid- or quadrupole-echo pulse sequence ($90^\circ_x\text{--}\tau\text{--}90^\circ_y\text{--}\tau\text{--FID}$) is used in order that dead time losses do not occur; these would otherwise severely distort the lineshapes.²

The problem with ^2H NMR in the solid state is generally one of resolution. The quadrupole coupling strength is generally much larger than the isotropic chemical shift range, so if spectra are recorded on static, i.e. non-spinning samples, the powder patterns from different chemical sites are extensively overlapped. Even under MAS, resolution is difficult. The width of the static quadrupolar-broadened powder pattern is generally much larger than any realistically achievable spinning rate, so numerous sidebands are always present in the spectra, which hamper resolution.

One solution to this problem is to perform a two-dimensional ^2H experiment, in which a DQ ^2H spectrum appears in one dimension, while some sort of powder pattern or spinning sideband pattern, reflecting the quadrupolar broadening appears in the other. The advantage of the DQ spectrum is twofold. (1) The DQ spectrum is unaffected (to first order) by the quadrupole coupling and chemical shift anisotropy, so the spectrum is necessarily high resolution, and moreover, is largely unaffected by any molecular motion that might be present. (2) The separation of signals in the DQ dimension is two times the isotropic chemical shift differences, increasing the available resolution considerably.

The simplest experiment based on this approach is shown in Fig. 21.³² This separates ^2H -spinning sideband patterns arising from quadrupole coupling in f_2 according to the ^2H DQ chemical shift in f_1 . An example of this approach on deuterated 4,4'-azoxyanisole is shown in Fig. 22.³²

A recent development uses off-angle spinning (OMAS), i.e. sample spinning away from the magic angle, to achieve the desired quadrupole-broadened powder patterns in f_2 in a similar DQ-SQ correlation experiment.³³ Spinning a sample at the magic angle averages the quadrupole coupling and chemical shift anisotropy to zero. In general, spinning the sample at an angle θ_R with respect to the applied field averages these anisotropic interaction by a factor $1/2 (3\cos^2 \theta_R - 1)$ (which is of course zero for the magic angle, $\theta_R = 54.74^\circ$).^{33,34} Thus, spinning the sample away from the magic angle yields not a sharp isotropic line, but a powder pattern (resulting from the

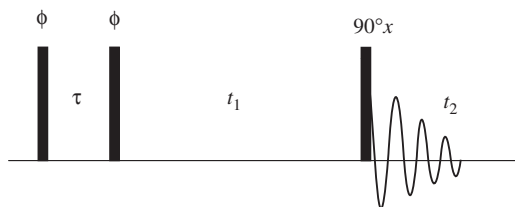


Fig. 21. The pulse sequence for the ^2H DQ experiment, which separates ^2H -spinning sideband patterns arising from the ^2H quadrupole coupling according to ^2H DQ isotropic chemical shifts.³²

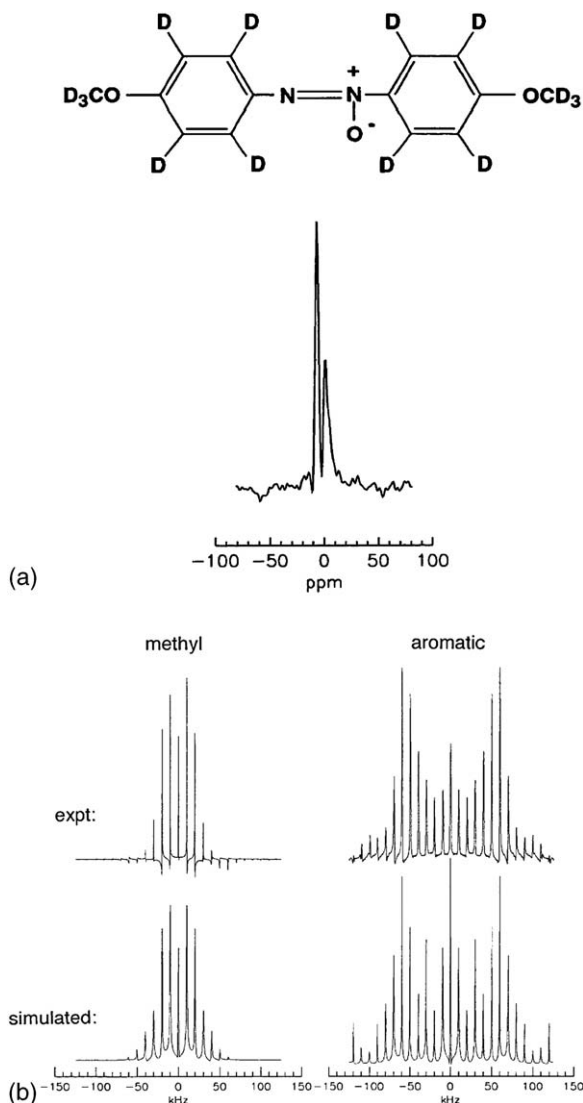


Fig. 22. The results of the experiment shown in Fig. 21 on 4,4'-azoxydianisole (top).³² (a) The 2H DQ spectrum, showing resolution of the signals from the methyl and aromatic 2H . This is the projection in the f_1 dimension of the two-dimensional experiment. (b) The associated f_2 projections showing the spinning sideband patterns arising from quadrupole coupling at the methyl and aromatic 2H sites.

quadrupole coupling) scaled by the factor $1/2 (3\cos^2 \theta_R - 1)$. In the 2H DQ OMAS experiment³⁴, such powder patterns are collected in the t_2 dimension of the experiment. Spinning sidebands in this dimension are avoided by synchronizing the data collection with the sample spinning, i.e. the dwell

time in $t_2 = \tau_R$, the rotor period. This necessarily restricts the spectral width in f_2 . However, this is not a great concern as for spinning angles close to the magic angle, the scaling factor on the quadrupole coupling powder patterns is small, resulting in powder patterns that are relatively easy to handle within the restricted spectral width. An example of the use of this experiment is shown in Fig. 23.³³

There has also been further work on the analysis of one-dimensional ^2H NMR spectra for the study of molecular motion. One interesting study

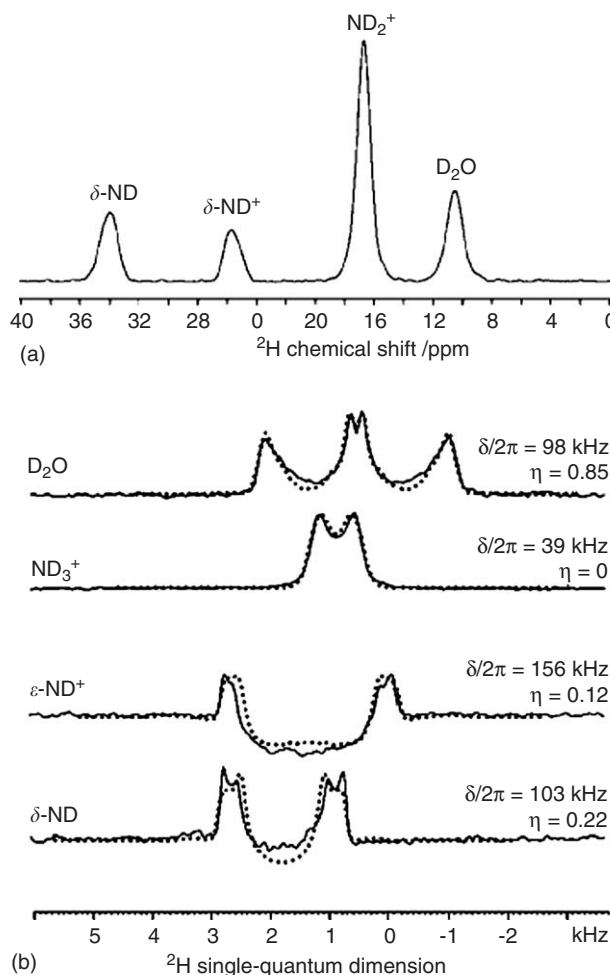


Fig. 23. The results of the ^2H DQ OMAS experiment on a sample of deuterated L-histidine hydrochloride monohydrate.³³ (a) The projection in the DQ dimension of the experiment (f_1). (b) The associated scaled ^2H quadrupole powder patterns arising in f_2 .

compares the utility of static quadrupole echo ^2H spectra versus MAS ^2H spectra, especially in the case where there is a distribution of correlation times for the motion.³⁵ ^2H quadrupole echo spectra are distorted by molecular motions with correlation times in the intermediate regime, that is $\tau_c^{-1} \sim \omega_Q$ where ω_Q is the quadrupolar splitting. The motion in this regime affects the T_2 -relaxation rate through the quadrupolar mechanism, and since ω_Q is dependent upon molecular orientation, affects T_2 differently for different molecular orientations, and hence different parts of the quadrupolar-broadened powder pattern. This results in distortions of the quadrupole powder pattern, which are characteristic of the molecular motion. The problem arises when there is a distribution of correlation times for the motion. Then there is a corresponding distribution of T_2 -relaxation rates at each frequency point in the quadrupole powder pattern. This is difficult to distinguish from a complex motion with a single correlation time, but reorientations around several non-coincident axes. The work³⁵ found through experiment and simulations that MAS spectra were sensitive to reorientational motions with correlations times in the region of 10^{-2} – 10^{-8} s, a considerably larger range than the intermediate motion regime (10^{-4} – 10^{-6} s) for which static quadrupole echo spectra are sensitive. The work also showed that MAS spectra are highly sensitive to distributions of correlation times in the motion, though no explanation is offered for this, nor for the extended range of sensitivity of MAS spectra. Fig. 24 compares simulated static quadrupole-echo spectra and MAS spectra for the twofold motion, which is assumed to occur in deuterated DMS, i.e. two-site hopping such that the principal axis of the ^2H quadrupole coupling tensor reorients through 106° .³⁵

New work has been performed on the simulation of static ^2H lineshapes under conditions of molecular motion. This work³⁶ utilizes a random walk model to generate a (random) series of molecular orientations occurring within a prescribed molecular motion, e.g. isotropic motion in jumps of χ° or random rotational motion about a specific axis with a defined range of jump angles. A Markov model for the motion is assumed, i.e. that the length of time it takes for a jump to occur is negligible compared to the time spent in each of the sites visited during the course of the motion and that the probability of a jump at any time point does not depend on the time since the last jump. A random number generator is used to generate a series of molecular orientations through the course of the motion. The waiting time between jumps is also created randomly from an exponential distribution of waiting times characterized by a jump correlation time τ_j . From the series of time-dependent molecular orientations so created, the time-dependent ^2H quadrupolar frequencies, $\omega_Q(t)$, are calculated. The evolution of the ^2H transverse magnetization during the τ periods of a quadrupole-echo pulse sequence $90^\circ_x\text{--}\tau\text{--}90^\circ_y\text{--}\tau\text{--FID}$ is then easily calculated, and hence the final

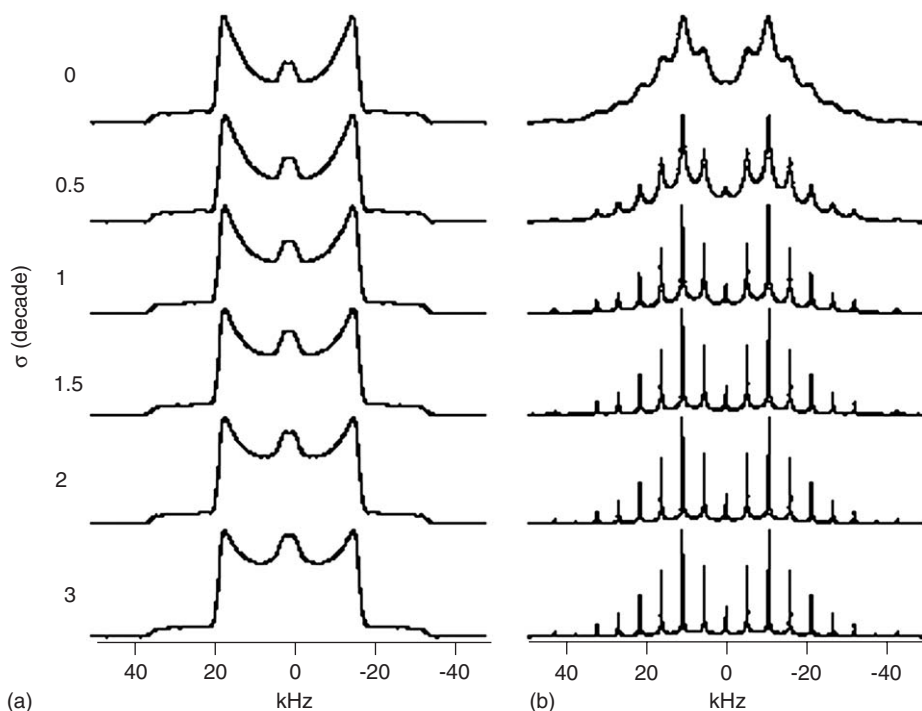
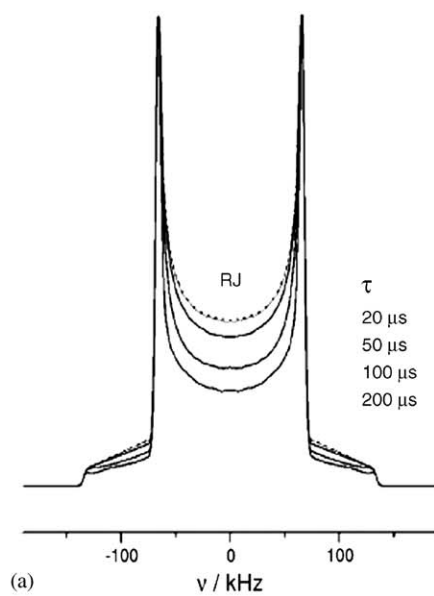


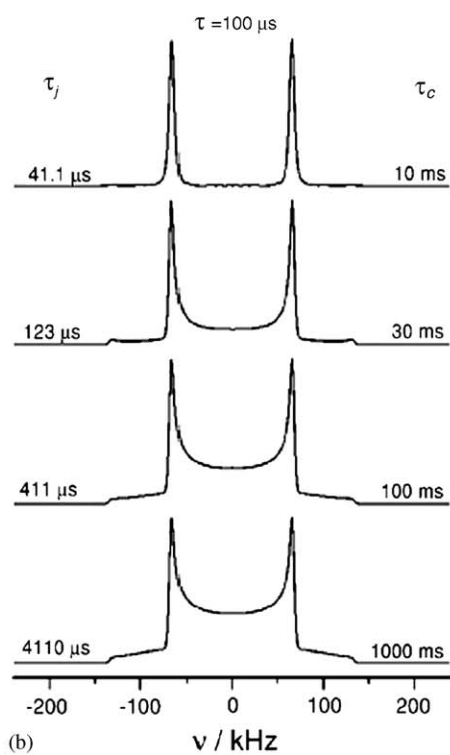
Fig. 24. Calculated ^2H quadrupole echo and MAS NMR spectra for a two-site reorientation³⁵ such that the ^2H quadrupole coupling tensor unique principal axis moves through 106° , i.e. the motion appropriate for the two-site motion of the methyl groups in deuterated DMS. The simulations assume an inhomogeneous symmetric log-Gaussian distribution of correlation times with a mean correlation time of 5×10^{-5} s and a standard deviation ranging from 0 to 3 decades. (a) Quadrupole echo spectra with echo delay time $\tau = 30 \mu\text{s}$. (b) MAS spectra.

observed FID produced. The ultimate aim of this work is to study the molecular dynamics associated with the α - and β -relaxation processes in supercooled liquids and glasses, but it is worth noting that this random walk approach is generally applicable for molecular motions that can be described by a Markov model and indeed may be a very valuable approach for describing complicated molecular dynamics. Fig. 25 shows some of the simulation results from the work.³⁶

There are many examples of ^2H lineshape analyses in the review period, but one of particular interest is the work by Drobny *et al.*³⁷ This study examines the conformational flexibility of the furanose ring, which is of particular importance in the functioning of DNA. They examined the nucleoside [$2''\text{-}^2\text{H}$]-2'-deoxycytidine deuterated at the C_3 position (Fig. 26(a)) and contained in the sequence $[\text{d}(\text{CGCGAATTCGCG})]_2$. The furanose ring



(a)



(b)

in general is known to have different conformations in the A and B forms of DNA (Fig. 26(b)), so some inherent conformational flexibility is to be expected. Moreover, the furanose ring may act as a link between the structurally labile phosphodiester backbone and the rigidly stacked base pairs, so a knowledge of the flexibility of this ring is vital in understanding the properties of DNA. The fitting of the static ^2H lineshapes is complicated by the fact that one has to consider the underlying motion of the DNA molecule as well as the furanose ring. This work assumes a Smoluchowski model for the motion, rather than the more usual stochastic model used in fitting ^2H lineshapes. The Smoluchowski model does not assume that the time taken for a motional hop is insignificant compared with the time spent in a site. Rather it assumes diffusion over a potential surface, which is probably much more suited to the case in hand. The best fits to the ^2H lineshapes are for a double-welled potential with equal barrier heights (5.5 kT), a ring-puckering amplitude of 0.4 Å and a diffusion coefficient characterizing the underlying stochastic jump rate between the potential wells of 9.9×10^8 Hz. Fig. 26(c) shows an example of an experimental ^2H lineshape and the best-fit simulation obtained in this work.

2.5.2. Half-integer spin spectroscopy

Although the application of the classical Bloch–McConnell equations to describe the effects of molecular dynamics on the lineshapes arising from first-order nuclear spin interactions (including quadrupole coupling) has been known for many years,^{38,39} there have been very few motional studies on half-integer quadrupolar nuclei, in particular those exhibiting relatively large quadrupole couplings. The reason for this is the complications introduced by the large quadrupole coupling, which means that the coupling effects must be considered to at least second order and the fact that the relaxation of such systems is necessarily multi-exponential (as the different possible transitions available to a quadrupolar nucleus have different frequency dependences and hence different transition probabilities at any given temperature) and thus difficult to describe. Headway has now been made in this area with three separate studies of half-integer quadrupolar nuclei with large quadrupole couplings for the purposes of characterizing molecular

Fig. 25. Random walk simulations for static ^2H NMR powder lineshapes arising from a quadrupole echo $90^\circ_x - \tau - 90^\circ_y - \tau$ -FID pulse sequence for the model of an isotropic 3° jump.³⁶ (a) Jump correlation time, $\tau_j = 411 \mu\text{s}$; correlation time for the motion, $\tau_c = 100$ ms, echo delays τ as given in the figure. Dotted line is the spectrum for an isotropic random jump with $\tau_j = \tau_c = 100$ ms and an echo delay $\tau = 200 \mu\text{s}$. (b) Jump correlation times τ_j and motional correlation times τ_c as given in the figure, echo delay $\tau = 100 \mu\text{s}$.

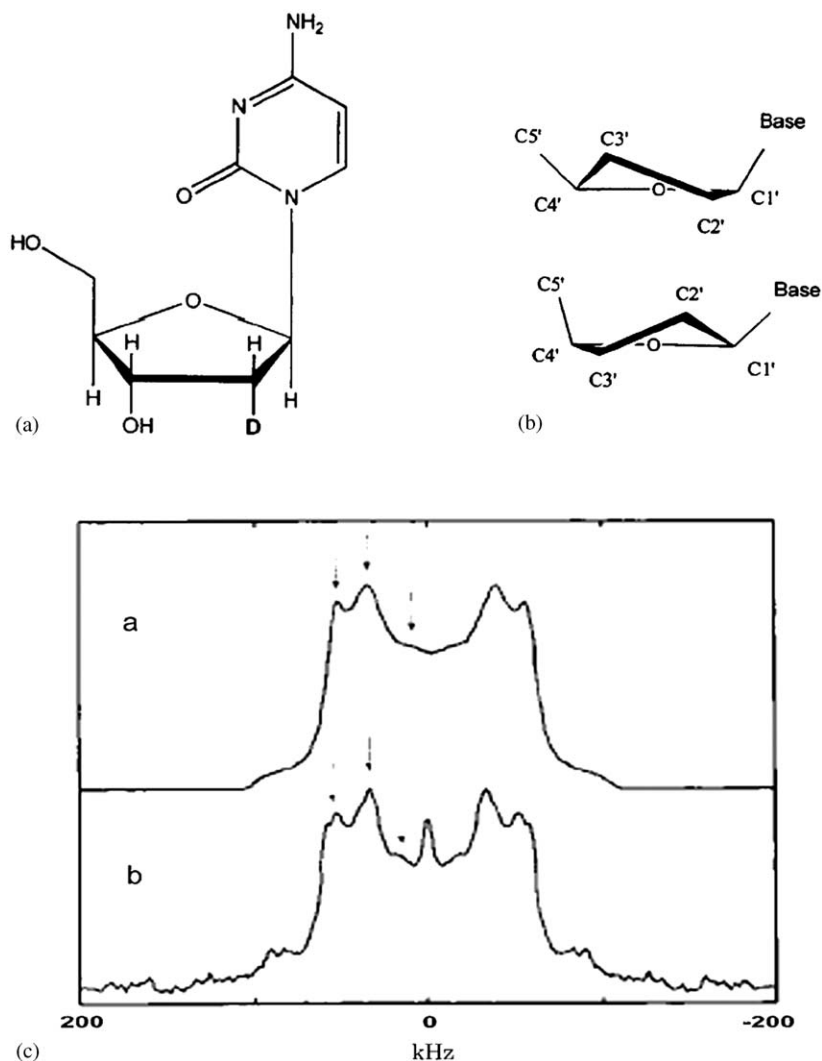


Fig. 26. (a) The $[2''\text{-}^2\text{H}]$ -2'-deoxycytidine nucleoside used in the work of ref. 37. (b) The different possible conformations of the furanose ring. Top: C_3' -endo conformation found in DNA-A; bottom: C_2' -endo conformation found in DNA-B. (c) Best-fit comparison of simulated ^2H NMR powder lineshape to experiment for $[2''\text{-}^2\text{H}]$ - C_3 from $[\text{d}(\text{CGCGAATTCGCG})_2]$.³⁷

dynamics. This has necessitated the further development of the theoretical approach to describe the effects of molecular motion in such a system, in particular, the anisotropic relaxation which occurs.⁴⁰ However, as pointed out by Frydman *et al.*⁴¹ in work published almost concurrently with that of Kristensen and Farnan,⁴⁰ this is just the beginning of the exploration of the

full effects of molecular motion on a half-integer quadrupolar spin system. One complication compared to a spin-1/2 or spin-1 system is the multitude of transitions available for the spin. The central transition ($+1/2 \rightarrow -1/2$) is not affected by quadrupole coupling to first order, and thus one might expect the central transition lineshape to be unaffected by molecular dynamics occurring on the first-order quadrupole coupling timescale (χ_Q^{-1} , χ_Q = quadrupole coupling constant). However, this is not the case. Such motion stimulates relaxation processes involving the satellite transitions, which affect the populations of the $\pm 1/2$ spin levels and so affect the central transition rates also.

The most detailed description of these effects is given in an elegant paper by Kristensen and Farnan. They start from the stochastic Liouville–von Neumann equation to describe the time dependence of the nuclear spin system:

$$\frac{\partial \tilde{\rho}(t)}{\partial t} = (-i\tilde{H}(t) + \Delta(t) + \Pi)\tilde{\rho}(t), \quad (2)$$

where $\tilde{\rho}(t)$ is the time-dependent rotating frame density operator, $\tilde{H}(t)$ the rotating frame Hamiltonian describing the spin system, $\Delta(t)$ the relaxation operator, the time dependence in each case being due to molecular motion. The need for rotating frame density operator and Hamiltonian is described in Section 3. Π is the stochastic operator describing the motional processes affecting the nuclear spins. In this approach, the Hamiltonian and density operators are expanded as a sum of terms, with each term corresponding to one of the sites involved in the molecular motion. In turn, each of these terms is expanded as a sum of terms pertaining to each matrix element of the operators in a matrix representation (in a Zeeman basis), i.e. a superoperator approach:

$$\tilde{H}(t) = \sum_{m=1}^M \sum_{n=1}^N \tilde{H}_m(\pi_n, t) \Gamma_m(\pi_n), \quad (3)$$

where π_n refers to the n th state or orientation involved in the motional process and Γ_m represents the m th element of the set of M elements of the matrix representation of the Hamiltonian and density operators.

Relaxation is treated quantum mechanically as in ref. 39, the original treatise on the subject. The relaxation operator in the usual rotating frame, Hilbert space representation is

$$\Delta(t) = - \int_0^{t-t_0} \langle \tilde{H}(t) \tilde{H} * (t - \tau) \rangle + \text{c.c.} \, d\tau, \quad (4)$$

where $\langle \tilde{H}(t) \tilde{H}(t - \tau) \rangle$ is the correlation function of the rotating frame spin Hamiltonian. This may be rewritten by substituting the expansion of the

Hamiltonians in Eq. (3):

$$\Delta(t) = - \sum_{m=1}^M \sum_{q,p=1}^M \Gamma_q(\pi_n) \Gamma_p(\pi_n) \int_0^{t-t_0} \langle \tilde{H}_p(\pi_n, t) \tilde{H}_q * (\pi_n, (t-\tau)) \rangle + \text{c.c.} d\tau \quad (5)$$

The correlation functions in Eq. (5) are then expanded in the usual way² in terms of spectral densities (see Section 3 for further details). As Eq. (5) shows, the relaxation operator involves products of Hamiltonian matrix elements and thus has the effect of redistributing coherence between the various matrix elements or coherences/populations of the density matrix through its involvement in Eq. (2). Kristensen and Farnan⁴⁰ use their formalism to calculate the central transition lineshapes for ^{17}O ($I = 5/2$) for both fully relaxed and partially relaxed conditions under different motional models. Some examples are shown in Fig. 27.

The work by Frydman *et al.*⁴¹ has some very nice examples of the dynamic effects on half-integer quadrupolar lineshapes. This work examines XO_4^- anions where X contains a quadrupolar nucleus, $^{185/187}\text{Re}$, ^{55}Mn and ^{75}As

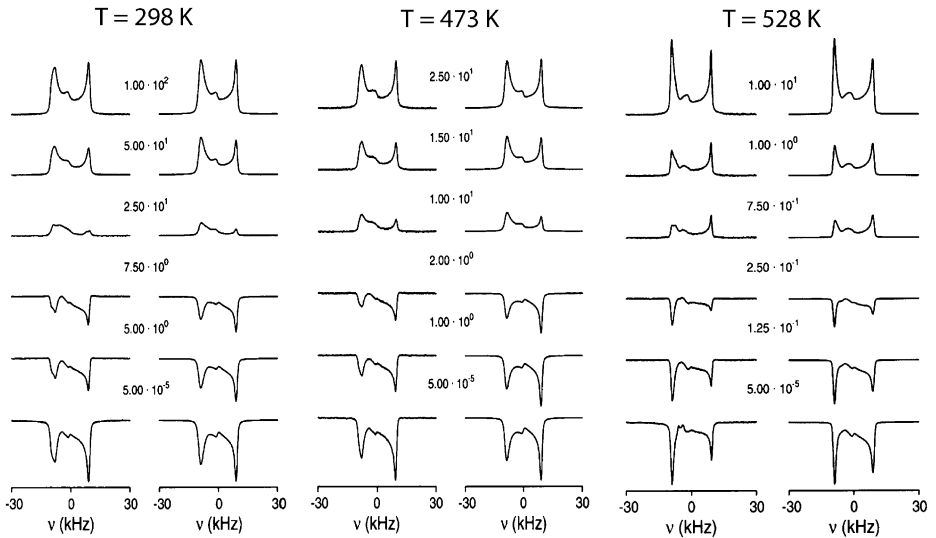


Fig. 27. Experimental (left) and simulated (right) central transition inversion recovery spectra of 47% enriched polycrystalline cristoballite for the temperatures given, recorded as a function of the length τ of the relaxation delay.⁴⁰ All simulations assume a six-site motion between six equally probable sites on a circle orthogonal to the Si–Si axis between adjacent SiO_4 tetrahedra, with rate constants $\log(k) = 3.50$ at $T = 298$ K, $\log(k) = 3.95$ at $T = 473$ K and $\log(k) = 5.80$ at $T = 528$ K.

suffering very large quadrupole couplings, cf. $e^2qQ/h = 278$ MHz for ^{185}Re in NaReO_4 ! Such cases are difficult to deal with experimentally, let alone theoretically. The theoretical treatment here is with McConnell's semi-classical exchange formalism,³⁸ i.e. assuming random hops of the groups between possible sites. This approach resulted in good agreement between experimental and simulated lineshapes with plausible motional models used in the simulations.

A purely experimental study on the ^{23}Na ions in a number of different sodalites⁴² has shown that for some sodalites, ^{23}Na ions are mobile at temperatures above ~ 500 K. The temperature-dependent ^{23}Na NMR spectra are analyzed in terms of effective quadrupole coupling constants (e^2qQ/h) and asymmetries. The temperature dependence of the quadrupole coupling was found to be correlated with the expansion of the β sodalite cage, as measured by X-ray diffraction. Two possible jump mechanisms were put forward, both involving two-site jumps between occupied and unoccupied tetrahedral sites, either within one cage, or via a six-membered ring window between two cages.

What is quite clear from all these studies of quadrupolar lineshapes is that molecular motion in inorganic ionic solids is relatively common. The lack of previous studies has led to the idea that motion in such systems is unlikely, yet the few studies that have now been done all report positive findings. This is clearly an area of further work, both to examine the extent of molecular motion in inorganic/ionic systems (with a view ultimately of understanding what effects such motions may have on the material properties of ionic systems) and to examine how far semi-classical methods may be employed to analyze the spectral data from such systems.

3. RELAXATION TIME MEASUREMENTS

3.1. Basics – theory

Relaxation time measurements have long been used to characterize molecular motion in solids. All nuclear spin-relaxation processes are mediated by fluctuating nuclear spin interactions with the fluctuations (generally) arising from molecular motion or lattice phonon modes. A very brief description of the theoretical basis for understanding relaxation processes is given here to serve as a framework for understanding the utility of relaxation time measurements in studying molecular motion and in order to understand what may come out of the results of relaxation time measurements.

Relaxation is the change in time of the density matrix describing the spin system as the system moves back towards equilibrium from some

non-equilibrium state imposed, for instance, by the action of a sequence of rf pulses.⁴³ Longitudinal or spin–lattice relaxation, for example, restores the populations of the various Zeeman spin levels to the equilibrium Boltzmann distribution. It therefore affects the diagonal elements of the density matrix (described in the Zeeman basis), which describe the populations of these spin levels (or in the more general case, the populations of whatever functions have been taken as the basis set for the density matrix).

The time dependence of the relaxation process necessitates the use of time-dependent perturbation theory, in which the total Hamiltonian of the system is described by

$$\hat{H}(t) = \hat{H}_0 + \hat{H}_1(t), \quad (6)$$

where \hat{H}_0 is the time-independent Zeeman interaction and $\hat{H}_1(t)$ describes the fluctuating nuclear spin interactions, their time dependence arising from the underlying molecular motion. In the perturbation theory approach, $\hat{H}_1(t)$ is considered as a perturbation on the Zeeman interaction, which itself is assumed to impose no time dependence on the system, i.e. the only time dependence in the system is assumed to come from the perturbing interaction $\hat{H}_1(t)$. This is not the case, of course, for NMR, where the Zeeman interaction described by \hat{H}_0 imposes a time dependence on the density matrix, namely, rotation at frequency ω_0 , the Larmor frequency, about the applied magnetic field of the NMR experiment. Moreover, the frequency of this time dependence is very similar to that of the molecular motions, which drive spin–lattice relaxation. Thus, before proceeding further, we must remove the time dependence, which is introduced by the Zeeman interaction. This is done in the usual way by transforming the whole problem to the rotating frame of reference, one which rotates about the applied magnetic field (z) at the Larmor frequency. The resulting Hamiltonian describing the spins system in this frame is simply

$$\begin{aligned} \tilde{H}(t) &= \hat{R}_0^{-1}(\omega_0 t) \hat{H}(t) \hat{R}_0(\omega_0 t) \\ &= \exp(i\omega_0 t \hat{I}_z) (\omega_0 \hat{I}_z + \hat{H}_1(t)) \exp(-i\omega_0 t \hat{I}_z) - \omega_0 \hat{I}_z \\ &\quad \exp(i\omega_0 t \hat{I}_z) \hat{H}_1(t) \exp(-i\omega_0 t \hat{I}_z). \end{aligned} \quad (7)$$

Using the results of time-dependent perturbation theory, the rate of transition between two spin levels j and k , which are subject to the rotating frame spin Hamiltonian of Eq. (7) is given by

$$W_{jk} = \frac{1}{\hbar^2} \int_{-\infty}^{+\infty} \langle j | \tilde{H}(t) | k \rangle \langle k | \tilde{H}(t + \tau) | j \rangle + \text{c.c.} \, d\tau, \quad (8)$$

where “c.c.” stands for complex conjugate. Eq. (8) is sometimes known as the Golden Rule of quantum mechanics. In turn, the rate of change of

population of a Zeeman level due to the fluctuation Hamiltonian can be written in terms of the transition rates to that level from all others and vice versa, as described by Eq. (8). Hence, one can use Eq. (8) to derive an equation for the total transition rate, and hence the relaxation rate due to the fluctuation Hamiltonian of Eq. (7). For the more general case of the rate of change of any density matrix element, the reader is referred to ref. ⁴³.

To gain some insight into the operation of Eq. (8) in practise, we shall write the time-dependent, perturbing operator in terms of spherical tensors and spherical tensor operators:

$$\hat{H}_1(t) = \sum_{M=-2}^{+2} (-1)^M A_{2M}(t) \hat{T}_{2M} \quad (9)$$

where the \hat{T}_{2M} are spherical tensor operators and the $A_{2M}(t)$ are components of the nuclear spin-interaction tensor expressed in irreducible spherical tensor form,² and time dependent due to molecular motion. We then need to express Eq. (9) in the rotating frame of reference according to Eq. (7).

$$\begin{aligned} \tilde{H}(t) &= \exp(i\omega_0 t \hat{I}_z) \hat{H}_1(t) \exp(-i\omega_0 t \hat{I}_z) \\ &= \sum_{M=-2}^{+2} (-1)^M A_{2M}(t) \exp(i\omega_0 t \hat{I}_z) \hat{T}_{2M} \exp(-i\omega_0 t \hat{I}_z) \\ &= \sum_{M=-2}^{+2} (-1)^M A_{2M}(t) \exp(-iM\omega_0 t) \hat{T}_{2M} \end{aligned} \quad (10)$$

The time dependence of the perturbing Hamiltonian due to molecular motion is expressed through the nuclear spin-interaction tensor, which changes the orientation of its principal axis frame as the molecule changes its orientation through motion with respect to the applied magnetic field, or changes its magnitude as internuclear distances vary through motion.

²The nuclear spin-interaction tensor is most readily expressed in its *principal axis frame* where only the $M = 0, \pm 2$ terms are non-zero (and only the $M = 0$ term is non-zero for axial symmetry cases). It can then be expressed in the rotating frame as required for Eq. (8) by performing the frame transformation from principal axis frame to rotating frame:

$$A_{2M} = \sum_{M'=0,\pm 2} D_{M'M}^2(\alpha, \beta, \gamma) \rho_{2M'},$$

where $\rho_{2M'}$ is the interaction tensor in its principal axis frame and α, β, γ are the Euler angles relating the principal axis and rotating frames; $D_{M'M}^2(\alpha, \beta, \gamma)$ are Wigner rotation matrix elements given by

$$D_{M'M}^K(\alpha, \beta, \gamma) = \exp(-i\alpha M') \exp(-i\gamma M) d_{M'M}^K(\beta),$$

where $d_{M'M}^K(\beta)$ is a reduced Wigner rotation function.

For a Hamiltonian of the form in Eq. (10), it is clear that matrix elements of the form $\langle j|\tilde{H}(t)|k\rangle$ in the equation for transition rate (Eq. (8)) are only non-zero if the Zeeman spin levels j and k differ in magnetic quantum number, m , by M , where M is the index in Eq. (10). The non-zero matrix elements $\langle j|\tilde{H}(t)|k\rangle$ then depend only on the corresponding A_{2M} and the matrix elements of the \hat{T}_{2M} operators, which are just numbers. Thus, the integral in Eq. (8) for the transition rate can be rewritten as a sum of integrals⁴³ labelled $J_M(M\omega_0)$ where

$$J_M(M\omega_0) = \int_0^\infty \exp(iM\omega_0 t) C_M(\tau) d\tau, \quad (11)$$

in which M is restricted to 0, 1, 2, i.e. $|M|$ and $C_M(\tau)$ is a correlation function describing the time dependence of the nuclear spin interaction, i.e. the molecular motion. The function $J_M(M\omega_0)$ is a spectral density function and the correlation times $C_M(t)$ are given by

$$C_M(\tau) = \left\langle A_{2M}(0)A_{2M} * (\tau) - |A_{2M}(0)|^2 \right\rangle. \quad (12)$$

The spectral density is a measure of the amplitude of the M -quantum component of the nuclear spin interaction oscillating at frequency $M\omega_0$ as a result of molecular motion. Of course, we should also recognize that since $\tilde{H}(t)$ varies randomly in time, otherwise identical spin systems will have different $\tilde{H}(t)$ at any given time t . Thus, we need to perform an average over the ensembles of spin systems making up the total sample. We denote this ensemble average by a bar, and thus we replace C_M in Eq. (11) with

$$\bar{C}_M(\tau) = \overline{\left\langle A_{2M}(0)A_{2M} * (\tau) - |A_{2M}(0)|^2 \right\rangle}. \quad (13)$$

In summary, then, all relaxation processes can ultimately be described as some linear combination of spectral density functions of the form shown in Eq. (11). We have here only considered explicitly the case of longitudinal or spin-lattice relaxation in the laboratory frame (the so-called spin-lattice relaxation in the rotating frame being a different process), but a similar case can be made for transverse relaxation, relaxation processes in the rotating frame and crossrelaxation processes. The spectral densities involved in each case are $J_M(M\omega)$ where ω is the frequency of rotating frame transformation required to remove the stationary part of the total spin Hamiltonian in each case. This will be the Larmor frequency, ω_0 , for any relaxation process taking place in the laboratory frame. For relaxation processes taking place

in the rotating frame, i.e. with the relaxing spin system under rf irradiation, an additional frame transformation will be required:

$$\begin{aligned}
 \tilde{H}(t) &= \hat{R}_{\text{rf}}^{-1}(\omega_{\text{rf}}t) \tilde{H}(t) \hat{R}_{\text{rf}}(\omega_{\text{rf}}t) \\
 &= \exp(i\omega_{\text{rf}}t \hat{I}_\alpha)(\omega_{\text{rf}} \hat{I}_\alpha + \tilde{H}_1(t)) \exp(-i\omega_{\text{rf}}t \hat{I}_\alpha) - \omega_{\text{rf}} \hat{I}_\alpha \\
 &= \exp(i\omega_{\text{rf}}t \hat{I}_z) \tilde{H}_1(t) \exp(-i\omega_{\text{rf}}t \hat{I}_z),
 \end{aligned} \tag{14}$$

where ω_{rf} is the amplitude of the rf irradiation, and α now represents the axis along which the rf irradiation is directed. Thus, the frequencies that appear in the resulting spectral density functions involve $M\omega_{\text{rf}}$ and hence it is components of motion with such frequencies that are active in stimulating relaxation. Since ω_{rf} is generally of the order of tens of kHz, rotating frame relaxation processes thus rely on molecular motions with significant components in the kHz range. One advantage of rotating frame relaxation measurements from the point of view of studying motion is that ω_{rf} is easily under the control of the experimenter, simply by changing the amplitude of the rf irradiation, which requires a simple change of the level of attenuation on the rf amplifier, generally done from the keyboard on today's modern spectrometers. Thus, one may investigate different frequency components of a molecular motion simply by varying the rf amplitude used in the experiment.

In the case of transverse relaxation, the transitions involved include zero quantum transitions, i.e. $M = 0$, and their respective frequencies then appear in the relevant spectral density; hence transverse relaxation proceeds even for very low-frequency motions.

For longitudinal or spin-lattice relaxation, $M \neq 0$, as the matrix elements $\langle j | \tilde{H}(t) | k \rangle$ in Eq. (8) for the transition rate between levels k and j are non-zero for $M = 0$ only when $j = k$, and clearly j cannot be the same k in a transition process between j and k , the $M = 0$ component in Eq. (11) does not exist. Hence, it is only molecular motion with frequency components at the Larmor frequency ω_0 and $2\omega_0$ (i.e. the $M = 1, 2$ components of Eq. (11)), which stimulate spin-lattice relaxation. The Larmor frequency is generally of order tens or hundreds of MHz and so longitudinal relaxation process probes a quite different molecular motion frequency range to other relaxation processes. Note that in contrast to rotating frame relaxation processes, it is rather more difficult to change the molecular motion frequency range to which a longitudinal relaxation process is sensitive. It requires a change of the Larmor frequency, which usually necessitates a new magnet!

This brings us to how to describe the time dependence of a molecular motional process. Although the Eqs. (8)–(14) tell us that relaxation

processes rely on an oscillatory time dependence at specific frequencies, molecular motions are not oscillatory processes.

Molecular motions in solids are incoherent processes, and as such are best described by *autocorrelation* functions. If $f(t)$ describes the time-dependent position (orientation) of a molecule in a sample of many such molecules, the autocorrelation function, $G(\tau)$ is defined by

$$G(\tau) = \overline{f(t)f(t+\tau)}, \quad (15)$$

where the bar indicates the ensemble average over all the molecules in the sample. $G(\tau)$ is a measure of what proportion of the molecules in the sample have the same position at time $t+\tau$ as they did at time t . If most molecules have moved during the intervening period τ , and moved in many different directions, then there will be a whole variety of different values for $f(t+\tau)$ describing all the new positions of the moved molecules. The sum of $f(t)f(t+\tau)$ over all the molecules in the sample then gives many cancellations between the values for different molecules, resulting in a small value for $G(\tau)$. If no molecules have moved in τ , then $f(t) = f(t+\tau)$ for all molecules, and so $G(\tau)$ is large. Clearly, $G(\tau)$ will decay with increasing τ ; as the gap τ between measurement of molecular positions increases, more of the molecules in the sample will have moved, resulting in decreased values for $G(\tau)$. Often the decay is assumed to be exponential, i.e.

$$G(\tau) = \exp\left(-\frac{|\tau|}{\tau_c}\right), \quad (16)$$

where τ_c is the *correlation time* for the molecular motion. We use the concept of a correlation time to describe molecular motion extensively throughout this chapter. The correlation time essentially provides a monitor for the speed of the motion; the smaller the τ_c , the shorter the typical time between changes of molecular position. For more detailed discussions of the theoretical basis of relaxation, the reader is referred to refs. ⁴⁴⁻⁴⁶ as well as the classical text by Abragam.³⁹

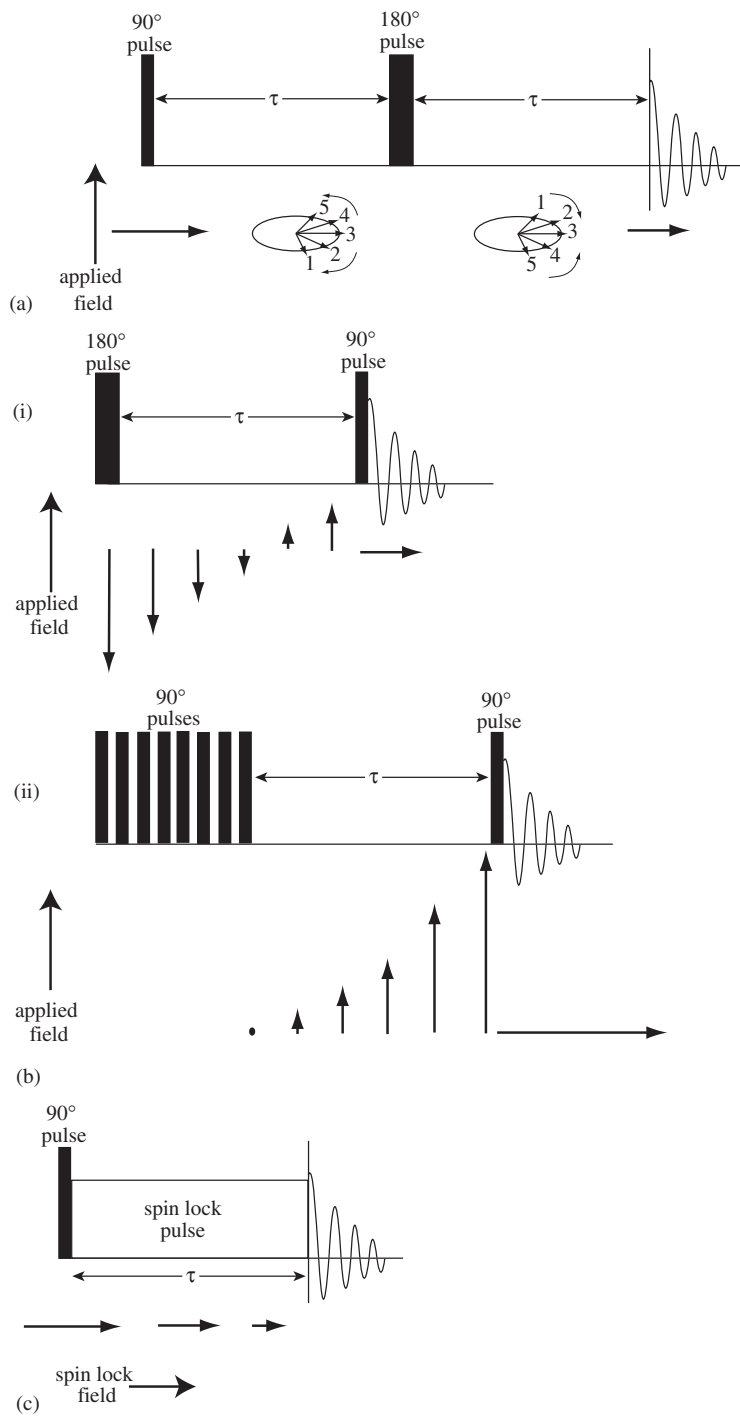
In analyzing relaxation time data, the dominant nuclear spin interaction effecting the relaxation process must be known and it must exceed other effects by at least an order of magnitude or the data become extremely complicated to interpret. Accordingly, relaxation time studies are often applied to ^2H where the dominant relaxation mechanism can usually safely be assumed to be the quadrupole coupling. Note that this is not always the case for quadrupolar nuclei however. There are many cases of ^7Li relaxation for instance, where it is the dipolar coupling between the quadrupolar ^7Li spins that dominates the relaxation. In other cases, nuclei with ^1H bonded to them often have a dominant mechanism involving dipolar coupling with the

^1H , provided that other interactions on the nucleus are small, owing to the particularly large magnetic moment of ^1H .

3.2. Basics – experiments

The next question is how do we measure relaxation times experimentally? Transverse or spin–spin relaxation is the decay of the transverse magnetization back to its equilibrium value of zero. Thus, if no other effects operated, it could be measured simply by observing the decay of the signal FID. However, other effects, such as an inhomogeneous applied magnetic field can act to cause transverse magnetization from different parts of the sample to precess at different rates, resulting over time in a net cancellation of the total transverse magnetization and so an apparent decay of the signal. In addition to this, there may be several signals in the spectrum, which each have their own characteristic relaxation properties and it would be difficult to separate these by analyzing the decay of a single FID. Accordingly, an *echo* pulse sequence is generally used to measure transverse relaxation (Fig. 28(a)). The echo pulse sequence serves to refocus the evolution of the transverse magnetization under whatever interactions it is exposed to via a τ -pulse– τ sequence. The transverse magnetization evolves under the spin interactions during the first τ period, during which transverse relaxation also occurs. The pulse then has the effect of reversing the precession of the transverse magnetization, which then retraces its steps in the second τ period, ending up back where it started after the whole 2τ period is completed. Thus at the end of 2τ , any decay of the signal is due to transverse relaxation. Different spin interactions require different pulses to refocus them: thus chemical shift effects, inhomogeneous magnetic field effects, etc. require a 180° pulse to refocus them, while quadrupole coupling and dipole coupling require a 90° pulse to refocus them. The evolution of the transverse magnetization associated with the *central transition only* of a half-integer quadrupolar spin is akin to that under chemical shifts and requires a selective 180° pulse to refocus it. So to measure the transverse relaxation, one performs a suitable echo experiment (Fig. 28(a)) for different τ delays. Fourier transform of the dataset acquired for each τ delay yields a spectrum whose deviation in intensity from the spectrum at $\tau = 0$ is determined by the transverse relaxation process.

To measure spin–lattice relaxation, i.e. the return to equilibrium of the longitudinal or z magnetization, one simply shifts the longitudinal magnetization away from its equilibrium position and then monitors its return. Two basic methods are (Fig. 28(b)): (i) inversion recovery, where the longitudinal magnetization is inverted to $-z$ and its recovery after time τ monitored by flipping the longitudinal magnetization at time τ into the transverse plane to



be measured in the usual way; (ii) saturation recovery, where the spin system is saturated by a series of rf pulses, so that the net longitudinal magnetization remaining is zero. The amount of longitudinal magnetization, which has been restored to z after time τ is then measured by once again, flipping it into the transverse plane to be measured. Fig. 28(b) shows these pulse sequences. There are many variations on these two general themes, including

Fig. 28. Pulse sequences for measuring relaxation times. The variation of the rotating frame nuclear spin magnetization through the pulse sequences are shown schematically below the sequence in each case. (a) Transverse relaxation. Initial transverse magnetization is created by a 90° pulse as shown here, or alternatively by CP and then allowed to relax for a period 2τ , at the end of which the remaining transverse magnetization is detected in the usual way. Apparent decay (or dephasing) of the transverse magnetization through evolution of different components under spin interactions of different strengths is refocussed by an echo pulse (shown here as a 180° pulse, suitable for chemical shift anisotropy and heteronuclear dipolar coupling) in the centre of the 2τ period – see text for details. (b) Spin–lattice relaxation. (i) Inversion recovery. An initial non-equilibrium state for the longitudinal magnetization is created with a 180° pulse resulting in the longitudinal magnetization being placed along $-z$ rather than its equilibrium position of z . A time τ is allowed for spin–lattice relaxation to occur before a 90° pulse places the current longitudinal magnetization into the transverse plane for measurement in the usual way. (ii) Saturation recovery. As series of pulses applied to the spin system creates the non-equilibrium state here from which recovery of the longitudinal magnetization is measured. The initial longitudinal magnetization after the saturation pulses is zero, when the equilibrium value would be some positive, finite number, M_0 along $+z$. A time τ is allowed for spin–lattice relaxation to occur before a 90° pulse places the longitudinal magnetization, which has recovered at this stage into the transverse plane for measurement in the usual way. (c) Spin–lattice relaxation in the rotating frame. An initial 90° pulse creates transverse magnetization, which is then spin locked by an rf pulse of length τ and amplitude ω_1 . The magnetization under these conditions is said to be longitudinal magnetization in the rotating frame, the rotating frame being defined as one that is rotating about the applied magnetic field of the NMR experiment at rate ω_{rf} , the frequency of the rf irradiation. When the rf pulse is on resonance, as it is assumed to be when discussing this relaxation process, the only magnetic field in the rotating frame is that due to the rf pulse, of amplitude B_1 ($= \omega_1/\gamma$). This field is thus taken to be the quantization axis of the spins in this frame, the rotating frame, and magnetization along this direction is then longitudinal magnetization in the rotating frame. There will be an equilibrium magnetization in this direction, which in general will be considerably less than the magnetization placed there by the initial 90° pulse. Hence, the transverse magnetization under spin lock (in terms of the laboratory frame) or equivalently, the rotating frame longitudinal magnetization will decay until it reaches its equilibrium value. This is spin–lattice relaxation in the rotating frame and occurs during the period τ of the spin lock. The extent of the decay during τ is then measured by recording the FID in the usual way.

some useful ones if the spin system to be measured is not abundant and CP is to be used to generate a signal from it.⁴⁷

Finally, spin–lattice relaxation in the rotating frame is measured by the pulse sequence in Fig. 28(c) or similar. Transverse magnetization is generated and then spin locked by an rf pulse of known amplitude (for the relaxation rate will depend on the amplitude of the rf irradiation) and length τ . The usual FID is then measured at the end of τ . Spectra are recorded in this manner for varying lengths of τ and the signal will be observed to decrease as τ is increased due to the decay of the spin-locked magnetization, i.e. the longitudinal magnetization in the rotating frame.

In all relaxation measurement experiments, spectra are recorded as a function of τ , a time during which relaxation is allowed to occur. The variation of the intensity of a particular signal in the spectrum as a function of τ then constitutes the relaxation decay curve, which we must analyze to retrieve motional data. As this curve will generally have an exponential form (or at least approximately), in order to define this curve properly, it is desirable to arrange to spread the τ points of measurement non-linearly and to concentrate them near the $\tau = 0$ end of the curve where the signal intensity varies most rapidly. A logarithmic distribution of τ points is usually optimal. It is essential that the spin system is fully relaxed before acquiring the next scan or spectrum and also that the τ data measurement is continued until the complete decay curve is measured, otherwise errors will inevitably result in its analysis.

3.3. Examples

This brings us to the question of how, in general, experimental relaxation data may be analyzed to give motional information.

We have already dealt with a relaxation study involving half-integer quadrupolar spins in Section 2.5, which utilizes the stochastic Liouville–von Neumann equation as its starting point.⁴⁰ The Liouville–von Neumann equation describes the time dependence of the density operator for the spin system and is derived from second-order perturbation theory, i.e. it has the same underlying physical basis as the brief analysis at the beginning of this section. This work⁴⁰ allows transverse and spin–lattice relaxation times to be analyzed in terms of molecular motional processes by a process of simulation. The central transition powder lineshapes and their relative intensity after time τ in the relaxation experiment may be simulated using the algorithms derived in this paper⁴⁰ for different motional models until agreement of both relative signal intensity and powder lineshape at each τ measurement point is obtained.

Another paper gives a very clear, concise account of the stochastic Liouville–von Neumann approach to the analysis of relaxation processes through

molecular dynamics for half-integer quadrupolar nuclei.⁴⁸ This work develops a computer simulation, which takes into account finite rf pulses, chemical shift anisotropy, dipolar coupling (between two spins) and first- and second-order quadrupole coupling. However, despite the title of the paper, it does not take into account spin-lattice relaxation. Nevertheless, this approach allows powder lineshapes under any of the nuclear spin interactions listed to be calculated under any molecular motion, for any pulse sequence. Thus, the approach may readily be used to calculate transverse or spin-spin relaxation, as determined by an echo pulse sequence, for instance, but in essence, the approach is no further theoretical advance on many other programmes for calculating powder lineshapes under conditions of molecular motion, although the generality of this programme is pleasing and much needed. Fig. 29 shows some results from this work.

More typically, relaxation data is analyzed in the form of a T_α versus temperature curve, where T_α denotes a relaxation time constant, derived from one of the experiments in Fig. 28. The motional process is either assumed to be known, or is a choice between a very restricted set. The knowledge of the form of the motional process and the spin interaction, which governs the relaxation then allows the correlation functions of Eq. (12) to be determined as a function of the motional correlation time, and this ultimately allows the determination of an equation for the characteristic relaxation time constant for the motional process as a function of its correlation time. The experimental T_α versus temperature curves are then fitted to the equation by varying the motional correlation time. The resulting variation in motional correlation time as a function of temperature then means that an activation energy for the motional process can be derived.

If the form of the motion is not known, then two or three possible models are considered, with the appropriate equations for the relaxation time constant as a function of motional correlation time being derived. The experimental T_α versus temperature curve is then attempted to be reproduced by each of the equations, with some variation of correlation time, in the hope that only one equation provides a suitable fit and that the corresponding motional model then represents a true picture of the molecular motion in the sample.

One such analysis in the review period involves the characterization of the rotation of the methyl groups in pyridoxine (vitamin B₆).⁴⁹ The temperature dependencies of the ¹H spin-lattice relaxation time T_1 and T_{1d} (the relaxation time constant characterizing the relaxation of dipolar order, a population distribution over the Zeeman spin levels, which corresponds to a density operator component \hat{T}_{20} , i.e. $I_{1z} I_{2z} - \mathbf{I}_1 \cdot \mathbf{I}_2$, to equilibrium) at three different applied field strengths and for a variety of temperatures were determined, yielding the curves in Fig. 30. The only motion that could affect

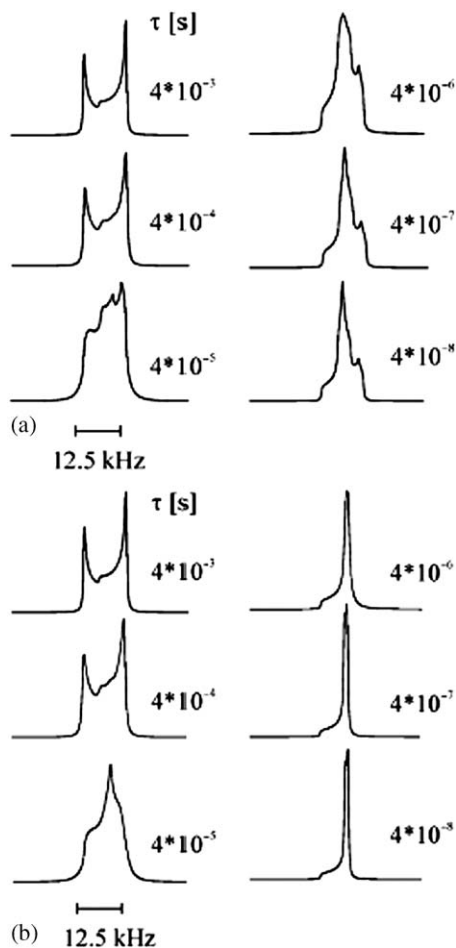


Fig. 29. Calculated central transition spectra⁴⁸ for a single spin-3/2 nucleus undergoing (a) four-site tetrahedral jumps and (b) 12-site icosahedral jumps between equally populated sites in each case. The motional correlation times are given in the figure in seconds for each lineshape. The quadrupole coupling constant (axially symmetric) used in the simulations was 3 MHz.

the ^1H relaxation was assumed to be the rotation of the methyl group (see Fig. 30), with possible motion involving the OH groups at higher temperature. The dipolar coupling between ^1H in the methyl group was considered to be the dominant mechanism for relaxation. Methyl groups are interesting in that they can reorient by thermally activated jumps over an energy barrier or by tunnelling through that same barrier. If the barrier is greater than $7\text{--}8\text{ kJ mol}^{-1}$, then the relaxation behaviour of the ^1H is as if the motion is entirely owing to thermally activated jumps. Below this, however, the

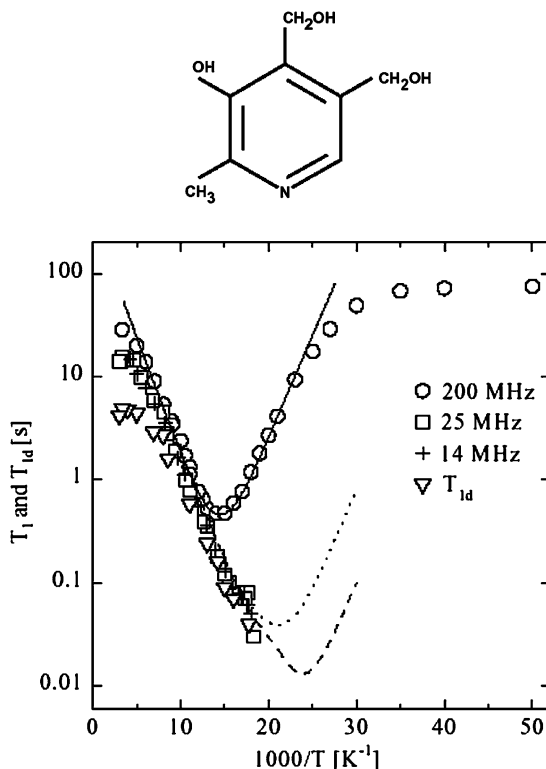


Fig. 30. The measured T_1 and T_{1d} -relaxation times as a function of temperature for pyridoxine (top).⁴⁹ ○ T_1 200 MHz data; □ T_1 25 MHz data; + 14 MHz T_1 data; ▽ T_{1d} data. The solid, dashed and dotted lines represent the best fits to the theoretical equations – see text for details.

relaxation is not only determined by the Larmor frequency and the correlation time of the motion, but by the tunnelling frequency. The form of the T_1 versus temperature curve then depends on the relative magnitudes of the Larmor frequency and the tunnelling frequency.⁵⁰ In the work on pyridoxine, it was concluded that there was a significant effect on the ^1H relaxation from tunnelling.

Relaxation studies have long been used in polymer work, both to separate signals from regions of different mobility and to assess the motion in those regions. As ever, there are many such studies in the current review period.

A typical study is one on butadiene rubber, treated with varying amplitudes of ultrasound.⁵¹ Here ^1H and ^{13}C T_2 measurements were made, the questions asked being, what happens to the structure of the material at a molecular level as a result of treatment with ultrasound. ^1H T_2 times are known to be dependent on interchain dynamics and, in particular, are

dependent on small sol molecules, while ^{13}C T_2 times depend more on intrachain dynamics. The ^1H T_2 measurements were analyzed in terms of a three-component model, consisting of long (L), medium (M) and short (S) relaxation time components. The fast relaxing components are considered to be due to the polymer network and highly entangled sol molecules, the slow relaxing components being due to lighter sol molecules and oligomers. It was found (Fig. 31(a)) that as the amplitude of the ultrasound (measured in) was increased, the T_2 associated with the short and medium T_2 components decreased, suggesting that the material is less intermolecularly mobile and therefore that there is more cross linking. Also, the fraction of the long and medium T_2 components increases as the ultrasound amplitude is increased (Fig. 31(b)), at the expense of the short T_2 component, suggesting that as the ultrasound amplitude increases, the polymer network degrades, generating detached fragments and dangling ends. The ^{13}C T_2 values, however, do not change with ultrasound treatment, showing that the main chain motion is unaffected by the treatment.

It is not surprising that relaxation time measurements are also being used in the assessment of molecular motion in biopolymers. Clearly in such systems, the major problem is one of resolution, and there have been a variety of ways suggested to overcome this. One such uses an effective three-dimensional experiment to measure the effective T_2 time constants for individual amide ^1H in an SH_3 protein domain in order to characterize the location and dynamics of water molecules involved in the protein structure.⁵² The role of water in proteins is very important, being significant in determining the stability of the protein structure and in modifying protein–protein interactions. Water molecules are often found to be associated with polar surface groups and any dynamics of the water molecules in these locations can be, as it were, transmitted to the protein groups, further affecting protein–protein interactions for instance. The pulse sequence used to measure the amide ^1H effective T_2 s is shown in Fig. 32(a). Initial excitation of ^1H transverse magnetization is followed by a T_2 filter, i.e. a simple echo pulse sequence, incorporating a ^1H 180° pulse to refocus chemical shift offsets, etc. What follows is simply a two-dimensional ^1H – ^{15}N correlation experiment, with phase-modulated Lee–Goldburg (PMLG-9) ^1H – ^1H decoupling in the ^1H -evolution period (t_1) followed by transfer of the remaining ^1H transverse magnetization to ^{15}N via CP and recording of the resulting ^{15}N FID in t_2 . In the work on the SH_3 protein,⁵² two-dimensional ^1H – ^{15}N correlation spectra were recorded for T_2 filter-relaxation delays, τ_f of 0.0, 0.2, 0.4, 0.6, 0.8 and 1.2 ms (Fig. 32(b)). The decay of crosspeak intensity with increasing τ_f allows the effective T_2 of the ^1H involved in the crosspeak to be determined (Fig. 32(c)). In this work,⁵² the X-ray crystal structure of the SH_3 protein was also determined, so that the approximate location of all

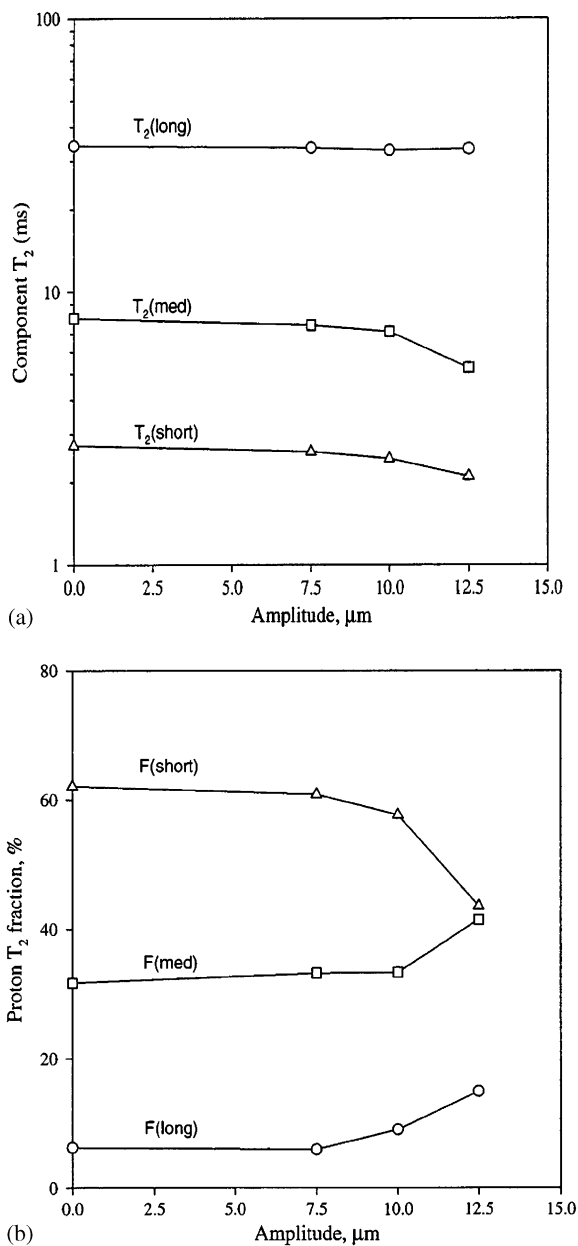
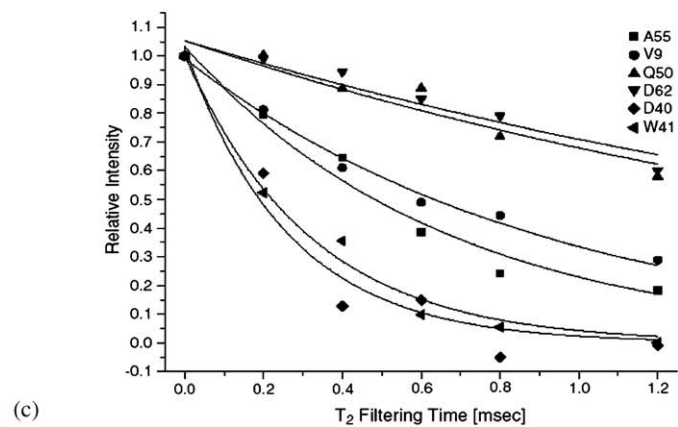
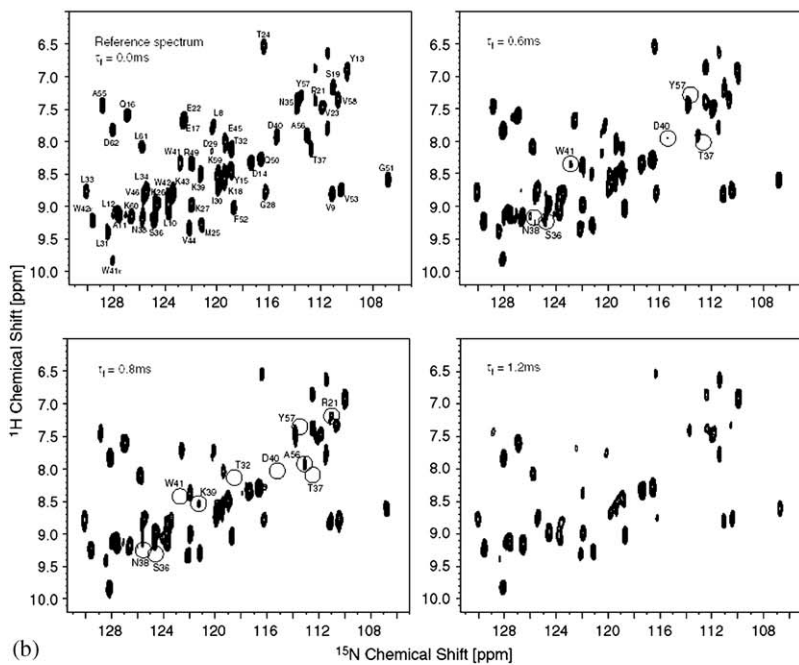
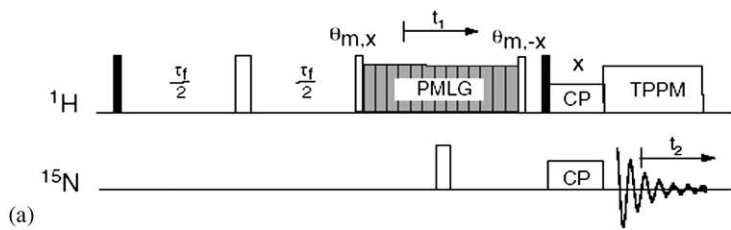


Fig. 31. ^1H T_2 results for butadiene rubber treated with ultrasound of different amplitudes (measured in μm).⁵¹ (a) ^1H T_2 measurements for the long, medium and short T_2 components as a function of ultrasound amplitude. (b) The amplitude of the long, medium and short ^1H T_2 components as a function of ultrasound amplitude.



^1H in close spatial proximity to each amide ^1H was known. Thus, the expected value of T_2 for each amide ^1H , assuming a static structure was able to be determined. Those experimental values, which deviate markedly from these are assumed to show the presence of motion of the nearby ^1H responsible for the relaxation, in particular, the presence of mobile water molecules.

Another interesting study⁵³ concerned the change to protein backbone dynamics upon forming a complex with another protein. The protein concerned was barstar and its complexation with binase. What is particularly interesting about this approach is that the authors performed ^{15}N T_1 and off-resonance $T_{1\rho}$ -relaxation time constant measurements and one-dimensional exchange experiments (centreband-only detection of exchange, CODEX – see Section 4) and fitted the results of all experiments simultaneously with a single-motional model. It was found that barstar in its uncomplexed form has two motional modes, one with correlation times in the range 10^{-7} – 10^{-9} s and one in the range 10^{-2} – 10^{-3} s in the temperature range 0–45°C. When the experiments were repeated for the barstar–binase complex, it was found that the amplitudes of both motional modes had significantly decreased, showing that the complex is considerably more rigid than the free barstar. The authors suggest that the complexed form is more stable, a conclusion they reach because of the reduced flexibility of the barstar molecule. However, this conclusion rather depends on one's definition of stability.

Fig. 32. (a) The pulse sequence used to measure amide ^1H T_2 -relaxation time constants in the work of ref. 52. After initial generation of ^1H magnetization via a 90° pulse, there is a ^1H T_2 filter, consisting of a simple Hahn echo pulse sequence with an echo delay of $\tau_f/2$. At the end of the T_2 filter, the ^1H magnetization is flipped to the “magic-angle” orientation with a pulse of nutation angle θ_m . The ^1H magnetization then evolves under its isotropic chemical shift for a period t_1 during which PMLG-9 ^1H – ^1H decoupling is applied. In the middle of the t_1 period, a ^{15}N 180° pulse is applied to refocus any ^1H – ^{15}N scalar couplings and any residual ^1H – ^{15}N dipolar couplings. At the end of t_1 , the remaining ^1H magnetization is once again flipped to the transverse plane and transferred to ^{15}N via CP. Finally, a ^{15}N FID is recorded. The pulse sequence results in a high-resolution, two-dimensional ^1H – ^{15}N correlation spectrum, of the form shown in (b), edited through the ^1H T_2 , such that those crosspeaks arising from ^1H spins with short T_2 will appear with significantly lower intensities than those arising from ^1H with longer T_2 . (b) The ^1H – ^{15}N correlation spectra obtained in the work of ref. 52 for a uniformly ^2H -, ^{15}N -labelled SH₃ domain for different filtering times, τ_f as given in the figure. (c) The T_2 decay rates for selected residues as a function of filtering time τ_f . These are obtained by running the pulse sequence in (a) for a variety of times τ_f and determining the relevant crosspeak intensities at each time.

4. EXCHANGE EXPERIMENTS

4.1. Basics

Exchange experiments are invaluable for studying slow molecular motions, with correlation times of the order of milliseconds or slower.^{1,2} Accordingly, they have seen many applications, particularly in polymers, and increasingly now, in biopolymers.

The essential concept of a two-dimensional exchange experiment is straightforward and illustrated in Fig. 33. Transverse magnetization is excited by an initial 90° pulse or CP and allowed to evolve during the period t_1 under its characteristic frequency ω_1 . This characteristic frequency arises from the nuclear spin interactions operating during t_1 , so if the experiment is conducted under MAS, this is simply the isotropic chemical shift. If the experiment is conducted on a static sample, or if recoupling pulses are applied under MAS during t_1 , then the spin interactions can include any or all of chemical shift anisotropy, dipole–dipole coupling (both homonuclear and heteronuclear) or quadrupole coupling.

At the end of t_1 , the magnetization is stored along z (the applied magnetic field in the NMR experiment) for a period τ_m , the mixing time, during which molecular dynamical processes may occur. Finally, the magnetization is returned to the transverse plane where it again evolves under its characteristic frequency, this time ω_2 , the evolution being recorded as an FID.

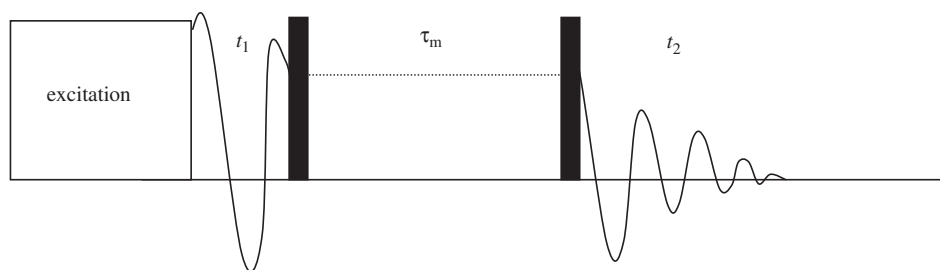


Fig. 33. Schematic diagram of a two-dimensional exchange experiment. It may be conducted on static samples or under MAS if resolution is an issue. An initial excitation period (90° pulse or CP from a suitable spin) creates transverse magnetization on the spin system of interest. This then evolves at its characteristic frequency during t_1 . A pulse (90° for spin-1/2 or 54.7° for spin-1) then stores the magnetization along z (the applied magnetic field of the NMR experiment) for a mixing time τ_m , during which the spin may be involved in some motional/exchange process that changes its resonance frequency. A further pulse (again, 90° for spin-1/2 or 54.7° for spin-1) at the end of the mixing time then recreates transverse magnetization, which now precesses at the new resonance frequency in t_2 , while an FID is recorded. The correlation time for the motion may be determined by repeating the two-dimensional experiment for different mixing times, τ_m .

Appropriate processing^{1,2} of the resulting two-dimensional time domain datasets yields a two-dimensional frequency correlation spectrum, correlating the characteristic frequency the spin had in t_1 , i.e. ω_1 , with that it had in t_2 , i.e. ω_2 . If molecular reorientation or site exchange has occurred during the mixing time τ_m (which happens if the correlation time for the motion $\tau_c < \tau_m$), the resonance frequency after the mixing time, ω_2 is different to the initial frequency ω_1 before molecular reorientation/exchange and so the two-dimensional frequency spectrum contains off-diagonal intensity at (ω_1, ω_2) . If there is no exchange during the mixing time, then $\omega_1 = \omega_2$ (and presumably, $\tau_c \gg \tau_m$) and spectral intensity appears only along the leading diagonal of the two-dimensional frequency spectrum.

Analysis of the resulting frequency spectrum in terms of molecular motion clearly relies on the resonance frequencies ω_1 and ω_2 being constant during the t_1 and t_2 periods, respectively, that is, on there being no motion during the evolution periods of the experiment. It is for this reason that exchange experiments are only suitable for studying slow molecular motions. The ultimate limit on how slow a motion may be studied depends on the T_1 spin-lattice relaxation time constant for the spin system. Clearly, spin-lattice relaxation will be operating during the mixing period τ_m , so τ_m should be significantly shorter than T_1 to avoid artifacts or significant loss of intensity in the final spectrum. At the other end of the scale, the shortest that τ_m may be is of the order of T_2 , the transverse relaxation time constant. This is because the 90° pulse at the start of the mixing period only flips one component of the transverse magnetization (x or y) to z for storage. The other component remains in the transverse plane and must decay away (via transverse relaxation with a decay constant T_2) before the next 90° pulse and recording of the FID, or a distorted and misleading spectrum will result.

By assessing exchange intensity as a function of mixing time (with $\tau_m \gg t_1$, t_2 and $T_2 < \tau_m < T_1$), the correlation time for the motion can be determined. The experiment may be run on static samples or under MAS, with or without recoupling pulses during t_1 and t_2 to recouple specific nuclear spin interactions. If the experiment is run under MAS with no recoupling, then the frequencies of the signals in ω_1 and ω_2 will simply be the isotropic chemical shifts of the nuclear spin in the sites it adopts during t_1 and t_2 . Clearly then, such an experiment is only of any use if the molecular motion during τ_m results in a change of isotropic chemical shift. A simple molecular reorientation will not, in general, cause a change to the isotropic chemical shift (unless it is part of a more concerted motion), and hence will not be detectable in a MAS experiment, unless recoupling is used to reintroduce an anisotropic nuclear spin interaction in t_1 and t_2 . Note that under MAS conditions, the mixing time τ_m must be an integral number of rotor periods, or distorted spectra will result.

Under static conditions or with recoupling pulse sequences appropriately applied, the frequencies in t_1 and t_2 , i.e. ω_1 and ω_2 will be determined by anisotropic spin interactions, and hence by molecular orientation. Thus, changes in molecular orientation will show up as a change in resonance frequency and hence be detectable in an exchange experiment. In such a case, the projection of the two-dimensional spectrum on f_1 and f_2 will be a powder pattern (corresponding to the static powder pattern arising from whatever anisotropic interactions operate during t_1 and t_2) and the two-dimensional correlation spectrum will show a pattern of exchange intensity that is determined by the geometry of the motion in τ_m ; the pattern is effectively a correlation map, linking the molecular orientations that occurred in t_1 and t_2 . This pattern may be used to extract the motional information *without the need for a motional model*.¹ This is one of the very few experiments that allows a truly model-free approach to its analysis.

For the most part, static exchange experiments in the solid state use chemical shift anisotropy for spin-1/2 and quadrupole coupling for spin $> 1/2$.

Three- (or higher) dimensional exchange spectra can be recorded by simple extensions of the basic two-dimensional pulse sequence (Fig. 34).^{1,2} The resulting multi-dimensional spectra can then be used to correlate molecular orientation at three (or more) points in time. This allows the assessment of the degree to which different motions are correlated in time, and so is particularly useful in heterogeneous systems, such as glasses and polymers. In such systems, there are often small-angle and large-angle jump motions present simultaneously and it is important when understanding the material properties of a system to know how these motions are correlated. A

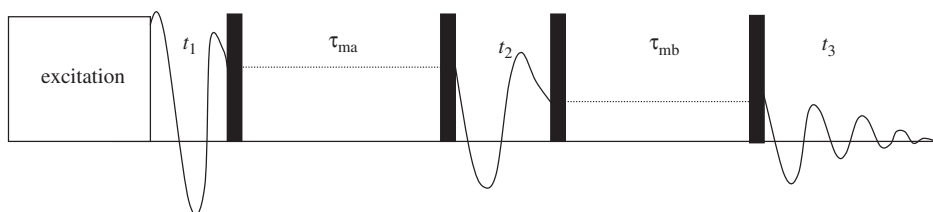


Fig. 34. A pulse sequence for a three-dimensional exchange experiment. This differs from the sequence in Fig. 33 only in the addition of a second mixing time period τ_{mb} and an extra evolution period, t_3 . The resulting three-dimensional spectrum then correlates the spin's characteristic frequency (and through this, its position and/or the containing molecule's orientation) at three different points in time, t_1 , t_2 and t_3 with motion potentially occurring during the (much longer) mixing times, τ_{ma} and τ_{mb} . The pulses after the initial excitation sequence move the magnetization to and from the z -axis (the applied magnetic field direction) as appropriate through the pulse sequence. Thus, these pulses are 90° pulses for spin-1/2 nuclei and 54.7° pulses for spin-1.

two-dimensional exchange experiment can reveal that both types of motion are present, but can give no information on how they occur over a sequence of time. In other words, it cannot answer the question of whether some parts of the system undergo small-angle jumps exclusively and others large angle or whether those parts that undergo a certain small-angle jump are then more likely to undergo a large-angle jump. A three-dimensional exchange spectrum, however, by revealing the molecular reorientation that occurs in three separate time periods can give the required information.

4.2. One-dimensional experiments

Static exchange experiments can give immense amounts of information on dynamical processes, but they suffer from an inherent lack of resolution. Clearly, this is not important if there is only one chemical site for the observed nucleus, but it is critical if there is more than one site, nearly always the case in interesting systems.

MAS can, of course, be used to achieve the required resolution, but in performing the experiment under MAS, we lose all the anisotropic information, which can tell us about molecular reorientation. Accordingly, methods are required that operate under MAS, but which still give information on molecular reorientational processes. Furthermore, if such an experiment could be one dimensional, and so require less time to perform, that would be a great advantage, as any exchange experiment is likely to have to be performed for many different mixing times τ_m in order that the correlation time for the motion can be properly measured.

The first such experiment became known as the exchange-induced sideband methods (EIS).⁵⁴ This method is based on the total suppression of spinning sidebands (TOSS) pulse sequence.⁵⁵ The four-pulse TOSS sequence (Fig. 35) acts on transverse magnetization that evolves under MAS modulation of the various (inhomogeneous) nuclear spin interactions so as to make the net evolution under the anisotropic terms of the interaction zero at the end of the pulse sequence (the second 90° pulse in Fig. 35). It does this by modulating the evolution of the transverse magnetization with a γ -dependent phase factor, such that when the evolution of magnetization arising from molecules with different γ orientation is summed together, there is net cancellation over the whole sample. In the EIS method, the TOSS pulse sequence is followed by a 90° storage pulse and a mixing period, τ_m (an integer number of rotor periods). At the end of the mixing period, the magnetization is returned to the transverse plane for recording an FID. If there is no motion during τ_m , then the TOSS pulse sequence works as normal, and just the centreband of each signal is observed in the final spectrum. If, however, there is molecular reorientation during τ_m , such that the γ angle for a

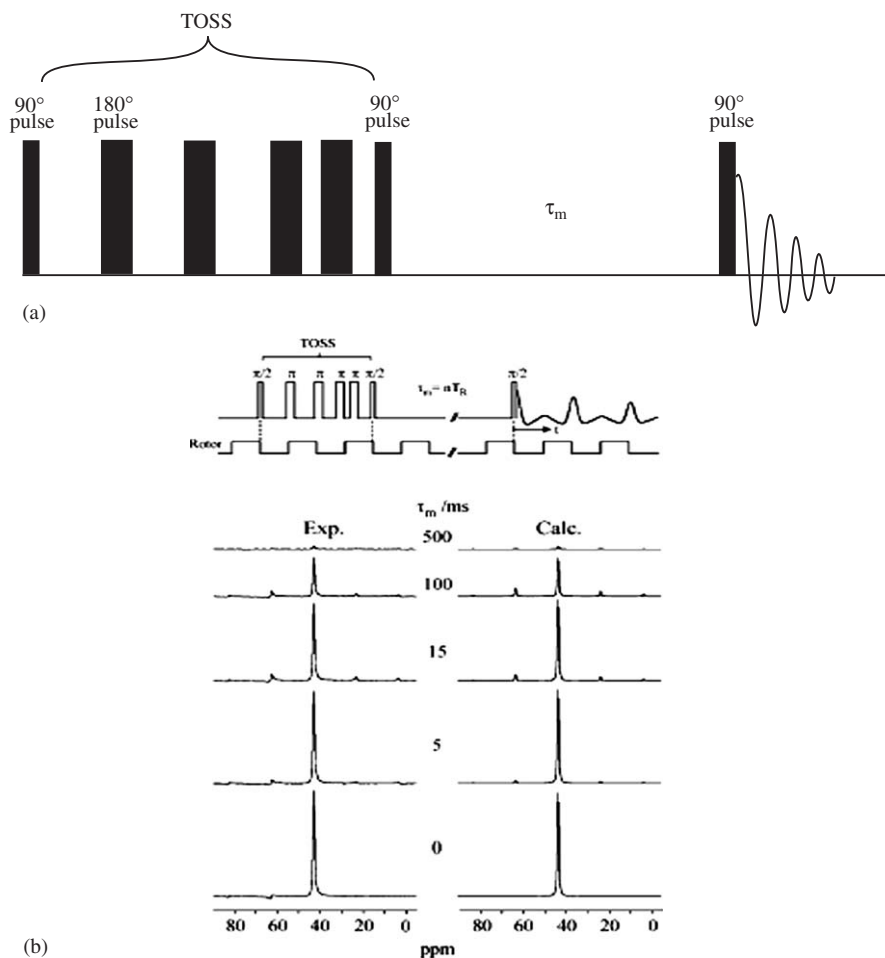


Fig. 35. (a) The EIS pulse sequence. The sequence consists of an initial 90° excitation pulse followed by the TOSS pulse sequence. At the end of the TOSS sequence, a further 90° pulse stores the magnetization along z for a mixing time (which must be an integer number of rotor periods) τ_m , before a final 90° pulse returns the magnetization to the transverse plane for recording of the FID. If exchange occurs during τ_m , spinning sidebands result in the spectrum, as shown in (b). (b) The results of applying the pulse sequence in (a) to ^{13}C in DMS at room temperature.⁵⁶ The spinning rate is 2 kHz; the simulations used: chemical shift principal values $\delta_{11} = 63.1$ ppm, $\delta_{22} = 60.8$ ppm, $\delta_{33} = 6.8$ ppm and assumed two-site hopping with the principal axis 1 reorienting through 108° with a correlation time 0.05 s.

molecule changes, then the phase modulation for each molecule in the sample is no longer such that the net sum over the sample is zero and spinning sidebands appear in the final spectrum. For a given exchange rate, the longer the mixing time, the larger the spinning sidebands, as illustrated in Fig. 35.⁵⁶

The TOSS experiment utilized by the EIS method is very sensitive to the exact timing of the 180° pulses used and errors may arise from the finite amplitude of these pulses, such that spinning sidebands may arise from imperfect 180° pulses one way or another, even in the absence of molecular motion. Thus, more robust experiments have been developed. One such experiment is the CODEX experiment⁵⁷ and its many variants. The CODEX pulse sequence is shown in Fig. 36. It is carried out under rapid MAS, so that only the centrebands at the isotropic chemical shift for each chemical site remain in the spectrum. For an initial $N/2$ rotor periods, the spins evolve under the anisotropic chemical shift, which is refocussed through the MAS by two 180° pulses per rotor cycle. The magnetization is then stored along z as usual in an exchange experiment, for a mixing time that is an integral number of rotor periods. The magnetization is then returned to the transverse plane and allowed to evolve for a further $N/2$ rotor periods under the

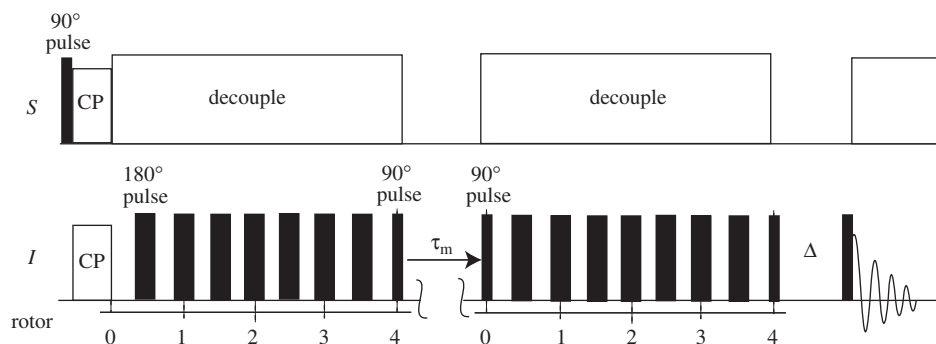


Fig. 36. The CODEX pulse sequence for spin-1/2 nuclei. The experiment is conducted under rapid MAS, so that only isotropic signals are recorded in the FID. The broad pulses are 180° pulses; the narrow ones 90° pulses. All gaps between the I spin 180° pulses are $\tau_R/2$ where τ_R is the rotor period. The mixing time τ_m and the z -filter delay, Δ , are both integral numbers of rotor periods. The series of I spin 180° pulses on either side of the mixing period refocus the chemical shift anisotropy during these periods shown here for $N = 8$. Any motion during the mixing time τ_m then prevents complete refocussing of the chemical shift anisotropy at point R, immediately prior to recording the isotropic FID. This results in a loss of intensity in the corresponding isotropic signal. Repeating the sequence for different mixing times τ_m then allows the correlation time for the motion to be determined. Varying N , the number of rotor periods for which the chemical shift anisotropy is refocussed and/or τ_R , the rotor period, allows the geometry of the motion to be determined.

anisotropic chemical shift (by virtue of two 180° pulses per rotor cycle again). Finally, a zero quantum or z -filter is used to remove the effects of unwanted coherences. If there is no molecular reorientation during the mixing time, the (anisotropic) chemical shift associated with a given chemical site is the same before and after the mixing time. Then, the evolution under the reintroduced chemical shift anisotropy is refocused at the end of the second sequence of $N/2$ rotor periods. If, however, the chemical shift changes during the mixing time as a result of molecular reorientation, then the chemical shift anisotropy is not completely refocused at this point. The resulting dephasing is observed as a decrease in the intensity of the isotropic chemical shift signal observed via the recorded FID. The signal from immobile sites is removed from the final spectrum by subtracting a reference spectrum containing signals only from immobile sites, so that the final spectrum contains only signals from sites that have undergone exchange during τ_m . The reorientation rate can be determined by varying τ_m in the normal manner for exchange spectroscopy (logarithmically is most preferable), and the reorientation angle can be determined by varying $N\delta\tau_R$, where δ is the chemical shift anisotropy. Thus, the reorientation rate can be found from plots of the CODEX intensity (for each site) as a function of τ_m , while the reorientation angle is determined from plots of the CODEX intensity as a function of $N\delta\tau_R$.

An alternative to the CODEX experiment is the ingenious one-dimensional exchange spectroscopy by sideband alternation (ODESSA) experiment⁵⁸ and the later time-reversed ODESSA (or trODESSA).⁵⁹ The ODESSA experiment achieves resolution by MAS as usual, but the MAS rate is set slow enough that the powder pattern for each chemically distinct site appears as a set of spinning sidebands, rather than simply an isotropic signal as would occur at higher spinning rates. The experiment takes the form of a normal two-dimensional exchange experiment (Fig. 33) except that the variable delay t_1 is fixed at half a rotor period, $\tau_R/2$. The mixing time is an integer number of rotor periods, as usual for an exchange experiment under MAS. The $t_1 = \tau_R/2$ delay causes the magnetization associated with the different sidebands to be polarized in alternate directions ($\pm z$) after transfer of the magnetization to the z -axis at the start of the mixing period. During the mixing time, dynamic processes redistribute the polarization, resulting in a modified spinning sideband pattern in t_2 . Analysis of the spinning sideband pattern then allows details of the reorientation process to be determined. Equations for simulating the sideband pattern are derived in ref. 58; each pattern consists of a sum of sub-spectra, one arising from those molecules that have not moved during the mixing time and others arising from molecules that have moved in some way.

In samples where there is more than one chemical site, and so more than one spinning sideband manifold, the different sidebands manifolds in general have different phases, so it becomes impossible to phase the spectrum for all manifolds simultaneously. The trODESSA sequence⁵⁹ and SELDOM ODESSA⁵⁶ overcome this problem.

For an excellent review of all the one-dimensional exchange methods, their relative efficacy and the analysis of their results, the reader is referred to ref. 56. An experimental comparison of CODEX and trODESSA is undertaken in ref. 60.

One potential problem with pulse sequences such as CODEX, which utilize recoupling of an anisotropic nuclear spin interaction is that molecular motion/reorientation may occur during the recoupling sequence, and this can clearly disrupt the recoupling. This possibility is explored by Salwächter and Fischbach⁸ in work which found that there is a highly selective signal loss for components of the sample reorienting at intermediate correlations times, that is, $\tau_c \sim$ anisotropy of the interaction being recoupled. The decay of the signal with the length of the recoupling period can be described by a single decay rate constant, T_2^{recpl} as discussed in Section 2.4. T_2^{recpl} is largely independent of sample-spinning rate; rather it depends most on the average value of the *recoupled* tensor, i.e. if the tensor principal values are scaled as a result of recoupling, then it is the scaled tensor, which determines the signal decay rate through the recoupling sequence. This work is discussed more fully in Section 2.2.

There are numerous examples in the recent literature of the use of one-dimensional exchange spectroscopy. To list just a few:

- (i) The dynamic structure of a genetically engineered, multi-domain protein hydrogel was examined using ^{13}C -detected ^{15}N CODEX, utilizing the ^{15}N chemical shift anisotropy.⁶¹
- (ii) In three separate pieces of work, ^{13}C CODEX and other one-dimensional exchange experiments were used in a series of glassy poly(alkyl methacrylate)s with varying side groups sizes, to examine the effect of the side group on the side-chain and main-chain dynamics.^{62–64} The results of a ^{13}C CODEX experiment on *i*-poly(ethyl methacrylate) are shown in Fig. 37.⁶⁴
- (iii) ^{13}C CODEX experiments with an additional $T_{1\rho}$ filter were applied to isotactic poly(4-methyl 1-pentene) to examine the dynamics of the main chain and side chains in the crystalline regions.⁶⁵ Data following the exchange intensity for the main chain CH_2 as a function of ^{13}C chemical shift anisotropy recoupling time shows that the main chain undergoes helical jumps motions with jump angles of 72° – 145° .

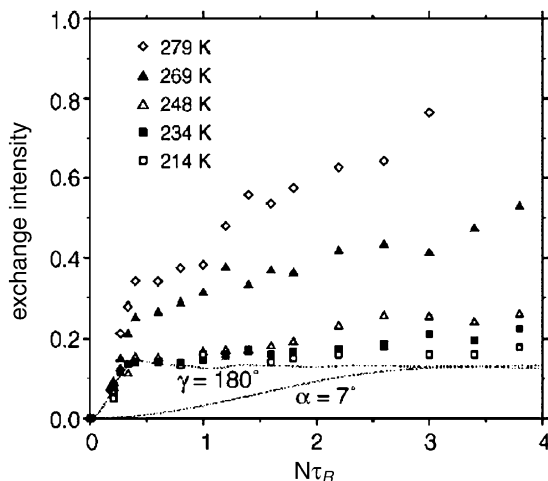


Fig. 37. CODEx exchange intensities of the carbonyl ^{13}C signal of *i*-poly(ethyl methacrylate) as a function of ^{13}C chemical shift anisotropy recoupling time $N\tau_R$ for various temperatures below the glass-transition temperature.⁶⁴ Each curve can be simulated by assuming a 180° flips of the side group and small-angle liberations of the main chain. Simulations of the expected CODEx curves for these motions are shown on the figure.

4.3. Pure-exchange spectra

If there are relatively few molecules in the sample involved in the exchange/molecular motional process, then if a two-dimensional exchange spectrum is recorded in the form shown in Fig. 33 or similar, then inevitably the two-dimensional correlation pattern is dominated by the diagonal intensity from molecules that have not moved during the mixing time τ_m . Even in cases where all the molecules in the sample are involved in a motional process, recording spectra when $\tau_c < \tau_m$ (which is necessary for accurate determination of the correlation time for the motion) will result in the same phenomenon: a strong diagonal ridge, which tends to obscure the exchange intensity. This is particularly a problem if the motional process only involves small-angle reorientations, as then the exchange intensity is always close to the diagonal. As this is often the case in polymers, for instance, much work has been devoted to producing pure-exchange spectra, the so-called PUREX spectra, which show intensity only from exchanging sites. The CODEx method does this by subtracting the intensity from non-exchanging sites. Other methods are required for two-dimensional exchange spectroscopy.

In order to suppress the diagonal ($\omega_1 = \omega_2$) intensity in a two-dimensional exchange spectrum,⁶⁶ it is necessary to modulate the two-dimensional spectrum, for instance, by $\sin^2(\omega_2 - \omega_1)\tau/2$ where ω_1 and ω_2 are the resonance

frequencies of a particular nuclear spin before and after the mixing time, as usual. Such a modulation will result in a conventional two-dimensional exchange spectrum S being converted into

$$\sin^2\left\{\frac{(\omega_2 - \omega_1)\tau}{2}\right\}S = \frac{1}{2}(1 - \cos\{(\omega_2 - \omega_1)\tau\})S. \quad (17)$$

The first term on the right-hand side of Eq. (17), $1/2 S$ simply corresponds to the normal two-dimensional exchange spectrum. Subtracted from this is a two-dimensional spectrum represented by the second term on the right-hand side of Eq. (17), which is equal to $1/2 S$ if $\omega_1 = \omega_2$, i.e. along the diagonal, resulting in the $\sin^2\{(\omega_2 - \omega_1)\tau/2\} S$ spectrum being devoid of diagonal intensity.

In order to see how such modulation can be achieved in practise, Schmidt-Rohr and co-workers⁶⁶ note the following trigonometric identity for the second term on the right-hand side of Eq. (17):

$$(1 - \cos\{(\omega_2 - \omega_1)\tau\})S = \cos(\omega_1\tau)\cos(\omega_2\tau)S + \sin(\omega_1\tau)\sin(\omega_2\tau)S. \quad (18)$$

Spectra with the form of the two terms on the right-hand side of Eq. (18) can be obtained by two extra modulation periods of length τ in the exchange pulse sequence, one before and one after τ_m . The sine.sine and cosine.cosine terms of Eq. (18) are selected by suitable choices of the phases of the flip back pulses, labelled a and b in Fig. 38. The spectrum of the form of Eq. (18) is produced by the pulse sequence in Fig. 38(a), for non-spinning samples, while the spectrum of the form $1/2 S$ is produced using the sequence of Fig. 38(b), which matches that in Fig. 38(a) in terms of pulses and delays and so should produce a “matched intensity” spectrum, so that when the relevant spectra from the pulse sequence in Fig. 38(a) are subtracted from it, the desired pure-exchange spectrum is obtained. The Δ periods in both sequences are simply Hahn echoes, implemented to achieve non-distorted powder patterns in both spectral dimensions.²

In order that only the diagonal ridge is removed from the two-dimensional exchange spectrum and that the rest of the two-dimensional exchange spectrum remains unaltered, it is necessary to co-add spectra obtained for several different τ values. As the number of τ values increases, the modulation function takes on the form of a sharp dip at the diagonal and smooth elsewhere in the two-dimensional spectral plane. Weighting the spectra for the different τ according to a Fourier series further smoothes the profile of the modulating function.⁶⁶ The results of this procedure for two-dimensional exchange spectra for ^{13}C in DMS are shown in Fig. 39.

An alternative to sine-squared modulation of the two-dimensional exchange spectrum to achieve pure-exchange spectra is sine modulation.⁶⁷ A very similar pulse sequence to that in Fig. 38 is used, as shown in Fig. 40, and the experiment again requires recording spectra for several different τ

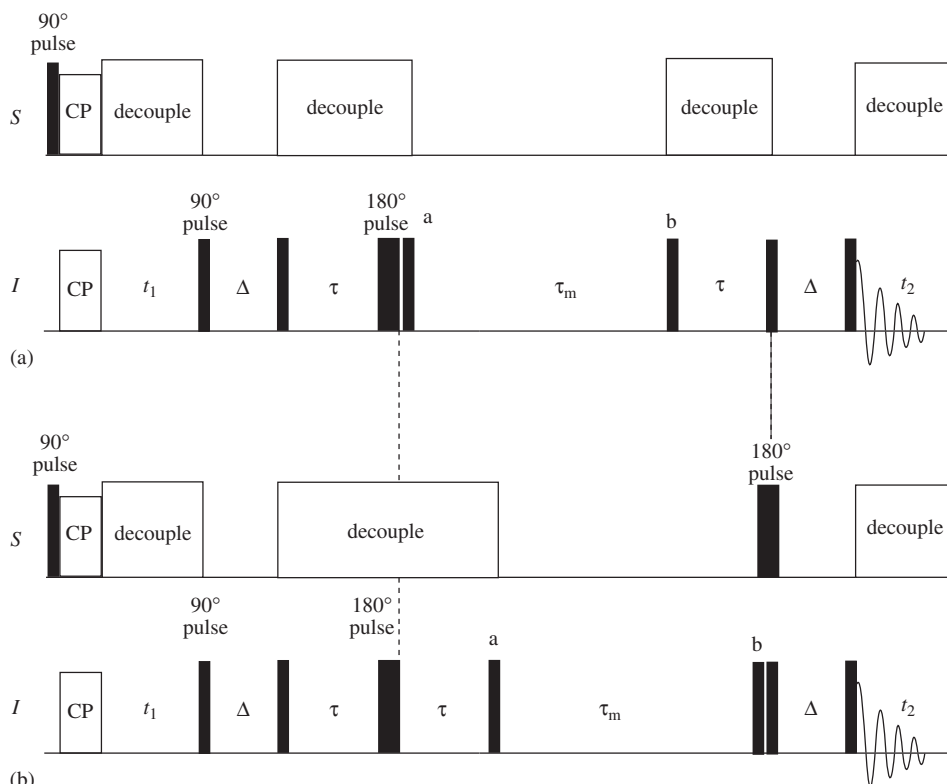


Fig. 38. The pulse sequences needed to produce pure-exchange spectra on static (non-spinning samples).⁶⁶ (a) The sequence for producing $\cos(\omega_2 - \omega_1)\tau$ modulation of the two-dimensional exchange spectrum. The 180° pulse is applied only to match that in the sequence in (b). (b) The sequence for producing the unmodulated exchange spectrum. Subtracting the data arising from the sequence in (a) from that arising from (b) results in a pure-exchange spectrum in which the diagonal intensity from non-exchanging sites is absent. In both sequences, the Δ period is a Hahn echo, used to obtain non-distorted powder patterns in both dimensions of the spectrum.

delays and co-adding the results, in this case, after first taking the absolute values of the intensities at every point, as the sine modulation results in negative intensity in parts of the spectrum, so there is a tendency to cancellation if the absolute intensities are not taken. The advantage of this modulation method is that it produces a sharper dip at the diagonal for the same number of τ values taken in the summation of spectra and so should be better for examining small-angle motions, where the exchange intensity is all close to the diagonal. The results from this work on DMS are shown in Fig. 41, which may be compared to Fig. 39 to judge the efficacy of the two modulation schemes.

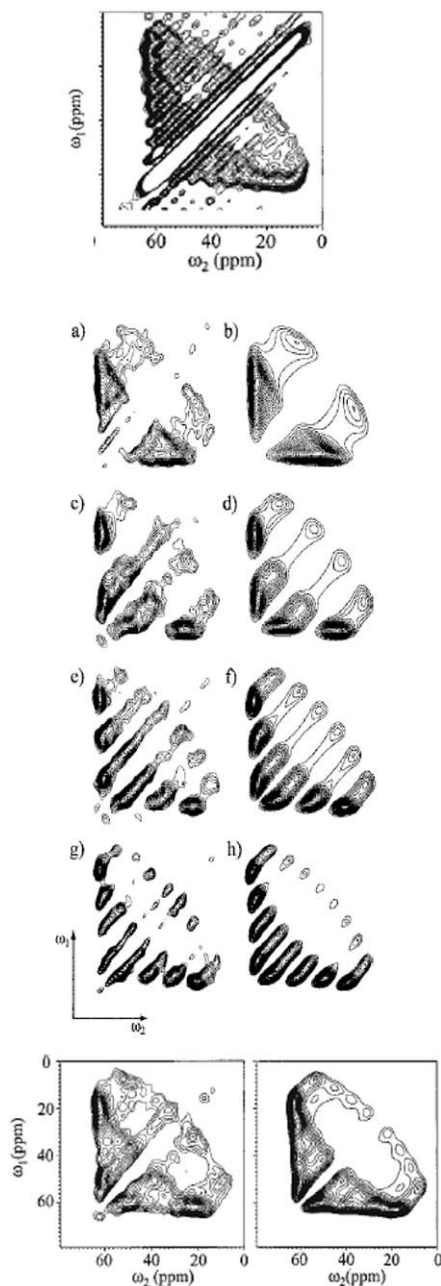


Fig. 39. Top: the normal two-dimensional exchange spectrum for ^{13}C in DMS exhibiting a strong diagonal ridge.⁶⁶ Below: two-dimensional exchange spectra obtained using the pulse sequences in Fig. 38 for different τ delays. (a) $\tau = 250 \mu\text{s}$ with the corresponding simulation (b); (c) $\tau = 500 \mu\text{s}$ with the corresponding simulation (d); (e) $\tau = 750 \mu\text{s}$ with the corresponding simulation (f); (g) $\tau = 1000 \mu\text{s}$ with simulation (h). Bottom: Two-dimensional pure-exchange spectra produced by adding the spectra above (a) + (c) + (e) + (g) and likewise for the simulations.⁶⁶

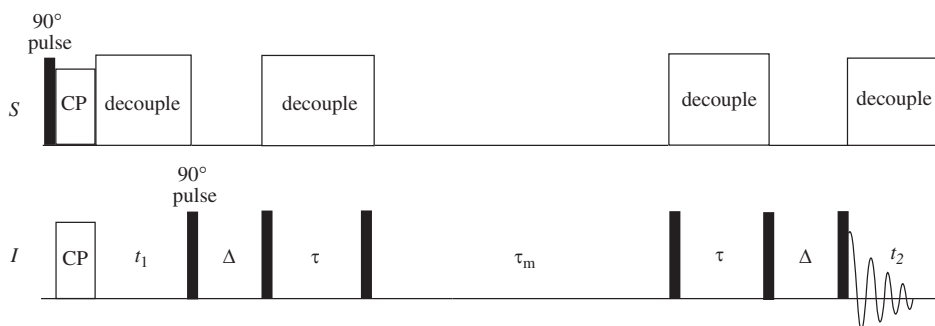


Fig. 40. The pulse sequence required to produce sine-modulated two-dimensional exchange spectra for static (non-spinning) samples, in order to achieve pure-exchange spectra.⁶⁷

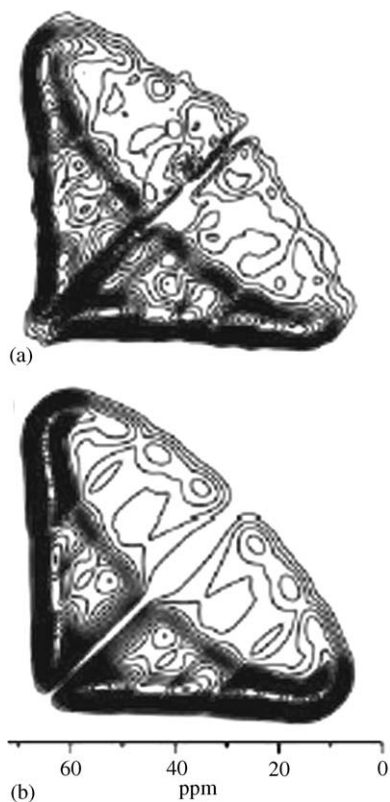


Fig. 41. The results from the pulse sequence in Fig. 40 for ^{13}C in DMS.⁶⁷ (a) Experimental result obtained from summing spectra for $\tau = 80, 160, 240$ and $320 \mu\text{s}$. (b) Simulation of the result in (a).

A one-dimensional version of these experiments can be performed by setting $t_1 = 0$.⁶⁶ This produces a one-dimensional spectrum of purely exchanging sites with some modulation that is a function of τ and the frequency change $|\omega_2 - \omega_1|$ involved in the motional process; the choice of τ determines whether large or small frequency changes are detected. This was used in a study of the segmental dynamics of glassy poly(alkyl methacrylates), where the COO ^{13}C signal was used to characterize the flips and small-angle motions of the side groups quantitatively.⁶²

4.4. Other methods

As explained previously, exchange methods most commonly use chemical shift anisotropy or quadrupole coupling as the molecular orientation-dependent interactions through which molecular reorientation is monitored. However, there are cases in which it would be desirable, or even essential to use dipolar couplings. For instance, if one wishes to measure the motion of ^1H spins, dipolar coupling may be more useful than chemical shift anisotropy as the chemical shift anisotropy of ^1H is generally small.

One method that utilizes (homonuclear) dipolar couplings is the DQ–DQ correlation spectroscopy of Spiess *et al.*⁶⁸ In this method, the dipolar coupling is observed through *rotor-encoded spinning sidebands* generated in the process of exciting and reconverting DQ coherence involving the dipolar-coupled spin pair. For an abundant homonuclear spin system, the sample is spun rapidly at the magic angle so that the network of dipolar-coupled spins can be approximated as a sum of spin pairs.⁶⁹ In the DQ–DQ correlation experiment, DQ coherence is excited for a period t_1 and reconverted back to zero-quantum coherence. The DQ coherence, which exists in t_1 does not evolve under the dipolar coupling. Nevertheless, the signal in t_1 is modulated by the sample spinning through *rotor encoding*. The result of this is a frequency spectrum in the indirect f_1 dimension, corresponding to t_1 in the time

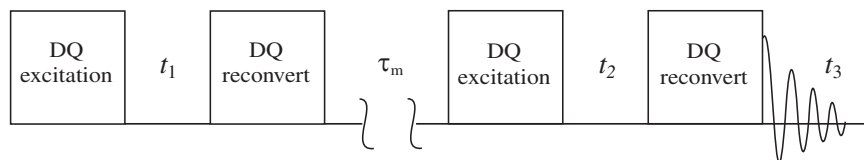


Fig. 42. The form of the DQ–DQ correlation experiment.⁶⁸ DQ coherence is excited and reconverted using a γ -encoding pulse sequence such as BABA. In the experiment, conducted under rapid MAS, t_1 is set equal to t_2 and the reorientation of a homonuclear dipolar tensor is monitored through the DQ rotor-encoded spinning sidebands that emerge from Fourier transforming in the $t' = t_1 = t_2$ time domain.

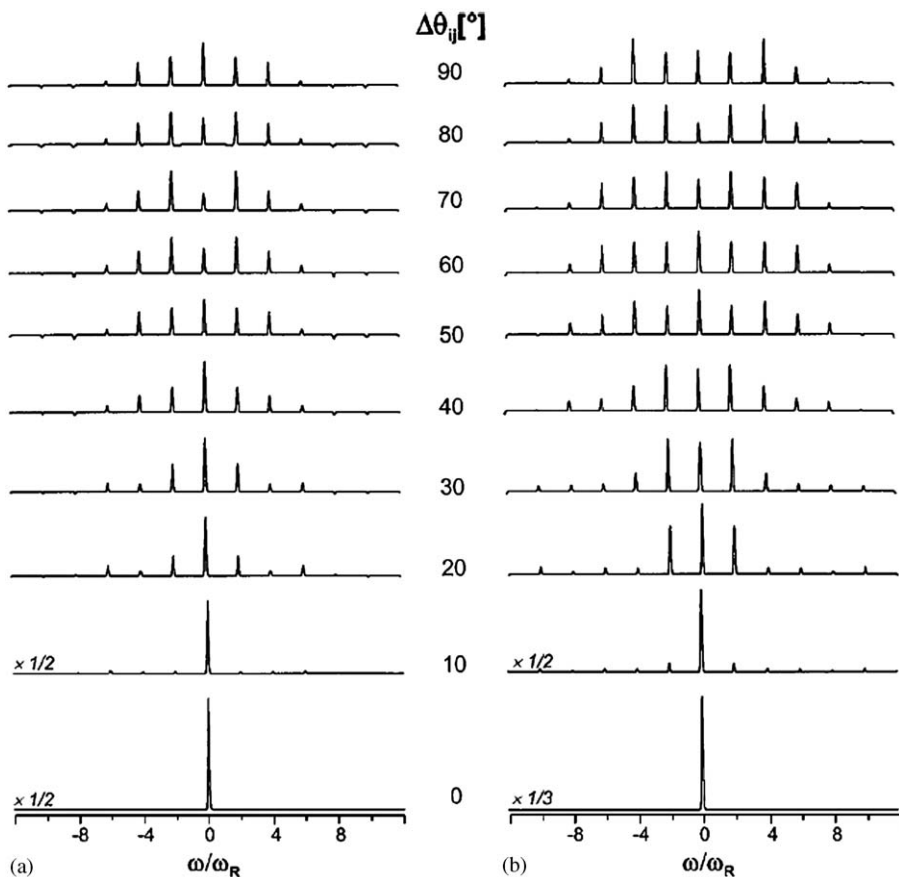


Fig. 43. Calculated sideband patterns (corresponding to the Fourier transform of the $t' = t_1 = t_2$ time domain data from the pulse scheme in Fig. 42) from a DQ–DQ exchange experiment, where the sideband pattern has been divided by a similar pattern obtained from the same experiment with a very short mixing time.⁶⁸ This ensures that the sidebands purely reflect the mobile sites in the sample. The patterns are calculated assuming a two-site exchange through angle $\Delta\theta_{ij}$. (a) $D_{ij}\tau_{\text{ex}} = 1$. (b) $D_{ij}\tau_{\text{ex}} = 1.5$, where τ_{ex} is the DQ excitation time and D_{ij} is the dipole coupling constant between spins i and j .

domain, which is split into sidebands. If the signal results purely from a DQ coherence from an isolated spin pair, only odd-order sidebands appear.

In the DQ–DQ correlation experiment, the initial DQ excitation–evolution–reconversion period (Fig. 42) is followed by a mixing time τ_m and then another DQ excitation–evolution–reconversion period. Finally, the signal is detected in t_3 . As it stands, this is a nominal four-dimensional experiment, with t_1 – t_3 and τ_m all being potential time variables. However, there is no

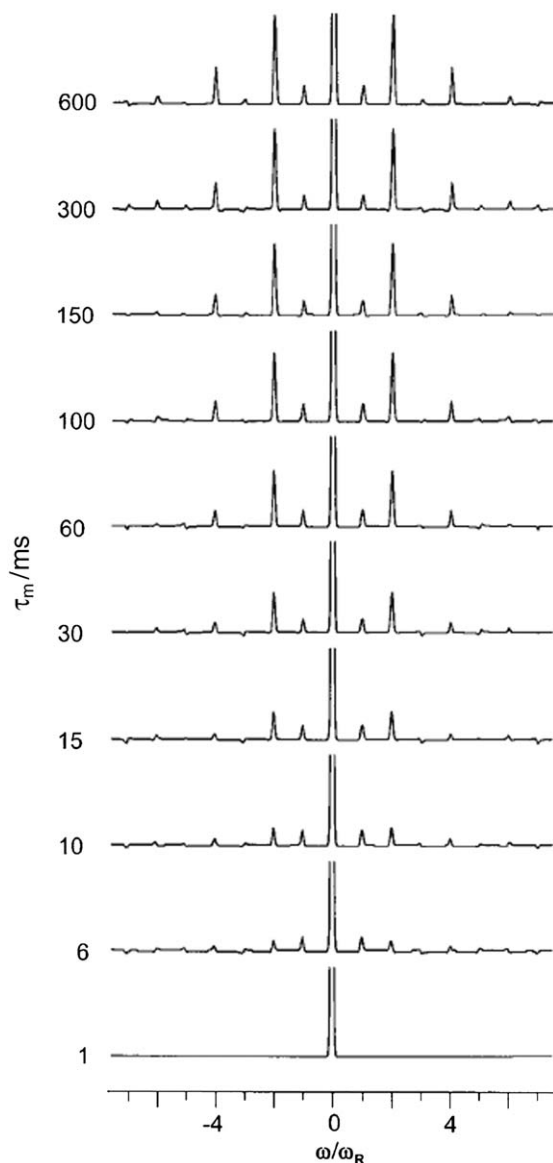


Fig. 44. Results from the DQ-DQ correlation experiment described in Fig. 42 and in text on ^{13}C - ^{13}C spin pairs in polyethylene.⁶⁹ The spinning sideband patterns agree with simulations assuming 70° jumps of the ^{13}C - ^{13}C internuclear vector.

need to vary all four time periods to achieve useful information. In practise, t_1 is set equal to t_2 and τ_m is only varied as much as required to determine the correlation time for the motion, as usual for an exchange experiment. The resulting signal will consist of a sideband pattern whose form will

depend on the reorientation of the dipolar tensor during the mixing time τ_m . It will contain contributions from both reorienting and non-reorienting sites, which could make interpretation difficult. This complication is removed by dividing the spectrum by a second spectrum obtained with a very short mixing time, i.e. in which no exchange occurs. This results in a spectrum whose sidebands purely reflect the moieties that have reoriented during the mixing time. Fig. 43 shows the sideband patterns expected for a spin pair system undergoing a two-site exchange through angle $\Delta\theta_{ij}$. Fig. 44 shows experimental results for ^{13}C – ^{13}C spin pairs in polyethylene.

REFERENCES

1. K. Schmidt-Rohr and H. W. Spiess, *Multidimensional Solid-State NMR and Polymers*, Academic Press, London, 1994.
2. M. J. Duer, *Introduction to Solid-State NMR Spectroscopy*, Blackwell, Oxford, 2004.
3. A. D. Bain, *Prog. Nucl. Magn. Reson. Spectr.*, 2003, **43**, 63.
4. V. Macho, L. Brombacher and H. W. Spiess, *Appl. Magn. Reson.*, 2001, **20**, 405.
5. H. Kaji, K. Fuke and F. Horri, *Macromolecules*, 2003, **36**, 4414.
6. Z. Gan, *J. Am. Chem. Soc.*, 1992, **114**, 8307.
7. J. -F. Shi, P. T. Inglefield, A. A. Jones and M. D. Meadows, *Macromolecules*, 1996, **29**, 605.
8. K. Saalwächter and I. Fischbach, *J. Magn. Reson.*, 2002, **157**, 17.
9. I. Fischbach, F. Ebery, H. W. Spiess and I. Schnell, *ChemPhysChem*, 2004, **5**, 895.
10. C. J. Pickard and F. Mauri, *Phys. Rev. B*, 2001, **63**, 245101.
11. M. D. Segall, P. L. D. Lindan, M. J. Probert, C. J. Pickard, P. J. Hasnip, S. J. Clark and M. C. Payne, *J. Phys.: Cond. Matt.*, 2002, **14(11)**, 2717.
12. R. W. Schurko, I. Hung, C. L. B. Macdonald and A. H. Cowley, *J. Am. Chem. Soc.*, 2002, **124**, 13204.
13. D. Casarini, L. Lunazzi, A. Mazzanti, P. Mercandelli and A. Sironi, *J. Org. Chem.*, 2004, **69**, 3574.
14. P. Mercandelli, M. Moret and A. Sironi, *Inorg. Chem.*, 1998, **37**, 2563.
15. M. Hong, X. Yao, K. Jakes and D. Huster, *J. Phys. Chem. B*, 2002, **106**, 7355.
16. P. Tekely, D. Canet and J. J. Delpuech, *Mol. Phys.*, 1989, **67**, 81.
17. K. Schmidt-Rohr, J. Clauss and H. W. Spiess, *Macromolecules*, 1992, **25**, 3273.
18. S. Hediger, A. Lesage and L. Emsley, *Macromolecules*, 2002, **35**, 5078.
19. P. Tekely, P. Palmas and P. Mutzenhardt, *Macromolecules*, 1993, **26**, 7363.
20. P. Palmas, P. Tekely and D. Canet, *Solid-State NMR*, 1995, **4**, 104.
21. A. Lesage and L. Emsley, *J. Magn. Reson.*, 2001, **148**, 449.
22. M. G. Munowitz, R. G. Griffin, G. Bodenhausen and T. H. Huang, *J. Am. Chem. Soc.*, 1981, **103**, 2529.
23. I. Schnell and H. W. Spiess, *J. Magn. Reson.*, 2001, **151**, 153.
24. K. Saalwachter, M. Krause and W. Gronski, *Chem. Mater.*, 2004, **16**, 4071.

25. K. Saalwachter and I. Schnell, *Solid-State NMR*, 2002, **22**, 154.
26. T. Guillion and J. Schaefer, *J. Magn. Reson.*, 1989, **81**, 196.
27. K. Saalwachter, R. Graf and H. W. Spiess, *J. Magn. Reson.*, 2001, **148**, 398.
28. A. Rapp, I. Schnell, D. Sebastiani, S. P. Brown, V. Percec and H. W. Spiess, *J. Am. Chem. Soc.*, 2003, **125**, 13284.
29. X. L. Xiao, V. P. Conticello and M. Hong, *Magn. Reson. Chem.*, 2004, **42**, 267.
30. M. Wang, M. Bertmer, D. E. Demco and B. Blumich, *J. Phys. Chem. B*, 2004, **108**, 10911.
31. K. Aimi and S. Ando, *Magn. Reson. Chem.*, 2004, **42**, 577.
32. M. J. Duer and E. C. Stourton, *J. Magn. Reson.*, 1997, **129**, 44.
33. A. Hoffmann and I. Schnell, *ChemPhysChem*, 2004, **5**, 966.
34. M. J. Duer and C. Stourton, *Bull. Magn. Reson.*, 1996, **17**, 27.
35. M. Hologne and J. Hirschinger, *Solid-State NMR*, 2004, **26**, 1.
36. M. Vogel and E. Rössler, *J. Magn. Reson.*, 2000, **147**, 43.
37. G. A. Meints, T. Karlsson and G. P. Drobny, *J. Am. Chem. Soc.*, 2001, **123**, 10030.
38. H. M. McConnell, *J. Chem. Phys.*, 1958, **28**, 430.
39. A. Abragam, *Principles of Nuclear Magnetism*, Oxford University Press, Oxford, 1961.
40. J. H. Kristensen and I. Farnan, *J. Magn. Reson.*, 2002, **158**, 99.
41. R. W. Schurko, S. Wi and L. Frydman, *J. Phys. Chem. A*, 2002, **106**, 51.
42. M. Fechtelkord, *Solid-State NMR*, 2000, **18**, 70.
43. C. P. Slichter, *Principles of Magnetic Resonance*, Springer, Berlin, 1992.
44. H. W. Spiess, *NMR: Basic Principles and Progress*, P. Diehl, E. Fluck, R. Kosfeld, eds., Springer, Berlin, 1978.
45. M. Mehring, *High-resolution NMR in solids*, Springer, Berlin, 1983.
46. R. Tycko ed., *Nuclear Magnetic Resonance Probes of Molecular Dynamics*, Kluwer, Dordrecht, 1994.
47. D. A. Torchia, *J. Magn. Reson.*, 1984, **30**, 613.
48. K. Müller, *Phys. Chem. Chem. Phys.*, 2002, **4**, 5515.
49. S. Glowinkowski, B. Peplinska and S. Jurga, *Solid-State NMR*, 2004, **25**, 1.
50. J. Haupt, *Z. Naturforsch.*, 1971, **26a**, 1578.
51. J. S. Oh, A. I. Isayev, T. Wagler, P. L. Rinaldi and E. von Meerwall, *J. Polym. Sci. B: Polym. Phys.*, 2004, **42**, 1875.
52. V. Chevelkov, K. Faelber, A. Diehl, U. Heinemann, H. Oschkinat and B. Reif, *J. Biomol. NMR*, 2005, **31**, 295.
53. A. G. Krushelnitsky, G. Hempel and D. Reichert, *Biochim. Et Biophys. Acta – Proteins and Proteomics*, 2003, **1650**, 117.
54. Y. Yang, M. Schuster, B. Blümich and H. W. Spiess, *J. Magn. Reson.*, 1987, **139**, 239.
55. W. T. Dixon, *J. Chem. Phys.*, 1982, **77**, 1800.
56. Z. Luz, P. Tekely and D. Reichert, *Prog. Nucl. Magn. Reson. Spect.*, 2002, **41**, 83.
57. E. R. de Azevedo, W. -G. Hu, J. Bonagamba and K. Schmidt-Rohr, *J. Am. Chem. Soc.*, 1999, **121**, 8411.
58. V. Géraudy-Montouillot, C. Malveau, P. Tekely, Z. Oleander and Z. Luz, *J. Magn. Reson. A*, 1996, **123**, 7.

59. D. Reichert, H. Zimmermann, P. Tekely, R. Poupkp and Z. Luz, *J. Magn. Reson.*, 1997, **125**, 245.
60. D. Reichert, O. Pascui and M. Beiner, *Macromol. Symp.*, 2002, **184**, 175.
61. S. B. Kennedy, E. R. de Azevedo, W. A. Petka, T. P. Russell, D. A. Tirrell and M. Hong, *Macromolecules*, 2001, **34**, 8675.
62. F. Becker-Guedes, E. R. de Azevedo, T. J. Bonagamba and K. Schmidt-Rohr, *Appl. Magn. Reson.*, 2004, **27**, 383.
63. O. F. Pascui and D. Reichert, *Appl. Magn. Reson.*, 2004, **27**, 419.
64. M. Wind, R. Graf, S. Renker and H. W. Spiess, *Macromol. Chem. Phys.*, 2005, **206**, 142.
65. T. Miyoshi, O. Pascui and D. Reichert, *Macromolecules*, 2004, **37**, 6460.
66. E. R. deAzevedo, T. J. Bonagamba and K. Schmidt-Rohr, *J. Magn. Reson.*, 2000, **142**, 86.
67. H. Kaji and F. Horii, *Chem. Phys. Lett.*, 2003, **377**, 322.
68. I. Schnell, A. Watts and H. W. Spiess, *J. Magn. Reson.*, 2001, **149**, 90.
69. C. Filip, S. Hafner, I. Schnell, D. E. Demco and H. W. Spiess, *J. Chem. Phys.*, 1999, **110**, 423.

NMR Studies of Phase Transitions

C. ODIN

*Groupe Matière Condensée et Matériaux, UMR6626 au CNRS, Université Rennes I,
Campus de Beaulieu Bat11A, 35042 Rennes Cedex, France*

1. Introduction	118
2. Phase Transitions and NMR: Generalities and Static Contribution	122
2.1. Introduction: diffraction and NMR	122
2.2. Phenomenology of phase transitions	125
2.3. NMR: lineshape and relaxation	128
2.4. NMR interactions and symmetry	130
2.5. Sensitivity and resolution: MAS and high fields	133
2.6. Temperature and pressure in static and MAS probes	138
3. Phase Transitions and NMR: Motions	140
3.1. Introduction: physical content of correlation times	140
3.2. Relaxation, correlation times and phase transitions	141
3.3. Lineshape and motion	145
3.4. Mean interaction tensor in the fast-motion regime	147
3.5. Incoherent quasielastic neutron scattering and NMR	148
3.6. Conclusion: pseudocritical features near a transition	152
4. Ferroelectric Phase Transitions, H-Bonded Systems	154
4.1. Introduction: mechanisms of ferroelectricity	154
4.2. Hybrid organic–inorganic compounds	157
4.3. Order–disorder or displacive phase transitions	163
5. Coexistence, Hysteresis and Kinetics	169
5.1. Introduction	169
5.2. Coexistence and hysteresis	171
5.3. Time-resolved NMR: kinetics	173
6. Single-Crystal Phase Transition Studies	174
6.1. Introduction: site selectivity, intrinsic disorder and slow motions	175
6.2. Polar and alignment disorder in molecular crystals	177
6.3. Parallel linear channels-inclusion compounds	181
7. Miscellaneous Phase Transitions	185
7.1. Pure NQR and phase transitions	185
8. Conclusion and Perspectives	188
Acknowledgment	194
References	194

Understanding the mechanisms of transformations between different polymorphs, that is between phases of different symmetries at constant atomic and molecular composition, has always been the touchstone of modern research. In addition to structural methods, nuclear magnetic resonance (NMR) always brought complementary informations of primary importance for the study of phase transitions. For solid matter, the improved high-field NMR resolution and sensitivity, combined with technical advances in probes as well as progresses in NMR methodology and ab initio methods, give new opportunities in the study of phase transitions. For instance, one of the most modern breakthroughs in modern solid-state NMR concerns the quasiroutine study of quadrupolar nuclei, reflected by the huge amount of publications per year. This work is intended to present a pedagogical review of modern solid-state NMR studies of solid–solid phase transitions. This review will not be exhaustive, but rather focuses on some contributions which mentions methods that can be used or tried when a phase transition has to be studied or evidenced by NMR. Nevertheless, the most recent results obtained with modern NMR are reviewed, and about 300 articles over the period 2000–2005 are reported. After a general and pedagogical introduction of the different solid-state NMR signatures of phase transitions, and the experimental cautions, the different concepts of NMR with applications to phase transitions are illustrated. The interplays between continuous- and discontinuous-phase transitions, order–disorder or displacive models, pretransitional effects, coexistence, phase diagrams and NMR parameters (lineshape, inhomogeneous or homogeneous broadening, relaxation, etc.) that permit distinction between different types of disorders, dynamics and slow motions are considered. The examples cover molecular crystals, ferroelectrics, intergrowth compounds, H-bonded systems, etc. We also tried to emphasize, through the choice of the examples, the complement informations between NMR, X-ray diffraction and incoherent neutron scattering. Although this review deals primarily with solid–solid structural phase transitions, almost all the concepts introduced and reported can be directly applied to soft and liquid-like matter such as polymers, liquid crystals or micellar systems

1. INTRODUCTION

Many molecular crystals exhibit polymorphism, that is different crystal structures, or phases, for the same chemical composition. A phase is a homogeneous part of the sample with identical properties, separated by the others by phase boundaries. The different polymorphs exhibit different physical properties as a consequence of the different packing of the same molecules. The transformation between different polymorphs may be driven by an intensive parameters such as temperature, hydrostatic pressure or also by external stimulating fields (electromagnetic field, light, etc.), and it is not

unusual to encounter phase transitions during the search of new materials. Differences in crystal structures are often related to modifications in the nature and dynamics of positional and orientational order-disorder of the constituent atoms or molecules, or to different molecular conformations. And understanding how the atomic and molecular properties such as charge distribution, moment of inertia, symmetry and strength of the site or intermolecular potential affect the stability of the different polymorphs has been a persistent area of inquiry motivated by industrial and fundamental quests. That an industrial process delivers the right polymorph with the expected physical, chemical, pharmacological properties is obviously of major importance. Whence, conventional methods that routinely characterize materials are of great importance, in the process of elaborating and designing new materials as well as for quality control after the fabrication process. But such an objective can only rely on a clear understanding of the transformation mechanisms, and relationships between macroscopic properties to crystal structure and molecular function at given molecular content, which is part of the academic fundamental area of search. The comprehension of the mechanism gives not only new insights into the physical and structural properties of the material, but also precious information concerning the dynamics and possible stability, as way to process the material.

When the polymorph changes its phase through a modification of a nonsymmetry-breaking intensive parameter like temperature or hydrostatic pressure, but not electric field or uniaxial stress that are symmetry-breaking parameters, we speak of a phase transition. Understanding phase transitions is one of the central issues of condensed matter physics and engineering science because of the large variety of potential applications. Many experimental techniques and methodology as well as theoretical frameworks have been developed to understand the driving mechanism of phase transitions. In general, any progress in sensitivity and resolution of experimental techniques brought new results, and opened new or reopened old questions concerning phase transitions. Moreover, fast progresses in methodology and computer-aided acquisition, fitting and modeling as well as commercial availability also democratize many experimental techniques with an increasing panel of almost "routine" experiments that were reserved until then to a few research laboratories or institutions.

Since the very beginning, nuclear magnetic resonance (NMR)¹ and nuclear quadrupolar resonance (NQR) belong to the family of experimental techniques, along with neutron or X-ray diffraction, thermodynamical or spectroscopic techniques, which were used as tools of primary importance in the study of phase transformations. This is because NMR probes, through the coupling of a nuclei having a nuclear spin to its close environment by different interactions, the chemical and structural nature of the phase under

consideration. Among the different reasons that may explain the large popularity of NMR in the study of phase transitions, one is the variety of the different time and length scales that can be studied with the sole NMR technique on the same sample, just by the choice of the nuclei, the interaction or by adjusting the pulse sequences to manipulate the apparent interaction Hamiltonian. Thus, there are many ways by which the signatures of a phase transformation can be tracked or observed on the position, the width or the shape of the spectra, on different relaxation times (spin–lattice relaxation, coherences), the different correlations that are built or not in 2D spectra, etc. Moreover, in phase transitions occurring in almost all the states of matter, NMR accepts any kind of samples irrespective of their nature (liquids of any viscosities, solids from the finest powder to a single crystal, soft matter, liquid crystals, etc.), and offers a large versatility concerning the sample environment to drive the phase transitions with specialized temperature or hydrostatic pressure NMR probes. But one of the major drawbacks of NMR has always been its low sensitivity (good signal-to-noise ratio requires large sample quantities and long acquisition times), and some lack of resolution, principally for quadrupolar nuclei. One also should keep in mind that the interpretation of the spectra is usually by no means straightforward (see below).

With the advent of new commercial spectrometers working at high and very high-magnetic fields, which include high-power irradiation, fast magic angle spinning (MAS), high-Q broad-band and multichannel probes, probes with variable temperature and goniometer heads, and the development of new two-dimensional sequences (MQMAS, STMAS, liquid-like correlation methods applied to the solid state, etc.) to increase resolution and selectivity, parts of the limitations quoted below were overcome. Certainly one of the most spectacular progress in NMR in the last 10 years concerns the overwhelming increase in studies related to quadrupolar nuclei. In addition, new simulations methods and easy-fitting procedures implemented in convivial and interactive programs^{2,3} helped in a renewed interest for solid-state NMR. The now large popularity of solid-state NMR is reflected by the large number of publications per year, roughly 1,000.^{4,5} All these advances as well as important progresses in *ab initio* calculation of chemical shifts and electric field gradients give new opportunities in the study of phase transitions.

A comprehensive survey of the entire literature referring to the use of solid-state NMR spectroscopy in phase transition studies would be a mammoth undertaking. The subject is now so vast that to discuss or even to mention all the publications appears virtually impossible, and anyway unsuitable to a review that should present, from our point of view, a guided tour (that is in practice restricted to the guide's mood) of a subject. The panel of subjects was thus restricted to solid–solid structural phase transitions

as monitored by solid-state NMR. But this area seemed still too large to be covered exhaustively, and we decided to point out some representative subjects that cover the application of routine and modern NMR techniques to the study of phase transitions.

The purpose of this review is thus to report simple, to the most elaborated, examples illustrating the various ways in which modern solid-state NMR method can be used to investigate the polymorphic solid–solid phase transitions. We do not try to review exhaustively all the subjects, nor to enumerate all articles, but rather to spotlight one or a few articles on a system as representative of a particular problem addressed with NMR spectroscopy to stimulate the readers interest to this area of research. Other similar work may be subsequently easily found in the literature, either from the references given in the articles quoted in this review as Ariadne's clues, or from a direct search. The methods introduced in this review can be, in most cases, directly applied to other areas (soft matter, anisotropic liquids, etc.) with minor modifications. Most of the articles reviewed in this contribution present a multitechnique approach, combining NMR with other conventional characterization methods. However, except when needed in the discussion, only the NMR contribution is reported. The bibliographic sources have also been chosen to highlight the complementarity between solid-state NMR and other techniques such as X-ray or neutron diffraction. The corpus was limited to the most recent and significant publications in the period 2000–2005 (with a preference to online available publications, which excludes books), with a few references to older work, and covers 300 articles, chosen over more than 500 articles.

This review is organized as follows. The first two sections, Sections 2 and 3, present a general and pedagogical introduction of the different solid-state NMR signatures of phase transitions. The style is intended to address the “non-NMR specialist” and beginners, and all the different NMR concepts are illustrated by applications to phase transitions. After a small introduction to the different space and time-scales probed by X-ray diffraction and NMR, Section 2 presents a brief summary of the phenomenology of phase transitions. A simplified model is then introduced to explain how structure and dynamics modifies the NMR internal interaction Hamiltonian. The last part of the section is devoted to the influence of the averaged part of the interactions to the NMR features: symmetry of the interactions and group validation/invalidation, MAS and high-field NMR and some experimental cautions are discussed. Section 3 focuses on dynamics, with an introduction to relaxation, motional effects on the lineshape and complementarity with incoherent quasielastic neutron scattering (IQNS) results. The following sections treat chosen examples. For their technological importance as well as the fundamental questions raised by ferroelectric phase transitions,

Section 4 is entirely devoted to ferroelectric and H-bonded systems. It also provides a nice illustration of results that always maintained the utility of proton NMR in solid state, even wide-line, or how the old question of the order–disorder or displacive nature of some ferroelectric phase transitions were reopened by progresses in NMR resolution. A number of structural phase transition is discontinuous, but the examples of coexistence in solid-state and kinetic studies are rather scarce; this is the object of Section 5. Section 6 is devoted to single-crystal studies that allow very precise comprehension of subtle phase transition mechanisms. Section 7 introduces the salient features of NQR that represent an interesting alternative to NMR in some cases. The section ends with a table of miscellaneous phase transitions that complete the references given in the text. Section 8 concludes and presents some perspectives in NMR phase transition studies.

2. PHASE TRANSITIONS AND NMR: GENERALITIES AND STATIC CONTRIBUTION

Phase transitions primarily concern change of symmetry. The symmetry might be broken by atomic or molecular motions (translation, rotation), but also by more subtle transformations like favoring an orientation in a dynamically disordered system, or like intra- or intermolecular charge transfers, leading to new structures and new macroscopic properties (ferroelectricity, ferromagnetism, ferroelasticity, etc.). Owing to the extreme diversity of the use of the available static or dynamical degrees of freedom by a system to make transformations between different polymorphs, it is essential to use complementary techniques with different intrinsic time-scales and correlation lengths to allow the determination, characterization and mechanism assignment of a phase transition.

2.1. Introduction: diffraction and NMR

In principle, any modification of the intra- or intermolecular relationships that break the averaged crystal symmetry on a macroscopic scale corresponds to a structural phase transition. Diffraction techniques (X-ray or neutron) are thus of primary importance to characterize the different phases. From the Bragg peaks that measure the long-range order of the mean crystal structure, the space groups, atomic positions and thermal parameters can be determined in each phases (Fig. 1). Moreover, in the most favorable cases, these methods can directly measure information on the “order parameter” and pretransitional ordering by following the superstructure at $T < T_c$,

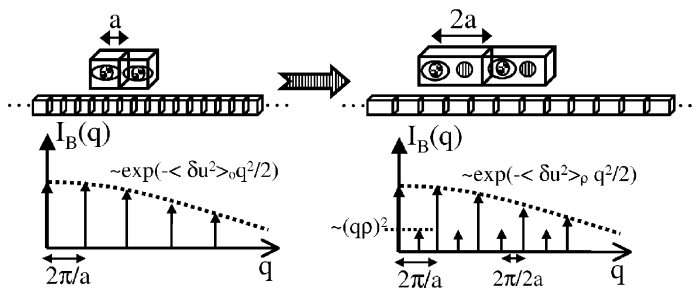


Fig. 1. Schematic of an RX pattern for a 1D doubling of unit cell by translation of one atom over two by ρ : the symmetry breaking induced by the phase transition modifies the extinction rules, and the Debye–Waller factors. Only the diffraction by the mean unit cell is considered, not diffuse scattering. Left: the Bragg peaks at $q_n = n2\pi/a$ are modulated by the Debye–Waller factor with mean square fluctuations $\langle \delta u^2 \rangle_0$. Right: by moving one atom over two by ρ in a given direction, the unit cell is doubled and superstructures at $q_m = (2m+1)2\pi/2a$ appear, with amplitude $\sim (q\rho)^2$ when $q\rho \ll 1$.

which increases usually as the square of the order parameter $\sim \rho^2$ (for the model of Fig. 1), or by collecting the diffuse scattering near the superstructure points corresponding to the critical wave vector, provided this very small signal distributed over all reciprocal space can be detected. However, by definition, conventional X-ray experiments probe long-range correlations by space and time averaging the electronic density over thousands of unit cells and all atoms. Thus, fast time fluctuations and slow motions are averaged out in spatial disorder, and this information is spread into diffuse scattering over all reciprocal space. More importantly, the small local ordering or disordering that only slightly modifies the diffracted intensities may be missed, because an average over all atoms is recorded. In particular, this average favors heavy atoms and the positioning of important atoms like hydrogen may be problematic in some disordered compounds.

In contrast, NMR is a local probe and nucleus-selective. In NMR, the degeneracy of the spin degrees of freedom of a nucleus is broken by the Zeeman interaction H_Z with a strong static magnetic field that splits the energy levels, and by the interaction H_{int} of the spins with the environment (dipolar interaction, chemical shift, quadrupolar interaction when $I \geq 1$, etc.). Energy can be absorbed by application of a resonant radio frequency field causing transitions between these levels. Immediately following the energy absorption, the spins start to exchange this energy among themselves and to transfer energy to the other degrees of freedom of the lattice to relax to equilibrium. Therefore, both the position and shape of the absorption line and the magnetization recovery curves contain structural and dynamical

information concerning the interactions of a given nucleus with its environment. The local structure around probing nuclei yields informations on the number of crystallographic sites present, their relative proportions and their connectivity. Motion correlation times can also be extracted. Interpretation of NMR experiments consists in relating the spectral and relaxation data to the different interactions that contain more or less direct informations on the structure (in the general sense) and dynamics of the compound.

For reasons of probing length scales, we expect differences in the detection of the building of an ordered phase by the two techniques. Being local, we expect NMR to detect local ordering as soon as the correlation length increases, but we do not expect further variation of the NMR features as soon as the correlation length covers many unit cells. On the other hand, X-ray needs a correlation length that covers many cells before the Bragg intensities are modified, favoring the quantification of long-range order. These features explain the reason why in the study of phase transitions, which involve the collective behavior of many atoms through their short- and long-range interactions, NMR and diffractions techniques were always intimately related.

After a short reminder of the phenomenology of phase transitions, we provide here a summary of some of the methods and parameters that can be extracted from NMR simple experiments in view of phase transition studies. All the methods and concepts are illustrated by examples. In view of the excellent introductions to modern NMR techniques available in several monographs, reviews or even courses accessible online, we only discuss some concepts along their uses to solve specific problems in the study of phase transitions. For completeness, we list some interesting reviews concerning modern NMR methodology that the reader can consult, among others. An outline of the basis of NMR accessible to the novice, with practical considerations concerning “routine” 1D or 2D sequences performed on modern NMR spectrometers are presented in refs. 6–9, NMR methods for materials in ref. 10, quadrupolar nuclei and numerical methods for simulation of solid-state NMR experiments in ref. 11. A wealth of interesting informations on NMR specialized to quadrupolar nuclei, and simulation JAVA applets, are compiled in the site of P. Man “<http://www.pascal-man.com>”. A presentation of the quadrupolar interaction, with related NMR methods covering DAS, DOR, MQMAS, etc. are given in refs. 12–13, and ref. 14 for deuterium NMR. For beginners who would like to avoid the formalism of irreducible tensors, Wigner matrices and spherical harmonics, a pictorial representation of the NMR interactions at first- or second-order only based on standard Cartesian coordinates is developed in refs. 15 and 16. An excellent introduction to *ab initio* quantum mechanical calculations of shielding tensors and spin–spin coupling is given in ref. 17. Books edited by

K.A. Müller on phase transitions or the *Encyclopedia of Magnetic Resonance* edited by Grant and Harris with, for instance, the contributions of F. Borsa, A. Rigamonti, R. Blinc and others to the high relevancy of NMR and NQR techniques to the studies of phase transitions in solid-state physics are very important sources of knowledge.^{18–22} The end of the section is particularly devoted to the static contribution of the average structure to the NMR lineposition and lineshape, and methods to gain resolution and sensitivity. The dynamics will be treated in the next section.

2.2. Phenomenology of phase transitions

Phase transitions are usually classified into two groups, continuous- or discontinuous-phase transitions. Phase transitions are discontinuous when the two phases that transform within each other are simultaneously present and at equilibrium at the transition point. Generally, the coexistence of the two phases also arises within a limited range of the driving intensive parameter, but one of the two phases is metastable. For such a phase transition, the entropy is always discontinuous at the transition point, and results in a latent heat of transformation of one phase into another. On the contrary, phase transitions are continuous when one phase transforms continuously to the second phase, the two phases never being in equilibrium with each other. Anomalies in the heat capacity can be observed at the transition temperature. Following the thermodynamical classification of Ehrenfest (1933), transitions that result in discontinuities of first derivatives of the free energy (like volume, enthalpy, entropy) are “first-order” phase transitions, and those where the first derivatives are continuous but a second derivative (heat capacity, coefficient of volume expansion, etc.) is discontinuous are called “second-order” phase transitions. In the following, the two terminologies will be used.

More generally, the occurrence of first- or second-order phase transitions can be rationalized within the framework of Landau theory (1937) that classifies phase transitions by symmetry considerations. In this theory, the symmetry relationship of the descendant phase with the parent phase is of primary importance in the description of the possible phase transitions. Within a group–subgroup filiation, continuous- (second order) or discontinuous-(first order) phase transitions are possible. On the other hand, if the two phases are not related by a group–subgroup relationship, then the phase transition cannot be continuous.

Landau also recognized that continuous phase transformations in a group–subgroup relationship could be described by an order parameter, which carries the information about the broken symmetry. This order

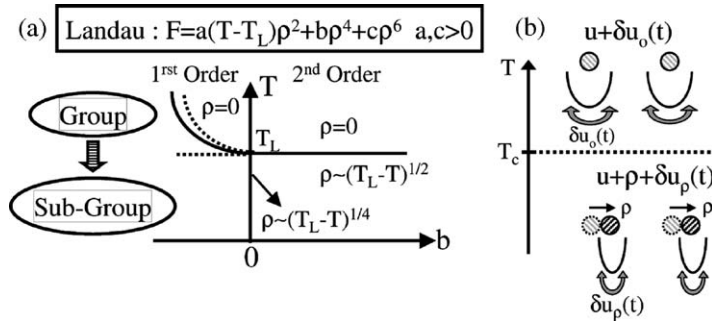


Fig. 2. (a) Schematic of Landau phase diagram as a function of the value of parameter b in the development of the critical free energy F as a function of the order parameter ρ up to sixth order. When $b > 0$, the phase transition is second order. For $b < 0$, the phase transition is first order. Transition lines are continuous, and for $b < 0$ the dotted lines show the coexistence region. $b = 0$ corresponds to a tricritical point. First-order phase transitions may also occur for symmetry reasons when third-order invariant is allowed in the free energy expansion. (b) Schematic representation of the microscopic modification of a variable $u(t) = u + \rho + u_\rho(t)$ in the parent ($\rho = 0$) and descendant phases ($\rho \neq 0$). Both the mean value $\langle u(t) \rangle = u + \rho$ and time fluctuations $\delta u_\rho(t)$ depend on the phase.

parameter ρ is essentially zero in the parent phase of higher symmetry and becomes different from zero in the lower symmetry-descendant phase.²³ For continuous or weak first-order phase transitions, a free energy expansion as a function of the order parameter near the transition point, and based on symmetry consideration was proposed (Fig. 2). The different equilibrium states of the system are obtained by minimizing this free energy with respect to the order parameter and other coupled variables. The theory is able to predict the different possible phases issued from the parent phase at the phase transition, and gives also the critical mean field exponents for the order parameter ($\rho \sim (T_c - T)^{1/2}$ for $T < T_c$), the susceptibility $\chi \sim \partial \rho / \partial f \sim |T_c - T|^{-1}$ with f the conjugate field to ρ . Note that in practice the measured exponent may be different from the mean field prediction ($\rho \sim (T_c - T)^\alpha$ with $\alpha \leq 1/2$) for a number of reasons, but the underlying symmetry analysis, which is the key point in Landau analysis, cannot be questioned. Theoretically, the Landau expansion is equivalent to a mean field theory where each atom evolves around the average potential built by all other atoms, that suppose infinite range interactions and neglects the fluctuations. Strong deviations from the Landau predictions have long been found in magnetic, gas–fluid or quantum phase transitions. But it was proved that in most ferroelectrics or structural phase transitions, the fluctuations occur so close to the transition that no deviation is experimentally detectable.²⁴

Another output of Landau theory is that any other physical quantities (tensors) that are coupled to the primary order parameter ρ contain components ξ that may exhibit also some anomaly. Typically, if ξ has the same symmetry as ρ , then $\xi \propto \rho$. Otherwise, $\xi \propto \rho^m$ with exponent $m = 2$ although other values are possible. As a consequence, the phase transitions can be detected in an indirect manner by the measurement of any physical tensorial quantity that is coupled to the order parameter: depending on the symmetry of the coupling, some components may become nonzero in the low-symmetry phase, or otherwise exhibit an anomalous behavior near the transition. Schematic evolution of different physical parameters at second- and first-order phase transitions is summarized in Fig. 3. These considerations are highly relevant to NMR because all interactions are second-rank tensors that may couple with the order parameter.

Apart from temperature, hydrostatic pressure is the other intensive thermodynamical parameter that can be modified with high-pressure cells to build (T, P) phase diagrams. By changing the relative distances between the atoms and molecules, the strength of the interactions are modified, thereby modifying the transition temperature or even inducing new phases. The change of the transition temperature as a function of pressure depends whether the transition is continuous (second order) or discontinuous (first order). The Clausius–Clapeyron $(dT_c/dP)_1$ and Ehrenfest $(dT_c/dP)_2$ relationships apply to first- and second-order phase transitions, respectively,

$$\left(\frac{dT_c}{dP}\right)_1 = \frac{\Delta V}{\Delta S}, \quad \left(\frac{dT_c}{dP}\right)_2 = T_c V \frac{\Delta \alpha}{\Delta C_p}, \quad (1)$$

where ΔV , ΔS , $\Delta \alpha$, ΔC_p , respectively the volume, entropy, volume expansion and heat capacity jump changes at the phase-transition temperature. V is the

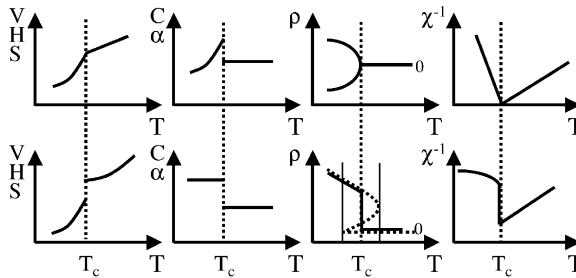


Fig. 3. Schematic of second-order (first line) and first-order (second line) phase transitions. The first and second columns are variables related to the first and second derivatives of the free energy, respectively. V = volume; H = enthalpy; S = entropy; C = heat capacity; α = coefficient of thermal expansion; ρ = order parameter; and χ^{-1} = the inverse of the susceptibility $\chi^{-1} \sim \partial f / \partial \rho$.

volume at the phase-transition temperature. In the phenomenology of Landau theory, the parameter $b = b(P)$ becomes a function of pressure and implicit T - $b(P)$ phase diagrams as in Fig. 2a can be obtained.

2.3. NMR: lineshape and relaxation

The internal spin interaction Hamiltonian H_{int} can be decomposed into spatial $T_m[\{u_\alpha(t)\}]$ and spin S_m degrees of freedom $H_{\text{int}}(t) = \sum_m T_m[\{u_\alpha(t)\}] S_m$. The spatial contribution, hereafter an NMR interaction rank-2 tensor \mathbb{T} , is a stochastic function of time $T_m[\{u_\alpha(t)\}]$ because it depends on generalized coordinates $\{u_\alpha(t)\}$ of the system (atomic and molecular positions, electronic or ionic charge density, etc.) that are themselves stochastic variables. To clarify the role of these coordinates in the NMR features, a simple model is developed below.^{19,20} At least one physical quantity should distinguish the parent and the descendant phase after a phase transition. For simplicity, we suppose that the components of the interaction tensor only depend on one scalar variable $u(t)$ whose averaged value is modified from u to $u + \xi$ at a phase transition. To take into account the time fluctuations, this variable is written as the sum of three terms, i.e. $u(t) = u + \xi + \delta u_\xi(t)$. The last term is a stationary stochastic process such that $\langle \delta u_\xi(t) \rangle_\xi = 0$, where $\langle . \rangle_\xi$ denotes a time (or ensemble if the system is ergodic) average. In this model, the normal behavior of the compound when an external parameter is varied (temperature, pressure, etc.) is carried by u , whereas the anomalous contribution attached to the phase transition is contained in ξ , with $\xi = 0$ by convention in the parent phase. Note, however, that ξ is not necessarily an order parameter (see Section 2.2), but if this variable is coupled to the real-order parameter, then it should reflect the phase transition. The modification of the nature of the fluctuations and of the averaging procedure in the different phases is indicated by the subscript ξ .

For sufficient small fluctuations $\xi + \delta u_\xi(t)$, each component $T[u(t)]$ of the interaction tensor \mathbb{T} can be developed up to second order. The result is separated into the average and the time fluctuations as $T_\xi = \langle T \rangle_\xi + \delta T_\xi(t)$ with $\langle \delta T_\xi(t) \rangle_\xi = 0$.

$$\langle T \rangle_\xi(u) = T(u) + A\xi + B[\xi^2 + \langle \delta u_\xi^2 \rangle_\xi], \quad (2)$$

$$\delta T_\xi(t) = [A + 2B\xi]\delta u_\xi(t), \quad (3)$$

where $A = A(u)$ and $B = B(u)$ depend on the first and second derivatives of T evaluated at u . The fluctuating contribution was truncated to first order in $\delta u_\xi(t)$. The different contributions $\langle T \rangle_\xi(u)$ and $\delta T_\xi(t)$ reflect the local

symmetry and can be used to determine or confirm the space group of the crystal, to observe any structural transformations that might occur, even to determine the order parameter and its variation with external parameters. The “normal” evolution of the mean components of the tensor is expected to be an almost linear variation as a function of temperature. (For a classical variable that obeys the equipartition theorem,²⁵ then the fluctuations $\langle \delta u_\xi^2 \rangle_{\xi \sim T}$.) This is the analogue to the Bayer model,²⁶ which predicts that for fast librations with $\langle \Delta\theta \rangle = 0$ around one axis, the averaged electric field gradient (EFG) component is $\langle V_{zz} \rangle = \langle V_{zz} \rangle_{(T=0)} (1 - 3\langle \Delta\theta^2 \rangle)$.

In high-field NMR, the total Hamiltonian is $H(t) = H_Z + H_{\text{int}}(t)$ where the Zeeman interaction H_Z is the preponderant term as compared to the interaction H_{int} of the spins with the close environment of the nuclei ($\|H_Z\| \gg \|H_{\text{int}}\|$), with the consequences that the Zeeman interaction tend to mask some components of the interaction Hamiltonian. Therefore, different parts of the Hamiltonian, after a hierarchy of motional averaging at different time-scales and truncation, govern the lineshape and the relaxation.²⁷ The strength of the Zeeman interaction fixes a time-scale at the Larmor frequency, and the direction of the external static magnetic field in the laboratory frame is also a favored axis that implies angular dependence of the NMR response. To interpret the NMR experiments, the resulting time-dependent Hamiltonian is written in the following simplified manner:

$$H(t) = H_Z + \langle H_{\text{int}} \rangle_s + \delta h_s(t) + \delta h_{\text{ns}}(t). \quad (4)$$

The second contribution is the secular part of the time-averaged interaction Hamiltonian. The third and fourth contributions are respectively the secular fluctuating part with $\langle \delta h_s(t) \rangle = 0$ and the nonsecular fluctuating part with $\langle \delta h_{\text{ns}}(t) \rangle = 0$ of the time-varying internal interaction Hamiltonian. The lineposition and lineshape depend principally on the first three terms. In particular, $\delta h_s(t)$ drastically modifies the lineshape when the correlation time of its fluctuations are of the order of magnitude of the inverse static linewidth. The fourth term, which induces incoherent transitions between the energy levels, governs the spin–lattice relaxation and also part of the linewidth. The relaxation rate can be measured by intentionally altering the equilibrium distribution among the Zeeman energy levels and subsequently monitoring the recovery toward equilibrium of the NMR signal. It is worth noting that the lineshape and spin–lattice relaxation are governed by different parts of the Hamiltonian, that is, contain complementary informations on the interactions.

With the hypothesis that the temporal fluctuations carried by $\delta u_\xi(t)$ are not on the linewidth time-scale, $\langle T \rangle_\xi(u)$ gives the linepositions and line-shapes and $\delta T_\xi(t)$ contributes to relaxation. Eqs. (2) and (3) clearly show that the sensitivity of the NMR features to a phase transformation depends

strongly on the strength of the coupling (A and B) and on the modification of the amplitudes of the fluctuations. Nevertheless, it is also clear that any discontinuous behavior of ξ should be reflected by a discontinuity (maybe extremely small) of the NMR features. In the rest of the section, we concentrate on static NMR governed by the average interaction $\langle T \rangle_\xi(u)$, and postpone the discussion of relaxation and motional narrowing to Section 3.

2.4. NMR interactions and symmetry

All NMR interactions are represented by tensors of rank 2, and enter the static NMR Hamiltonian after averaging over the fast degree of freedoms. The lineposition and lineshape are determined by this *mean tensor*, which should reflect the local symmetry. How the NMR interaction tensors are transformed by the symmetry operations is consequently highly relevant to structural phase transition that are characterized by a loss of some symmetry operations.

The most common interactions are dipolar coupling between two spins, chemical shielding and quadrupolar interaction for spins $I \geq 1$. The chemical-shielding interaction arises from the motion of electrons around a nucleus induced by the external applied static magnetic field. This motion generates local magnetic fields that modify the total field experienced by the nucleus, and are characteristic of the local chemical environment of the nuclei. All nuclei with a spin $I \geq 1$ possess a quadrupolar moment Q that interacts with the EFG $V_{rs} = \partial^2 V / \partial x_r \partial x_s$ at the nuclear site. The EFG tensor V_{rs} is a symmetric tensor with zero trace $\text{Tr}(V) = \Delta V = 0$ (from Laplace equation).

At first order, it can be shown that only the symmetrized part of the interaction tensor contributes to the frequency shift. The majority of second-order contributions arise from large EFG, the EFG tensor being symmetric by definition. Thus, only symmetric second-rank tensors \mathbb{T} can be considered, which can be decomposed into two contributions $\mathbb{T} = t_{\text{iso}} \mathbb{I}_3 + \Delta \mathbb{T}$ with \mathbb{I}_3 the identity matrix. The first term is the isotropic part $t_{\text{iso}} = 1/3 \text{Tr}(\mathbb{T})$ that is invariant by any local symmetry operation. The second term is the anisotropic contribution $\Delta \mathbb{T}$, a symmetric second-rank traceless tensor, which depends then on five parameters: the anisotropy δ and the asymmetry parameter η that measures the deviation from axial symmetry, and three angles to orient the principal axes system (PAS) in the crystal frame. The most common convention orders the eigenvalues of $\Delta \mathbb{T}$ such that $|\lambda_{xx}| \leq |\lambda_{yy}| \leq |\lambda_{zz}|$, and defines $\delta = \lambda_{zz}$ and $\eta = (\lambda_{xx} - \lambda_{yy}) / \lambda_{zz}$.

All the features of an interaction tensor can only be determined by single-crystal NMR. For instance, for a first-order spectrum, the frequency is

proportional to $v \sim \sum_{r,s} B_r \mathbb{T}_{r,s} B_s$ where $\mathbb{T}_{r,s}$ and B_r are respectively the components of the second-rank interaction tensor and magnetic field in an axis system. This formula is at the basis of orientation-dependent experiments to completely determine a tensor. In the PAS of the interaction tensor, the frequency as a function of the polar angles (θ, ϕ) of the magnetic field simplifies to

$$v(\theta, \phi) = v_{\text{iso}} + \frac{\delta}{2} [(3 \cos^2 \theta - 1) + \eta \sin^2 \theta \cos 2\phi]. \quad (5)$$

Spectra of isotropic powder samples have characteristic singularities of only two types, steps and divergences, whose positions, if resolved, permit the extraction of the tensor parameters v_{iso} , δ and η either by direct inspection, by using the moments, or by lineshape fitting.^{28–31}

2.4.1. Site symmetry

The local symmetry fixes the number of independent components of the tensor, which results in constraints on the anisotropy or the asymmetry parameters as well as on the direction of some principal axes.³² For instance, when the point group symmetry contains an n -fold axis with $n \geq 3$, one of the PAS axis is parallel to the n -fold axis and the asymmetry parameter is zero, i.e. $\eta = 0$. For cubic symmetry, only the isotropic contribution remains. Different symmetry restrictions are summarized in Table 1.

In the parent phase $\xi = 0$, the lineposition and shape (see Eq. (2)) depend on the variance of the fluctuations $\langle \delta u_\xi^2 \rangle_0$ and should be approximatively linear in temperature if the classical equipartition theorem can be applied. In the phase characterized by $\xi \neq 0$, the total mean tensor $\langle \mathbb{T}_\xi \rangle$ should obey the new site symmetry of the new phase. Since the linear term is preponderant, the isotropic part of the tensor is thus a linear function of ξ and its behavior as a function of temperature should reflect whether the phase transition is continuous or discontinuous. The exact behavior of the lineshape cannot be

Table 1. Restrictions on the symmetric tensor elements and PAS due to local symmetry

Symmetry	PAS	δ, η
C_2	PA twofold axis	No constraints
$m, 2/m$	PA $\perp m$, two PA in the mirror plane	No constraints
$222, mmm, mm2$	PAS parallel to the symmetry axes	No constraints
$C_n (n \geq 3)$	PA n -fold axis	$\eta = 0$
Cubic	Isotropic	$\delta = 0, \eta = 0$

Note: PA is one of the principal axis of the PAS.

directly predicted without taking into account all the components of the tensor with a more precise model because the anisotropy and asymmetry parameters are obtained after diagonalization of the full tensor. But it is clear that as functions of u and ξ , they may also reflect the phase transformation.

Effects of site symmetry are particularly spectacular on the EFG. Since the NMR quadrupolar interaction magnitudes $\sim V_{zz}Q$ are in general rather large (kHz to MHz), very small local distortions from cubic symmetry, for instance, can be detected because the zero value results from the perfect compensation by symmetry between large values of the EFG. It explains, in particular, the ^{35}Cl linewidth from NaCl as-grown powders, where stacking faults slightly perturb the cubic symmetry. The extreme sensitivity of the EFG to distortions from cubic symmetry is a powerful tool in structural assignment for crystal systems near cubic symmetry. For instance, the structure of perovskite LaGaO_3 and its doped derivative $\text{La}_{1-x}\text{Sr}_x\text{Ga}_{1-x}\text{Mg}_x\text{O}_{3-x}$ are not strictly resolved between cubic or orthorhombic structure by conventional diffraction methods. The interest in the last compound comes from superionic oxygen-conduction properties. A $^{69,71}\text{Ga}(I = 3/2)$ and $^{139}\text{La}(I = 7/2)$ NMR static and MAS study of the quadrupolar broadened central transition $(-1/2, 1/2)$ helped in solving the structural discrepancies. Different spectra acquired at different irradiation frequencies were needed to cover a frequency range of ~ 400 kHz. Nonzero EFG asymmetry parameters definitely confirm the nonaxial distortion from cubic symmetry.³³

2.4.2. Space group validation or invalidation

Apart from the site symmetry, the symmetry operations of the point or space group transform different atomic or molecular units within each other. When different sites are related by a symmetry operation in the crystal, they share the same eigenvalues but do not need to have the same orientation of their principal axis system with respect to the crystal frame. Considering the isotropic lineposition, tensors with the same eigenvalues cannot be distinguished, thus the number of isotropic lines give the number of inequivalent sites. The knowledge of the site symmetry, the site multiplicities and relative intensities offers the possibility to validate or invalidate the crystallographic structure, especially when conventional crystallographic techniques have difficulties in detecting the main structural units.³⁴ NMR experiments that validate or invalidate the assignment of the space group of a given phase can be reported in pure silica ferrierite,^{35,36} $\text{Rb}_3\text{D}_x\text{H}_{1-x}(\text{SO}_4)_2$,³⁷ $\text{Si}(\text{SnMe}_3)_4$ and $\text{Si}(\text{SnMe}_3)_4$,³⁸ Ag_7PSe_6 ,³⁹ etc. The selection or determination of space groups by comparison of NMR

measured and calculated EFG (from first-principle methods) is another possibility, for instance, in YD_3 with ^2H NMR,⁴⁰ or CaTaOAlO_4 with ^{27}Al MAS NMR.⁴¹

The use of 1D and 2D correlation experiments is also very fruitful. The $\text{M}^{4+}\text{P}_2\text{O}_7$ ($\text{M} = \text{Si}, \text{Ge}, \text{Sn}, \text{Pb}, \text{Ti}, \text{Zr}, \text{Hf}, \dots$) crystalline or disordered phosphate compounds family have small or even negative dilatation coefficients of thermal expansion. In contrast to other materials of negative thermal expansion, $\text{M}^{4+}\text{P}_2\text{O}_7$ have *isotropic* negative thermal coefficients over a broad temperature range. The high-temperature phase is in general a simple cubic structure, which develops at room temperature, a superstructure with a tripled ($3 \times 3 \times 3$) unit cell ($Z = 108$) through a first-order phase transition.⁴² An enumeration of the different compatible low-temperature subgroups from the high-temperature space group gives 12 possible choices. Therefore, a structural refinement of such superstructures are challenging, because of the large Z value, and of the very subtle differences in the intensities of the Bragg peaks in powder X-ray diffraction of the different phases. However, the multiplicities of the $\text{P}_2\text{O}_7^{4-}$ groups in the asymmetric unit depend on the space group, and range from 6 to 108. Thus, measuring the multiplicities of the $\text{P}_2\text{O}_7^{4-}$ groups by NMR can limit the number of space groups, which could represent the room temperature structure. The space groups of TiP_2O_7 ,⁴³ ZrP_2O_7 ⁴⁴ and $\text{M}^{4+}\text{P}_2\text{O}_7$ ⁴⁵ were determined (or restricted to a choice within 2) with the use of sophisticated 1D and 2D experiments that exploit the through-bond P–O–P connectivities via the homonuclear J coupling, and homonuclear dipolar through-space connectivities. Note that through-bond correlation methods are also useful for the glass phase to characterize the various PO_4 tetrahedral units in the disordered network, and their connectivities (see refs. 46 and 47 and references therein). Using a through-bond selection of ^1H – ^{13}C pairs and ^1H spin different, different length scales can also be characterized.⁴⁸

2.5. Sensitivity and resolution: MAS and high fields

The quest of sensitivity and resolution has always been a major source of progress in NMR technology and methodology. The enhancements in NMR sensitivity (the signal-to-noise ratio scales as $B^{1.5-2}$) provided by increasingly high-magnetic fields are well known and are one of the major driving forces in the development of superconducting magnets with highly stable, homogeneous fields. It also yields improvements in acquisition, processing, probes (acquisition of liquid-state NMR spectra with volumes as small as nanoliters⁴⁹ is claimed) and sequences. But high-magnetic fields also modify the weight of the different interactions with respect to each other.

In liquids, the molecular tumbling is almost isotropic with very small correlation times, which is sufficient to average out the anisotropy of the NMR interactions. This explains why well-resolved lines are obtained. But the information on the anisotropy of the tensors are lost. A slight anisotropy of the NMR interaction tensors can be restored by weak alignment of the molecules under interest using their magnetic susceptibility anisotropy or the one of anisotropic liquids to restore a preferential direction.^{50–52} This gain in information content is used for structural and dynamics studies. Examples of spontaneous alignment of loosely packed powders by high fields were also observed for hexagonal metal hybrids $\text{ZrBe}_2(\text{H,D})_x$ or trideuterides $\text{LuD}_3, \text{YD}_3$ at 4.4–8.3 T,⁵³ and increases strongly the resolution. By dispersing the powder in wax and allowing the powder to orient in the static magnetic when the wax is liquid, the authors obtained a solid axially oriented sample after subsequent freezing, which could be used to perform angle-dependent studies, analogue to single-crystal studies. For instance, the orientation of the PAS of the EFG tensor in LuD_3 was partly determined.⁵⁴ A structural phase transition was detected in $\text{ZrBe}_2(\text{H,D})_x$ by ^2H NMR.⁵⁵ The nature of this phase transition was clarified by $^9\text{Be}(I = 3/2, 100\%)$ NMR using oriented samples.⁵⁶ In particular, two types of Be sites were evidenced in the low-temperature phase (LTP), and only one in the high-temperature phase (HTP). A coexistence region shows that the transition is first order.

In the solid state or when motions are not symmetric and fast enough to average out the anisotropic contribution of the NMR tensors, information on the strength and asymmetry of the interaction is present. But the static orientational disorder of powder samples spans the frequencies over a broad range, which results in a strong loss of resolution due to strong inhomogeneous broadening. The strategy is the opposite as to liquids: either to average the anisotropic contribution to gain resolution (at the price of a loss of information) or to use perfectly oriented samples, that is single crystals.

Thus, reaching high resolution is always a matter of compromise depending on the kind of informations needed and strategies to cancel or reintroduce anisotropies of selected interactions were developed in direct space (powdered or single crystal, mechanical spinning (MAS), etc.), in the space of coherences (averaged Hamiltonians, multidimensional NMR sequences, etc.) or combined methods (MQMAS, etc.).

2.5.1. MAS NMR: sensitivity and low- γ nuclei

The major sources of linebroadening such as chemical shift anisotropy, heteronuclear dipolar interaction, *first-order* quadrupolar interaction as well as magnetic susceptibility broadening, can be almost time-averaged to zero

by mechanical fast spinning (that is the spinning frequency is much larger than the anisotropy of the interaction) of the sample about an axis oriented at the magic angle that verifies $(3 \cos^2 \theta_M - 1) = 0$ ($\theta_M \approx 54.7^\circ$) with respect to the static magnetic field. This is MAS. Even homonuclear dipolar interactions are removed if spinning is fast enough. The spinning frequency of standard probes reaches now currently 15–35 kHz. The principle of high-spinning probes (MAS) as well as new trends is described, for instance, in refs. 57 and 58. The theory of MAS for multiple-quantum coherences in ^1H and its application to H-bond systems was reviewed in ref. 59. The influence of the precision of the magic angle setting on the linewidth of ^{13}C as well as temperature inhomogeneities is presented in ref. 60. The cost of the drastic increase in spectral resolution by MAS methods is the loss of information on the anisotropy of the interaction, but the recent trends are precisely to design new sequences to reintroduce this information without losing resolution.

Apart from the enhanced resolution, MAS also favors the detection of the anisotropic powder pattern as compared to a static spectrum by concentrating the intensity into the isotropic line and spinning sidebands, resulting in an increased signal to noise ratio. Note that enhancement of signal-to-noise ratio by collapsing the continuous broad powder spectra into a manifold of spikes, similar to MAS sidebands, was also achieved with static samples by multiple pulse sequences (see ref. 61 and references therein). This property is very useful for low- γ nuclei or very large quadrupolar interactions, because recent progress in high- Q transmission-line tuning MAS probes, and NMR MAS simulation programs, render possible the precise measurement of NMR parameters (isotropic shift, anisotropy and asymmetry) from iterative simulations of the complete MAS sidebands manifold.

An important application concerns the NMR of ^{14}N , which is a low- γ $I = 1$ quadrupolar nuclei, of natural abundance 99.63% and quadrupolar moment $Q \approx 2 \times 10^{-30} \text{ m}^2$. As compared to ^2H , which is only present at 0.001%, ^{14}N does not need enriched samples, but the low- γ value is not favorable for solid-state NMR. Moreover, the quadrupolar interaction of ^{14}N is almost 10 times larger than the corresponding quadrupolar interaction of deuterium, typically 1–5 MHz. Despite this inherent low sensitivity, different methods were already developed for ^{14}N NMR in the solid state to probe slow motions.⁶² Note also that when low temperatures are needed, liquid argon may be used to avoid the spurious ^{14}N signal of liquid nitrogen.⁶³ The feasibility of MAS detection of ^{14}N spectra with moderate quadrupolar coupling was shown in ref. 64. Subsequently, use of the complete spinning sideband manifold to precisely evaluate the quadrupolar parameters of ^{14}N when $C_q < 1 \text{ MHz}$ was achieved,⁶⁵ and recently applied to the characterization of amino acids.⁶⁶

The first application of natural abundance ^{14}N MAS NMR in characterizing a solid-state phase transition was reported by the study of the phase transition between phase III and IV of ammonium nitrate (NH_4NO_3), which occurs at 35°C .⁶⁷ Using a naturally abundant isotope NH_4NO_3 sample, and a sample enriched in ^{15}N ($^{15}\text{NH}_4\text{NO}_3$), the authors could separate the contributions of both NH_4^+ and NO_3^- ions. The ^{14}N MAS sidebands manifold of both ions was shown to be extremely sensitive to the phase transition, indicating that the ^{14}N quadrupolar parameters (C_q and η_q) are clearly different in both phases. In contrast, the change in the ^{14}N isotropic chemical shift was very small (~ 3 ppm), and consistent with values deduced from ^{15}N , $I = 1/2$ NMR spectra. The demonstrated sensitivity of the ^{14}N quadrupolar interaction to local properties gives potentialities to the method for the study of phase transitions.

The method was generalized to other nuclei, for instance, to recover ^2H chemical shifts at high field (14 T).⁶⁸ The nonmetallic/metallic phase transition of VO_2 was studied by ^{51}V high-field and MAS NMR,⁶⁹ and is reflected by a large negative Knight shift. The multiplicity of the ^{51}V site was considered, and the magnitude and relative orientation of the quadrupolar tensor and chemical shift were determined in both phases by analysis of the spinning sideband patterns. The phase transition at $\approx 307\text{ K}$ between two polymorphs of Friedels salts, $\text{Ca}_2\text{Al}(\text{OH})_6\text{Cl}\cdot 2\text{H}_2\text{O}$, was followed by precise measurement of the quadrupole ^{27}Al -coupling parameters C_q and η_q by MAS NMR over the temperature range $\sim 150\text{--}380\text{ K}$.⁷⁰ An abrupt jump of C_q and η_q was evidenced at the transition, and interpreted from point monopole calculations of the ^{27}Al EFG over a large cluster of atoms around the aluminum sites. The authors deduced that modifications in hydrogen bonding were certainly an important mechanism in the phase transition.

There is no doubt that the complete sideband analysis method will be useful in the study of phase transitions of compounds with low- γ nuclei.

2.5.2. *Quadrupolar nuclei and high-field NMR*

Quadrupolar nuclei account for nearly 75% of the stable magnetic nuclides in the Periodic Table. Certainly, the most important breakthrough of the recent years is the widespread applications of quadrupolar NMR to all fields in physics.

Within quadrupolar nuclei, ^2H , ^6Li , ^{14}N have spin $I = 1$, ^{10}B spin $I = 3$. All the other nonradioactive nuclei are half-integer spins. Half-integer spins have the distinctive characteristic that the central transition ($-1/2 \leftrightarrow 1/2$) is not affected by quadrupolar interaction to first order, and the second-order terms are necessary to take into account of this interaction. As a result, the

shape and the angular behavior of the part of the spectrum that corresponds to the central transition differ dramatically from usual first-order spectra.

Typically, the frequency shift $\delta = (v - v_L)/v_L$ relative to the Larmor frequency $2\pi v_L = \gamma B$ can be written as

$$\begin{aligned} \delta \sim v_{\text{CS}}^{\text{iso}} + A_Q^{\text{iso}(2)} \left(\frac{C_q}{v_L} \right)^2 + \left[\sigma_{\text{CSA}}^{(1)} + \frac{v_{DD}^{(1)}}{v_L} + A_Q^{(1)} \left(\frac{C_q}{v_L} \right)^2 \right] P_2(\cos \psi) \\ + A_Q^{(2)} \left(\frac{C_q}{v_L} \right)^2 P_4(\cos \psi). \end{aligned} \quad (6)$$

The first two contributions are isotropic, and correspond to the shift of the center of gravity of the line by the chemical shielding and second-order quadrupolar isotropic interactions, respectively. The term in brackets contains the first-order anisotropic contribution of the chemical shift and dipolar interaction, and part of the anisotropy of the second-order quadrupolar interaction, while the last term describes the second part of the anisotropy of the second-order quadrupolar interaction. The angular dependences depend on second- and fourth-order Legendre polynomial, respectively. The most spectacular difference with first-order spectra is that mechanical spinning at the magic angle MAS cannot average the anisotropic contribution of second-order quadrupolar interaction, even at “infinite” spinning rate. On the one hand, the remaining inhomogeneous broadening gives a typical second-order powder pattern that contains information on the EFG parameters, but on the other it reduces the resolution.

As shown in Eq. (6), the resolution and weight of the different interactions can be varied by changing the magnetic field value B .^{71,72} For inorganic materials, the reduction in second-order quadrupolar broadening in one-dimensional MAS spectra, which, relative to the chemical shift (in ppm), scales as the inverse square of the field, is of particular interest in systems where the chemical shift carries structural information that complements that which is contained in quadrupolar parameters. From Eq. (6), it is also easily seen that the acquisition of spectra at different magnetic fields will give the chemical shift and quadrupolar interaction. For instance, ⁹³Nb ($I = 9/2$, 100%) and ¹⁹F MAS at different fields (8.4/11.7 T) and spinning frequencies up to 35 kHz were used to study K₂NbF₇, a compound where the metal atom has a heptacoordinate environment.⁷³ An irreversible phase transition near 433 K was observed, which was confirmed by synchrotron X-ray powder diffraction time-resolved experiments.

The main progresses in NMR since now more than 10 years concern NMR of quadrupolar nuclei,¹² in particular, with the MQMAS method introduced by L. Frydman and J. Harwood in 1995,⁷⁴ and subsequent

sequences like STMAS.^{75,76} MQMAS is a 2D experiment, which provides an additional isotropic dimensions to separate the inequivalent second-order inhomogeneously broadened and overlapping contributions.

A very interesting application of powder MAS and MQMAS NMR to the investigation of the high-temperature sequence of phase transitions of LiRbSO_4 appeared.⁷⁷ The central transition of ^{87}Rb was investigated within 373–488 K, where five phases separated by four phase transitions are expected. The three main phase transitions affect the EFG parameters and the spin–lattice relaxation rate, and a critical behavior was evidenced and related to a damped soft mode. The MQMAS experiment permits to separate the chemical shift contribution from the second-order-induced quadrupolar isotropic shift in a single experiment, and indicates that the evolution of the chemical shift is almost continuous. Two different rubidium sites are clearly evidenced above 438 K, while X-ray could detect them only above 457 K. MQMAS data show a similar electronic environment for these two sites.

2.6. Temperature and pressure in static and MAS probes

2.6.1. *Temperature gradients*

To obtain information on the nature and mechanism of a phase transition, a precise measurement of the NMR parameters as a function of temperature is necessary. This necessitates obviously a precise and reproducible controlling and monitoring of temperature, but most importantly a good temperature homogeneity. Obviously, temperature gradients inside the probe may broaden the transition, or the NMR lines if the NMR interactions are strongly temperature-dependent. The limitations introduced by temperature gradients in the detection of phase transitions by spin–lattice relaxation were nicely illustrated by Woessner and Snowden⁷⁸ in the study of the order–disorder weak first-order phase transition of NH_4Cl . They showed how the expected correlation time discontinuity is smeared out with a conventional static NMR probe as compared to a special probe designed to minimize temperature gradients. The authors pointed out that large temperature gradient may completely obscure the effect of the phase transition. Thus, the quantification of temperature shifts and temperature gradients by reference compounds is crucial, and is a prerequisite to any variable-temperature experiment, especially for MAS experiments that accentuate the problems.

Owing to frictional heating, the effective temperature of the MAS probe may be strongly increased since the heating is proportional to the second power of the spinning frequency.⁷⁹ For instance, a rough estimation of the

temperature increase in 4 mm Bruker MAS zirconia rotors was found to be ~ 1 K/kHz,⁷⁹ which means that several tenths of degrees of heating are not unusual. Strong temperature gradients are also observed due to differences in densities or filling distribution. If the sample transition temperature is close to the operating temperature, high-spinning frequencies may lead either to temperature or pressure-induced phase transitions. A spurious temperature induced phase transition in (–)-scopolamine derivatives was observed by ^{13}C CPMAS NMR for moderate spinning frequencies of 13.5 kHz, with a temperature increase estimated to be 18 K.⁸⁰ Inversely, the phenomenon of frictional heating was used to vary the sample temperature with a standard MAS probehead. The phase transition between phases III and IV of NH_4NO_3 occurs at 35°C, and was clearly evidenced from the manifold of spinning sidebands of ^{14}N MAS NMR by varying the spinning frequency.⁶⁷ It was also the first application of natural abundance ^{14}N MAS NMR in characterizing a solid-state phase transition.

Many methods were proposed to accurately measure temperatures inside the MAS probe as well as estimation of temperature gradients from the profile of the lineshape.^{81–84} Most of these methods use an internal reference compound to monitor temperature through the appreciable variation of the ^{207}Pb chemical shift. Recently, temperature calibration methods for spinning probes up to 35 kHz were also proposed⁸⁵ as well as for non-spinning probes.⁸⁶ Note that the most common method to control temperature of nonspinning probes uses a strong dried air (or nitrogen or argon) stream to cool or heat the sample. This method has the advantage of simplicity, but usually strong temperature gradients are observed. A more stable and precise experimental setup (but more expensive and less flexible) is to use a specially designed cryostat, which can be inserted into the magnet.⁸⁷

2.6.2. *Hydrostatic pressure cells and pressure gradients in MAS probes*

High-hydrostatic pressure is a thermodynamical parameter that changes the strength of the interactions via a modification of the intermolecular and interatomic distances.⁸⁸ Temperature/pressure-phase diagrams can be established by NMR with high-pressure NMR cells, which are unfortunately not commercial to date, and should be designed in the laboratory. Moreover, drastic safety standards should be respected because high-hydrostatic pressures are needed to observe an effect (typically 7 kbar for fluid pressure cells). A review of NMR under high-gas pressure as well as the special precautions to be taken is given in ref. 89. The description of different high-resolution NMR pressure probes at high field and other references can be found in refs. 90–93.

In MAS experiments, fast spinning also introduces a pressure gradient inside the rotor that may smear out the transitions because the phase-transition temperatures are pressure-dependent, as reflected by the dT_c/dP relationship given by the Clapeyron and Ehrenfest formula (Eq. (1)) for first-order and second-order (continuous) phase transition, respectively. Typically, the centripetal force increases the internal pressure of a material of density ρ as $\Delta P(r) \sim 2\pi^2 \rho v^2 r^2$, that is varies as the square of the spinning frequency and radius. Since new MAS probes may spin up to 35 kHz, it is important to consider an order of magnitude of the maximum pressure, which we found may attain 1 kbar. Therefore, the spinning temperature shift is expected to be nonnegligible when $|dT_c/dP| \sim 10$ K/kbar.

These orders of magnitude indicate that, in principle, the observed transition temperature as well as the width of the transition should depend on the rotor-spinning frequency. However, to my knowledge, no effects of the MAS centripetal forces on phase transitions were reported to date.

3. PHASE TRANSITIONS AND NMR: MOTIONS

Conventional X-ray diffraction measures a space and time average of the electronic density. Therefore, any dynamical disorder will be transformed into spatial disorder between positions whose probabilities are determined by the average time spent on each position. Certainly, one of the most tremendous advantages of NMR compared to X-ray diffraction is its ability to measure the occurrence of motion at different time-scales. Whether the motion correlation time is on the Larmor frequency scale, the linewidth scale or much slower (exchange NMR) will affect differently the NMR parameters like relaxation rates, apparent anisotropy and asymmetry of the interaction and 1D or 2D lineshape. With suitable sequences, the motion correlation times and site probabilities as a function of an external parameter (temperature or pressure) can be explicitly measured.

3.1. Introduction: physical content of correlation times

From the physical point of view, the motion correlation time τ_c alone carries precious informations concerning the microscopic times related to the motion as well as the activation energy, enthalpy or volume of the motion. The activation enthalpy ΔH_a (activation volume ΔV_a) is a measure of the excess enthalpy (volume) needed to enable the given motion (translation, rotation, etc.). This is an important information to be correlated to the structure, and it may give important hints to distinguish different phases as well as

mechanisms of phase transitions. From the thermodynamical point of view, at fixed temperature and pressure, the correlation time may be related to a free enthalpy of activation $\Delta G_a(T, P) = \Delta H_a - T\Delta S_a$ by

$$\tau_c = \tau_o \exp(\beta \Delta G_a) \quad (7)$$

with τ_o being a microscopic time which inverse is the attempt frequency; $\beta = 1/k_B T$ where k_B is the Boltzmann constant and T the absolute temperature. The entropic contribution is usually included in τ_o . Eq. (7) reduces to the usual Arrhenius relation when $P\Delta V_a$ is small as compared to typical activation energy E_a (as it is the case at ambient pressure and temperature where $E_a \sim 0.1-0.5$ eV and $\Delta V_a < 10^{-27} \text{ m}^3$, that is $P\Delta V_a < 10^{-3}$ eV).

Using the general thermodynamical relations expressing the enthalpy H and the volume V as a function of the free enthalpy G , $H = \partial(\beta G)/\partial\beta$ and $V = \partial G/\partial P$, one can deduce the following informations from the correlation time. At constant pressure, the slope of $\ln \tau_c$ as a function of $\beta = 1/k_B T$ is the activation enthalpy. Similarly, at constant temperature, a study as a function of pressure gives the activation volume as $\Delta V_a = k_B T \partial \ln(\tau_c)/\partial P$. A more complete discussion may be found in ref. 88.

In this section, we outline some concepts concerning the relationships between the NMR spectral and relaxation features with the magnitude of the fluctuations induced by motions as well as their correlation times. For instance, the use of proton spin-lattice relaxation time alone is sufficient to construct a T - P phase diagrams. For fast motions over different sites of different NMR frequencies, a single averaged NMR frequency is obtained, which depends on the probability of occupation of the different sites, and NMR provides methods to estimate these probabilities. Along with NMR, IQNS is also a local probe that measures proton motions, and some examples of complementarity are given with hydrogen carbonates and hydrogen sulfides compounds. Pseudocritical behaviors in the vicinity of the transition are reported in the conclusion.

3.2. Relaxation, correlation times and phase transitions

Relaxation theory describes the irreversible loss of memory of the spin system and evolution toward thermal equilibrium. In principle, one must distinguish between the relaxation of the populations (the spin-lattice relaxation T_1 for spins 1/2, but in general $2I$ different relaxation rates are necessary to describe the return of a spin I to thermodynamical equilibrium) and of the nQ coherences (the T_2 transverse relaxation time for spins 1/2). For simplicity, we use the spin 1/2 terminology as a generic terminology.

The nonsecular part of the Hamiltonian induces transitions between the energy levels of the spin system, with two effects. First, this exchange of energy with all the nonspin degrees of freedom of the compound (the so-called lattice) modifies the populations of the spin system until they reach their equilibrium values compatible with Boltzmann factors. The recovery time of the populations to their equilibrium values gives the spin–lattice relaxation times. In parallel, the coherences irreversibly decay to zero. However, in addition to the nonsecular contribution, the secular fluctuating Hamiltonian also contributes to this decay, although with no energy exchange with the lattice. The inverse of the total decay rate of the coherences is usually called the transverse relaxation time T_2 . Since relaxation is sensitive to both the magnitude and correlation time of the fluctuations, a measure of the relaxation times provides important informations on the dynamics of the system.

The theory of relaxation is complicated, and hence a rigorous analysis is out of the scope of this review. The interested readers can consult the following literature and references therein. The historical and still most popular, the so-called BPP model of the spin–lattice relaxation rate coming from the modulation of an NMR interaction by very fast motions was given by Blombergen *et al.*⁹⁴ in 1948. A pedagogical introduction to relaxation was given by Slichter,⁹⁵ and a modern introduction by Goldman.⁹⁶ Typical examples of modelization for dipolar and quadrupolar spin relaxation in solids with two- and three-site jump potentials were treated in ref. 97. In this section, we outline the information content of relaxation times, and how they may be modified by phase transitions.

Within the usual formalism of BPP relaxation theory, the relaxation rates depend on the spectral densities of the correlation function of the fluctuations of the component of the interaction tensor $\langle \delta T_\xi(t) \delta T_\xi(0) \rangle_\xi = [A + 2B\xi]^2 \langle \delta u_\xi(t) \delta u_\xi(0) \rangle_\xi$. Only the first-order contribution was kept to interpret spin–lattice relaxation in this model, which is equivalent to the hypothesis that direct relaxation processes are preponderant. The resulting relaxation rate is

$$\frac{1}{T_r} \sim [A + 2B\xi]^2 \left\langle \delta u_\xi^2 \right\rangle_\xi J_\xi(\omega_L) \quad (8)$$

with ω_L the Larmor pulsation, and the normalized spectral density $J_\xi(\omega)$ is defined by

$$J_\xi(\omega) = \int_{-\infty}^{\infty} e^{i\omega t} \frac{\langle \delta u_\xi(t) \delta u_\xi(0) \rangle_\xi}{\left\langle \delta u_\xi^2 \right\rangle_\xi} dt \quad (9)$$

Assuming an exponential correlation function $\sim \exp(-|t|/\tau_\xi)$ with correlation time τ_ξ depending on the phase, we finally obtain

$$\frac{1}{T_r} \sim [A + 2B \xi]^2 \left\langle \delta u_\xi^2 \right\rangle_\xi \frac{2\tau_\xi}{1 + (\tau_\xi \omega_L)^2} \quad (10)$$

The relaxation rate is the product of three contributions that depend on the nature of the phase. The first is the coupling strength that depends on the interaction involved (dipolar, chemical shielding, quadrupolar, etc.). The second represents the mean-squared amplitude of the fluctuations of the generalized coordinate that is modified by the motion. The product of these two contributions gives the total magnitude ΔV_ξ of the coupling of the spin system to the lattice. The third term is the normalized spectral density, which represents the available fluctuation power per unit frequency to induce the transitions. It shows that the fluctuations are the most efficient in relaxing the system when $\omega_L \tau_\xi \approx 1$, which corresponds to the minimum of T_r . When the correlation time follows an Arrhenius-like formula $\tau_\xi = \tau_o \exp E_a/kT$ (see Eq. (7)), the plot of $\log T_r$ as a function of $1/kT$ gives a characteristic U-shape, with two linear parts of slopes $\pm E_a$ (Fig. 4a). This model has the advantage of being relatively simple with two parameters, the motion correlation time τ_ξ and the strength of the fluctuations ΔV_ξ , but for only one measure, the relaxation time. However, if the minimum can be observed, ΔV_ξ can be determined. The evolution of τ_ξ as a function of temperature follows from a fit of the relaxation data at each temperature. When the minimum is not observed, one still measures the activation energy or volume. Indeed, in the fast motion limit $\omega_L \tau_\xi \ll 1$, $T_r^{-1} \sim (\Delta V_\xi)^2 \tau_\xi$ is proportional to τ_ξ and independent of frequency. On the other hand, for slow motions $\omega_L \tau_\xi \gg 1$, the spin-relaxation time becomes frequency-dependent, i.e. $T_r^{-1} \sim (\Delta V_\xi)^2 / (\tau_\xi \omega_L^2)$ and is inversely proportional to the motion correlation time. Therefore, as soon as the spin-lattice relaxation time is far from its minimum, the study of $\ln(T_1) \sim \ln(\tau_\xi)$ yields the activation enthalpy or the

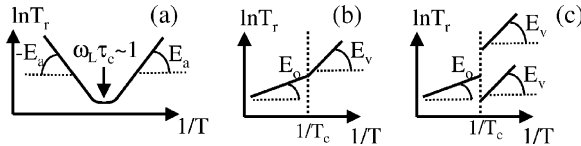


Fig. 4. Schematic of the variation of spin-relaxation time. (a) Typical behavior with no phase transition; (b) continuous-phase transition; (c) discontinuous-phase transition with a jump upward or downward depending on the jump of the magnitude of the fluctuations. In (b) and (c), it was assumed that $\omega_L \tau_\xi(T) \gg 1$ in both phases.

activation volume, the sign being determined by whether the slow or fast motion limit is used.

In the same logarithmic scale as a function of $1/T$, which gets rid of the complicated factor arising from the coupling strength, magnitude of fluctuations, attempt frequency and Larmor frequency, it is very easy to detect a phase transition by the differences in activation energies of the different phases. Schematic examples are presented in Figs. 4b and c in the slow-motion regime.

An interesting example of a T - P phase diagram obtained by proton spin-lattice relaxation at 25 MHz is NH_4I (temperature range 90–300 K and pressures up to 8 kbar).⁹⁸ At given pressure, T_1 as a function of $1/T$ presents either a large discontinuous drop or marked changes in slopes as temperature decreases, followed by a T_1 minimum. Assuming that each breaking point indicates a phase transition, the authors reconstructed the phase diagram, which was found in agreement with previously established diagrams with other experimental techniques like Raman scattering or dielectric measurements. The diagram covers the cubic CsCl-type structures II and IV, and low-temperature low-pressure tetragonal phase III with antiparallel ordering of the ammonium ions. Fitting the minimum of T_1 leads to the activation enthalpy and volume in the different phases. Surprisingly, the activation volume of phase III was found to be zero. This knowledge was used to establish the T - P phase diagram of $\text{Rb}_{1-x}(\text{NH}_4)_x\text{I}$.⁹⁹

Nevertheless, care should be taken in interpreting relaxation anomalous behavior when complex motions are suspected. An interesting example of single or double T_1 minimum was studied by A. Watton¹⁰⁰ for the motion of the tetrahedral ammonium cation NH_4^+ in the cubic phase of NH_4Cl . The importance of cross-relaxation contributions should also not be underestimate, especially when different abundant nuclei (spin $I = 1/2$ or quadrupolar nuclei) are present in the sample.¹⁰¹ Cross-relaxation between two ensembles of nuclei occurs when the splitting of the energy levels of the two systems is comparable, allowing energy transfers between them. This is the case, for instance, when the Larmor frequency of protons is equal to the quadrupole splittings of a quadrupolar nucleus, which may span a nonnegligible range due to its high sensitivity to slight disorders. In general, the recovery curves for spins $I = 1/2$ become nonexponential in the presence of cross-relaxation. On the other hand, strongly nonexponential recovery curves are also the result of broad distributions of correlation times like in glasses, which yield stretched-exponential recovery curves $\sim [1 - \exp(-(t/T_1)^\alpha)]$ with a shape parameter $\alpha < 1$.^{102,103} An interesting interpretation of the observed evolution of the exponent α with temperature at the ferroelastic phase transition of thallium dihydrogen arsenate TlH_2AsO_4 was proposed in terms of both cross-relaxation and distribution of correlation times due to microdomains.^{104,105}

3.3. Lineshape and motion

When the characteristic frequencies of the motions modulating the interaction are of the same order of magnitude as the frequency strength of the interactions themselves, then the lineshape is drastically distorted by motional narrowing. Typically for a stochastic Gaussian process of correlation time τ_c , the lineshape in the adiabatic approximation is Gaussian with second moment without motion M_{20} when $\tau_c\sqrt{M_{20}} \gg 1$, and Lorentzian when $\tau_c\sqrt{M_{20}} \ll 1$ with a transverse relaxation time $1/T_2 \sim M_{20}\tau_c$. This gives the opportunity to estimate correlation times and exchange constants that are on the static linewidth time-scale as well as structural data.

It is important to recognize that the second moment or full linewidth at half height (FWHH) measured at different temperatures (or other different external intensive parameters) can only be quantitatively compared within each other when the lineshapes do not change. By no modification is meant that the function describing the lineshape remains the same at all temperatures but with different scaling parameters (for instance, $g(\omega/\sqrt{M_2(T)})$). For instance, when the lineshape remains Gaussian at all temperatures, the FWHH $\Delta v_{1/2} = 2\sqrt{\log 2 M_2}$ probes modifications of the second moment resulting from changes in structure and molecular dynamics. But if the lineshape becomes Lorentzian, $\Delta v_{1/2} = 2M_2\tau_c$ depends on both the second moment and the motion correlation time τ_c , and carries obviously different informations. For nondipolar interactions, the influence of the lineshape is even more important, and great care should be taken in comparing linewidth at half height.

The second-moment analysis method has the advantage to give informations about structure and dynamics without relying on any fine details of the lineshape, and was historically developed to study dipolar broadened lines. It usually connotes old fashion NMR, but it is still (since the very beginning of NMR) and will remain in the future an irreplaceable source of information concerning structure and slow molecular motions (see Section 4.2 for an application to ferroelectrics). The power of this method relies on the fact that the second moment M_2 can be calculated from an exact theoretical formula, the celebrated Van Vleck's formula¹⁰⁶ derived from first-principle physics (quantum and statistical physics) from the knowledge of all the atomic coordinates of the nuclei that carry spins, allowing comparison between NMR experiment and structural data (X-ray or neutron diffraction) or estimation of structural data (bond length, angles, etc.) from NMR lineshape analysis. Calculations of the second moment are greatly simplified because it is an additive quantity. All the basis of second-moment calculations for dipolar interaction are described in the books of Abragam¹⁰⁷ and Slichter,⁹⁵ methods for efficient computer implementation were developed by R. Goc.^{108,109}

The reduction of the second moment by motions occurring on the static linewidth time-scale can be used to measure a corresponding correlation time. The integration of the spectral density gives the following interpolation formula between the static M_{20} and motionally averaged $M_{2\infty}$ second moments expressed in angular units ((rad/s)²):

$$M_2(\tau_c) = M_{20} + (M_{2\infty} - M_{20}) \frac{2}{\pi} \arctan\left(\alpha \sqrt{M_{20} \tau_c}\right), \quad (11)$$

with α a constant of the order of unity. A nonlinear least-squares fit of $M_2(\tau_c(T))$ with Eq. (11) yields the activation enthalpy.

For fast molecular motions, $M_{2\infty} = RM_{20}$ with a reduction factor R that can be calculated from suitable models.^{110,111} The most useful reduction factor is given for rotations of symmetry C_n with $n \geq 3$, where $R = (3 \cos^2 \beta - 1)/2$ with β the angle between the rotation axis and the internuclear vector. Using the rigid values (which give an upper bounds of the second moment), different motional models may be used to estimate the second-moment reduction for fast motion ($\tau_c \sqrt{M_2} \ll 1$), and compared to experimental data. This approach was fruitful since the first beginning of NMR. Different combinations of more or less complex internal motions may lead to comparable agreement with the experimental data, as discussed, for example, in the case of $(\text{CH}_3)_3\text{NBH}_3$.¹¹² Only physical arguments brought by complementary techniques like IQNS, or the philosophical choice that the simplest model is the better, may help in deciding which model is the most suitable.

In the more general cases where chemical shielding and quadrupolar interaction are preponderant over dipolar interaction, the powder (or single crystal) lineshape is more structured. Under static or MAS conditions, different formalisms were developed to simulate the lineshape in the intermediate motional regime in order to extract kinetic constants and correlation times,¹¹³ for the satellite and central transition of half-integer quadrupole nuclei in nonrotating or rotating (MAS) samples.^{114,115} The necessity to include motion in powder patterns simulations of static or MAS spectra was illustrated by Kristensen and Farnan¹¹⁴ in the case of ^{17}O MAS studies of the polymorphism of the silicate (SiO_2) mineral cristobalite. The low-temperature α to the high-temperature polymorph β interconversion occurs at a transition temperature that is typically in the range 493–543 K. This $\alpha \leftrightarrow \beta$ interconversion is reversible since it involves only small rotation of SiO_4 tetrahedra. In the β phase, the oxygen atoms are disordered over six to 12 sites on a circle orthogonal to the Si–Si axis. A careful study of spin echo and MAS ^{17}O spectra as a function of temperature was performed by the authors, using simulations of the ^{17}O central transition that take into account the EFG and chemical shielding interaction, and oxygen motion over

six sites for the first time. The authors showed in a convincing manner that the modifications in the quadrupolar parameters observed at the transition are not a consequence of motional averaging, and that the motion of the oxygen atoms is not significantly modified by the phase transition. The authors concluded that β cristobalite is not an average of α -cristobalite domains, and that the $\alpha \leftrightarrow \beta$ interconversion is related to an increase of the Si–O–Si bond angle.

3.4. Mean interaction tensor in the fast-motion regime

When the correlation time that modulates the NMR frequencies is much smaller than the dispersion of the frequencies without motion, the multi-component structure collapses into a single line at averaged frequency $\langle \nu \rangle$. When the motion occurs between well-defined sites with occupation probabilities p_α ($\sum_\alpha p_\alpha = 1$) and NMR frequencies ν_α , then the averaged frequency is $\langle \nu \rangle = \sum_\alpha p_\alpha \nu_\alpha$. The advantage of such a formulation in terms of averaged frequencies is that it is always valid. On the other hand, a recalculation is necessary for each magnetic field direction and the underlying symmetries are hidden.

For first-order perturbation of the Zeeman Hamiltonian, it can be proved that fast motion leads to an averaged tensor $\langle \mathbb{T} \rangle = \sum_\alpha p_\alpha \mathbb{T}_\alpha$, which can be characterized by its effective anisotropy δ_a and asymmetry η_a parameters, as well as its principal axes of the averaged tensor, as a function of the probabilities p_α . Then the averaged frequency can be easily calculated for every sample orientation in the laboratory frame, or the shape of the powder sample directly predicted from the values of δ_a and asymmetry η_a . This approach is particularly relevant for symmetry-related sites: the interaction tensors have equal eigenvalues (that is identical t_{iso} , δ and η), but differ by the relative orientation of their principal axes. In that case, the symmetry of the motion also imposes constraints on the averaged tensor $\langle T \rangle$, and the rules of Table 1 are valid. For instance, a motion of symmetry C_n with $n \geq 3$ always gives a zero-effective asymmetry $\eta_a = 0$, the PAS of the averaged tensor has one axis along the symmetry axis and the other two perpendicular to this axis. On the other hand, an asymmetric motion, even between sites with original tensors of zero asymmetry $\eta = 0$, may lead to a nonzero asymmetry parameter $\eta_a \neq 0$. It is important to note that the second-order quadrupolar broadened central transition of a half-integer spin in the fast-motion regime cannot be represented by an average interaction tensor.¹¹⁴

With appropriate hypothesis and simplifications (symmetry, previous structural knowledge from other techniques, etc.) the probabilities of occupation $\{p_\alpha\}$ may be deduced from the spectra as a function of temperature.

The probabilities are related to the site enthalpy $H_{\alpha a}$ and entropy S_{α} by

$$p_{\alpha} = Z^{-1} \exp(k_B S_{\alpha} - \beta H_{\alpha}), \quad Z = \sum_{\alpha} p_{\alpha}. \quad (12)$$

where Z is the normalization constant and $\beta = 1/k_B T$. The entropic contribution is necessary for degenerated sites. In practice, whether this contribution is important or not may be seen from the behavior at very high temperatures ($\beta \rightarrow 0$). For N sites of multiplicity 1, the probability of occupation of each site becomes $p_{\alpha} \rightarrow 1/N$. Any deviation from this limit behavior is a sign of degenerated sites.

Once the probabilities are known, other physical quantities, which are function of the occupation probabilities, can be calculated from $\langle A \rangle = \sum_{\alpha} p_{\alpha} A_{\alpha}$, or order parameters for order–disorder phase transitions. Different examples will appear in the following. For instance, the orientational contribution to the absolute polarization of the ferroelectric compound pyridinium tetrafluoroborate was estimated from ^2H NMR temperature-dependent measurements on the perdeuterated pyridinium cations.¹¹⁶ The pyridinium cation evolves around a pseudo C_6 axis, and the occupation probabilities of the different potential wells were deduced from the study of ^2H NMR powder spectra at different temperatures. The same orientational probabilities can be used to estimate the thermodynamical properties, which depend on the orientational order of the cation. Using a generalized van't Hoff relationship, the orientational enthalpy changes were calculated and compared with differential scanning calorimetry (DSC) measurements.¹¹⁶

3.5. Incoherent quasielastic neutron scattering and NMR

IQNS is another local probe, but in the reciprocal space.¹¹⁷ In general, the incoherent cross-section of hydrogens dominates all the others, and the incoherent scattering function $S_{\text{inc}}(Q, \omega)$ carries information on the hydrogen space and time trajectory

$$S_{\text{inc}}(Q, \omega) \sim E(Q) \delta(\omega) + [1 - E(Q)] L(\tau, \omega), \quad (13)$$

where the Debye–Waller factors, inelastic contributions and convolution with the apparatus resolution have been omitted. The elastic contribution (elastic incoherent scattering factor as EISF) $E(Q) = |\langle \exp(iQr) \rangle|^2$ is the square modulus of the spatial Fourier transform of the proton trajectory. The inelastic contribution $L(\tau, \omega)$ is generally a sum of Lorentzians, whose width reflects the correlation times and the geometry of the motion (Fig. 5).

How NMR, IQNS and MD provide complementary informations on molecular motions was presented, for instance, in ref. 118. It is usually

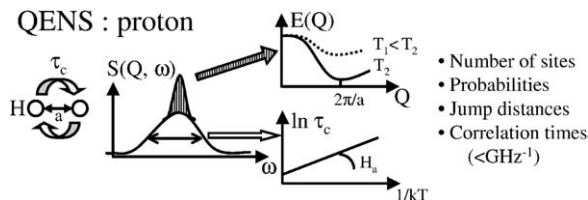


Fig. 5. Schematic of IQNS results with the elastic and quasielastic incoherent scattering of protons. Elastic scattering gives the geometry of the motion, while quasielastic scattering contains informations on the correlation times.

found that NMR is less sensitive to details of the potential shape than IQNS.¹¹⁹ In contrast to NMR, IQNS is able to measure jump distances, the number of sites and their geometry by direct comparison with models, provided the number of sites is small. This information can be subsequently injected into NMR models to fit relaxation or lineshape features. In principle, the local potential governing the molecular motion should be considered as consistent if it can model NMR and IQNS data simultaneously.

The importance of IQNS, X-ray and NMR to study proton dynamics and quantum effects in hydrogen-bonded system was discussed by F. Fillaux.¹²⁰ A number of zero-dimensional hydrogen-bonded systems are arranged as hydrogen-bonded dimers. The stochastic concerted jump of the protons (or deuterons) of the hydrogen bonds (HBs) between the two minima of an asymmetric or symmetric double-minimum potential mediates the conversion between two tautomers, which modulates the atomic positions and the NMR interactions. The formalism of two-site stochastic jump is therefore very useful, and can be equally applied to analyze the typical behavior of NMR-relaxation times or lineshapes, depending on the probed time-scales (an example is the ^2H spin-lattice relaxation anisotropy in solid tropolone $\text{C}_7\text{O}_2\text{H}_6$ ¹²¹) as well as quasielastic neutron scattering (for instance, IQNS and relaxometry study of benzoic acids¹²²).

In general, IQNS data are used to infer the geometry of the molecular motion, which can be used as a starting information to modelize NMR features. An example of application and complementarity of NMR and IQNS to phase transitions of potassium and rubidium hydrogen carbonates is presented below. The second example treats the order-disorder phase transitions in hydrogen sulfides.

3.5.1. Hydrogen carbonate family XHCO_3

The hydrogen carbonate XHCO_3 family with $\text{X} = \text{Na}, \text{K}, \text{Rb}, \text{Cs}$ is interesting in the context of both supramolecular engineering and HB studies, because it gives a series of ionic compounds with hydrogen-bonded dimers

(the dianions $(\text{HCO}_3^-)_2$ form centro-symmetric dimers linked by two adjacent HBs) with the notable exception of NaHCO_3 , which forms infinite chains of HBs. Some of these compounds are known to undergo different phase transitions as a function of temperature, stress or hydrostatic pressure. Thus, hydrogen carbonates give the opportunity to analyze in detail the competition between ionic and hydrogen bonding, the structure and dynamics of HBs as well as phase transitions connected to hydrogen disorder. This family is also well suited for NMR studies because all nuclei except oxygen (if not enriched in ^{17}O) can be studied with reasonable sensitivity.

Among the AHCO_3 compounds, only potassium hydrogen carbonate KHCO_3 was systematically studied as a function of temperature. In the high-temperature phase with one dimer per unit cell, the protons are dynamically disordered in a symmetric double-minimum potential. A nonferroic structural phase transition occurs at $T_c = 318\text{ K}$, and the unit cell is doubled with two inequivalent dimers. Incoherent neutron scattering experiments¹²³ proved that the double-well potential associated to the two dynamically disordered tautomers becomes asymmetric in the low-temperature phase. This phase transition has thus an order-disorder character, and can be described by an order parameter $\Delta p = p_1 - p_2$, which measures the difference of occupation probabilities of the two sites.

The proton and potassium spin-lattice relaxation curves as a function of temperature have a pronounced dip at the transition, indicating a critical behavior.¹²⁴ A study of the powder static and MAS ^{13}C and ^{39}K lineshapes as a function of temperature in the range $200 \leq T \leq 340\text{ K}$ was also performed.¹²⁵ It was shown that the evolution of the different NMR parameters (CSA and EFG eigenvalues) during the phase transition of KHCO_3 could be completely rationalized with a two-site jump model whose occupation probabilities are governed by the order parameter Δp as measured by incoherent neutron scattering experiments. In particular, by revisiting the two-site jump model, a method of correlation of NMR data with results from other local probes was proposed to obtain the static eigenvalues of the interaction tensor, the jump angle as well as some geometric indications. In contrast to KHCO_3 , rubidium hydrogen carbonate (RbHCO_3) was almost not studied. The existence of two monoclinic phases of RbHCO_3 with an estimated temperature of transition near -3°C was reported, but the nature of the low-temperature phase was not clearly established. However, a detailed comparison of the room temperature structure of RbHCO_3 and high-temperature phase of KHCO_3 proves that both structures are isomorphic,¹²⁶ raising the question of the similarities in phase transitions of RbHCO_3 and KHCO_3 . In fact, two results support this parallelly, at least from the local point of view probed by the NMR technique. First, variable

temperature ^{13}C data showed that the evolution of the carbon CSA tensor in RbHCO_3 was exactly reproduced by using the same parameters as for KHCO_3 if the shift of the transition temperatures is taken into account. Second, the EFG values at the ^{87}Rb site also compares well with the values at the ^{39}K site.¹²⁶

3.5.2. Hydrogen sulfides of alkali metals $\text{M}^+(\text{HS}^-)$

The polymorphism of hydrogen sulfides of alkali metals $\text{M}^+(\text{HS}^-)$ with $\text{M} = \text{Na}, \text{K}, \text{Rb}, \text{Cs}$ was studied with neutron and X-ray diffraction, quasi-elastic neutron scattering, DSC and proton NMR. These compounds have three polymorphs and two known phase transitions. When $\text{M} = \text{Na}, \text{K}, \text{Rb}$, the LTP is monoclinic, the medium-temperature phase (MTP) is rhombohedral and the HTP is cubic with a NaCl-type structure. Owing to the fact that the sequence of phase transitions is the same for the three cations, this series is expected to be a model where coulombic interaction is modulated by the cation radii, which increases in the order Na, K, Rb, Cs.

But differences in the phase transition mechanisms between NaHS on the one hand, and KHS or RbHS on the other are indicated by the IR and Raman spectroscopy. The hypothetical order relationship related to cation radii is already broken by the transition temperatures between the $\text{HTP} \leftrightarrow \text{MTP}$, which is lower ($\sim 360\text{ K}$) for the smallest cation, sodium than for larger cations K ($\sim 420\text{ K}$) and Rb ($\sim 410\text{ K}$). The IQNS mainly measures the HS^- reorientation because of the preponderant proton incoherent scattering cross-section. The IQNS data were performed with a typical resolution of $\sim 25\text{ GHz}$, and were best fitted with a two-site jump model in the MTP and an eight-site jump model in the HTP.¹²⁷ The extracted correlation times for the three compounds drop by roughly one order of magnitude on increasing temperature at the $\text{MTP} \leftrightarrow \text{HTP}$ transition, indicating a first-order phase transition (Fig. 6). But no indication on differences on the

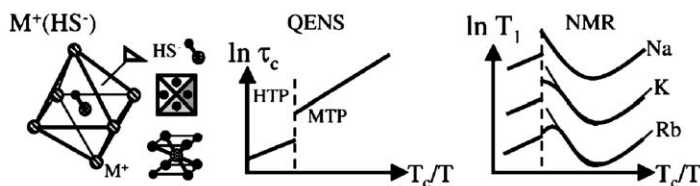


Fig. 6. Schematic of IQNS and NMR studies of MHS compounds. From left to right: schematic of the close environment of the HS^- anion. The EISF shows that the orientation occurs within eight sites in the HTP and two sites in the MTP. The correlation time is discontinuous at the transition. Schematic variation of the proton spin-lattice relaxation. The thick lines sketch data and thin lines fits.

mechanism could be drawn from the IQNS data, and proton NMR experiments were carried out to probe the dynamics at a different time-scale. The three compounds were studied by proton NMR at 400 MHz over the temperature range of 180–560 K, which covers the HTP \leftrightarrow MTP transition for all of them, and additional experiments on lower temperature and frequency were performed on KHS.¹²⁸ Although the second moment has been considered, we only discuss here the behavior of the spin–lattice-relaxation time T_1 as a function of $1/T$. Starting from the HTP and decreasing temperature, T_1 is a linear increasing function of $1/T$ followed by a discontinuity at the transition temperature HTP \leftrightarrow MTP to a higher T_1 value. This discontinuity increases T_1 by a factor of ~ 5 for Na, by a factor ~ 1.5 for K and almost cannot be distinguished for Rb that displays a quasi-continuous T_1 . In the MTP and continuing decreasing temperature, T_1 decreases to a minimum and increases again for all three compounds. Using the 180° -rotation model of the HS^- used to interpret IQNS data in the MTP yields calculated T_1 values, which agree well with the experimental data for temperature lower than 360 K, and the attempt frequency and activation enthalpy determined from the fits compare well with the corresponding IQNS values. In particular, the activation enthalpy decreases as the cation radii increases, which was interpreted as a reduction of coulombic interactions by larger distances that softens the coordination potential. For temperature higher than 360 K and in the vicinity of the transition temperature, the shape of T_1 as a function of temperature differs substantially for the three compounds. In particular, the range of validity of the 180° -rotation model covers all the MTP phase for Na but not for K and Rb. Such a deviation occurs when different motion models or relaxation mechanisms become activated. New relaxation mechanisms are necessary to explain the HTP behavior where T_1 increases as $1/T$ increases, and the increase in T_1 at the transition. As in the MTP the relaxation is in the fast motion limit $T_1 \sim 1/\tau_c$, but since IQNS observe a decrease of τ_c at the transition MTP \rightarrow HTP, T_1 should increase though a decrease is measured by NMR. Diffusion of the anion or cation was proposed as the new relaxation mechanism, which onsets in the MTP of KHS and RbHS would explain the difference in the mechanism of phase transitions.

The case of CsHS and CsHD, which are related to the CsCl-type structure, was studied by the same authors but will not be considered here.¹²⁹

3.6. Conclusion: pseudocritical features near a transition

In the two previous sections, it was shown how the normal mean behavior of each phase can be used to characterize phase transitions from the NMR

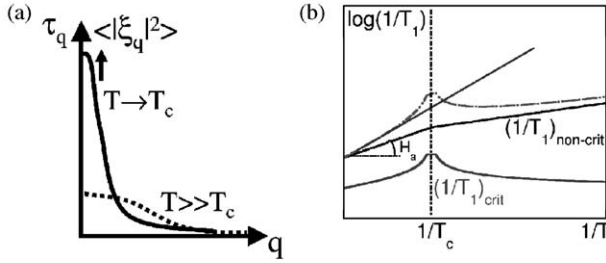


Fig. 7. (a) Schematic of the evolution of τ_q or $\langle |\xi_q|^2 \rangle$ as a function of q for two different temperatures. A divergence occurs at $q \rightarrow 0$ and $T \rightarrow T_c$, corresponding to critical slowing down and enhanced fluctuations, respectively. (b) Critical and noncritical contributions to the total relaxation rate. Vertical scale is logarithmic. If the critical contribution is not taken into account, the apparent activation enthalpy is over or underestimated (H_x is the true activation enthalpy of HTP).

lineshape or relaxation times, but we did not consider the *critical collective* effects coming from the enhanced fluctuations, critical slowing down and increasing correlation lengths on approaching a phase transition.

On approaching the transition point of a continuous-phase transition, a critical slowing down of the fluctuations occurs ($\tau_q \sim [a(T - T_c) + Dq^2]^{-1}$) and the amplitudes of the fluctuations increase ($\langle |\xi_q|^2 \rangle \sim [a(T - T_c) + Dq^2]^{-1}$) at wave vector q (Fig. 7a). It can be proved that apparent pseudodivergences of the relaxation rate $(1/T_r)_c \sim (T - T_c)^{-\gamma}$ (with $\gamma = 1/2$ in mean field theories) can be observed near a phase transition if $\tau_q \omega_p \ll 1$ where ω_p is the probing frequency.^{18–21,130,131} In that case, the associated spectral density $J_c(\omega_p) \sim J_c(0) \sim \sum_q \langle |\xi_q|^2 \rangle \tau_q$ increases pseudocritically on approaching the phase transition, thereby strongly increasing the corresponding relaxation rate. An example comes from the order–disorder phase transition of NH_4Cl . The structure is cubic of Cs–Cl type, with the N–H bonds of the NH_4 tetrahedra pointing toward four of the eight chlorine anions, with two possible orientations. In the HT, the NH_4 tetrahedra occupy the two orientations with equal probabilities. NMR or IQNS showed that the disorder is dynamical. Lowering the temperature below ~ 243 K yields a weak first-order phase transition to a cubic structure with NH_4 tetrahedra ordered with the same orientation within cells. A subtle anomaly of the proton spin–lattice relaxation was measured by Woessner and Snowden⁷⁸ at 9.5 and 25 MHz in the vicinity of T_c , but no critical behavior was evidenced.^{132,133} However, recently, Lee *et al.*¹³⁴ observed a critical behavior on the proton second moment and solid echo decay rate, manifested by a sharp increase in the values of M_2 and $1/T_2$ on approaching T_c from both sides. The pseudodivergence was fitted with a three-dimensional Ising model.

The total relaxation rate being the sum of the normal “non-critical behavior” (subscript nc) and “critical behavior” $1/T_r = (1/T_r)_{nc} + (1/T_r)_c$, the critical behavior is manifested by a pseudodivergence at the transition (Fig. 7b). It is important to keep in mind this possibility when extracting activation enthalpies from the slope of $\ln(1/T_r)$ as a function of $1/T$. As shown in Fig. 7b, the critical rate contains an almost linear contribution that cannot be easily distinguished from the true linear contribution of the non-critical rate, leading to a false value of the activation enthalpy. Therefore, a special attention is necessary to treat the data near a phase transition when critical fluctuations are suspected.

In recent years, the number of publications treating pretransitional and critical effects in solid–solid classical structural phase transitions is very small. For instance, critical behaviors were observed with proton NMR in decylammonium chloride ($C_{10}H_{21}NH_3Cl$)^{135–137} and T_1 and T_2 of squaric acid.¹³⁸ Relaxation of ^{87}Rb in $LiRbSO_4$ appeared also critical.⁷⁷ One of the reasons is certainly that critical behavior is usually not observed at discontinuous-phase transitions, which is the most common situation in solid–solid structural phase transition. Another reason may also be that such observations, however spectacular they can be, are very difficult to interpret and are usually poor in information content because they occur in the close vicinity of the transition. The current trend in the study of phase transitions by NMR favors a pragmatic approach, which consists in detecting an anomalous behavior of the NMR features (peak position and multiplicity, linewidth, relaxation), and to extract physical parameters like strength of the NMR interaction, activation energies or correlation times that can be correlated to the structure or atomic or molecular dynamics. This approach is reviewed in the following section.

4. FERROELECTRIC PHASE TRANSITIONS, H-BONDED SYSTEMS

A ferroelectric phase transition is defined by the appearance of a spontaneous polarization component. At the paraelectric–ferroelectric transition, the most remarkable anomaly is an abrupt increase in the dielectric constant in the vicinity of the phase-transition temperature.

4.1. Introduction: mechanisms of ferroelectricity

Ferroelectric behavior can be obtained by two mechanisms via the relative displacement of the anion and cation sublattices against each other (classical

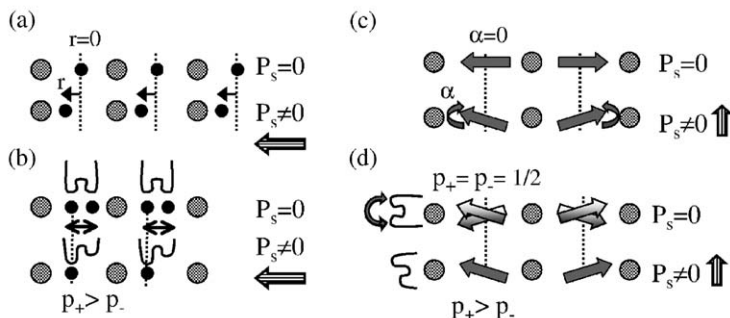


Fig. 8. Simple model of order–disorder or displacive ferroelectric phase transition. Left, ferroelectricity by relative displacement of the anion and cation sublattices: (a) displacive model, where $r = 0$ in the HTP and the atoms are translated by $r \neq 0$ in the LTP. The order parameter is r . (b) Order–disorder model: in the high-temperature phase, the ions are symmetrically disordered with equal probabilities $p_+ = p_- = 1/2$ over two positions $r = \pm r_0$. In the low-temperature phase, the occupancies of the sites become unequal with probabilities $p_- \neq p_+$. The order parameter is the difference $\Delta p = p_+ - p_-$. The spontaneous polarization $P_s \propto r$ and $P_s \propto \Delta p$ for the displacive model and order–disorder model, respectively. Right, ferroelectricity by alignment of molecular dipoles: (c) displacive model: in the HTP, all the molecules are aligned with $\alpha = 0$; in the LTP, the molecules are rotated around the center of inversion with angles $\pm \alpha \neq 0$, the order parameter is α . (d) Order–disorder model. The spontaneous polarization $P_s \propto \alpha$ and $P_s \propto \Delta p$ for the displacive model and order–disorder model, respectively.

ferroelectric mechanism), and/or by the ordering of the different electric dipole moments carried by the ions or molecules. A very simple pedagogical model may exemplify the differences between the two mechanisms as well as the distinction between pure order–disorder or displacive phase transitions (Fig. 8). For the order–disorder type (Fig. 8b, d), the high-temperature phase is the average between two configurations of equal probabilities, here corresponding to two defined atomic positions or molecular orientations. The low-temperature positions or orientations, which already exist in the HTP, become inequivalent in the LTP by a change in their relative probabilities. Thus, the order parameter is of probabilistic nature, and is the difference between the probabilities of occupation of both sites $\Delta p = p_+ - p_-$. Because of the static or dynamical average, the molecules may have a symmetry lower than the apparent HT mean site symmetry, but the molecular symmetry (and structure) is conserved through the phase transition. The large positional or orientational disorder may appear in anomalously large temperature factors in X-ray diffraction experiments.

In contrast, displacive phase transitions (Fig. 8a, b) involve small motions of atoms or molecules to new positions to change the symmetry of the

crystal structure. In the HTP the molecules, which are perfectly centered at site of given symmetry, should have a symmetry compatible with the site symmetry, and only small and fast nonsymmetry-breaking fluctuations around the equilibrium position are allowed. In the LTP, the molecules are translated (by $r \neq 0$) or rotated by angle $\pm \alpha \neq 0$, which may serve as an order parameter. On lowering the site symmetry by the phase transition, the molecule should also change its symmetry to cope with the new symmetry, which induces molecular distortions.

The distinctions between these two pure types may also be viewed from entropic considerations and the nature of the driving mode. The entropic change in an order–disorder phase transition is mainly configurational, and the driving mode is of diffusive (nonpropagating) nature. On the contrary, for a displacive phase transition, the entropy change is mainly vibrational, with an associated underdamped soft phonon.

Barium titanate BaTiO_3 is usually considered as the prototype of compounds having a purely displacive ferroelectric phase transition, which exhibits a soft mode describable by an anharmonic phonon. The nonferroelectric compound NH_4Cl is another example of compound with pure order–disorder phase transition, with two phases that differ from the ordering of the ammonium (NH_4^+) cation in the unit cell.

A large class of ferroelectric materials is hydrogen-bonded insulating crystals, with a large variety of H-bond networks. The dimensionality of the H-bond network can be zero-dimensional (0D) when isolated dimers exist ($\text{K}_3\text{H}(\text{SO}_4)_2$ with $\text{SO}_4\text{--H}\cdots\text{O}_4\text{S}$ dimers, KHCO_3 with $\text{CO}_3\text{--H}\cdots\text{H--O}_3\text{C}$ dimers, etc.), 1D for chains (CHSO_4 , NaHCO_3 , etc.), 2D when the H-bonded units extant in sheets (squaric acid) (Fig. 9) and 3D (KH_2PO_4 (KD-P)...). For instance, in H-bonded ferroelectrics like KH_2PO_4 , the key role in the build up of ferroelectricity is played by the ordering of the protons in double-well potentials within the HBs $\text{O--H}\cdots\text{O}$. The transition temperature may shift by several tens of degrees when the hydrogens are substituted by

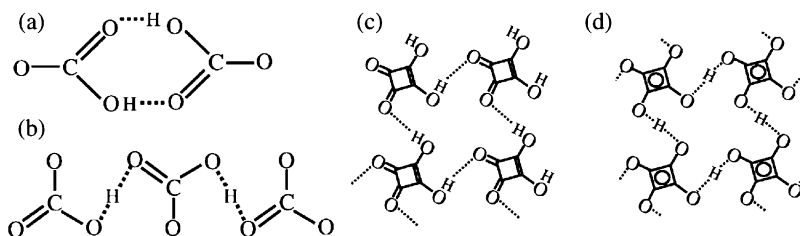


Fig. 9. Schematic of H-bond systems. (a) 0D H bonds in dimers of KHCO_3 ; (b) 1D H bonds in NaHCO_3 ; (c) 2D H bonds in SQA for the ferroelectric; (d) and paraelectric phases.

deuterium. The connectivity of the H bonds that connect different structural elements, the ordering and dynamics of the H-bonded protons, possibly coupled to the more heavy units motion is of crucial importance in determining the physical properties of the material. Isotopic effects upon isotope substitution of hydrogen by deuterium are usually observed on the phase-transition temperature.

Therefore, understanding the detailed dynamics and ordering of the anions and cations is a necessary step in the comprehension of ferroelectric phase transitions. Historically, proton absorption line second-moment and spin–lattice relaxation as well as ^2H NMR were the preponderant methods to study molecular dynamics and ordering of H-bonded systems. But other quadrupolar nuclei also bring a wealth of information.

The first illustration is provided by ferroelectrics belonging to the family of pyridinium salts. Complex interplay between the contributions of van der Waals, Coulomb, dipolar and hydrogen-bonding interactions are expected because of the hybrid nature of the compound. The majority of reported NMR experiments are proton second-moment and relaxation studies on polycrystalline samples. The most sophisticated NMR methods with regard to resolution, symmetry and time-scale interpretations applied to the historical problem of assigning a pure order–disorder or displacive mechanism to a ferroelectric phase transition will provide the second example with the study of squaric acids and perovskites compounds like BaTiO_3 .

4.2. Hybrid organic–inorganic compounds

A novel class of hybrid organic–inorganic ferroelectric molecular ionic compounds based on pyridinium salts was discovered in the 1990s.¹³⁹ The pyridinium salt compounds $(\text{C}_5\text{H}_5\text{NH})^+ \text{A}^-$ (denoted PyA) with A^- a monovalent anion present antiferroelectric or ferroelectric phase transitions depending on the nature of the anion. These compounds were classified as a function of the number of phase transitions,¹⁴⁰ and of the parent paraelectric phase. For pyridinium chloride, bromide, iodide and hexafluorophosphate $\text{A} = \text{Cl}, \text{Br}, \text{I}, \text{PF}_6$, only one phase transition of paraelectric–antiferroelectric nature was detected. When the anion is a tetrahedral unit BF_4 , ClO_4 , ReO_4 , IO_4 or a pseudo-tetrahedral unit FSO_3 , PyFCrO_3 , the pyridinium tetrafluoroborate, perchlorate, perrhenate, periodate, fluorosulfonate and fluorochromate exhibit two or three phase transitions, and ferroelectric properties arise. Some properties are summarized in Table 2. As can be seen, the parent prototype paraelectric phase I have either a trigonal or an orthorhombic symmetry. The pyridinium cations are parallel to each other in the crystal lattice. For the trigonal $\text{R}\bar{3}\text{m}$ structure, the Py are

Table 2. Some properties of the pyridinium salts

Compound	NT	$T_{I \leftrightarrow II}$ (K)	Order	Phase I	dT/dP	Reference
PyCl	1	350	1	$R\bar{3}m$		
PyBr	1	270	1	$R\bar{3}m$	> 0, CC	141
PyI	1	250	1	$R\bar{3}m$	> 0, CC	142,141
PyPF ₆ [−]	1	210	1	$R\bar{3}m$	> 0, CC	143
PyBF ₄	2	238	2	$R\bar{3}m$	> 0, E	116,144,145
PyClO ₄	2–3?	245	1	$R3m$		146,147
PyReO ₄	2	336	2	$Cmcm$	< 0, E	148–150
PyIO ₄	2	323	2	$Cmcm$		140
PyFSO ₃	3	282	1	$R\bar{3}m$		151
PyFCrO ₃	2	258	1	$Cmcm$		152

Note: For type I, the transition is paraelectric–antiferroelectric. For type II or III, only the paraelectric(I)/ferroelectric phase transitions are considered. Abbreviations are: NT, number of phase transitions; CC or E means that dT/dP obeys Clausius–Clapeyron or Erhenfest relationships, respectively.

perpendicular to the C_3 symmetry axes along the body diagonal of the rhombohedral unit cell, with the anion at the center of the cell. For the six compounds enumerated below of type 2 or 3, phase II is ferroelectric. Extensive studies by X-ray, DSC, differential thermal analysis (DTA), dilatometry, dielectric and NMR measurements as a function of temperature and hydrostatic pressure of the pyridinium salts family have been reported to understand the factors governing the nature of the phase transitions. Among the different possible factors, the contribution of the alignment of the permanent dipole of the pyridinium cations to the ferroelectric polarization, the positional or orientational order of the anionic sublattice, the polarization of the respective sublattices and the role of the network of HBs that reinforce the structure are of crucial importance. Mixed order–disorder and displacive mechanisms were also suggested. In addition to temperature, hydrostatic pressure is an important parameter because it decreases all the intramolecular distances, thereby modifying the coulombic and van der Waals intermolecular interactions. High pressure should thus significantly change the shape of the potential wells into which pyridinium cations re-orient. Thus, the most obvious incentive to use ¹H NMR of polycrystalline samples is that the proton mainly probes the pyridinium orientational disorder and dynamics.

Although the simple pyridinium salts $A = Cl, Br, I, PF_6$ are of type 1 and antiferroelectric, similarities in structure with other ferroelectric members of the family motivated studies of their phase behavior with the hope to precise

the ferroelectric mechanism by comparison. From ^1H and ^{19}F second-moment and spin-lattice relaxation data,^{142,143} and symmetry considerations, the motion of the pyridinium cation $(\text{C}_5\text{H}_5\text{NH})^+$ was modeled by reorientations around the pseudohexad C_6 axis perpendicular to the ring plane. In paraelectric phase I, the sixfold potential has symmetric wells of equal depths, in agreement with entropy measurements.¹⁴¹ Upon decreasing temperature, the ordering of the cation with antiparallel dipole moments breaks the high-temperature symmetry, and results in asymmetric wells of unequal depths in the low-temperature phases. For instance, the hexafluorophosphate ($\text{A} = \text{PF}_6$) data could be interpreted with an asymmetry varying linearly with temperature. The second moment was found to be a continuously decreasing function of temperature for $T < T_{\text{I-II}}$. When $T > T_{\text{I-II}}$, M_2 is constant at the fast-motion value. No apparent anomaly of the relaxation times at the transition temperature appears. An interesting comparison between correlation times measured by dielectric, quasielastic neutron scattering (IQNS) and proton relaxation time (spin-lattice and rotating frame relaxation) was presented in ref. 143. In particular, dielectric and NMR correlation time showed excellent agreement.

The T - P phase diagrams of PyI and PyBr were constructed from the influence of high-hydrostatic pressure up to 7 kbar by dielectric, dilatometric and DTA experiments.^{141,142} For both compounds, the transition line follows $dT/dP > 0$. The authors stressed the similarity of this behavior with the observed inverse correlation between the transition temperature and the anion radii, the transition temperatures being a decreasing function of the anion radius. Like high-hydrostatic pressures that shrink the material, reducing the anion radius brings closer the pyridinium sheets, which results in an increased cost to order the cation with antiparallel dipoles. Analysis of the ^1H relaxation data in PyI also yields the activation volume and enthalpy of Py reorientation, and compared to the one deduced from macroscopic dielectric measurements, with comparable values.¹⁴² The asymmetry of the potential well was found to be a decreasing function of increasing pressure.

Pyridium tetrafluoroborate BF_4 , perchlorate ClO_4 , perrhenate ReO_4 and periodate IO_4 compounds exhibit two temperature-induced solid-solid phase transitions of different natures, but the intermediate phase II of all compounds is ferroelectric. These four compounds have ideally tetrahedral anions with no permanent dipole moment by symmetry. But slight distortions from the ideal geometry could induce a dipole that may subsequently interact with the cation dipole. Whether such a hypothetical anion-cation dipole-dipole interaction is important for the onset of ferroelectricity was checked by using pseudotetrahedral anions $\text{A} = \text{FSO}_3$, FCrO_3 with high-permanent dipole. Three solid-solid phase transitions were observed for the former,¹⁵¹ and two for the latter.¹⁵² Again, phase II was of ferroelectric nature.

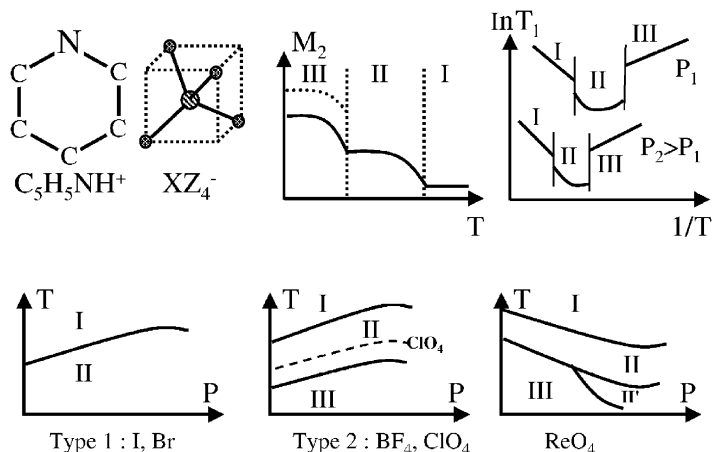


Fig. 10. Schematic summary of the results on pyridinium salts. Up, from left to right: pyridinium cation and tetrahedral or pseudotetrahedral anion; proton second moment as a function of temperature; logarithm of the proton spin-lattice relaxation time as a function of inverse temperature for different hydrostatic pressures. Down, schematic representation of the different T - P phase diagrams.

The typical behavior of the proton (or fluor) second moment as a function of temperature for all six compounds is rather similar, and can be summarized as the following (Fig. 10). Starting from phase III or IV at the lowest temperatures, the measured second-moment value was always found in good agreement with the calculated Van Vleck's value from the crystal structure. Thus, at these temperatures, the lattice is rigid on the NMR time-scale. Upon increasing temperature, the second moment decreases until the phase transition IV-III or III-II occurs. Depending on the compound, the second moment is continuous or discontinuous at the transition. In ferroelectric phase II, and across the phase transition to the paraelectric phase I, M_2 is a continuous function, which decreases with increasing temperature in phase II, and attains the plateau value at the transition or just above the transition temperature. The plateau value in phase I is interpreted by isotropic rotation of the pyridinium cation around a pseudosixfold axis with equal potential depths. This model was also confirmed by the anisotropy of the spin-lattice relaxation time, measured with a single crystal of pyridinium perchlorate.¹⁴⁶ Different models of the potential wells were compared in ref. 144.

In contrast to the second moment that bears strong analogies between the six compounds, the spin-lattice relaxation times show a very wide variety of behaviors as a function of inverse temperature. With PyIO_4 , the proton spin-lattice relaxation $T_1(\text{H})$ as a function of $1/T$ presents a typical U-shape with no anomaly over a temperature range that covers the three phases, and

was almost perfectly fitted with the BPP theory.¹⁴⁰ For PyReO_4 , $\ln T_1(\text{H})$ decreases linearly and continuously as a function of $1/T$ across the transition $\text{I} \leftrightarrow \text{II}$, and discontinuously increases by two orders of magnitude at transition $\text{II} \leftrightarrow \text{III}$.¹⁴⁸ For PyFSO_3 and PyCrSO_3 , $\ln T_1(\text{H})$ decreases linearly and continuously as $1/T$ increases from phase I to II.^{151,152} $\ln T_1(\text{F})$ is a continuous linear function of $1/T$ with positive slope over a temperature range covering the four phases of PyFSO_3 . Activation enthalpies were deduced from the linear parts in the different phases.

The second-moment and relaxation data indubitably show that the pyridinium cations are still dynamically disordered in the ferroelectric phase II, but that the anisotropy of the motion in phase II introduces sufficient bias to produce a nonzero macroscopic averaged dipolar contribution from the pyridinium molecular dipole. Microscopic mechanisms of the phase transition of PyBr , I¹⁴¹ and PyClO_4 ¹⁴⁷ were proposed. The results of deuterium NMR ^2H experiments on powdered pyridinium tetrafluoroborate PyBF_4 with deuterated d_5 -pyridine were used by two different groups to quantify the contribution of the dipole moment of the pyridinium cation to the macroscopic polarization.^{116,144} This was carried out from the analysis of the lineshapes with three- or six-site models for the reorientation potential of Py in the fast motion limit (see Section 3.4), to extract the different site probabilities of occupation. Combining the values of the probabilities with the value of the cation electric dipole moment, the orientational polarization was calculated, and compared with macroscopic spontaneous polarization data obtained from pyroeffect measurement. At first sight, the results of refs. 116 and 144 are surprisingly completely in disagreement with each other, the first group obtaining consistency between the NMR estimation and measured polarization in phase II with the three-site model, while the second group obtained almost no superposition between the two curves except at the lowest temperature. However, a close inspection of the methodology applied in the two articles indicates that the later group normalized their NMR estimation of the polarization to the measured polarization at the lowest temperature, which explains their findings. The method used by the first group¹¹⁶ seems more reliable because they used a value of the molecular pyridinium dipole determined by quantum mechanical *ab initio* methods, and calculated the averaged dipole from the NMR probabilities using this value. This method thus permits direct comparison without any other hypothesis. They obtained perfect agreement of the three-site model with the measured polarization in phase II, whereas in phase II or for both phases with the six-site models, the NMR estimation was also much larger than the real polarization. The authors concluded that the accordance and discrepancies between the two data sets support a combined mechanism of both dipole ordering and anion/cation displacement in the building of

ferroelectricity in the low-temperature phase. ^2H relaxation was also analyzed in ref. 116.

The temperature–pressure phase diagrams of PyBF_4 ,¹⁴⁵ PyClO_4 ,¹⁴⁷ PyReO_4 ¹⁵⁰ were established from various techniques (X-ray diffraction, dielectric, DSC and dilatometry measurements). Under pressure, the signatures of the phase transitions on proton spin–lattice relaxation seem clearer than at ambient pressure. For pyridinium perchlorate, upon decreasing temperature $\ln T_1(\text{H})$ decreases linearly as a function of $1/T$ in phase I, discontinuously decreases at the $\text{I} \leftrightarrow \text{II}$ transition. Then a minimum occurs in phase II, followed by a discontinuous increase at transition $\text{II} \leftrightarrow \text{III}$, and again a linear increase in phase III.¹⁴⁶ Both transitions are of first-order type, with transition temperatures that have a positive slope with increasing pressure $dT/dP > 0$. The activation enthalpy and volume in phases I and III were determined, and found in reasonable agreement with those extracted from dielectric measurements. Both techniques also still find reorientations of the pyridinium cations in phase III. A subsequent calorimetric, dielectric and dilatometric study found a new line of transitions in phase II.¹⁴⁷ The phase diagram of PyH ReO_4 perrhenate was also investigated with dielectric, neutron and proton NMR experiments.¹⁵⁰ The results have shown the occurrence of a new high-pressure phase. Interestingly, the phase diagram differs substantially from the other compounds, with a triple point corresponding to the pressure of 100 MPa and the temperature of 240 K.

Related compounds such as $(\text{CH}_3\text{NH}_3)_5\text{Bi}_2\text{M}_{11}$ with $\text{M} = \text{Cl}$, Br and $(\text{Py})_5\text{Bi}_2\text{Br}_{11}$ are ferroelectrics.¹⁵³ The first two compounds are interestingly ferroelectric near ambient temperature, whereas the third compound becomes ferroelectric below 118 K. $(\text{Py})_5\text{Bi}_2\text{Br}_{11}$ was studied by proton NMR at two frequencies 25 and 90 MHz.¹⁰¹ In this structure, five pyridinium cations are connected to $\text{Bi}_2\text{Br}_{11}^{5-}$ anions by weak $\text{N-H} \dots \text{Br}$ HBs. In addition to the second-order paraelectric/ferroelectric phase transition at 118 K, this compound undergoes a first-order structural phase transitions at ≈ 404 K. The complex behavior of the dielectric response near 118 K was explained by two relaxational modes. The two structural phase transitions are well distinguished by the behavior of the relaxation time T_1 and second moment as a function of temperature. In the intermediate phase, the anions and cations are dynamically disordered. Interestingly, the T_1 relaxation minimum occurring in the intermediate phase was interpreted by cross-relaxation of the protons by the quadrupolar nuclei ^{69}Br and ^{71}Br . In the low-temperature ferroelectric phase, a wide symmetric spin–lattice relaxation minimum T_1 was measured for the first time in pyridinium salts. At such low temperatures, the large-jump motions invoked to explain the room temperature behavior cannot occur, and the interpretation of this relaxation minimum relied on small librations of the pyridinium cation around the

pseudohexad axis, which is perpendicular to the cationic ring. That the second moment slightly decreases as temperature increases in this temperature range supports the interpretation. According to the authors, such Py librations may be the high-frequency relaxational mode needed to interpret dielectric measurements.

Analogous multitechnique approaches combining thermodynamical, structural, dielectric data with (mainly) proton NMR have been applied to the family of compounds $R_xM_yX_{3y+x}$ (R is an organic cation, $M = \text{Sb(III)}, \text{Bi(III)}$, $X = \text{Cl, Br, I}$). Ferroelectric and nonferroelectric phase transitions are considered. Halogenantimonates(III) and halogenobismuthates(III) of formula $R_3M_2 \times 9$ that crystallize with the two-dimensional anionic sublattice have ferroelectric properties. The complex cation motion was considered in ferroelectric $[\text{C}(\text{NH}_2)_3][\text{Sb}_2\text{B}_2]$.¹⁵⁴ $(i\text{-C}_4\text{H}_9\text{NH}_3)_3\text{Bi}_2\text{Br}_9$ has two phase transitions but is not ferroelectric.¹⁵⁵ Similar studies were performed on RSbX_4 with $X = \text{Cl, Br}$, $R = n\text{-NH}_2\text{C}_5\text{H}_4\text{NH}$ ($n = 2$ or 4).^{156,157}

We would like to emphasize that in the present context of “high fields race”, the nice results of wide line proton NMR presented in this section were obtained at low fields (typically at frequencies < 100 MHz). It should give convincing arguments to urge persons in charge of NMR laboratories to keep their “old” resistive variable field magnets and spectrometers.

4.3. Order–disorder or displacive phase transitions

4.3.1. Introduction

As already discussed in the introduction of the section, the ferroelectric phase transitions are traditionally classified as pure order–disorder or displacive phase transitions (Fig. 8). However, as will be shown below, the situation is less simple, and it was long suggested that the classification between pure order–disorder or displacive driving mechanism is simply too sharp to cope with some real materials, which phase transitions may be of mixed nature. For instance, the status of the pure order–disorder phase transition of NaNO_2 was recently questioned from X-ray experiments.^{158,159} The NO_2^- anions are disordered between two configurations (as revealed by anomalously large thermal anisotropy factors), and their ordering leads to ferroelectricity. But a large anisotropic displacement of the sodium cation Na^+ along the ferroelectric axis was also found anomalous, and only compatible with a displacive behavior.

Despite a number of indications of transitions that cannot be classified within one pure type, strong experimental evidences were usually lacking to support the existence of mixed-type phase transitions. The examples discussed below show that recent progresses in NMR resolution and sensitivity,

for spin 1/2 or quadrupolar nuclei, brought convincing experimental results of the coexistence of order–disorder and displacive behavior in the phase transitions of prototype compounds like squaric acids, KDP-like samples, BaTiO₃ or SrTiO₃.

4.3.2. *Displacive component in order–disorder phase transition: H-bonded compounds*

A priori, it seemed easier to evidence a displacive contribution in an order–disorder phase transition. As early as 1981, it was proposed that the isotropic chemical shift of spin 1/2 nuclei could distinguish between pure order–disorder and pure displacive phase transitions.¹⁶⁰ The argument is as follows. The isotropic chemical shift δ_{iso} being the trace of the chemical shift tensor ($\delta_{\text{iso}} = (\delta_{11} + \delta_{22} + \delta_{33})/3$), it is insensitive to any rotation of the CSA tensor with respect to the external magnetic field. Therefore, any modification of δ_{iso} is a consequence of a change of the electronic (and/or conformational environment) of the NMR-probing nuclei. In other words, since the molecular structure is not modified in an order–disorder phase transition, any (anomalous) modification of δ_{iso} through a phase transition should indicate a displacive contribution, through a coupling between the chemical shift tensor and the atomic displacement or molecular distortion induced by the displacive mechanism. Note that this property of invariance of the trace of the interaction tensor to translation and rotation was commonly used in the study of glasses to quantify molecular conformational local disorder. Indeed, since at very high MAS spinning frequency all anisotropic interactions (CSA, dipolar, quadrupolar, etc.) are averaged to zero, the resulting linewidth comes mainly from a distribution of δ_{iso} due to local bond or conformational disorder.¹⁶¹

However for order–disorder phase transitions, the isotropic chemical shift difference due to very tiny and subtle molecular distortion is expected to be very small (typical < 1 ppm), which always puts a doubt when no isotropic chemical shift modification is measured through a phase transition since it can be the obvious consequence of a lack of spectral resolution.

A breakthrough in spectral resolution of 1D spectra was achieved by combining the use of single crystal with MAS at high-spinning rates.¹⁶² As compared to powders, it was proved on different nuclei and samples that the residual linewidth measured by spinning single crystal (usually packed into the rotor with silica) instead of powders could be five times to one order of magnitude narrower than the corresponding linewidth obtained from a powdered sample under the same experimental conditions. The spectral resolution was even found better than the one observed from static single-crystal NMR.¹⁶⁰ As explained by the authors A. Klymachyov and N. Dalal,

Andrew utilized single crystals in his pioneering MAS experiments (1959), and Van der Hart *et al.*¹⁶³ also noted that single crystals give narrower peaks than powders. At first, the difference in residual linewidth between powder and single crystal was attributed to different bulk magnetic susceptibility anisotropies. But the spectra of a given sample powder dispersed in silica are not significantly narrower than spectra acquired from a rotor completely filled with powder of the same sample.¹⁶⁴ Therefore, the explanation of the spectral enhancement observed when spinning single crystals is still an open question, and should be considered as an experimental fact.

This method permits to find displacive contributions, and was subsequently successfully applied to the study of the possibility of the existence of displacive contributions in phase transitions, which were considered of the pure order-disorder type. A. Klymchyov, N. Dalal *et al.* performed a solid-state single-crystal MAS NMR study of the antiferroelectric phase transition of squaric acid $\text{H}_2\text{C}_4\text{O}_4$ (henceforth SQA) by ^{13}C (natural abundance) and ^{17}O ($I = 5/2$, enriched samples) NMR. SQA is composed of planar layers where each C_4O_4 group is connected to the four nearest neighbors by strong intermolecular $\text{O}-\text{H}\cdots\text{O}$ bonds (Fig. 9). The two-dimensional layers are bonded by weak van der Waals interactions. In the HT paraelectric phase, the hydrogen is disordered within two equivalent sites, and the squarate C_4O_4 groups have a mean 4/m symmetry. Below $T_c \sim 373\text{ K}$, the protons become more localized in the antiferroelectric phase, and the squarate units distort concomitantly (C_4O_4 molecular symmetry is modified). Both ^{13}C and ^{17}O NMR spectra show four well-resolved isotropic peaks in the LTP in contrast to previous ^{13}C single-crystal experiments, which could only resolve two peaks.¹⁶⁰ The squarate unit is therefore less symmetric than the trapezoidal unit inferred from previous results. The four ^{13}C peaks merge into one peak in the paraelectric phase,^{162,165} whereas the four ^{17}O peaks merge into two peaks that persist over 20 K above T_c .^{164,166} This last observation indicates that the squarate units have not a true four-fold symmetry above T_c on the NMR time-scale. The mean of the four isotropic chemical shifts measured in the LT do not coincide with the ^{13}C singlet-HT position, nor with the mean position of the ^{17}O doublet in the HTP. Instead, the mean isotropic chemical shift shows an “S-shape” or a cusp as a function of temperature in the vicinity of T_c (Fig. 11b, c). This behavior clearly indicates a change in the electronic environment of the probe near T_c , which is a displacive component in the phase transition. The mixed nature of the antiferroelectric phase transition of SQA was further interpreted with density functional calculations,¹⁶⁷ the coupled nonlinearly polarizable lattice pseudospin model^{168,169} or vibronic models.¹⁷⁰ Similar experiments and models were used to prove a displacive component in $\text{KD}_{1.8}\text{H}_{0.2}\text{PO}_4$ and RbH_2PO_4 with ^{31}P NMR.¹⁷¹

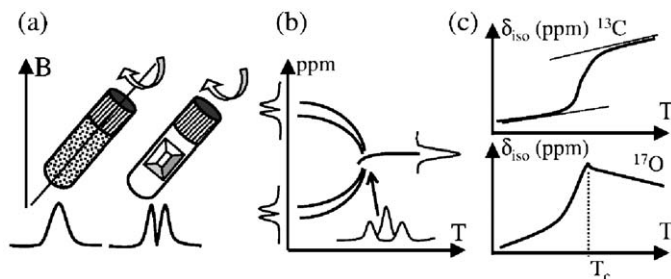


Fig. 11. (a) Gain of spectral resolution by MAS spinning of a single crystal; (b) schematic behavior of ^{13}C or ^{17}O MAS lines of SQA as a function of temperature, with coexistence region; (c) schematic of ^{13}C or ^{17}O isotropic chemical shift, obtained by the average of all the line positions.

A coexistence region in SQA was also evidenced by ^{13}C 2D temperature jump correlation NMR.¹⁷² Proton ^1H spin–lattice and spin–spin relaxation measurement on SQA was performed within 320–460 K.¹³⁸ In addition to a typical critical behavior manifested at the known temperature of the anti-ferroelectric phase transition near $T_c \approx 373$ K, both relaxation data also show a second critical behavior around 420 K, which opens the question of a second phase transition for SQA.

Bisquaric acid was also studied by ^{13}C CPMAS NMR between 123 and 523 K, with powdered crystals.¹⁷³ This material has also potential for non-linear optical and dielectric applications. The low-temperature spectra resolve three peaks instead of four in SQA. This compound has no dipole moment, and no phase transition was detected in the studied temperature range, although the lineshape suggests the occurrence of a phase transition below 373 K. An explanation proposed by the authors is the lack of resolution due to the accidental overlapping of the two resonances of the C–OH and C = O carbons participating to the HBs, an interpretation also supported by GIAO *ab initio* chemical shift calculations.

4.3.3. Order–disorder component in displacive phase transition: perovskites

Ferroelectrics of the perovskite-type structure CTiO_3 with different cations $\text{C} = \text{Ba}, \text{Ca}, \text{Pb}, \text{Sr}$ are of fundamental importance in the comprehension of the mechanism governing ferroelectricity, because the simple perovskite structure gives the opportunity to study the onset of ferroelectricity from a highly symmetric cubic phase.

For instance, in the paraelectric phase of the first discovered perovskite-type compound, barium titanate BaTiO_3 , the Ti cation is at the center of the oxygen octahedron, which is itself centered in a cubic cell with the cations

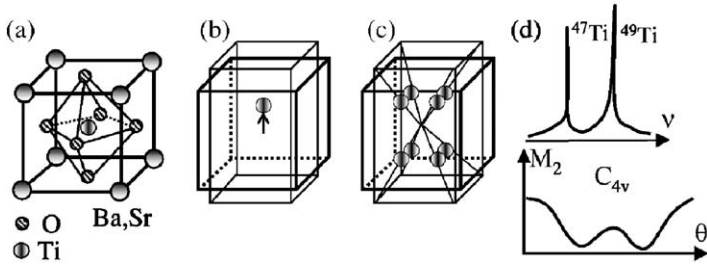


Fig. 12. Schematic of BaTiO_3 NMR results. (a) Cubic structure; (b) displacive model with the tetragonal distortion; (c) order-disorder model with eight sites along the body diagonals; (d) HT paraelectric phase $T > T_c$. Up: spectra with the satellite background; down: second moment as a function of rotation in the HT paraelectric phase $T > T_c$ indicating a tetragonal local symmetry breaking.

Ba^{+} at the corners (Fig. 12a). BaTiO_3 has a complex sequence of ferroelectric phase transitions as follows:

$$|\text{cubic}| - 393\text{IK} - |\text{tetragonal}| - 278\text{IK} - |\text{orthorhombic}| - 193\text{IK} - |\text{rhombohedral}|$$

From ^{137}Ba ($I = 3/2$), ^{47}Ti ($I = 5/2$) and ^{49}Ti ($I = 7/2$) quadrupole-perturbed static and MAS NMR acquired with polycrystalline recrystallized strain-free samples,¹⁷⁴ or a multidomain crystal to determine the EFG principal axes,¹⁷⁵ the EFGs at the Ba and Ti sites were characterized in the ferroelectric tetragonal, orthorhombic and rhombohedral phases. SrTiO_3 has three phases (cubic-tetragonal-orthorhombic), but CaTiO_3 remains cubic at all temperatures. PbTiO_3 has a first-order cubic-tetragonal ferroelectric phase transition, but the existence of a second-order tetragonal-orthorhombic phase transition around 170 K is still controversial, although recent ^{207}Pb variable temperature NMR experiments¹⁷⁶ detect no anomaly and no departure from axial symmetry of the ^{207}Pb chemical shift tensor over 123–333 K. An empirical linear relation between chemical shift anisotropy and tetragonal distortion parameter was also reported.

Barium titanate (BaTiO_3) was considered as the prototype of pure displacive compound for the cubic-tetragonal phase transition. At the phase transition, the softening of a transverse optic phonon was observed, which corresponds in the displacive picture to a motion of the Ti cation from the center position in the paraelectric phase to an off-center position in the tetragonal phase. However, recent NMR experiments indicate that this picture is too simple. Whether the titanium cation is at the center of the cubic cell in the paraelectric phase or disordered within equivalent off-centered sites may be investigated using the high sensitivity of the frequency shift of quadrupolar nuclei to tiny EFGs variations (Fig. 12a–c). Indeed, the EFG

tensor being zero by symmetry at site with cubic symmetry, any departure either from the cubic site symmetry or any displacement of the Ti cation to off-centered positions should induce a resulting nonzero EFG, which is a quadrupolar shift of the NMR frequency.

Blinic *et al.*^{177,178} performed $^{47}\text{Ti}(I = 5/2)$ and $^{49}\text{Ti}(I = 7/2)$ quadrupole-perturbed NMR experiments with very high-quality single crystal of BaTiO_3 . The authors observed that in the paraelectric cubic phase $T > T_c$, the narrow central ($-1/2 \leftrightarrow 1/2$) transition lines are surrounded by a broad background component, which was interpreted as unresolved satellite transitions due to a nonzero EFG in the high-temperature phase (Fig. 12d). This result clearly indicates a breaking of the local cubic symmetry by off-center Ti displacement in the paraelectric phase. The authors argued that since the same broad component is observed several 10 K above T_c , the result cannot be attributed to pretransitional effects, but to real distortions of noncubic symmetry of the potential surface governing Ti motion. By analyzing the variation of the quadrupolar second moment of the lines as a function of crystal orientation, and by comparison with different models, the authors unambiguously showed that the EFG resulted from a tetragonal distortion of the mean HT cubic symmetry of the cell. In the low-temperature phase $T < T_c$, the broad components coalesce into well-resolved satellites, and the number of central transition lines is doubled, indicating 90° domains. The tetragonal distortion below T_c was confirmed by *ab initio* EFG calculations.¹⁷⁹

Although these data prove the existence of tetragonal distortion in the cubic paraelectric phase, subtle considerations concerning the probing time-scale and the possible site positions are necessary to attribute observed local symmetry breaking to a displacive or disordered off-center mechanism. The NMR observed tetragonal distortion suggests a displacement of the Ti cation parallel to the cell edges $\langle 100 \rangle$, whereas EXAFS data measure Ti shifts parallel to the cubic diagonal directions $\langle 111 \rangle$. Different probing time-scales of the two techniques may solve the contradiction. At first inspection, the local symmetry breaking may also be compatible with the eight-site order-disorder model, where the Ti cations jump other eight symmetrical sites disposed on the diagonal of the cube (Fig. 12c). Since the off-center EFG is nonzero, a nonzero EFG may arise from different occupation probabilities. However, the authors showed that the averaged EFG of the eight-site model is always zero in a given domain, even for unequal occupation probabilities, because the diagonal of a cube are tilted by the magic angle with respect to the cubic axes thus yielding $(3 \cos^2 \theta_m - 1) = 0$. Thus, the pure eight-site model always predicts a zero EFG, which is obviously in contradiction with the experimental results. But the author could interpret all the data by combining this order-disorder model with a tetragonal

displacive distortion of the unit cell. The readers are referred to ref. 178 for details. Discussions of the nature of this mixed order–disorder/displacive phase transition from the analysis of different experimental results and theoretical models are presented in refs. 180 and 181.

The case of SrTiO_3 is complicated by quantum effects, which inhibit the ferroelectric transition: SrTiO_3 is paraelectric down to 0 K. However, a ferroelectric transition can be induced by oxygen isotope exchange, which suppresses the quantum fluctuations: replacing 99% of ^{16}O by ^{18}O leads to a dielectric peak.¹⁸² Nevertheless, the same authors also proved by NMR that both order–disorder and displacive components are present in the cubic–tetragonal phase transition of SrTiO_3 and $\text{SrTi}^{18}\text{O}_3$.¹⁷⁸

5. COEXISTENCE, HYSTERESIS AND KINETICS

First-order phase transitions are characterized by a coexistence region and thermal hysteresis. The kinetics of the overall phase transformation is a mixed process of nucleation, and growth of the different phase boundaries upon complete completion of the process, which occur more or less simultaneously.

5.1. Introduction

The onset of the transition usually begins with random nucleation of one phase within the other. The free enthalpy difference between the two phases is the driving force since the production of the new phase into the old phase decreases the total free enthalpy. However, the existence of boundaries between the phases introduce frustrations (for instance, misfit strains) that cost energy, and nucleation occurs depending on the competition between the two contributions. The subsequent growth extension of the phase boundaries of an already nucleated domain (interface-controlled growth) is slowed down by the free enthalpy barrier needed to move the interface (Fig. 13a). Another possibility of phase growth would be by the segregation of mesodomains into mobile microscopic domains (diffusion-controlled growth), but for phase transitions among different polymorphs, the interface-controlled growth model is preponderant.

All these transformations occur at different time-scales that govern the built up of the new phase. Therefore, the time-scale of the temperature-driving ramp as compared to the domain growth rate is an important parameter, which may determine the span of the thermal hysteresis between heating and cooling transformations. When the time-scale of temperature

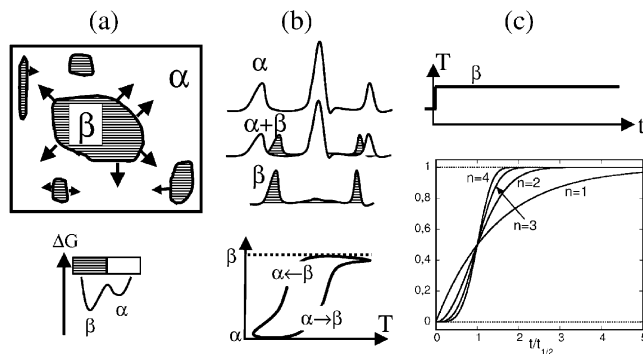


Fig. 13. Coexistence, hysteresis and kinetics. (a) Schematic of interface-controlled growth of phase β into phase α ; (b) superposition of spectra and thermal hysteresis; (c) time evolution of volume fraction of phase β : Avrami model (Eq. (14)) for different exponents n .

change is very slow as compared to phase growth rate, the hysteresis is almost inexistent and a jump in the NMR parameters is expected. On the other hand, for fast temperature ramps, the incoming phase has not enough time to grow completely and coexistence of the metastable phase with the thermodynamically stable phase occurs (Fig. 13b).

The kinetics of the transformation process of the old phase to the new phase depends on the nucleation process, the dimensionality and mechanism of growth. Despite the interplay of a number of mechanisms, the time variation of the fractional volume of the new phase β in phase α , $v(t) = V_\beta(t)/V$ (V is the total volume) can be usually described by a single simple formula, the Johnson–Mehl–Avrami–Kolmogorov model^{183–186}

$$v(t) = 1 - \exp[-(t/\tau)^n] = 1 - \exp[-\log 2(t/t_{1/2})^n], \quad (14)$$

where τ is a time constant related to the growth and nucleation process. The exponent n is the key parameter of the relationship. For domain boundary controlled growth, and depending on the nucleation process, it can be shown that the exponent varies as $d \leq n \leq d+1$, with d the dimensionality of the growth process ($d = 1$ for dendritic growth, 2 for cylinders, 3 for spheres). The lower bound occurs when growth centers are well defined and constant in number; the upper bound corresponds to the continuous nucleation process. The second formula with $t_{1/2}$, the time at which half of the old phase has been transformed, indicates that the shape of $v(t)$ as a function of the reduced time, $t/t_{1/2}$, is only a function of the exponent n whatever the time constant τ (Fig. 13c).

The principle of studies of coexistence and kinetics in solid–solid phase transitions by NMR is rather simple, since it relies on peak attribution and

time-resolved experiments. Within the coexistence region, the spectrum is expected to be the sum of two sets of lines corresponding to the two different phases, one growing at the expense of the other as temperature increases or decreases, or as time passes. Provided the LT and HT phases have been characterized and assigned, a simple integration of the different lines leads the fraction of the different phases as a function of temperature or time. When resolution is not sufficient to resolve the different lines corresponding to the two phases, possible differences in relaxation times of the two phases open another route to distinguish between them, provided the ratio of the two relaxation rates is sufficiently far from 1. These two methods are illustrated by three examples in the following section.

Concerning kinetics, time-resolved experiments need principally two experimental conditions. First, a good signal-to-noise ratio in an acquisition time much smaller than the time constant of the kinetical process to be studied; second, a high sensitivity of the measured quantity to the differences in the short- and long-ranged structural deviations produced by the transformation process. For NMR, the sensitivity condition is usually met by a suitable choice of the nuclei and interaction coupling, but the low sensitivity and long recycle time necessitated by long spin-lattice relaxation times results in too long acquisition times for a reasonable signal-to-noise ratio. In general, NMR is not suited for time-resolved experiments. However, in some rare cases, both conditions can be satisfied. We report in Section 5.3 three time-resolved NMR experiments, two in the solid state at high temperature, and one in the crystal-liquid state.

5.2. Coexistence and hysteresis

Thermal hysteresis and coexistence in the transformations between the polymorphs of 2-(2,4-dinitrobenzyl)-3-methylpyridine was studied by ^{13}C and ^{15}N MAS NMR by Eichen *et al.*¹⁸⁷ This compound exists in three crystal-line polymorphic forms A, B, C, which were characterized by X-ray diffraction and NMR. The phase transformation $A \leftrightarrow B$ as a function of temperature was best monitored by ^{15}N . Phases A and B share the same monoclinic space group $P2_1/c$ with four molecules per unit cell, and almost identical unit-cell parameters except a 2% elongation of the *a*-axis of the HTP B with respect to the LTP A. The major differences in the structure of A and B concern the packing and interplanar angles between *o*- and *p*-nitro groups and the phenyl ring. Starting from phase A and recording spectra at different temperatures, a superposition of the set of lines of pure compounds A and B was clearly evidenced in a given temperature range, and the transformation ends at HT with the set of pure phase B. Integration of the

different lines gave the fraction of A and B content as a function of temperature and the thermal hysteresis upon heating and cooling. The interesting point concerning this study comes from the observation of a gradual and continuous conversion of A into B with no apparent metastability. After a temperature step, a new amount of A and B phases was observed to establish instantaneously, and appears stationary on the experimental time-scale (~ 24 h). Moreover, fast dynamical processes like local exchange between the two phases or mobile melt zones were excluded by the authors for time-scales lower than 1 min after exchange experiments. They concluded that the $A \leftrightarrow B$ interconversion, as monitored by NMR, can be described by a collective change of a large number of molecules that constitute domains. Although NMR indicates that local equilibrium is rapidly established after a temperature change and stationary, X-ray diffraction patterns gradually evolve over days, which implies a slower process. According to the authors, the image that emerges from this study is a system where local equilibrium is established in domains of different transition temperatures (resulting from interfacial and strain energies between domains of different phases). Macroscopic equilibrium between domains is further installed on a much smaller time-scale by thermal annealing. We should note that it is also an illustration of the short- and long-range complementary probing scale of NMR and X-ray diffraction, respectively. Fast local equilibrium is evidenced by NMR, while long-range order, that conducts to almost identical NMR features, is established by diffraction methods.

Another example of coexistence detection from the superposition of pure sample spectra concerns potassium nitrate. Within ambient temperature and 480 K, potassium nitrate KNO_3 has two stable phases α and β and a metastable phase γ , which appears on cooling from phase β . The influence of thermal history and time on the metastable phase γ was investigated by enriched ^{15}N MAS NMR by direct inspection of the occurrence of the different set of lines of each phase in the spectra.¹⁸⁸

Wąsicki *et al.*⁹⁸ used proton spin-lattice relaxation times to show the coexistence of cubic and LT tetragonal phases of NH_4I . This compound was studied at 60 MHz in the temperature range 128–372 K. Upon cooling or heating, the magnetization recovery as a function of time changes from a monoexponential behavior to a biexponential behavior, and back to a monoexponential behavior. The long spin-lattice relaxation time was attributed to the cubic phase. It was found more than one order of magnitude larger than the short relaxation time, which characterizes the tetragonal phases. By using the relative weight of the two components of the magnetization recovery curve, the authors built the phase diagram of the cubic phase, resulting in a thermal hysteresis of about ~ 50 K, with coexistence regions spanning ~ 10 K.

5.3. Time-resolved NMR: kinetics

The nucleation growth of one phase within the other at fixed temperature was successfully followed in *m*-carborane $B_{10}H_{10}C_2D_2$ by deuterium NMR.¹⁸⁹ *m*-Carborane is an orientationally disordered crystal with two phase transitions within three phases, a cubic HTP (I), an intermediate orthorhombic phase (II) and a monoclinic LTP (III). Böhmer *et al.*¹⁸⁹ remarked that the 2H spin-lattice relaxation abruptly decreases by one order of magnitude at transition III to II, and again abruptly increases by roughly one order of magnitude at transition II to I, with a minimum in between. These T_1 discontinuities mark first-order phase transitions, and were used to follow the kinetics of the solid-solid transitions. As a matter of fact, within coexistence regions, these high differences in relaxation times allow the selection of the phase with the shortest relaxation time by application of a saturation comb followed by a suitable recovery time. A monitoring of the phase content as a function of time is therefore possible with a time resolution of the order of the shortest T_1 , typically 1 s or lower for this compound. Using this method, large thermal hystereses were observed at the two transitions $I \leftrightarrow II$ or $II \leftrightarrow III$. Moreover, the growing of phase II into I as a function of time was shown to follow a Johnson-Mehl-Avrami-Kolmogorov kinetics, Eq. (14), whose parameters were estimated.¹⁸⁹ In particular, the author pointed out that the Avrami exponent n was incompatible with an isotropic growth process.

$CuAlCl_4$ exhibits two polymorphs, α - $uAlCl_4$ of pseudocubic close-packed structure and the pseudohexagonal close-packed β - $CuAlCl_4$ structure. The β phase interconverts into the α phase at temperature ~ 473 K. Martin *et al.*¹⁹⁰ performed time-resolved ^{63}Cu ($I = 3/2$, 69% natural abundance) and synchrotron PXRD experiments to follow the kinetics of interconversion at different temperatures. PXRD indicates a first-order phase transition with no intermediate phase. The feasibility of the NMR experiment relied on two observations. First, ^{63}Cu is a quadrupolar nucleus highly sensitive to small local distortions. Considering that the Cu cation is located on a special position of symmetry $\bar{4}$ in the α phase, the C_q parameter is expected to be zero by symmetry. On passing to a general position in the β phase, this parameter should change drastically and broaden the MAS spectra. Characterization of the two phases yields that in the α phase, C_q is close to zero but not zero, indicating a small deviation from the expected ideal tetrahedral geometry. Second, the very small quadrupolar spin-lattice relaxation time ~ 1 ms allows for fast data acquisition. The conversion of phases β to α was recorded as a function of time, varying over three orders of magnitude, at different temperatures, and the fraction of α phase was extracted. The typical sigmoidal shape as a function of time was fitted with

an Avrami–Erofe’ev rate law (Eq. (14)). By using the reduced time $t/t_{1/2}$, all the curves acquired at different temperatures almost overlay, showing an isokinetic $\beta \rightarrow \alpha$ transformation, with identical exponent $n \approx 1.5$. The value of the exponent is compatible with a one-dimensional growth process. Interesting considerations on the mechanism of the phase transformation were further developed, and the reader is referred to the article for details.¹⁹⁰

Relaxation of a shear-induced alignment of worm-like micelles in the isotropic phase was followed by ^2H NMR of D_2O , using an integrated miniature shear cell. The ^2H doublet splitting of D_2O reflects the degree of alignment of the phase because $\Delta\nu$ is proportional to the nematic-order parameter $P_2 \sim (3\cos^2\theta - 1)$, and a single line centered at zero frequency is observed in the isotropic phase. After cessation of the steady shear stress that align the medium in a nematic-like phase, spectra could be acquired with a time resolution of 14 s, for a relaxation process that took ~ 300 s. All the spectra are doublets, with no presence of a central line, except at the end of the process when the doublet coalesces into a single line corresponding to the isotropic phase.¹⁹¹ The result of R. Angelico *et al.* proves that the nematic phase disorders gradually into an isotropic phase, with no nematic/isotropic nucleation and growth processes, in agreement with previous rheo-SANS (small-angle neutron scattering) results performed by the same authors. The time constant of the relaxation process was extracted from the evolution of the line splitting as a function of time. The authors pointed out that this NMR study was motivated to confirm or infirm the SANS results, NMR being more sensitive to detect domains than SANS.

A very recent article concerning methodology to record solid-state reaction kinetics by in situ time-resolved NMR at very high temperatures ($> 1,000$ K) is worth quoting despite the absence of phase transitions because the method may be useful. It was applied to monitor the kinetics of the reaction of powdered Na_2CO_3 with SiO_2 with static ^{23}Na NMR.¹⁹²

No doubt that the progress in both sensitivity and methodology will increase the range of applicability of time-resolved in situ NMR studies, which are important for the comprehension of first-order and reconstructive phase transitions, but also in solid-state reaction kinetics.

6. SINGLE-CRYSTAL PHASE TRANSITION STUDIES

The NMR internal interaction symmetric second-rank tensors are characterized by three eigenvalues, and three angles are required to orient the corresponding PAS with respect to crystal axes. Only the eigenvalues of the interaction tensors can be extracted from a powder spectra by least-squares fitting of the lineshape. Although absolute orientations cannot be obtained,

the powder pattern depends on the relative orientations of two interaction tensors if their magnitude are comparable. For instance, when chemical shift anisotropy and second-order quadrupolar anisotropy both contribute to the inhomogeneous broadening, a careful fit of the spectra leads to the two sets of eigenvalues and to the relative orientation of the PAS of the two tensors,²⁹⁻³¹ with a satisfactory accuracy if at least two spectra acquired at different magnetic fields are fitted simultaneously.³⁴ But generally simplification of the description of the relative orientations are necessary, and this approach is nevertheless limited to a very few inequivalent sites. On the other hand, powder NMR is also very interesting to quantify motions with exchange rates that are in the intermediate regime, since the symmetry and dynamics usually deform the whole powder pattern in a characteristic manner.

For some systems, the presence of two or more interactions, and two or more chemically distinct sites induce so strong overlaps between the different contributions that the analysis of the NMR powder spectra is too intricate to be possible. Even when the powder pattern singularities are well resolved, it is not unusual that the eigenvalues of the interaction tensor do not show any obvious anomaly at a phase transition. In that case, only a complete determination of the interaction tensor (including the direction of the principal axes) may lead sufficient information to characterize the different phases.

Single-crystal NMR experiment requires a special probehead with a goniometer. Some probeheads are now commercially available. Different improvements in methodology^{193,194} and probe design to optimize sensitivity and goniometer precision^{193,195,196} appeared recently as well as simple programs to extract the tensor parameters from the rotation patterns.¹⁹⁷ In fact, the most demanding condition for single-crystal NMR remains the achievement of the growing of single crystals.

6.1. Introduction: site selectivity, intrinsic disorder and slow motions

Provided that sufficiently large single crystals can be grown, the spectral signature of each site can be resolved by single-crystal NMR. By following the variation of the different spectral features (lineposition, linewidth, relaxation) as the crystal is rotated in the magnetic field, both the eigenvalues and the orientation of the principal axes of each interaction tensors with respect to the crystal frame can be unambiguously obtained, providing a description of the various sites in the crystal. For instance, when the second-order quadrupolar interaction is negligible, the orientation dependence of the central transition of a half-integer spin is governed solely by the chemical shielding interaction, whereas the orientation dependence of the satellite

transitions is determined by the first-order quadrupolar interaction alone. Subsequently, the features of the tensors can be correlated with the crystal structure.

With single crystal, site-selective relaxation measurements are also possible. The orientational dependence of the different energy levels in single-crystal NMR gives also a parameter to adjust the energy spacing between different nuclei to control cross-relaxation. For instance, cross-relaxation can be used to shorten the relaxation time of a low- γ nuclei by adjusting its energy spacing to the quadrupolar splitting of a quadrupolar nuclei. This effect was used to study phase transitions in proustite Ag_3AsS_3 by $^{109}\text{Ag}(I = 1/2)$ NMR cross-relaxed by $^{75}\text{As}(I = 3/2)$.¹⁹⁸ The resulting spin-lattice relaxation time was reduced from 30 h to 20 min at 80 K, and allowed lineshape studies of the 3q-incommensurate phase as well as slow motions.

The possibility to measure highly resolved spectra with almost nonoverlapping lines is an obvious advantage provided by single-crystal NMR compared to powder NMR. It offers the opportunity to study orientational *intrinsic* disorder which broaden inhomogeneously the lines, to characterize whether an observed linebroadening is of homogeneous or inhomogeneous nature, and to follow ultraslow motions that are too slow to narrow the linewidth, but fast enough or of the order of the spin-lattice relaxation to be detectable. It is usually impossible to answer these questions from powder NMR because all the subtle deviations or differences are hidden by the 3D disorder of the powder that inhomogeneously broaden the spectrum by mixing all frequencies. The nature of the intrinsic orientational disorder can be inferred from the linewidth anisotropy as a function of crystal orientation. Homogeneous-inhomogeneous broadening discrimination and ultraslow motion kinetics rely on selective saturation experiments.¹¹³ The principle of a typical selective saturation experiment consists of a soft and long selective π or $\pi/2$ pulse followed by a mixing period, and a final reading sequence with hard pulses that excites uniformly the whole spectrum (Fig. 14a). The aim of the first selective pulse is to label the nuclei at the irradiation frequency. If the broadening is inhomogeneous, the selective pulse dips a hole (like optical “hole-burning” experiment) at the irradiation frequency, in contrast to homogeneously broaden lines (Fig. 14b). The depth of the hole in the inhomogeneously broaden line depends on the mixing time, and it relaxes following the spin-lattice relaxation time if no slow or ultraslow motion occurs. On the other hand, if the labeled nuclei change their environments during the mixing time, which mean that their resonant frequency are no longer at the selective pulse irradiation frequency, the shape of the line is modified. By following the difference with a reference spectrum at infinite mixing time (typically $t_e \gg 5T_1$), the occurrence of

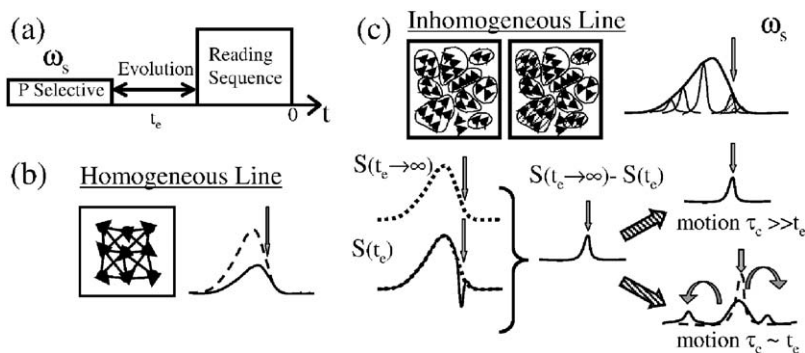


Fig. 14. Schematic of selective excitation and 1D exchange spectroscopy. (a) Typical pulse sequence with a soft selective pulse centered at pulsation ω_s with a frequency dispersion $\Delta\omega_p \ll \Delta\omega_l$ much smaller than the typical linewidth. After an evolution time t_e smaller or of the order of the spin–lattice relaxation time, a reading sequence of hard pulses that covers uniformly the whole broad line is applied. (b) Effect of a selective excitation on a homogeneously broaden line. (c) Selective frequency labeling of an inhomogeneously broaden line at the irradiation pulsation ω_s of the first soft pulse. For a soft π pulse, the magnetizations of all the spins that can exchange energy at this pulsation are reversed. By following the difference spectra between the spectra acquired at different evolution times t_e and the fully relaxed spectrum $\Delta S(t_e) = S(t \rightarrow \infty) - S(t_e)$, limits or evaluation of the correlation time τ_c of the motion can be achieved.

ultraslow motions is evidenced and exchange rates can be determined (Fig. 14c). This 1D experiment is complementary to the 2D exchange experiments that sometime leads to impracticable time-consuming acquisitions.

The unique opportunities offered by the high selectivity of single-crystal NMR are illustrated below with two examples. The power of single-crystal NMR to detect very small orientational disorder and slow motions, and its complementarity with X-ray diffraction, is well illustrated by the study of polar and alignment disorder in molecular crystals with deuterium NMR. The second examples concern the importance of selectivity to follow the properties of the strongly disordered sublattice of guest included in oriented nanotubular intergrowth inclusion compounds based on urea or thiourea. Evidence of inhomogeneous line broadening in pretransitional phenomena, full characterization of the phase transitions and ordering was achieved, again with deuterium NMR.

6.2. Polar and alignment disorder in molecular crystals

Assuming that the orientation of an asymmetric molecule can be represented by a vector or a spin, the flip-flop orientational disorder within the different

lattice sites characterizes “polar disorder”. The symmetry operation that transforms one position to the other being an inversion or a C_2 rotation, polar disorder is easily quantified by diffraction methods that measure, through a space and time average, the probability of occupation of the two directions, whereas NMR is completely blind to it because the NMR interactions are invariant under inversion. For a given molecular orientation, an “alignment disorder” is also possible by slight misorientations of the molecules around the mean polar direction. The usually very small angular deviation of a few degrees is hardly detected by diffraction methods because it is hidden by the thermal factors. On the other hand, single-crystal NMR offers exceptional angular resolution, in orienting the interaction tensor principal axes and in quantifying orientational disorder from linewidth measurements (Fig. 15).

Both types of disorder are expected when a polar disorder of statistical nature exists, which means that is of statistical nature, which means that the correlation between parallel orientations is short-ranged. If this is so, the polar disorder modulates the local and intermolecular potentials from one lattice site to another, thereby introducing alignment disorder of the

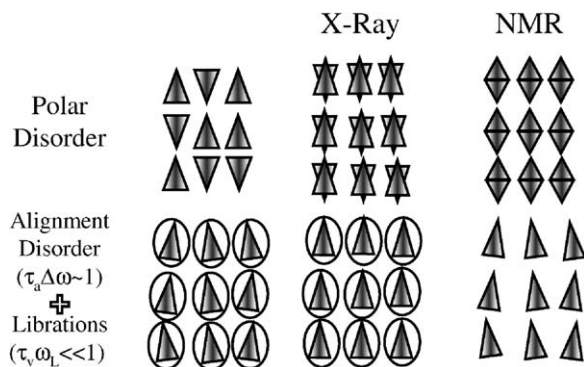


Fig. 15. Schematic of polar and alignment disorder as measured by XRD and NMR. Upper line: polar disorder with random up or down orientations of the direction of the molecules with equal probabilities to restore the inversion symmetry; for X-ray, the two directions are possible with equal probabilities on each site; NMR cannot measure polar disorder, all sites are equivalent. Lower line: alignment disorder of the molecules characterized by a long correlation time as compared to the inverse Larmor frequency ω_L , and librational disorder represented by ellipses of thermal-induced rotations (with angular amplitude possibly larger than the corresponding disalignment) around the mean alignment direction of the molecules. The frequencies of librations $1/\tau_v$ is much larger than the Larmor frequency. For X-ray, both orientational disorders are mixed up with a preponderant contribution of the high-frequency librations; for NMR, only alignment disorder remains.

molecules. Another important issue in close-packed crystal concerns the possibility of dynamical inversion of the molecules within the two polar directions. In general, such flip-flop exchange was thought to be impossible for steric reasons, or at least to occur very rarely due to very large activation enthalpies or small attempt frequencies. Provided that the flip-flop rate falls in the NMR time-scale, which can detect rates as slow as mHz, 2D and 1D selective saturation exchange experiments should shed light on such rare motions.

Example of polar-alignment disorder was evidenced in 2,3-dimethylnaphthalene¹⁹⁹ and azulene by Luz *et al.*²⁰⁰ with single-crystal deuteron NMR. In these compounds, polar disorder results from the packing of molecules lacking inversion symmetry that occupies special crystallographic sites with inversion symmetry. The local inversion symmetry is restored by random orientations of the molecules within two directions. The authors quantified the resulting alignment disorder from linewidth anisotropy studies, and found a tilt dispersion of about $\sim 1\text{--}2^\circ$. Interestingly, this small value was compared to the observed angular dispersion of the molecules with respect to their principal axes as estimated from the thermal factor measured by X-ray diffraction. The corresponding angular dispersion is in the range $3\text{--}4^\circ$, much larger than the angular alignment disorder estimated from NMR studies. The discrepancy was explained by different time-scales, the former corresponding to very high frequencies in the far IR that are averaged out by NMR. The latter NMR estimation corresponds to much slower or quasi-static orientational processes, which are apparently too small or too rare to be detected by X-ray diffraction. In addition to the alignment disorder, it emerges from extensive 2D and 1D selective saturation exchange experiments that slow and ultraslow molecular motions proceed in these samples with rates of the order 0.1 Hz, and the authors characterized the nature of these motions. Similar methods were used to investigate the hindered flip of phenyl rings in *o*-terphenyl,²⁰¹ or the dynamics of ammonium group ND_4^+ in ammonium persulfate²⁰² for instance.

Powder and single-crystal ^2H NMR experiments were also carried out to study the phase transitions of 1,2,3-trichloro-4,5,6-trimethylbenzene TCTMB-*d*3²⁰³ and *o*-dichlorotetramethylbenzene DCTMB-*d*12,²⁰⁴ which show considerable dynamical disorder in their room temperature phase.

Both compounds have three phases referred to as III, II, I in order of increasing temperature. Phase II is monoclinic with two symmetry-related molecules per unit cell, the molecules being at sites with center of inversion like the examples already presented in the previous paragraphs. In these compounds, the competition between energy and entropy is in favor of orientational disorder because the gain in orientational entropy is much larger than the small increase in energy introduced by depacking because the

van der Waals radii of the methyl group CH_3 (3.54 Å) and chlorine Cl (3.56 Å) are very similar. The local inversion symmetry broken by the asymmetric molecule is restored on average by molecular planar rotational disorder; other six orientations about an axis perpendicular to the benzene ring. On decreasing the temperature, the phase transition of TCTMB leads to phase III by an ordering of the molecules with almost no change in position, resulting in a triclinic structure by loss of the symmetry relationship between the two molecules (twofold screw-axis rotation along *b*). The situation is different for DCTMB because the transition is isostructural, phase III having the same monoclinic space group as the parent phase II with similar unit-cell parameters and atomic coordinates.²⁰⁴ The authors could even show from the analysis of the single-crystal rotation patterns that the molecules of DCTMB are slightly tilted by $\sim \pm 1^\circ$ from the mean benzene plane. This tilt was not detected by X-ray experiments. What differs in the two isostructural phases III and II of DCTMB is the relative ordering of the molecules, which become ordered in phase III, the para-axes pointing along one direction with left–right disorder of the Cl groups. Despite the differences in the structures of phase III, the discussion of the properties of both compounds can be drawn in parallel.

Interestingly, the II–III phase transition of both compounds seems to be related to molecular ordering rather than modification in crystal packing. Therefore, the transformations involved in these two compounds suggest that the probabilities of occupation of the six residence sites of the molecules are very important parameters, whose measurement might give some clues concerning the mechanism of these phase transitions. As already abundantly illustrated in previous sections, NMR is the technique to achieve this goal. The inversion symmetry relating the six sites by pairs, and using the normalization condition of the probabilities, it leaves two independent occupation probabilities to be measured.

The nature of the orientational disorder in phases III and II was investigated first by powder experiments to give an overview of the evolution of the anisotropy and asymmetry parameter of the averaged EFG interaction. In all phases, the EFG asymmetry parameter is different from zero, and continuously decreases as temperature increases, with no observed anomaly at the transition temperature. That the asymmetry is definitively nonzero over the whole temperature range shows that the planar reorientational motion consists of jumps over six asymmetric potentials wells, which retain the centrosymmetry on average, and that the population of the different sites continuously evolves with temperature. The authors argued that a precise estimation of the two unknown occupation probabilities cannot be drawn from powder spectra without simplifying assumptions. The reasons come from the model of sixfold jump around the axis normal to the benzene

ring, which predicts that the two occupation probabilities affect the asymmetry parameter η_a and the direction of the principal axes in the plane of the motion of the averaged EFG tensor, but not the largest eigenvalue $\langle T \rangle_{zz}$. Consequently, since the powder spectra provide only one measure (the asymmetry parameter η_a of the averaged tensor) for two unknowns, single-crystal experiments that measure both the eigenvalues and the orientation of the principal axes of the averaged tensor are necessary.^{203,204}

From single-crystal experiments, the authors extracted the three different probabilities of occupation in phase II. Even at the largest temperature, they differ from the expected value of equiprobable probability 1/3 suggested by X-ray diffraction experiments, demonstrating that the rotational planar disorder is far from being uniform in phase II, with favored orientations with respect to the others. As temperature decreases, the probability corresponding to the ordered site increases for both compounds. A fit of the variation of the probabilities with temperature could only be achieved with an entropy contribution, Eq. (12), and the site degeneracies and enthalpies were determined. Different considerations and interpretation concerning the ordering and the phase transition mechanisms were proposed by the authors. The probabilities in the triclinic phase III of TCTMB were also determined, and the molecular ordering becomes only complete below 100 K.²⁰³ The authors concluded that although the phase transition of TCTMB is weakly first order, the molecular disordering takes place over a very large temperature range, and the disordering remains biased in the HTP II. Other results concerning relaxation, dynamics and tunneling not reported here can be found in the quoted articles (Fig. 16).

6.3. Parallel linear channels-inclusion compounds

The cocrystallization of molecules of different shapes may lead to a host/guest structure where the guests are included in more or less open cavities

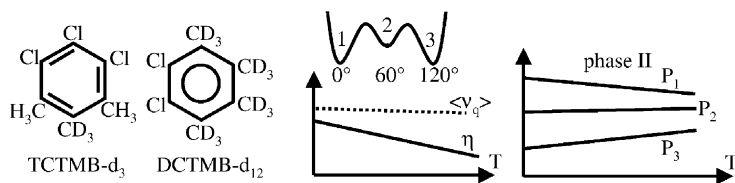


Fig. 16. Schematic of the occupation probabilities in phase II of TCTMB and DCTMB. From left to right: molecules under study, three well potential, averaged quadrupolar interaction and asymmetry parameters measured from powders spectra, occupations probabilities calculated from single-crystal experiments.

built by the hosts. In this section, we are primarily concerned with the important family of the intergrowth compounds that grow as single crystal with parallel linear channels of host that cross the whole sample, with a quasi-one-dimensional sublattice of guests in each channel.

Oriented structures composed of parallel linear channels are important from both the practical and fundamental point of view, because new properties are expected due to their low dimensionality and confinement effects.^{205,206} Among the different materials that build parallel linear channels, urea, perhydrotriphenylene (PHTP) or thiourea-based intergrowth compounds form a very interesting family of inclusion compounds.²⁰⁷ For instance, when the guest molecules are well chosen, the urea builds a hexagonal array of parallel one-dimensional channels encapsulating the guest molecules. Hexagonal urea can host numerous molecules such as *n*-alkanes, dibromo-alkanes,²⁰⁸ dioctanoyl peroxide,²⁰⁹ and decanedicarboxylic acids.²¹⁰ Another important property of intergrowth compounds based on urea comes from the misfit between the periodicity of the urea and guest sublattices along the channel axis *c*. This incommensurate property along *c* opens new degrees of freedom that can be used by the system to minimize its free energy.

The interest of such compounds concerns fundamental physics (incommensurate compounds, physical properties of low-dimensional and strongly correlated systems, etc.), but also applications when the guest molecules have a given function (nonlinear optical properties, 1D conductivity, etc.).²¹¹ The macroscopic physical properties of such compounds result from the competition between host/host, host/guest and guest/guest interactions. It is thus of fundamental importance to be able to precisely quantify the guest orientational and translational disorder. In the channels, the disorder of the guests has very large amplitudes and is mainly of dynamical nature. Traditional X-ray or neutron diffraction methods were found almost blind to the guest orientation in the plane perpendicular to the channel axis. Although IQNS studies brought a number of information on the guests' trajectories into the channel, the resolution usually limited the time-scales to a few GHz, leaving the slower motion tracking to NMR techniques. Solid-state NMR is particularly suited because of its high versatility. The contribution of CPMA⁵ ¹³C powder NMR to follow the motion and conformations of the guests was reviewed in ref. 212. The elastic properties of the ultraconfined chains of *n*-alkane in the urea linear channels could even be measured from powder ²H high-pressure NMR.²¹³ A small review by Prout,²¹⁴ discussed "the synergy between X-ray diffraction and solid-state NMR" in the study of molecular motion. In particular, the phase transitions in thiourea intergrowth compounds as studied by ¹³C and ²H NMR and X-ray diffraction (XRD) were considered.^{214–217}

The examples chosen below were limited to compounds whose growth leads to sufficiently large single crystals to be studied by deuterium ^2H NMR. The guest motion is probed by the C–D bond orientation and dynamics through the dynamical averaging of the quadrupolar interaction carried by the covalent bond. Therefore, static or dynamical orientational disorder can be characterized by the orientation distribution around the main channel axis c , and *single-crystal* NMR measurement as a function of the magnetic field orientation around the c -axis will give the guest axial orientation. When orientational disorder occurs, a method to extract the orientational probability density of the guests from single-crystal studies, based on an inversion procedure with Tikhonov regularization and non-negativity constraints that also implements the nonideal response of the pulse sequence, was developed.²¹⁸

The phase transitions of nonadecane $\text{C}_{19}\text{D}_{40}$ ⁸⁷ or 1,10-decanedicarboxylic acids²¹⁹ in hydrogenated urea, $\text{CO}(\text{NH}_2)_2$, were followed from room temperature down to 90 K. In contrast to nonadecane where the guests are more or less decoupled within a channel, decanedicarboxylic acids are expected to form infinite one-dimensional intrachannel H-bonded chains of guests. From rotation patterns at the lowest temperature, it was shown that nonadecane chains are ordered with a residual orientational disorder smaller than $\sim 3^\circ$,²²⁰ and point toward the corner of the hexagons. An unexpected *pretransitional broadening* of the lines was also evidenced on approaching the phase transition from above, which started tens of degrees above T_c with a value of ~ 5 kHz to reach ~ 25 kHz near T_c (see Fig. 17). The decrease in the linewidth bears similarities with the evolution of the static susceptibility measured by neutron scattering that exhibits a critical behavior. From hole-burning experiments, it was proved that the broadening was *inhomogeneous* and static on the linewidth time-scale. Although inhomogeneously

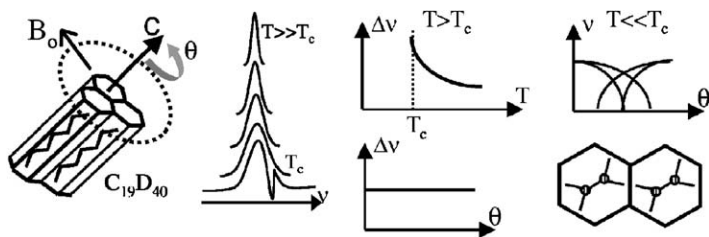


Fig. 17. Schematic of the nonadecane/urea-inclusion compound. From left to right: single-crystal experiment by rotation around the channel axis. Critical inhomogeneous linebroadening on approaching the transition temperature from above, with a lineshape invariant by rotation around c ; “hole burning” in the last spectrum proves the inhomogeneous nature of the broadening. Schematic of rotation patterns that gives the chain orientation in the low-temperature phase.

broadened, the lineshape was proved invariant by rotation around the c -axis. This critical inhomogeneous broadening was interpreted with a model of distributions of local-order parameters that breaks locally the high-temperature symmetry, but in a conserved manner to restore the symmetry on average over the whole sample.⁸⁷ Note the similarity of these results with the recent interpretation of local high-temperature symmetry breaking in BaTiO₃. This line broadening was not observed on powder spectra for obvious reasons.

In contrast to nonadecane/urea, the diacid compound exhibits strong inhomogeneously broadened spectra at all temperatures, which are also invariant by rotation around c in the HTP. This difference was attributed to the strong intrachannel coupling of the guests by the HBs. At the lowest temperature, the single-crystal spectra were surprisingly close to the theoretical spectra obtained from a 2D uniform disorder. However, the small differences measured as a function of rotation around the channel axis contained sufficient information to lead the orientational distribution.²¹⁸ By adapting second-moment methods to two-dimensional rotational disorder, the decrease as a function of temperature of the quadrupolar second moment of the single-crystal spectra acquired with a magnetic field perpendicular to the channel axis gave informations on the phase transition.²¹⁹

An example of space-group symmetry analysis and use of the Landau theory framework concerns one of the two phase transitions of an inclusion compound with hydrogenated thiourea host and perdeuterated cyclohexane C₆D₁₂ guests. This compound was studied by Desmedt *et al.*²²¹ with powder synchrotron XRD, and powder and single-crystal ²H NMR. The space groups of the three phases as well as the evolution of the cell parameters as a function of temperature were determined. The rhombohedral parent phase I transforms into a monoclinic phase II at 149 K, and the transition was shown of second-order nature and order–disorder type. Further decreasing the temperature below 129 K gives rise to an isostructural phase transition to another monoclinic phase III, and the transition has a first-order nature. From the NMR measurements, the authors have shown that the rotation of the cyclohexane molecule around its molecular C₃ axis is always fast on the NMR time-scale at all temperatures. The motion of this molecular axis with respect to the host frame occurs within six sites related by the symmetries of the D₃ point group, and can be interpreted in the fast-motion regime with a multidimensional pseudospin model based on symmetry adapted linear combinations of the occupation probabilities of the different sites. Typically, the averaged deuterium quadrupolar tensor is thus a function of three unknown variables, the tilt angle λ of the C₃^m molecular axis with respect to the channel c -axis and two “order” parameters ρ_i . Because the analysis of powder spectra only gives two parameters (the anisotropy and asymmetry

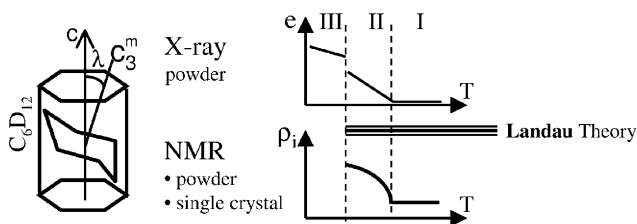


Fig. 18. Schematic of the cyclohexane/thiourea-inclusion compound. The strain e and the order–disorder pseudospin variables extracted from NMR experiments were interpreted in the framework of Landau theory for phase transition I \rightarrow II.

parameters of the motionally averaged quadrupolar tensor), single-crystal experiments are necessary for determining these parameters completely. Part of the indetermination on the angles coming from the inherent $\pm v$ symmetry of deuterium NMR spectra was solved by the use of molecular dynamics (MD) simulations. The evolution of the three parameters in phases I and II could be extracted as a function of temperature. In particular, the motion of the molecular C_3 symmetry axis occurs within six equivalent sites in phase I, that become inequivalent in phase II, $\rho_i \neq 0$. In phase III, this motion is frozen. The authors could interpret the continuous-phase transition I \rightarrow II within the framework of Landau theory, with the strains as secondary order parameters. The reader is referred to the ref. 221 for details²²¹ (Fig. 18).

7. MISCELLANEOUS PHASE TRANSITIONS

7.1. Pure NQR and phase transitions

For site with point symmetry lower than cubic, the quadrupolar interaction partially splits the $2I+1$ degenerated nuclear energy levels into subgroups with energy differences proportional to the product QV_{zz} . Depending on the strength of the quadrupolar interaction QV_{rs} compared to the Zeeman interaction γB , resonance techniques can be divided into two limit cases: the high-field extreme of NMR when the Zeeman splitting dominates the quadrupolar interaction or the low-field limit of NQR when the quadrupolar interaction is predominant.²²² When only the Earth's magnetic field is present, the pure NQR technique directly probes the natural energy splitting resulting from the quadrupolar interaction with a radio frequency field.

Unlike NMR where the dominant Zeeman interaction fixes the reference frequency of the nuclei, the NQR frequency of the nucleus is not known since it specifically depends on the nuclear environment, that is of the

physics of the material under study (Note that the considerations of Section 2.3 concerning Eqs. 2–3 are valid for the NQR frequencies and relaxation times). Other drawbacks are small sensitivities, spurious signals, sometime frequencies that are too small to be detected with actual NMR high-field spectrometers that cover higher and higher frequencies, or unsuitable probes, etc. As a consequence, the search of the NQR resonant frequencies is a very tedious and time-consuming task, mainly incompatible with the availability of the spectrometers. However, recent progress in methodology, probe design and signal detection helped in overcoming some of the acquisition technical problems.^{222–227} As a result, NQR techniques are still interesting and promising in the detection of drugs or explosives,²²⁸ even for much demanding disciplines like pharmacology.^{229,230}

7.1.1. *NQR features*

Once the resonance frequencies of the nucleus under interest are found, it is important to emphasize the ability of NQR techniques to detect subtle structural modifications and motions that NMR cannot easily distinguish, or that are ambiguous. This is because the NQR frequency directly probes the EFG, and thus its variations with internal or external parameters. Another important difference between NQR and NMR concerns the angular dependence of frequencies and amplitudes. In NMR, the external magnetic field breaks the isotropic symmetry, and the frequencies depend on the polar angles relative to the orientations of the PAS of the EFG at the nucleus with respect to the laboratory frame. In presence of strong intrinsic disorder of the material (glasses, incommensurate phases, etc.), the intrinsic distribution of EFG is often hidden by the inhomogeneous broadening introduced by the powder or polycrystalline average. On the other hand, in NQR, the resonant frequencies depend only on the eigenvalues of the EFG, whereas both the excitation and the reception of the signal are affected by the relative orientation of the emitting/receiving coil with respect to the PAS of the EFG. Therefore, in pure NQR, it is the amplitude of the signal that is angular-dependent. A powder sample gives a single line, which is an inhomogeneous superposition of lines, whose intensity depend on the relative orientation between the EFG tensor and the coil axis but not the frequency. Thus in contrast to NMR, the line broadening in pure NQR would only reflect the distribution of EFG (neglecting dipolar broadening and the residual external magnetic fields). This property was abundantly used in the study of incommensurate phases because the shape of the spectrum as a function of frequency is directly related to the modulation of the quadrupolar interaction. Indeed, a development in series of the EFG as a function of the modulation $\mu(x)$ leads as a first approximation of the NQR resonant frequency

$\nu_q(x) \sim \mu(x)$, whereas for NMR $\nu_q(x, \theta, \phi) \sim \mu(x)f_\mu(\theta, \phi)$ the frequency is also a function of the polar angles of static magnetic field with respect to the EFG PAS.

Although the studies of phase transitions by NQR methods stay an active field that draw important results, they are not considered in this review article, the reader can refer to the reviews of K.B. Dillon²²³ in the book series *Spectroscopic Properties of Inorganic and Organometallic Compounds*. We only give an example below of the utility of NQR to solve ambiguous NMR site multiplicities.

7.1.2. Ferroelastics, site multiplicity and NQR

Ferroelastic compounds are characterized by the buildup of a homogeneous spontaneous strain. As a consequence of the phase transition, the low-symmetry phase splits into different domains of identical free energy that are related by some of the lost symmetries of the high-symmetry phase, and that could be switched within each other by application of an external stress. Single-crystal NMR is uniquely suited to study such transitions, but also NQR to retrieve informations about chemical equivalence.

For LiCsSO_4 , the variation of the EFG parameters ($eQV_{zz}/h, \eta_q$) at the lithium ^7Li and cesium ^{133}Cs sites²³¹ are linear other than the whole temperature range, which includes the second-order ferroelastic phase transition at 202 K. However, the HT ^7Li and ^{133}Cs single-crystal lines split into two and three lines, respectively, in the LTP. In addition, the orientation of the ^{133}Cs PAS do not change with temperature, but the ^7Li PAS is modified, indicating a rotation of the LiO_4 tetrahedra. The line splitting was interpreted by the creation of different kinds of ferroelastic domains. This is an example where a powder NMR experiment, which is only sensitive to the eigenvalues of the EFG, would not detect the phase transition because no anomaly would appear in the evolution of the spectra, nor of the EFG parameters calculated from the spectra singularities or fit. Only single-crystal experiments are able to evidence a line splitting, or a modification of the orientation of the PAS.

For quadrupolar nuclei $I \geq 1$ with strong quadrupolar interaction as compared to the CSA anisotropy ($\delta_q \gg \delta_{\text{CSA}}$) and MAS frequency, chemical equivalence is carried out by the EFG eigenvalues. In this case, NQR is sometime an interesting alternative to NMR because it probes directly the eigenvalues of the quadrupolar Hamiltonian whatever the nature (powder, single or polycrystal) of the sample. As a result, only one set of line per chemically inequivalent sites appears. NQR is fruitful when there are suspicions that the crystal is split into domains. Then it is possible to erroneously interpret the single-crystal NMR line splitting without any other

information. We give two examples of applications of NQR to determine chemical equivalence.

Tetramethylammonium cadmium chloride, $(\text{CH}_3)_4\text{NCdCl}_3$ (TMCC) experiences two successive structural phase transitions at 118 and 104 K. The high-temperature hexagonal phase I $\text{P6}_3/\text{m}(\text{Z} = 2)$ first transforms to a monoclinic $\text{P2}_1/\text{m}(\text{Z} = 2)$ phase II that converts into phase III of symmetry $\text{P2}_1/\text{b}(\text{Z} = 12)$ below the second transition temperature. Of particular interest is the analysis of the phase transitions with respect to the contribution of the organic cation $(\text{CH}_3)_4\text{N}^+$ and the structure of the inorganic chain $-\text{CdCl}_3-$. But XRD and single-crystal NMR patterns are complicated by additional splitting coming from the ferroelastic domains appearing in phases II and III. A complete determination and consistent understanding of the ferroelastic domain structure of phases II and III could only be achieved by a thorough combined analysis of XRD data,²³² ^{35}Cl single-crystal NMR and NQR spectra^{233,234} and ^{14}N single-crystal NMR results.⁶³ ^{35}Cl probes the inorganic anion and ^{14}N the organic anion. The ^{35}Cl NQR experiments were necessary to determine the true number of chemically inequivalent sites whatever the domain structure. The angle between the twins was measured from the rotation patterns of both nuclei. The two values are consistent, and also agree with estimations derived from symmetry considerations and XRD data.

The second example comes from a 3D H-bonded ferroelectric and ferroelastic system, $(\text{CH}_3)\text{NH}_2\text{Al}(\text{SO}_4)_2 \cdot 6\text{H}_2\text{O}$, investigated by single-crystal ^{27}Al NMR.²³⁵ The number of lines observed from NMR was twice the number of lines expected from symmetry considerations. To check whether the doubling of the number of lines was a consequence of twinning, double-resonance experiments were performed to indirectly detect the zero-field NQR quadrupolar interaction of ^{27}Al via the protons. Two chemically distinct sites were found, in contradiction with the measured space group, but the very similar EFG parameters are compatible with a pseudo two-fold axis.

Miscellaneous phase transitions are listed in Table 3.

8. CONCLUSION AND PERSPECTIVES

In this review, we tried to highlight the possibilities of using NMR approaches for exploring phase transformations. The merit and achievements of NMR in the study of phase transitions is quite clear. Owing to its selectivity and sensitivity, NMR helps in discovering the existence of a transition, the identification of the different phases and the characterization of structural and dynamical order in the different phases. In favorable cases,

Table 3. Miscellaneous phase transitions

Compound	Method and comment	Reference
NH ₄ Br	¹ H relaxation, high-hydrostatic pressure → 8 kbars	236
Betaine phosphate—phosphite mixed crystals	² H SC, 2D exchange, T- <i>x</i> phase diagram	237
Ag ₇ P ₃ S ₁₁	³¹ P, ¹⁰⁹ Ag MAS NMR, X-ray, Raman scattering, electrical conductivity, Reentrant phase transition	238
Ag _x Cu _{1-x} I	⁶³ Cu, X-ray, phase diagram	239
Liquid crystal	¹ H relaxation at different frequencies, critical behavior	240
Ferroelectric liquid crystal	² H, SAXS, order parameter	241
Decylammonium chloride	² H NMR, order parameter	242
Liquid crystal	² H NMR, smectic ordering	243
Banana mesogens	² H NMR, homogeneous broadening	244
Betaine phosphate	³¹ P relaxation, critical slowing down	245
ClC ₆ H ₄ .2SO ₂	³⁵ Cl, normal-incommensurate, critical features	246
Rb ₂ ZrBr ₄ , Rb ₂ ZrCl ₄	³⁵ Cl, ⁸⁷ Rb, normal-incommensurate, critical frequency shift	247
CCl ₃ CONH ₂	¹ H relaxation at ≠ frequencies, FE, proton-proton distances are estimated	248
H ₃ NCH ₂ COOH ... H ₂ PO ₃ and deuterated analogue	¹ H, ¹³ C, ³¹ P spin-lattice relaxation, FE	249
Li ₂ Ge ₇ O ₁₅	⁷ Li SC, FE	250
(C ₂ NH ₂ COOH) ₃ H ₂ BeF ₄	⁹ Be SC NMR, exchange NMR, FE	251
NaNO ₂ + 20% KNO ₃ impurities	²³ Na, FE, influence of impurities	252
PbSc _{1/2} Nb _{1/2} O ₃	⁴⁵ Sc, ⁹³ Nb, ²⁰⁷ Pb SC, ferroelectric relaxor, local method necessary	253,254
(C ₄ H ₈ NH ₂)SbCl ₆ ... (C ₄ H ₈ NH ₂)Cl	¹ H, RX, DSC, dielectric, FA	255
Cs ₃ H(SeO ₄) ₂	¹ H, X-ray, FA, domain structure	256
TiH ₂ PO ₄	¹ H T _{1ρ} , ³¹ P MAS (243 MHz, 14 T), FA, ³¹ P linewidth evolution	257

Table 3. (Continued)

Compound	Method and comment	Reference
LiNH_4SO_4	^1H SC, FA	258
LiXSO_4 family, $\text{X} = (\text{Na}, \text{K}, \text{Rb}, \text{Cs})$	^7Li SC, FA, short review	259
LiKSO_4	^7Li , ^{39}K SC, FA	260–262
BiVO_4	^{51}V SC, relaxation, FA doping with Eu_2O_3 , ferroelastic	256
$\text{LiK}_{0.9}\text{Rb}_{0.1}\text{SO}_4$	^{87}Rb SC, FA domains, mixed phases, T_c shifted by 50 K by impurities	263
CsPbCl_3	^{133}Cs , ^{207}Pb SC, FA twin structure	264, 265
$[\text{NH}_2(\text{CH}_3)_2]_2\text{SeBr}_6$	^1H , lists of NMR results on polymethyl ammonium compounds, OD	266
Ethyl ammonium halide salts $\text{C}_2\text{H}_5\text{NH}_3^+ \text{X}$ ($\text{X} = \text{Cl}, \text{Br}$ or I)	^1H , ^2H , DSC, lists of NMR results on similar compounds, OD	267
van der Waals solid C_{60}	^{13}C static, MAS, relaxation, NMR/IQNS, OD	268
C_2 or CN	^{13}C MAS, synchrotron powder diffraction, OD	269
NH_4HSO_4	^1H relaxation, SC, FE	270
KHSO_4	^1H , ^{39}K , SC, FE	271, 272
RbHSO_4	^{87}Rb SC, FE	273
MHSO_4 family	M and ^1H SC, short review	274
$(\text{Py})_2\text{PdCl}_4$	^1H NMR, ^{35}Cl NQR, X-ray, DSC	275
Cyclohexane, benzene	^1H , confinement in MCM-41, SBA-15	276
5CB	^1H , confinement in MCM-41	277
$\text{C}_6\text{H}_{11}\text{Cl}/\text{SC}(\text{NH}_2)_2$	^1H , inclusion compound	278
Bromo and iodo pentamethylbenzene	^1H relaxation, DSC	279
$(\text{C}_4\text{H}_9)_4\text{NI}$	^1H , RX, DSC, conductivity, ionic conduction	280
$[\text{N}(\text{CH}_3)]_2\text{CuCl}_4$	^1H SC	281
Thermotropic liquid crystal	$^{1,2}\text{H}$ PGSE NMR, anisotropy of diffusion	282
$[\text{Cd}(\text{H}_2\text{O})_6](\text{BF}_4)_2$	^1H , ^{19}F , DSC, FT-MIR	283
15-Crown-5NaI, 15-crown-5NaClO ₄ , 21-crown-7KI	^2H , DSC, RX	284

Table 3. (*Continued*)

Compound	Method and comment	Reference
9-Hydroxyphenalenone derivatives	^2H powder and SC, low temperatures 5–60 K	285
Oleic acid	^{13}C	286
4-Iodobenzoic acid	^{13}C , RX, DSC	287
Benzene	^{13}C relaxation, confined benzene inside titanate nanotubes	288
(TMTTF) $_2\text{XF}_6$, X = As, P	^{13}C SC, charge ordering	289
bis(4-chlorophenyl) sulphone	^{35}Cl , incommensurate phase	290
TlGaSe $_2$	$^{69,71}\text{Ga}$, ^{205}Tl , incommensurate, FE, layered compound	291
Rb $_2\text{CoCl}_4$	^{87}Rb SC, relaxation	292
Chiral liquid crystal	^{129}Xe , diffusion	293
Cs $_2\text{CaCl}_4 \cdot 2\text{H}_2\text{O}$	^{133}Cs SC, relaxation	294

Note: SC = single crystal; FE = ferroelectric; FA = ferroelastic; OD = order–disorder.

a direct observation of the precursory ordered clusters as well as informations about the anisotropy of the correlations is possible.

Although the pulse sequences used to study phase transitions are usually quite simple in the examples presented in this review (one to maximum four pulses), the interpretation may be subtle. Solid-state NMR nevertheless remains a difficult technique since quantitative interpretation of the spectra rely on a profound knowledge of the chemical composition and structure of the sample: analysis of NMR results also requires a model to relate the observed NMR spectral shapes or relaxation behavior to hypothesis concerning the structure and dynamics of the atoms or molecules carrying spins. That NMR motionally average the atomic and molecular displacements that occur on a time-scale faster than $\sim 10^{-8}$ – 10^{-9} s is an important point that should be considered in the interpretation of data. In particular, the difference in perception between NMR and X-ray diffraction with regard to fast and slow dynamical disorder in molecular crystals undergoing phase transitions between different polymorphs was illustrated. In fact, the interpretation of NMR data almost always needs the support of other data obtained by different techniques. Therefore, we emphasized the different complementarities with X-ray (or neutron) diffraction, IQNS and other spectroscopic methods to provide, by cross-correlation of the different data, consistent picture of the phase transition.

Evidence of phase transitions are usually based on the presence of an anomalous behavior of NMR features, that is a jump from a value to another, a discontinuity in slopes, a dip or divergence, etc., the underlying idea of the detection of an anomaly being that atoms or molecules that are important in the mechanism of phase transition should modify their physical parameters in the vicinity of the phase transition, and thereby change the NMR internal Hamiltonian by coupling. However, this idea should be taken with great care because NMR averages fast motions and therefore the time-scale is an essential parameter. In general, significant changes in the NMR behavior are not always a sign of structural phase transition, but always imply a significant change in the motional behavior of the atom or molecule carrying the probing nuclei. The abrupt reduction of the proton second moment of benzene for temperature higher than $\sim 100\text{ K}$ ⁹⁵ is not the signature of a phase transition because no macroscopic crystal symmetry is broken. The second moment reduction only signs the reduction of the rotational correlation time τ_c of benzene around its hexad axis from the static $\tau_c\sqrt{M_2^{\text{static}}} \gg 1$ to the fast $\tau_c\sqrt{M_2^{\text{static}}} \ll 1$ motional regime on the NMR time-scale. A much more modern example of strong anomalies appearing in NMR parameter behaviors as a function of temperature, that may be erroneously interpreted as signatures of first-order phase transitions, is provided by the ferroelectric and ferroelastic system, $(\text{CH}_3)\text{NH}_2\text{Al}(\text{SO}_4)_2 \cdot 6\text{H}_2\text{O}$,²³⁵ which presents a very complicated 3D H-bonded network. The evolution of this compound as a function of temperature was followed by single-crystal ^1H and ^{27}Al NMR. In the paraphase and ferroelectric phases, the ^{27}Al lines show splittings and anomalous behaviors, which are reproduced at the same temperature by dips in the spin-lattice relaxation rate, whereas the lines and relaxation rate vary continuously across the para/ferro phase transitions. These anomalies were interpreted by rearrangements of the structural units to minimize energy, but they could not be interpreted as macroscopic phase transitions since the average crystal symmetry seems unchanged during the process.

Thus, NMR signatures of phase transitions are mainly indirect, and should be confirmed at least by DTA or DSC experiments. In principle, only a body of experimental data with different techniques is able to characterize a phase transition. Structural refinement will give an insight into the different phases. On the other hand, NMR is able to confirm a phase transition (for instance, from a steplike jump in an NMR parameter as a consequence of the jump of an NMR interaction tensor due to the phase transition), or to study dynamical ordering–disordering that cannot be detected otherwise.

That the probe is local in nature does not mean that collective behavior cannot be observed. In general, it can be shown that NMR measures the contribution of collective variables through a filter function, which partially

averages the different contributions as a function of the wave vector \mathbf{q} .²¹ For instance, the EFG at the deuterium nucleus in a C–D bond is almost entirely fixed by the electronic density of the bond. This is precisely this invariance of the strength of the quadrupolar interaction with external parameters that makes deuterium NMR so powerful, because deuterium NMR principally provides a local measure, after time averaging, of the relative orientation of a C–D bond with respect to the static magnetic field. But this local probe is sensitive to the collective variables governing both ordering and dynamics through an effective potential whose well depths and activation energies reflects the collective behavior of the system.

Further developments using NMR techniques are anticipated in the area of the characterization of space groups in complex systems. As a matter of fact, the assignation of the space groups of two polymorphs is usually the most important step to point out the broken symmetry associated with the phase transition, before searching for a plausible microscopic mechanism. The new strategies rely on new progresses in NMR, *ab initio* methods, MD simulation as well as fitting procedures. The improved high-field NMR resolution and sensitivity gives the opportunity to implement a large panel of correlation 2D pulse sequences, either to probe the homonuclear and heteronuclear connectivities or to separate 1D overlapping contribution, which gives NMR new opportunities to complement classical structural methods (X-ray, neutrons). Recent *ab initio* programs provide more and more reliable estimations of the main NMR parameters (chemical shielding, EFGs, etc.), whereas MD simulations can be used to generate physically consistent structural configurations. Finally, the fitting procedures can tackle a growing number of variables and constraints to reproduce the experimental data. This growing area of interest is reflected by a recent thematic volume of *Solid State Science*, edited by F. Taulelle in 2004, dedicated to “NMR crystallography”.²⁹⁵ Note that the most ambitious program, developed by F. Taulelle, claims that space groups, including the translational symmetries, can be extracted from a complete set of NMR measurements.^{296,297}

All the concepts introduced in this review are pertinent to other materials such as soft matter, liquid crystals and micellar systems. How soft matter or anisotropic fluids selforganize into mesophases with varying translational and orientational order through thermal phase transitions was reviewed in ref. 298. NMR methods to study micelles were recently reviewed by Furo.²⁹⁹ Methods to build binary or ternary “phase diagrams” from NMR data of physical gels,³⁰⁰ membranes,³⁰¹ water and lipid and peptides,^{302,303} bicelles,^{304–306} etc. were developed. A discussion of the potentialities of NMR and magnetic resonance imaging (MRI) in assessing phase transition in food can be found in ref. 307. Some articles containing more specialized

informations concerning important areas such as phase transitions of superconductors,^{308–310} incommensurate systems,^{311,312} glass transition,^{313,314} liquid crystals³¹⁵ and minerals.³¹⁶ See also the proceedings of the XVth (Leipzig 1999)³¹⁷ or XVIth (Hiroshima 2001)³¹⁸ *International Symposiums on Nuclear Quadrupole Interactions* that covers phase transitions.

Among the promising techniques that shall bring a lot of breakthrough in the study of phase transitions in soft matter, mesophases and solid inclusion or nanoporous materials, are the field-cycling NMR relaxometry methods,^{319,320} and the measurement of the anisotropy of diffusion coefficient by ^1H spin echo or PSGE. The latter gives important informations about mesophases in the liquid crystalline phase^{298,321} or aqueous solutions of surfactants.^{322,323} The use of ^{129}Xe NMR chemical shift and T_1 is also promising in the study of anisotropic environment and therefore phase transitions.³²⁴

The possibilities of the now available NMR techniques are far from being exploited in the study of phase transitions. Note, however, that wide line proton NMR at low fields (<100 MHz), variable temperature and high-hydrostatic pressure, in combination with structural data, thermodynamical and dielectric measurements, has been used with great success in studying the antiferroelectric and ferroelectric phase transitions in organic–inorganic hybrids, and building the T – P phase diagrams.

It is hoped that the present overview will encourage beginner and non-beginner researchers to make increasing use of the now available modern NMR techniques as well as help to convince NMR specialists that the study of phase transition still presents a promising challenge for further development.

ACKNOWLEDGMENT

I am indebted to B. Toudic for fruitful discussions.

REFERENCES

1. E. R. Andrew and E. Szczesniak, *Progr. Nucl. Magn. Spect.*, 1995, **28**, 11–36.
2. D. Massiot, F. Fayon, M. Capron, I. King, S. Le Calvé, B. Alonso, J. -O. Durand, B. Bujoli, Z. Gan and G. Hoatson, *Magn. Res. Chem.*, 2002, **40**, 70–76.
3. M. Bak, J. T. Rasmussen and N. Chr. Nielsen, *J. Magn. Res.*, 2000, **147**, 296–330.
4. A. E. Aliev and R. V. Law, *Nucl. Magn. Res.*, 2003, **32**, 238–291.
5. C. Dybowski, S. Bai and S. Van Bramer, *Anal. Chem.*, 2002, **74**, 2713–2718.
6. D. L. Bryce, G. M. Bernard, M. Gee, M. D. Lumsden, K. Eichele and R. E. Wasylshen, *Can. J. Anal. Sci. Spectr.*, 2001, **46**, 46–82.

7. D. L. Bryce, G. M. Bernard, M. Gee, M. D. Lumsden, K. Eichele and R. E. Wasylishen, <http://casgm3.anorg.chemie.unituebingen.de/klaus/nmr/index.html>.
8. D. D. Laws, H. -M. L. Bitter and A. Jerschow, *Angew. Chem. Int. Ed.*, 2002, **41**, 3096–3129.
9. S. P. Brown and H. W. Spiess, *Chem. Rev.*, 2001, **101**, 4125–4155.
10. M. E. Smith and J. H. Strange, *Meas. Sci. Technol.*, 1996, **7**, 449–475.
11. P. Hodgkinson and L. Emsley, *Progr. Nucl. Magn. Res. Spectr.*, 2000, **36**, 201–239.
12. A. Jerschow, *Progr. Nucl. Magn. Res. Spectr.*, 2005, **46**, 63–78.
13. M. E. Smith and E. R. H. van Eck, *Progr. Nucl. Magn. Res. Spectr.*, 1999, **34**, 159–201.
14. T. M. Alam and G. P. Drobny, *Chem. Rev.*, 1991, **91**, 1545–1590.
15. C. Bonhomme and J. Livage, *J. Phys. Chem. A*, 1998, **102**, 375–385.
16. C. Bonhomme and J. Livage, *J. Phys. Chem. A*, 1999, **103**, 460–477.
17. T. Helgaker, M. Jaszunski and K. Ruud, *Chem. Rev.*, 1999, **99**, 293–352.
18. K. A. Müller and A. Rigamonti (eds.), *Proceedings of the International School of Physics "Enrico Fermi"*, Course LIX, Local Properties at Phase Transitions, Societa Italiana Di Fisica, Bologna, 1976.
19. F. Owens, C. Poole and H. Farach, eds., *Magnetic Resonance of Phase Transitions*, Academic Press, New York, 1979.
20. A. Rigamonti, *Adv. Phys.*, 1984, **33**, 115–191.
21. F. Borsa and A. Rigamonti, Topics in current physics, *Structural Phase Transitions II*, Vol. 45, K. A. Müller and H. Thomas (eds.), Springer, Berlin, 1991, 82–183.
22. D. M. Grant and R. K. Harris, Wiley, Chichester, 1996.
23. L. D. Landau and E. M. Lifshitz, *Statistical Physics*, 3rd edition, Pergamon Press, New York, 1980 Chapter XIV.
24. M. T. Dove, *Am. Miner.*, 1997, **82**, 213–244.
25. F. Reif, *Fundamentals of Statistical and Thermal Physics*, McGraw-Hill, Kogakusha, Tokyo, 1965.
26. H. C. Bayer, *Z. Phys.*, 1951, **130**, 227–238.
27. M. H. Levitt, *Spin Dynamics: Basics of Nuclear Magnetic Resonance*, Wiley, Chichester, 2001.
28. B. Herreros, A. W. Metz and G. S. Harbison, *Sol. State Nucl. Magn. Res.*, 2000, **16**, 141–150.
29. J. M. Koons, E. Hughes, H. M. Cho and P. D. Ellis, *J. Magn. Reson. A*, 1995, **114**, 12–23.
30. J. T. Cheng, J. C. Edwards and P. D. Ellis, *J. Phys. Chem.*, 1990, **94**, 553–561.
31. W. P. Power, R. E. Wasylishen, S. Mooibroek, B. A. Pettitt and W. Danchura, *J. Phys. Chem.*, 1990, **94**, 591–598.
32. J. A. Weil, T. Buch and J. A. Clapp, *Adv. Magn. Res.*, 1973, **8**, 183–257.
33. T. J. Bastow, T. Mathews and J. R. Sellar, *Sol. State Ionics.*, 2004, **175**, 129.
34. A. Goldbach, F. Fayon, T. Vosegaard, M. Wachhold, M. G. Kanatzidis, D. Massiot and M. -L. Saboungi, *Inorg. Chem.*, 2003, **42**, 6996–7000.
35. R. J. Darton, P. Wormald and R. E. Morris, *J. Mater. Chem.*, 2004, **14**, 2036–2040.
36. I. Bull, P. Lightfoot, L. A. Villaescusa, L. M. Bull, R. K. B. Gover, J. S. O. Evans and R. E. Morris, *J. Am. Chem. Soc.*, 2003, **125**, 4342–4349.

37. A. Titze, J. Kusz, H. Böhm, H. -J. Weber and R. B'öhmer, *J. Phys. Condens. Mater.*, 2002, **14**, 895–913.
38. R. E. Dinnebier, P. Bernatowicz, X. Helluy, A. Sebald, M. Wunschel, A. Fitch and S. van Smaalen, *Acta Cryst. B*, 2002, **58**, 52–61.
39. E. Gaudin, F. Boucher, M. Evain and F. Taulelle, *Chem. Mater.*, 2000, **12**, 1715–1720.
40. O. J. Zogal, W. Wolf, P. Herzig, A. H. Vuorimäki, E. E. Ylinen and P. Vajda, *Phys. Rev. B*, 2001, **64**, 214110/1–214110/7.
41. T. Malcherek, M. Borowskib and A. Boseniekc, *J. Appl. Cryst.*, 2004, **37**, 117–122.
42. V. Korthuis, N. Khosrovani, A. W. Sleight, N. Roberts, R. Dupree and W. W. Warren Jr., *Chem. Mater.*, 1995, **7**, 412.
43. X. Helluy, C. Marichal and A. Sebald, *J. Phys. Chem. B*, 2000, **104**, 2836.
44. I. J. King, R. K. Harris, J. S. O. Evans, F. Fayon and D. Massiot, *Chem. Comm.*, 2001, **18**, 1766–1767.
45. F. Fayon, I. J. King, R. K. Harris, R. K. B. Gover, J. S. O. Evans and D. Massiot, *Chem. Mater.*, 2003, **15**, 2234–2239.
46. F. Fayon, G. L. S. Saout, L. Emsley and D. Massiot, *Chem. Comm.* 2002, 1702–1703.
47. F. Fayon, I. J. King, R. K. Harris, J. S. O. Evans, C. R. Chimie and D. Massiot, 2004, **7**, 351–361.
48. B. Alonso and D. Massiot, *J. Magn. Res.*, 2003, **163**, 347–352.
49. M. E. Lacey, R. Subramanian, D. L. Olson, A. G. Webb and J. V. Sweedler, *Chem. Rev.*, 1999, **99**, 3133–3152.
50. D. E. Warschawski, M. Traikia, P. F. Devaux and G. Bodenhausen, *Biochimie*, 1998, **80**, 437–450.
51. K. Gawrisch, N. V. Nadukuddy and I. V. Polozov, *Chem. Phys. Lipids*, 2002, **116**, 135–151.
52. Ad Bax, *Protein Sci*, 2003, **12**, 1–16.
53. V. D. Kodibagkar, C. D. Browning, X. Tang, Y. Wu, R. C. Bowman and M. S. Conradi, *Sol. State Nucl. Magn. Res.*, 2003, **24**, 254–262.
54. V. D. Kodibagkar, C. D. Browning, T. J. Udovic and M. S. Conradi, *Phys. Rev. B*, 2003, **67**, 174115/1–174115/8.
55. V. Kodibagkar, J. L. Herberg, R. C. Bowman Jr. and M. S. Conradi, *J. Alloys Compd.*, 2002, **330–332**, 179–182.
56. V. D. Kodibagkar, P. A. Fedders, C. D. Browning, R. C. Bowman, N. L. Adolphi and M. S. Conradi, *Phys. Rev. B*, 2003, **67**, 45107/1–45107/7.
57. A. Samoson, *The Encyclopedia of Nuclear Magnetic Resonance*, D. M. Grant and R. K. Harris (eds.), Vol. 9., Wiley, Chichester, 2002, 59–64.
58. A. Samoson, T. Tuherm, J. Past, A. Reinhold, T. Anupõld, I. Heinma, *Topics in Current Chemistry*, Vol. 246, Springer, Berlin, Heidelberg, 2004, 15–31.
59. I. Schnell and H. W. Spiess, *J. Magn. Res.*, 2001, **151**, 153–227.
60. S. Antonijevic and G. Bodenhausen, *Angew. Chem. Int. Ed.*, 2005, **44**, 2935–2938.
61. R. Siegel, T. T. Nakashima and R. E. Wasylshen, *Concepts Magn. Res. A*, 2005, **26A**, 62–77.
62. E. A. Hill and J. P. Yesinowski, *J. Chem. Phys.*, 1997, **107**, 346–354.
63. S. Mulla-Osman, D. Michel and Z. Czapla, *Phys. Stat. Sol. (b)*, 2003, **236**, 173–181.

64. G. Jeschke and M. Jansen, *Angew. Chem. Int. Ed.*, 1998, **37**, 1282–1283.
65. H. J. Jakobsen, H. Bildsøe, J. Skibsted and T. J. Giavani, *J. Am. Chem. Soc.*, 2001, **123**, 5098–5099.
66. T. Giavani, H. Bildsøe, J. Skibsted and H. J. Jakobsen, *J. Magn. Res.*, 2004, **166**, 262–272.
67. T. Giavani, H. Bilds, J. Skibsted and H. J. Jakobsen, *J. Phys. Chem. B*, 2002, **106**, 3026–3032.
68. A. Hauch, H. Bildsøe, H. J. Jakobsen and J. Skibsted, *J. Magn. Res.*, 2003, **165**, 282–292.
69. U. Gro Nielsen, J. Skibsted and H. J. Jakobsen, *Chem. Phys. Lett.*, 2002, **356**, 73–78.
70. M. D. Andersen, H. J. Jakobsen and J. Skibsted, *J. Phys. Chem. A*, 2002, **106**, 6676–6682.
71. Z. Gan, P. Gorkov, T. A. Cross, A. Samoson and D. Massiot, *J. Am. Chem. Soc.*, 2002, **124**, 5634–5635.
72. J. F. Stebbins, L. -S. Du, S. Kroeker, P. Neuhoff, D. Rice, J. Frye and H. J. Jakobsen, *Sol. State Nucl. Magn. Res.*, 2002, **21**, 105–115.
73. L. S. Du, R. W. Schurko, K. H. Lim and C. P. Grey, *J. Phys. Chem. A*, 2001, **105**, 760–768.
74. L. Frydman and J. S. Harwood, *J. Am. Chem. Soc.*, 1995, **117**, 5367–5368.
75. S. E. Ashbrook and S. Wimperis, *Progr. Nucl. Magn. Res. Spectr.*, 2004, **45**, 53–108.
76. J. P. Amoureux, C. Huguenard, F. Engelke and F. Taulelle, *Chem. Phys. Lett.*, 2002, **356**, 497–504.
77. H. J. Kim, M. Pruski, J. W. Wiench, D. Y. Jeong and S. H. Choh, *Phys. Rev. B*, 2001, **63**, 64107/1–64107/6.
78. D. E. Woessner and B. S. Snowden, *J. Phys. Chem.*, 1967, **71**, 952–956.
79. F. G. Riddell, R. A. Spark and G. V. Gunther, *Magn. Res. Chem.*, 1996, **34**, 824–828.
80. R. Glaser, D. Shiftan and M. Drouin, *Can. J. Chem.*, 2000, **78**, 212–222.
81. A. Bielecki and D. P. Burum, *J. Magn. Reson. A*, 1995, **116**, 215–220.
82. A. N. Klymachov and N. S. Dalal, *Sol. State Nucl. Magn. Res.*, 1996, **7**, 127–134.
83. G. Neue, C. Dybowski, M. L. Smith, M. A. Hepp and D. L. Perry, *Sol. State Nucl. Magn. Res.*, 1996, **6**, 241–250.
84. G. Neue and C. Dybowski, *Sol. State Nucl. Magn. Res.*, 1997, **7**, 333–336.
85. B. Langer, I. Schnell, H. W. Spiess and A. -R. Grimmer, *J. Magn. Reson.*, 1999, **138**, 182–186.
86. P. A. Beckmann and C. Dybowski, *J. Magn. Reson.*, 2000, **146**, 379–380.
87. H. Le Lann, C. Odin, B. Toudic, J. C. Ameline, J. Gallier, F. Guillaume and T. Breczewski, *Phys. Rev.*, 2000, **62**, 5442–5451.
88. J. E. Anderson and W. P. Slichter, *J. Chem. Phys.*, 1966, **44**, 1797–1802.
89. I. T. Horvath and J. M. Millar, *Chem. Rev.*, 1991, **91**, 1339–1351.
90. L. Ballard, A. Yu, C. Reiner and J. Jonas, *J. Magn. Res.*, 1998, **133**, 190–193.
91. M. de Langen and K. O. Prins, *Rev. Sci. Instrum.*, 1995, **66**, 5218–5220.
92. A. Zahl, A. Neubrand, S. Aygen and R. van Eldik, *Rev. Sci. Instrum.*, 1994, **65**, 882–886.
93. H. Huber, M. Mali, J. Roos and D. Brinkmann, *Rev. Sci. Instrum.*, 1984, **55**, 1325–1327.

94. N. Blombergen, E. M. Purcell and R. V. Pound, *Phys. Rev. B*, 1948, **73**, 679–712.
95. C. P. Slichter, *Principles of Magnetic Resonance*, Springer, Berlin, 1990.
96. M. Goldman, *J. Magn. Res.*, 2001, **149**, 160–187.
97. D. A. Torchia and A. Szabo, *J. Magn. Res.*, 1982, **49**, 107–121.
98. D. P. Kozlenko, S. Lewicki, J. Wasicki, A. Kozak, W. Nawrocik and B. N. Savenko, *Mol. Phys.*, 2001, **99**, 427–433.
99. J. Wasicki, S. Lewicki, D. P. Kozlenko, A. Kozak, W. Nawrocik, S. E. Kichanov, B. N. Savenko and T. Shchedrina, *J. Phys. Condens. Matter*, 2004, **16**, 3889–3900.
100. A. Watton, *J. Chem. Phys.*, 1976, **65**, 3653–3656.
101. W. Medycki and R. Jakubas, *Sol. State Nucl. Magn. Res.*, 2002, **21**, 44–52.
102. O. Kanert, R. K  chler, K. L. Ngai and H. Jain, *Phys. Rev. B*, 1994, **49**, 76–82.
103. M. Meyer, P. Maas and A. Bundle, *Phys. Rev. Lett.*, 1993, **71**, 573–576.
104. C. E. Lee, C. H. Lee, K. W. Lee and E. M. Lee, *Phys. Rev. B*, 2002, **66**, 012101.
105. C. E. Lee, C. H. Lee, K. W. Lee, E. M. Lee, J. Y. Choi and J. Kim, *Sol. State Commun.*, 2001, **118**, 283.
106. J. H. Van Vleck, *Phys. Rev.*, 1948, **74**, 1168–1183.
107. A. Abragam, *Principles of Nuclear Magnetism*, Oxford University, New York, 1994.
108. R. Goc, *J. Magn. Res.*, 1997, **132**, 78–80.
109. R. Goc, *Sol. State Nucl. Magn. Res.*, 1998, **13**, 55–61.
110. L. Latanowicz and E. C. Reynhardt, *J. Magn. Res.*, 1996, **121A**, 23–32.
111. J. G. Powles and H. S. Gutowsky, *J. Chem. Phys.*, 1955, **23**, 1692–1699.
112. R. Goc, *J. Phys. Condens. Mater.*, 1999, **11**, 2977–2982.
113. K. Schmidt-Rohr and H. W. Spiess, *Multidimensional Solid-State NMR and Polymers*, Academic, London, 1994.
114. J. H. Kristensen and I. Farnan, *J. Chem. Phys.*, 2001, **114**, 9608–9624.
115. D. Reichert, G. Hempel, H. Zimmermann, H. Schneider and Z. Luz, *Sol. State Nucl. Magn. Res.*, 2000, **18**, 17–36.
116. B. Beck, J. A. Villanueva-Garibay, K. Muller and E. Roduner, *Chem. Mater.*, 2003, **15**, 1739–1748.
117. G. L. Squires, *Introduction to the Theory of Thermal Neutron Scattering*, Dover, Mineola, 1996.
118. F. Guillaume, *J. Phys. IV*, 2000, **10**, 165–190.
119. F. Guillaume, J. P. Ryckaert, V. Rodriguez, L. Gonzalez Mac Dowell, P. Girard and A. J. Dianoux, *Phase Trans*, 2003, **76**, 823–830.
120. F. Fillaux, *Int. Rev. Phys. Chem.*, 2000, **19**, 553–564.
121. A. Detken, H. Zimmermann, U. Haeberlen and Z. Luz, *J. Magn. Res.*, 1997, **126**, 95.
122. M. Neumann, D. F. Brougham, C. J. McGloin, M. R. Johnson, A. J. Horsewill and H. P. Trommsdorff, *J. Chem. Phys.*, 1998, **109**, 7300–7311.
123. G. Eckold, H. Grimm and M. Stein-Arsic, *Physica B*, 1992, **180–181**, 336–338.
124. A. R. Lim and S. Y. Jeong, *Phys. State Sol.(b)*, 2001, **226**, 413–418.
125. C. Odin, *J. Phys. Chem. B*, 2004, **108**, 7402–7411.
126. C. Odin, *Magn. Reson. Chem.*, 2004, **42**, 381–388.

127. F. Haarmann, H. Jacobs, B. Asmussen, C. Nöldeke, G. J. Kearley and J. Combet, *J. Chem. Phys.*, 2000, **113**, 8161–8167.
128. F. Haarmann, H. Jacobs, J. Senker and E. Rössler, *J. Chem. Phys.*, 2002, **117**, 1269–1278.
129. F. Haarmann, H. Jacobs, J. Senker, E. Rössler, P. Müller, C. A. Kennedy, R. A. Marriott, L. Qiu and M. A. White, *J. Chem. Phys.*, 2002, **117**, 4961–4972.
130. R. Blinc and B. Žekš, *Soft Modes in Ferroelectrics and Antiferroelectrics*, North-Holland, Amsterdam, 1974.
131. S. Zumer and R. Blinc, *J. Phys. C: Sol. State Phys.*, 1981, **14**, 465–484.
132. K. H. Michel, *J. Chem. Phys.*, 1973, **58**, 142–152.
133. R. G. Petschek and B. I. Halperin, *Phys. Rev. B*, 1979, **19**, 166–176.
134. K. W. Lee, C. H. Lee, C. E. Lee and J. K. Kang, *Phys. Rev. B*, 1995, **52**, 16028–16030.
135. K. W. Lee, D. K. Oh, C. E. Lee, J. K. Kang, C. H. Lee and J. Kim, *J. Chem. Phys.*, 2002, **117**, 8004–8007.
136. K. W. Lee, C. E. Lee and J. -K. Kang, *J. Phys. Soc. Jpn.*, 2001, **70**, 2888–2891.
137. K. W. Lee, C. H. Lee, D. K. Oh, J. K. Kang, C. E. Lee and J. Kim, *Phys. Rev. E*, 2001, **64**, 042903/1–042903/3.
138. C. E. Lee, C. H. Lee and M. W. Park, *Sol. State Commun.*, 2004, **129**, 565–567.
139. P. Czarnecki, W. Nawrocik, Z. Pajak and J. Wasicki, *Phys. Rev. B*, 1994, **49**, 1511–1512.
140. Z. Pajak, P. Czarnecki, J. W. Wasicki and W. Nawrocik, *J. Chem. Phys.*, 1998, **109**, 6420–6423.
141. M. Szafranski and I. Szafraniak, *J. Phys.: Condens. Matter*, 2003, **15**, 5933–5944.
142. S. Lewicki, J. W. Wasicki, P. Czarnecki, I. Szafraniak, A. Kozak and Z. Pajak, *Mol. Phys.*, 1998, **94**, 973–979.
143. J. W. Wasicki, A. Kozak, Z. Pajak, P. Czarnecki, A. V. Belushkin and M. A. Adams, *J. Chem. Phys.*, 1996, **105**, 9470–9477.
144. Z. Fojud, R. Goc, S. Jurga, A. Kozak and J. Wasicki, *Molecular Phys*, 2003, **101**, 1469–1476.
145. I. Szafraniak, P. Czarnecki and P. U. Mayr, *J. Phys.: Condens. Matter*, 2000, **12**, 643–652.
146. J. Wasicki, S. Lewicki, P. Czarnecki, C. Ecolivet and Z. Pajak, *Mol. Phys.*, 2000, **98**, 643–649.
147. I. Szafraniak and P. Czarnecki, *J. Phys.: Condens. Matter*, 2002, **14**, 3321–3331.
148. J. W. Wasicki, P. Czarnecki, Z. Pajak, W. Nawrocik and W. Szczepański, *J. Chem. Phys.*, 1997, **107**, 576–579.
149. P. Czarnecki and H. Mauszyńska, *J. Phys. Condens. Mater.*, 2000, **12**, 4881–4892.
150. P. Czarnecki, A. I. Beskrovny, L. Bobrowicz-Sarga, S. Lewicki and J. W. Wasicki, *J. Phys.: Condens. Matter*, 2005, **17**, S3131–S3138.
151. Z. Pajak, P. Czarnecki, H. Mauszyńska, B. Szafranska and M. Szafran, *J. Chem. Phys.*, 2000, **113**, 848–853.
152. Z. Pajak, H. Maluszynska, B. Szafranska and P. Czarnecki, *J. Chem. Phys.*, 2002, **117**, 5303–5310.
153. J. Józków, R. Jakubas, G. Bastor and A. Pietraszko, *J. Chem. Phys.*, 2002, **114**, 7239–7246.

154. P. Szklarz, J. Zaleski, R. Jakubas, G. Bator, W. Medycki and K. Falińska, *J. Phys. Condens. Mater.*, 2005, **17**, 2509–2528.
155. J. Józkowa, R. Jakubasa, G. Batora, J. Zaleskib and R. Decressain, *J. Phys. Chem. Sol.*, 2000, **61**, 887–897.
156. W. Medycki, K. Holderna-Natkaniec, J. Swiergiel and R. Jakubas, *Sol. State Nucl. Magn. Res.*, 2003, **24**, 209–217.
157. B. Kulicka, R. Jakubas, G. Bator, Z. Ciunik and W. Medyck, *J. Phys. Condens. Mater.*, 2004, **16**, 8155–8172.
158. T. Gohda, M. Ichikawa, T. Gustafsson and I. Olovsson, *Phys. Rev. B*, 2001, **63**, 014101/1–014101/7.
159. M. Ichikawa, T. Gustafsson and I. Olovsson, *Sol. State Commun.*, 2002, **123**, 135–139.
160. M. Mehring and J. D. Becker, *Phys. Rev. Lett.*, 1981, **47**, 366–370.
161. H. Eckert, *NMR Basic Principles and Progress*, Vol. 33, P. Diehl, E. Fluck, H. Günther, R. Kosfeld, J. Seelig and B. Blümich (eds.), Springer, Berlin, 1994, 125–198.
162. A. N. Klymachyov and N. Dalal, *Sol. State Nucl. Magn. Res.*, 1997, **9**, 85–89.
163. D. L. Van der Hart, W. L. Earl and A. N. Garroway, *J. Magn. Res.*, 1981, **44**, 361–401.
164. N. S. Dalal, K. L. Pierce, J. Palomar and R. Fu, *J. Phys. Chem. A*, 2003, **107**, 3471–3475.
165. A. N. Klymachyov and N. S. Dalal, *Z. Phys. B*, 1997, **104**, 651–656.
166. N. S. Dalal, K. L. Pierce, J. Palomar and R. Fu, *Ferroelectrics*, 2004, **302**, 23–27.
167. J. Palomar and N. S. Dalal, *J. Phys. Chem. B*, 2002, **106**, 4799–4805.
168. N. S. Dalal, A. N. Klymachyov and A. Bussmann-Holder, *Phys. Rev. Lett.*, 1998, **81**, 5924–5927.
169. A. Bussmann-Holder, N. S. Dalal and K. H. Michel, *J. Phys. Chem. Sol.*, 2000, **61**, 271–274.
170. S. P. Gabuda, S. G. Kozlova and N. S. Dalal, *Sol. State Commun.*, 2004, **130**, 729–733.
171. A. Bussmann-Holder, N. Dalal, R. Fu and R. Migoni, *J. Phys. Condens. Mater.*, 2001, **13**, L231–L237.
172. R. Fu, A. N. Klymachyov, G. Bodenhausen and N. S. Dalal, *J. Chem. Phys. B*, 1998, **102**, 8732–8735.
173. J. Palomar, A. N. Klymachyov, D. Panizian and N. S. Dalal, *J. Phys. Chem. A*, 2001, **105**, 8926–8930.
174. T. J. Bastow and H. J. Whitfield, *Sol. State Commun.*, 2001, **117**, 483–488.
175. A. Taye, G. Klotzsche, D. Michel, S. Mulla-Osman and R. Böttcher, *J. Phys. Condens. Mater.*, 1999, **11**, 871–879.
176. D. A. Bussian and G. S. Harbison, *Sol. State Commun.*, 2000, **115**, 95–98.
177. B. Zalar, V. V. Laguta and R. Blinc, *Phys. Rev. Lett.*, 2003, **90**, 037601/1–037601/4.
178. B. Zalar, A. Lebar, J. Seliger, R. Blinc, V. V. Laguta and M. Itoh, *Phys. Rev. B*, 2005, **71**, 064107/1–064107/12.
179. R. E. Alonso, C. O. Rodríguez and A. López García, *Phys. Rev. B*, 2004, **69**, 212106/1–212106/3.
180. E. A. Stern, *Phys. Rev. Lett.*, 2004, **93**, 037601/1–037601/4.
181. R. Pirc and R. Blinc, *Phys. Rev. B*, 2004, **70**, 134107/1–134107/7.
182. M. Itoha, T. Yagi, Y. Uesu, W. Kleemann and R. Blinc, *Sci. Technol. Adv. Mater.*, 2004, **5**, 417–423.

183. M. Fanfoni and M. Tomellini, *Eur. Phys. J. B*, 2003, **34**, 331–341.
184. M. Avrami, *J. Chem. Phys.*, 1941, **9**, 177–184.
185. M. Avrami, *J. Chem. Phys.*, 1940, **8**, 212–224.
186. M. Avrami, *J. Chem. Phys.*, 1939, **7**, 1103–1112.
187. A. Schmidt, S. Kababya, M. Appel, S. Khatib, M. Botoshansky and Y. Eichen, *J. Am. Chem. Soc.*, 1999, **121**, 11291–11299.
188. B. V. Schonwandt and H. J. Jakobsen, *J. Solid State Chem.*, 1999, **145**, 10–14.
189. M. Winterlich, H. Zimmermann and R. Böhmer, *J. Non-Cryst. Sol.*, 2002, **307**, 442–448.
190. H. M. Liu, R. M. Sullivan, J. C. Hanson, C. P. Grey and J. D. Martin, *J. Am. Chem. Soc.*, 2001, **123**, 7564–7573.
191. R. Angelico, D. Burgemeister, A. Ceglie, U. Olsson, G. Palazzo and C. Schmidt, *J. Phys. Chem. B*, 2003, **107**, 10325–10328.
192. J. Senker, J. Schnert and S. Correll, *J. Am. Chem. Soc.*, 2005, **127**, 337–349.
193. T. Vosegaard, E. Hald, P. Daugaard and H. J. Jakobsen, *Rev. Sci. Instrum.*, 1999, **70**, 1771–1779.
194. B. Tesche, H. Zimmermann, R. Poupko and U. Haeberlen, *J. Magn. Res. A*, 1993, **104**, 68.
195. T. Osegaard, P. Daugaard, E. Hald, H. J. Jakobsen and J. Hans, *J. Magn. Res.*, 2000, **142**, 379–381.
196. T. Vosegaard, V. Langer, P. Daugaard, E. Hald, H. Bildsøe and H. J. Jakobsen, *Rev. Sci. Instrum.*, 1996, **67**, 2130–2133.
197. T. Vosegaard, E. Hald, V. Langer, H. J. Skov, P. Daugaard, H. Bildsøe and H. J. Jakobsen, *J. Magn. Res.*, 1998, **135**, 126–132.
198. R. K. Subramanian, L. Muntean, J. A. Norcross and D. C. Ailion, *Phys. Rev. B*, 2000, **61**, 996–1002.
199. P. Speier, H. Zimmermann, U. Haeberlen and Z. Luz, *Mol. Phys.*, 1998, **95**, 1153–1167.
200. T. Bräuniger, R. Poupko, Z. Luz, P. Gutsche, C. Meinel, H. Zimmermann and U. Haeberlen, *J. Chem. Phys.*, 2000, **112**, 10858–10870.
201. M. Stumber, H. Zimmermann, H. Schmitt and U. Haeberlen, *Mol. Phys.*, 2001, **99**, 1091–1098.
202. T. Schmidt, H. Schmitt, U. Haeberlen, Z. Olejniczak and T. Lalowicz, *J. Chem. Phys.*, 2002, **117**, 9818–9827.
203. T. Bräuniger, R. Poupko, Z. Luz, D. Reichert, H. Zimmermann, H. Schmitt and U. Haeberlen, *Phys. Chem. Chem. Phys.*, 2001, **3**, 1891–1903.
204. T. Bräuniger, R. Poupko, Z. Luz, H. Zimmermann and U. Haeberlen, *J. Chem. Phys.*, 2001, **115**, 8049–8059.
205. B. Q. Wei, R. Vajtai, Y. Jung, J. Ward, R. Zhang, G. Ramanath and P. M. Ajayan, *Chem. Mater.*, 2003, **15**, 1598–1606.
206. G. P. Crawford, L. M. Steele, R. Ondris-Crawford, G. S. Iannacchione, C. J. Yeager, J. W. Doane and D. Finotello, *J. Chem. Phys.*, 1992, **96**, 7788–7796.
207. M. D. Hollingsworth and K. D. M. Harris, *Comprehensive Supramolecular Chemistry*, Pergamon Press, Oxford, 1996 177–237.
208. F. Guillaume, S. P. Smart, K. D. M. Harris and A. J. Dianoux, *J. Phys.:Condens. Matter*, 1994, **6**, 2169–2184.

209. P. Girard, A. E. Aliev, K. D. M. Harris, M. D. Hollingsworth and P. Jonsen, *J. Chem. Phys.*, 1998, **109**, 4078–4089.
210. P. Girard, *Ph.D. Thesis*, University of Bordeaux I, 1998, unpublished.
211. P. J. Langley and J. Hulliger, *Chem. Soc. Rev.*, 1999, **28**, 279–291.
212. J. Lu, P. A. Mirau and A. E. Tonelli, *Progr. Polym. Sci.*, 2002, **27**, 357–401.
213. C. Odin and J. C. Ameline, *Europhys. Lett.*, 2004, **66**, 378–384.
214. K. Prout, *Croat. Chem. Acta*, 2002, **75**, 817–833.
215. T. Maris, M. J. Henson, S. J. Heyes and K. Prout, *Chem. Mater.*, 2001, **13**, 2483–2492.
216. K. Prout, S. J. Heyes, C. M. Dobson, A. McAid, R. Maris, M. Müller and M. Seaman, *Chem. Mater.*, 2000, **12**, 3561–3569.
217. M. Muller, A. J. Edwards, K. Prout, W. M. Simpson and S. J. Heyes, *Chem. Mater.*, 2000, **12**, 1314–1322.
218. C. Odin and J. C. Ameline, *Sol. State Nucl. Magn. Res.*, 2005, **27**, 257–265.
219. C. Odin and P. Garcia, *Magn. Reson. Chem.*, 2004, **42**, 687–694.
220. C. Odin and C. R. Chimie, 2006, **9**, 485–492.
221. A. Desmedt, S. J. Kitchin, F. Guillaume, M. Couzi, K. D. M. Harris and E. H. Bocanegra, *Phys. Rev. B*, 2001, **64**, 54106/1–54106/21.
222. A. D. Bain and M. Khasawneh, *C. Magn. Res.*, 2004, **22A**, 69–78.
223. K. B. Dillon, *Spectr. Prop. Inorg. Organomet. Compd.*, 2005, **37**, 1–16.
224. A. S. Peshkovsky, J. Forgue, L. Cerioni and D. J. Pusiol, *J. Magn. Res.*, 2005, **177**, 67–73.
225. J. B. Miller, B. H. Suits and A. N. Garroway, *J. Magn. Res.*, 2001, **151**, 228–234.
226. C. Odin, *J. Magn. Res.*, 2000, **143**, 299–310.
227. C. Odin, *J. Magn. Res.*, 1999, **141**, 239–255.
228. R. Blinc, T. Apih and J. Seliger, *Appl. Magn. Res.*, 2003, **25**, 523–534.
229. E. Balchin, D. J. Malcolm-Lawes, I. J. F. Pople, M. D. Rowe, J. A. S. Smith, G. E. S. Pearce and S. A. C. Wren, *Anal. Chem.*, 2005, **77**, 3925–3930.
230. J. N. Latosinska, *J. Pharm. Biomed. Anal.*, 2005, **38**, 577–587.
231. Ae. R. Lim, S. Ho Choh and S. -Y. Jeong, *J. Phys. Condens. Mater.*, 1999, **11**, 8141–8147.
232. I. Peral, G. Madariaga, A. Pérez-Etxebarria and T. Breczewski, *Acta Cryst. B*, 2000, **56**, 215–225.
233. S. Mulla-Osman, D. Michel, Z. Czapla and W. -D. Hoffmann, *J. Phys.: Condens. Matter*, 1998, **10**, 2464–2476.
234. S. Mulla-Osman, D. Michel, G. Völkel, I. Peral and G. Madariaga, *J. Phys.: Condens. Matter*, 2001, **13**, 1119–1131.
235. J. Dolinšek, M. Klanjšek, D. Aršon, H. J. Kim, J. Seliger, V. Žagar and L. F. Kirpichnikova, *Phys. Rev. B*, 1999, **59**, 3460–3467.
236. D. P. Kozlenko, S. Lewicki, J. Wasicki, W. Nawrocik and B. N. Savenko, *J. Phys. Condens. Matter*, 1999, **11**, 7175–7183.
237. J. Totz, H. Braeter and D. Michel, *J. Phys. Condens. Mater.*, 1999, **11**, 1575–1588.
238. C. Brinkmann, H. Eckert, D. Wilmer, M. Vogel, J. Schmedt auf der Günne, W. Hoffbauer, F. Rau and A. Pfitzner, *Sol. State Sci.*, 2004, **6**, 1077–1088.
239. K. Endo, T. Ida, J. Kimura, M. Mizuno, M. Suhara and K. Kihara, *Chem. Phys. Lett.*, 1999, **308**, 390–396.

240. F. Vaca Chávez, F. Bonetto and D. J. Pusiol, *Chem. Phys. Lett.*, 2000, **330**, 368–372.
241. D. Catalano, M. Cifelli, V. Domenici, K. Fodor-Csorba, R. Richardson and C. A. Veracini, *Chem. Phys. Lett.*, 2001, **346**, 259–266.
242. R. Y. Dong, *Chem. Phys. Lett.*, 2003, **375**, 517–521.
243. A. Yethiraj, Z. Sun, R. Y. Dong and E. E. Burnell, *Chem. Phys. Lett.*, 2004, **398**, 517–525.
244. V. Domenici, M. Geppi, C. A. Veracini, R. Blinc, A. Lebar and B. Zalar, *J. Phys. Chem. B*, 2005, **109**, 769–774.
245. R. Murashima, Y. Sanjo and M. Machida, *J. Phys. Soc. Jpn.*, 2004, **73**, 1423–1425.
246. A. Taye, D. Michel and J. Petersson, *Phys. Rev. B*, 2002, **66**, 174102/1–174102/7.
247. F. Deckera, K. -P. Holzer, P. Mischo, J. Petersson and D. Schüßler, *Eur. Phys. J. B*, 1999, **8**, 507–510.
248. M. Kunitomo, R. Etoh, T. Hayashi, T. Kohmoto, Y. Fukuda and M. Hashimoto, *J. Phys. Soc. Jpn.*, 2002, **71**, 955–959.
249. T. Ishibashi and M. Machida, *J. Phys. Soc. Jpn.*, 2003, **72**, 1554–1559.
250. E. G. Il'in, A. A. Vashman, Yu. B. Muravlev, A. M. Vilyanskii, O. K. Mel'nikov and Yu. A. Buslaev, *Dok. Phys. Chem.*, 2001, **380(4–6)**, 239–242.
251. F. Qi, T. Jörg and R. Böhmer, *Sol. State Nucl. Magn. Res.*, 2002, **22**, 484–500.
252. J. K. Jung, Y. M. Seo, S. K. Song and S. H. Choh, *Sol. State Commun.*, 2001, **120**, 401–405.
253. R. Blinc, A. Gregorovi, B. Zalar, R. Pirc, V. V. Laguta and M. D. Glinchuk, *J. Appl. Phys.*, 2001, **89**, 1349–1354.
254. V. V. Laguta, M. D. Glinchuk, I. P. Bykov, R. Blinc and B. Zalar, *Phys. Rev. B*, 2003, **69**, 54103/1–54103/9.
255. B. Bednarska-Bolek, R. Jakubas, W. Medycki, D. Nowak and J. Zaleski, *J. Phys.: Condens. Matter*, 2002, **14**, 3129–3142.
256. I. G. Kim, T. H. Yeom, D. Y. Jeong, A. R. Lim, S. H. Choh and K. S. Hong, *J. Phys. Soc. Jpn.*, 2002, **71**, 2546–2549.
257. C. E. Lee, N. S. Dalal and R. Fu, *Curr. Appl. Phys.*, 2003, **3**, 405–408.
258. A. R. Lim, J. K. Jung and S. -Y. Jeong, *J. Phys. Chem. Sol.*, 2002, **63**, 625–630.
259. Ae. R. Lim, S. Ho Choh and Se. -Y. Jeong, *J. Phys. Condens. Mater.*, 2000, **12**, 9293–9305.
260. A. R. Lim and S. Y. Jeong, *J. Phys. Chem. Sol.*, 2002, **63**, 221–226.
261. Ae. R. Lim and Se. -Y. Jeong, *J. Phys. Chem. Sol.*, 2001, **62**, 881–885.
262. A. R. Lim and S. -Y. Jeong, *Sol. State Commun.*, 2000, **166**, 231–236.
263. H. J. Kim, D. Y. Jeong, B. Zalar, R. Blinc and S. H. Choh, *Phys. Rev. B*, 2000, **61**, 9307–9313.
264. Ae. R. Lim and Se. -Y. Jeong, *Physica B*, 2001, **304**, 79–85.
265. A. R. Lim and I. G. Lim, *J. Phys. Soc. Jpn.*, 2004, **73**, 475–479.
266. B. V. S. Murthy, K. P. Ramesh and J. Ramakrishna, *J. Phys. Chem. Sol.*, 2000, **61**, 961–968.
267. C. I. Ratcliffe, *Can. J. Chem.*, 2004, **82**, 1517–1526.
268. H. Y. He, J. T. Dias, J. Foulkes and J. Klinowski, *Phys. Chem. Chem. Phys.*, 2000, **2**, 2651–2654.

269. B. Zibrowius, C. Bähitz, M. Knapp and U. Ruschewitz, *Phys. Chem. Chem. Phys.*, 2004, **6**, 5237–5243.
270. Ae. R. Lim, T. J. Han, J. K. Jung and H. M. Park, *J. Phys. Soc. Jpn.*, 2002, **71**, 2268–2270.
271. Ae. R. Lim, H. W. Shin and D. Y. Jeong, *J. Phys. Soc. Jpn.*, 2003, **72**, 1308–1309.
272. Ae. R. Lim, D. Y. Jeong and H. -M. Park, *J. Phys.: Condens. Matter*, 2001, **13**, 3511–3517.
273. Ae. R. Lim, J. K. Jung and H. M. Park, *J. Phys. Soc. Jpn.*, 2001, **70**, 3708–3712.
274. Ae. R. Lim and K. -Y. Lim, *Phys. Status Solidi (b)*, 2005, **242**, 2417–2426.
275. T. Asaji, H. Fujimori, H. Ishida, K. Eda, M. Hashimoto and M. Oguni, *J. Phys. Chem. Sol.*, 2005, **66**, 869–875.
276. G. Dosseh, Y. Xia and C. Alba-Simionesco, *J. Phys. Chem. B*, 2003, **107**, 6445–6453.
277. I. Gnatyuk, G. Puchkovska, I. Chashechnikova, F. Nozirov, S. Jurga and B. Peplinsk, *J. Mol. Struct.*, 2004, **700**, 183–189.
278. T. Ishibashi, M. Machida, T. Kobayashi and N. Koyano, *J. Phys. Soc. Jpn.*, 2004, **73**, 2458–2463.
279. S. Sato, A. Ishikawa, H. Matsumoto, A. Sasane and C. Kitazawa, *J. Mol. Struct.*, 2003, **644**, 125–131.
280. R. Asayama, J. Kawamura and T. Hattori, *Chem. Phys. Lett.*, 2005, **414**, 87–91.
281. A. R. Lim, K. S. Hong and S. -Y. Jeong, *Sol. State Commun.*, 2000, **114**, 321–324.
282. S. V. Dvinskikh, I. Furo, H. Zimmermann and A. Maliniak, *Phys. Rev. E*, 2002, **65**, 61701/1–61701/9.
283. E. Mikuli, B. Grad, W. Medycki and K. Höderna-Natkaniec, *J. Sol. State Chem.*, 2004, **177**, 3795–3804.
284. G. W. Buchanan, M. Gerzain and C. I. Ratcliffe, *Can. J. Chem.*, 1999, **77**, 1911–1921.
285. T. Mochida, D. Kuwahara, S. Miyajima and T. Sugawara, *J. Phys. Chem. B*, 2003, **107**, 12315–12319.
286. C. Akita, T. Kawaguchi, F. Kaneko, H. Yamamoto and M. Suzuki, *J. Phys. Chem. B*, 2004, **108**, 4862–4868.
287. C. L. Nygren, C. C. Wilson and J. F. C. Turner, *J. Phys. Chem. A*, 2005, **109**, 2586–2593.
288. X. -P. Tang, J. -C. Wang, L. W. Cary, A. Kleinhammes and Y. Wu, *J. Am. Chem. Soc.*, 2005, **127**, 9255–9259.
289. D. S. Chow, F. Zamborszky, B. Alavi, D. J. Tantillo, A. Baur, C. A. Merlic and S. E. Brown, *Phys. Rev. Lett.*, 2000, **85**, 1698–1701.
290. A. Taye, D. Michel and J. Petersson, *Phys. Rev. B*, 2004, **69**, 224206/1–224206/7.
291. A. M. Panich, D. C. Ailion, S. Kashida and N. Gasanly, *Phys. Rev. B*, 2004, **69**, 245319/1–245319/7.
292. Ae. R. Lim and K. S. Hong, *J. Appl. Phys.*, 2005, **98**, 043906/1–043906/4.
293. M. Cifelli, J. Saunavaara, J. Jokisaari and C. A. Veracini, *J. Phys. Chem. A*, 2004, **108**, 3973–3979.
294. Ae. R. Lim and H. S. Yoon, *J. Phys. Chem. Sol.*, 2005, **66**, 1004–1007.
295. F. Taulelle ed., Thematic Section: NMR Crystallography, *Sol. State Sci*, 2004, **6**, 1019–1180.
296. F. Taulelle, *Sol. State Sci.*, 2004, **6**, 1053–1057.

297. J. Dutour, N. Guillou, C. Huguenard, F. Taulelle, C. Mellot-Draznieks and G. Férey, *Sol. State Sci.*, 2004, **6**, 1059–1067.
298. S. Singh, *Phys. Rep.*, 2000, **324**, 107–269.
299. I. Furo, *J. Mol. Liq.*, 2005, **117**, 117–137.
300. P. Terech, C. Rossat and F. Volino, *J. Coll. Int. Sci.*, 2000, **227**, 363–370.
301. Y. -W. Hsueh, M. Zuckermann and J. Thewalt, *Concepts Magn. Res.*, 2005, **26A**, 35–46.
302. E. Strandberg, T. Sparrman and G. Lindblom, *Adv. Coll. Interf. Sci.*, 2001, **89–90**, 239–261.
303. S. Morein, E. Strandberg, J. A. Killian, S. Persson, G. Arvidson, R. E. Koeppe II and G. Lindblom, *Biophys. J.*, 1997, **73**, 3078–3088.
304. I. Marcotte and M. Auger, *Concepts Magn. Res.*, 2005, **24A**, 17–37.
305. J. -P. Douliez, *Langmuir*, 2004, **20**, 1543–1550.
306. F. Aussenac, M. Laguerre, J. -M. Schmitter and E. J. Dufourc, *Langmuir*, 2003, **19**, 10468–10479.
307. A. LeBail, L. Boillereaux, A. Davenel, M. Hayert, T. Lucas and J. Y. Monteau, *Innov. Food Sc. Emerg. Techn.*, 2003, **4**, 15–24.
308. Y. Kitaoka, S. Kawasaki, T. Mito and Y. Kawasaki, *J. Phys. Soc. Jpn.*, 2005, **74**, 186–199.
309. K. Miyagawa, K. Kanoda and A. Kawamoto, *Chem. Rev.*, 2004, **104**, 5635–5653.
310. A. Rigamonti, F. Borsa and P. Carretta, *Rep. Progr. Phys.*, 1998, **61**, 1367–1439.
311. R. Blinc and T. Apih, *Progr. Nucl. Magn. Spect.*, 2002, **41**, 49–82.
312. F. Decker, U. Haoeker, K. -P. Holzer, M. Irsch, D. Michel, P. Mischo and J. Petersson, *Adv. Sol. State Phys.*, 2001, **41**, 565–576.
313. J. E. Wolak, X. Jia and J. L. White, *J. Am. Chem. Soc.*, 2003, **125**, 13660–13661.
314. R. Böhmer, G. Diezemann, G. Hinze and E. Rössler, *Progr. Nucl. Magn. Spect.*, 2001, **39**, 191–267.
315. R. Y. Dong, *Progr. Nucl. Magn. Spect.*, 2002, **41**, 115–151.
316. B. L. Phillips, Review in Mineralogy and Geochemistry, *Transformation Processes in Minerals*, Vol. 39, S. A. T. Redfern and M. A. Carpenter (eds.), The Mineralogical Society of America, Washington, DC, 2000, 203–240.
317. Proceedings of the XVth International Symposium on Nuclear Quadrupole Interactions (Leipzig 1999), *Z. Naturforsch. A*, 2000, 55a, 1–368.
318. Proceedings of the XVIth International Symposium on Nuclear Quadrupole Interactions (Hiroshima 2001), *Z. Naturforsch. A*, 2002, 57a, 285–640.
319. R. Kimmich and E. Anoardo, *Progr. Nucl. Magn. Spect.*, 2004, **44**, 257–320.
320. R. 553 A. C. Ribeiro, P. J. Sebastiao and C. Cruz, *Pramana*, 2003, **61**, 205–218.
321. S. V. Dvinskikh and I. Furo, *J. Chem. Phys.*, 2001, **115**, 1946–1950.
322. A. Yethiraj, D. Capitani, N. E. Burlinson and E. E. Burnell, *Langmuir*, 2005, **21**, 3311–3321.
323. N. Garti, A. Spornath, A. Aserin and R. Lutz, *Soft Matter*, 2005, **1**, 206–218.
324. B. Jagadeesh, A. Prabhakar, M. H. V. Ramana Rao, C. V. S. Murty, V. G. K. M. Pisipati, A. C. Kunwar and C. R. Bowers, *J. Phys. Chem. B*, 2004, **108**, 11272–11279.

Application of Multi-Way Analysis to 2D NMR Data

HENRIK T. PEDERSEN¹, MARIANNE DYRBY², SØREN
B. ENGELSEN³ AND RASMUS BRO³

¹*Protein Structure and Biophysics, Novo Nordisk A/S, Novo Nordisk Park, 2760
Måløv, Denmark*

²*Umetrics AB, Stortorget 21, 211 34 Malmö, Sweden*

³*Quality and Technology, Department of Food Science, The Royal Veterinary and
Agricultural University, Rolighedsvej 30, 1958 Frederiksberg C, Denmark*

1. Introduction	208
2. General theory	210
2.1. Multivariate data analysis	210
2.2. Multi-way data analysis	211
2.3. Constraints	214
2.4. Compression of data	214
2.5. Validation	215
2.6. Software	216
3. Analysis of 2D and 3D NMR data	216
3.1. Traditional data analysis of 2D NMR experiments	217
3.2. Two-way multivariate analysis	219
3.3. True multi-way analysis	221
3.4. Other two- and three-way methods	230
4. Conclusions	231
Acknowledgements	231
References	232

Two- and three-dimensional or even higher-dimensional NMR spectroscopy is changing from specialised techniques to more commonly used ones. As the complexity of the acquired NMR data increases, the task of analysing these data constantly becomes more and more demanding and new methods are required to facilitate the analysis. With one-dimensional NMR data multivariate data analysis has proven to be a strong tool, but how should one analyse higher-dimensional NMR data in order to extract as much relevant information as possible without having to break data down into smaller dimensions and thus lose the inherent structure? A class of

multivariate data analytical techniques called multi-way analysis encompass techniques that have been designed to handle and analyse such data structures directly. In this paper, the theory of some of the most commonly used multi-way methods will be described and examples of their application to three-way arrays of NMR data reported in the literature will be given. The focus will be on the generic principles of multi-way analysis using three-way data in order to gently introduce the new concepts.

1. INTRODUCTION

Two-dimensional nuclear magnetic resonance (2D NMR) has evolved from acquiring multiple one-dimensional (1D) data using simple pulse experiments with different experimental settings to highly specialised pulse experiments probing different properties of the molecules in the sample using Fourier transformation in both directions. Some of the more common 2D experiments are: nuclear Overhauser spectroscopy (NOESY), diffusion ordered spectroscopy (DOSY), correlation spectroscopy (COSY), total correlation spectroscopy (TOCSY), heteronuclear single-quantum spectroscopy (HSQC) and heteronuclear multiple-quantum spectroscopy (HMQC). The possibilities are numerous and new experiments are continuously being developed either based on substantially new ideas or derived from already existing experiments.

2D and 3D or even higher-dimensional NMR spectroscopy are changing from being specialised techniques to more commonly used techniques primarily driven by the strength of NMR in relation to elucidation of molecular structures for large molecules such as proteins. NMR has become an invaluable tool as a substitute for or complement to X-ray diffraction. X-ray diffraction requires that high-quality single crystals of the molecule in interest are grown, while structural elucidation using NMR can be performed directly in the liquid state. More importantly, for most biologically relevant molecules the natural environment is the liquid state and hence the information of the active conformation(s) is preserved.

As the complexity of the acquired NMR data increases, the task of analysing these data constantly becomes more and more demanding and new methods are required to facilitate the analysis. Data analytical tools that can handle large numbers of collinear variables as usually collected in NMR experiments are known from the field of multivariate analysis, which in recent years has gained increasing popularity also in the NMR community, primarily driven by the rapidly expanding field of metabonomics. In brief, metabonomics covers the application of multivariate data analytical techniques (pattern recognition) to NMR or MS (mass spectroscopy) data acquired from bio-fluid samples in the search of changes in the endogenous

metabolites that in turn can be used as biomarkers for, e.g. diagnosis of a disease. The strength of multivariate data analysis lies in the fact that large numbers of variables can be analysed simultaneously and structures in the data as well as important variables can be interpreted quantitatively and visually by inspecting plots of the resulting model.

If 2D NMR data are acquired from a series of comparable samples, the resulting data can be arranged in a three-way array as shown in Fig. 1A. Each horizontal slab will be a matrix containing the 2D data obtained from one sample. An obvious question arises: How should one analyse such data in order to extract as much relevant information as possible without having to break the information down into smaller dimensions and thus lose the inherent structure of the data? The answer is highly dependable on the nature of the data and the information sought. We will try to answer this question in this paper, starting with a brief introduction to the general concept of multivariate data analysis, but the focus of the paper will be on

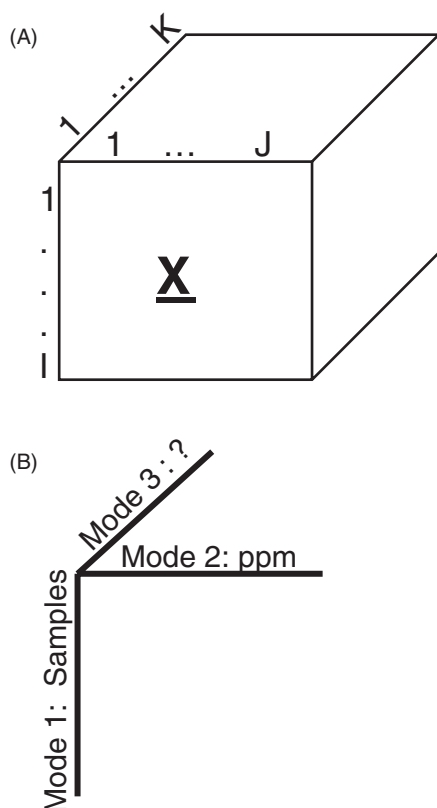


Fig. 1. (A) Typical representation of a three-way array with index on the three modes. (B) An example of the structure of a three-way array.

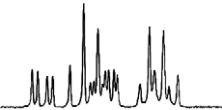
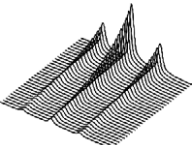
the theory and application of so-called multi-way methods to three-way arrays of NMR data. Multi-way methods are multivariate methods specifically aimed at analysing data as those shown in Fig. 1A. Although most multi-way models are designed to be able to handle data structures of higher dimensionality than the three shown in Fig. 1A, four- and higher-way data are difficult to visualise and handle for human recognition. In this paper, we will focus on the generic principles using three-way data in order to gently introduce the new concepts.

2. GENERAL THEORY

2.1. Multivariate data analysis

From a data analytical point of view, data can be categorised according to structure, as exemplified in Table 1. Depending on the kind of data acquired, appropriate data analytical tools must be selected. In the simplest case, only one variable/number is acquired for each sample in which case the data are commonly referred to as zeroth-order data. If several variables are collected for each sample, this is referred to as first-order data. A typical example could be a 1D spectrum acquired for each sample. Several 1D spectra from different samples may be organised in a two-way table or a matrix. For such a matrix of data, multivariate data analysis is commonly employed. It is clearly not possible to analyse zeroth-order data by multivariate techniques and one is restricted to traditional statistics and linear regression models. When first- or second-order data are available, multivariate data analysis may be used and several advantages may be exploited,

Table 1. Presentation of different data structures

Graphical example	Data	Advantage
×	Zeroth order (scalar)	—
	First order (vector, spectrum)	Outlier detection, interference compensation, noise reduction
	Second order (matrix, 2D)	All of the above plus unique solutions and possibly pure component spectra

including interference compensation, noise reduction and outlier detection (see [Table 1](#)).

The power of multivariate data analysis relies on the fact that simultaneous analysis of many variables from each sample enables the appreciation of relations (covariance) and patterns between variables. In the case of NMR spectra this is important, since one molecule commonly gives rise to several peaks throughout the spectral range, which leads to variables in different parts of the spectrum varying in a similar fashion (correlated). Such correlation can be used in multivariate calibration models to quantify individual components even in the presence of overlapping signals.¹ Or it can be used to detect abnormal samples (outliers) that would remain undetected, if only univariate measurements were used. Multivariate analysis has proven to be a very strong tool in many applications and may replace tedious or expensive chemical analysis.² Perhaps, of even greater importance is the fact that the application of multivariate data analysis adds an exploratory dimension to the NMR measurements,³ which is utilised in, for example, metabonomics in which NMR spectra of complex bio-fluids reflect the fact that several molecules covary for direct or indirect biochemical reasons.

Most well known is the two-way multivariate data analysis, which is designed for analysing matrices. Two-way multivariate analysis utilises the fact that the 2D data matrices analysed are normally low-rank bilinear. Being low-rank bilinear simply implies that any spectrum in the matrix can be described as a sum of a few underlying spectral profiles and that all spectra can be described by different amounts of the same underlying profiles. In the case of spectroscopy, this is appropriate if the data approximately follows Beer's law, i.e. a given peak is linearly dependent on the concentration of the analyte that gives rise to this peak. Such bilinearity implies that the data can be compressed into a lower dimensional space facilitating the interpretation of the major sources of variation in a parsimonious model.

In a recent paper by Alam and Alam,⁴ a good overview of the different two-way multivariate methods and their application to NMR data is given. Also some of the important issues such as phase correction, alignment, line shape and resolution that should be kept in mind when using multivariate methods for the analysis of NMR data are discussed (see also ref.⁵).

2.2. Multi-way data analysis

If 2D data matrices are acquired for a series of samples, these data can be arranged in a three-way array and second-order data is the result (see [Table 1](#)). Commonly, the three directions in a three-way array are termed

“modes”, as seen in Fig. 1B. In the case of NMR, the setup could be that mode 1 is the direction of samples and mode 2 is the primary NMR direction (chemical shift). Mode 3 is then whatever extends the NMR data acquired on each sample from 1D to 2D, such as experimental delays, time of acquisition, gradient strength, number of echoes, etc.

If the three-way data array can be considered a collection of 2D NMR data matrices (slabs) and each of these 2D matrices can be thought of as a collection of 1D spectra, a simple way of analysing these data would be to analyse each individual two-way array using standard two-way multivariate techniques and subsequently compare the individual models. To avoid the step of comparing multiple models, the three-way array can be unfolded into one big two-way array and simultaneous analysis of data from the entire three-way array can be performed. If the first mode is of samples, this unfolding is typically performed in one of the two ways as seen in Fig. 2, resulting in a two-way array of size $I \times (J \times K)$ by concatenating the K slabs or $(I \times K) \times J$ by stacking the K slabs. Then standard two-way multivariate techniques can be used to analyse all the data in one model.

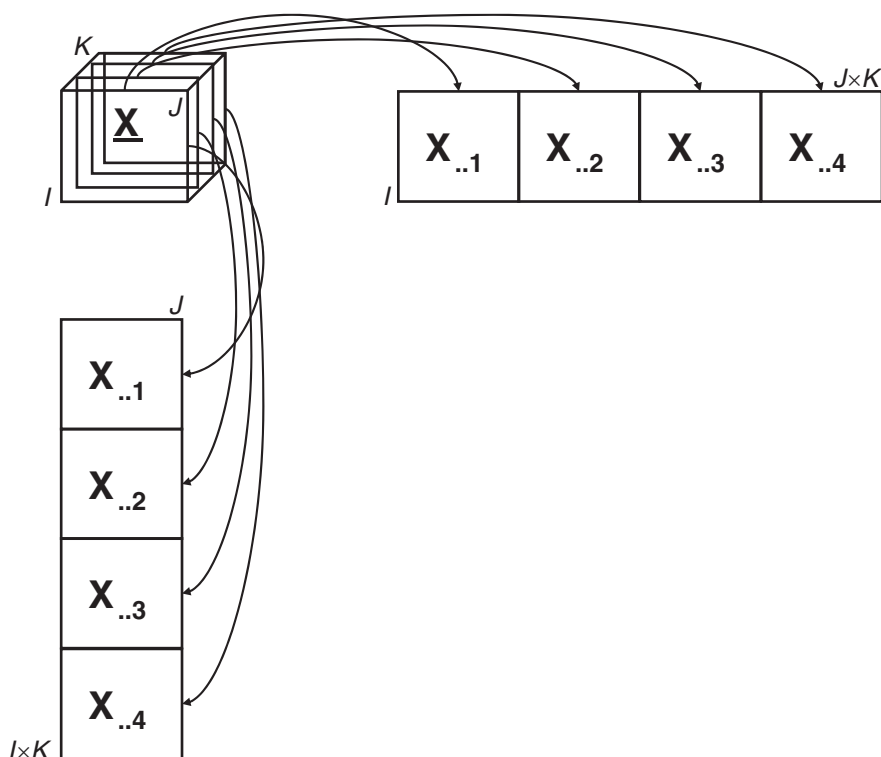


Fig. 2. Two schemes for unfolding a three-way array into a two-way array.

The interpretation of such two-way models on unfolded three-way data tends to become quite complicated, because the three-way structure is not maintained in the modelling and visualisation steps. Furthermore, several unique properties inherent to the original three-way data structure will be lost.

Some three-way data arrays can be assumed to be low-rank trilinear, similar to two-way data matrices being low-rank bilinear. If data are low-rank trilinear, three-way mathematical models can be applied, which are able to directly extract chemically meaningful components containing pure spectra, concentrations, etc. This has been coined as mathematical chromatography.⁶ If this can be accomplished, chemical and physical isolation or purification of chemical species in a sample is no longer necessary, as this can be obtained mathematically. However, it is important to remember that when several bilinear two-way data matrices are collected into a three-way array, this new array is not necessarily trilinear and it is not always trivial to ascertain whether or not this is the case.

If the underlying structure of a three-way data set is not trilinear, other three-way data analytical methods exist, but these do not usually result in pure component spectra. However, through application of appropriate constraints, pure component spectra may still be extracted, as argued by de Juan and Tauler.⁷ By using three-way decomposition methods, the data structure is maintained and used in the model. Interpretation is facilitated by relating the extracted patterns directly to the structure of the data.

As described above, not all three-way data can be meaningfully approximated as low-rank trilinear, and consequently multi-way methods may be divided into two groups based on whether or not the methods require low-rank trilinear data structure. It is therefore important to perform a preliminary analysis to determine the inner structure of a three-way array before choosing a suitable resolution method. The models discussed in this paper are listed in Table 2, also stating whether or not a given model requires low-rank trilinear data and therefore results in direct chemically meaningful solutions.

In Section 3, the most commonly used three-way models (listed in Table 2) will be described and examples of application to NMR data will be given.

Table 2. Comparing model characteristics

Model	Require low-rank trilinear data	Unique unconstrained solutions
PARAFAC	Yes	Yes
Tucker3	No	No
MCR	No	No

2.3. Constraints

Depending on the quality of data and the method selected, constraints on the parameters to be estimated may be required in order to get a chemically meaningful solution. In the case of multivariate curve resolution (MCR) (see Section 3.2) performed on one 2D NMR spectrum, application of constraints is mandatory. If constraints are not applied, it can be shown that there is an infinity of equally well-fitting solutions and hence the true underlying parameters (spectra, concentrations) cannot be estimated directly. This is known as the rotational ambiguity of two-way low-rank models.

A variety of constraints exists which may be relevant to NMR data. A commonly applied constraint is non-negativity (e.g. of spectra), which in the case of NMR makes sense, if it is known that the experiment applied should only produce positive signals. Thus, it is possible to force the algorithm to only allow positive signals in the NMR spectral direction (ppm mode). Other constraints include unimodality where only one peak is allowed; or closure which can be used if a limited number of components exist in the system and their signal should add up to 100% in intensity. Many more constraints exist and the reader is referred to the literature for further information (e.g. refs.^{6,7}).

2.4. Compression of data

With the simultaneous analysis of all data in a three-way array, the amount of data may become very large, putting heavy demands on computational power and memory capacity. To solve this problem, one might work on a sub-set or reduce data dimensionality by averaging a given number of variables, but neither of these possibilities is the best way to solve the problem, since important information may be lost in these processes.

A better solution may be to compress using a principal component analysis (PCA)-based approach,^{2,8} or alternatively apply Tucker3⁹ or similar approaches¹⁰ on the three-way array directly (see description of PCA and Tucker3 in Sections 3.2 and 3.3, respectively). The principle in such compression is to compress each mode into a lower-dimensional sub-space. This sub-space is made large enough so that it captures all the significant variation, but is typically much smaller than the original dimension. On the basis of the compression, a new three-way array of reduced dimensionality is constructed and this new array is used as input for the actual analysis. After fitting a model to the compressed array, the derived model parameters can be decompressed to the original dimensionalities and refined in the full dimensional mode. To the extent that the compression retains the information in

the original data, the same model is obtained from the compressed and the raw data, however, with the advantage of significantly increased speed of computation.

2.5. Validation

An important step in building multivariate models is to check the validity of the model. The purpose is first of all to make sure that an appropriate model has been chosen^{7,11,12} and that the right dimensionality (number of components) has been found.^{12,13} These aspects are important for proper outlier detection, for the visual and quantitative interpretation and for the model to be valid for scientific evaluation.

There are several routes to validate the choice of model and dimensionality. In the case of two-way methods (see Section 3.2), a commonly used approach is cross-validation where a number of different schemes have been designed.¹⁴ Additionally, validity of a PCA model is often confirmed by means of the interpretability of the model and its consistency with external information such as grouping of samples, relation to quantitative measures, etc.

With three-way methods such as Tucker3 and PARAFAC (see Section 3.3) cross-validation is less trivial compared to cross-validation in two-way models, since sub-sampling may be performed in more ways. Furthermore, cross-validation of three-way models may be rather time-consuming and may therefore not be the optimal method to choose.

Different schemes have been developed to allow the validation of three-way models. One method used for PARAFAC models is split-half analysis, where the data set is split into two parts and individual modelling is performed on the two halves. If the two models show similar spectral loadings, the variation expressed in the two halves is comparable and it can be assumed that an appropriate number of components have been chosen. As for PCA, visual interpretability is also important and usually substantially easier for PARAFAC, because the components directly represent chemically meaningful phenomena. Other tools that may aid in deciding the correct number of components can be found in the literature.¹⁵

With least-squares (LS) algorithms for non-linear problems such as multi-way methods, the problem of local minima solutions⁶ is well known and it is common practice to repeat the calculation a number of times using different starting estimates for the components. This way the results of several models are compared and if the calculated models are sufficiently similar, it is likely that the global LS minimum has been found, whereas if the models are dissimilar, local LS minima are likely to be present. In case of local LS minima, more repetitions can be made in order to see if a consistent pattern

can be found, indicating that the global LS minimum is among the found solutions.

2.6. Software

With access to MATLAB (The MathWorks, Natick, MA, USA), the N-Way Toolbox by Andersson and Bro.¹⁶ (<http://www.models.kvl.dk/source/nwaytoolbox>) is a good place to start. It is freeware and covers the major multi-way methods.

The PLS_Toolbox (Eigenvector Research, Inc, Wenatchee, WA, USA) also covers a large range of both two- and three-way multivariate methods including MCR.

An implementation of Multivariate Curve Resolution Alternating Least Squares (MCR-ALS) can be downloaded from <http://www.ub.es/gesq/mcr/mcr.htm>.⁷ MCR is also available in The Unscrambler (Camo Inc., Woodbridge, New Jersey, USA).

PCA and related two-way multivariate techniques can be performed in several commercial chemometrics softwares, such as SIMCA-P/P+ (Umetrics AB, Umeå, Sweden) and The Unscrambler (Camo Inc., Woodbridge, New Jersey, USA). Batch analysis can be performed in SIMCA-P+ only.

3. ANALYSIS OF 2D AND 3D NMR DATA

This section is divided into four parts. The first part gives examples of how traditional analysis of NMR data can be performed. The aim is not to give an in-depth description of how multi-dimensional NMR data are traditionally analysed, but rather to highlight some of the main characteristics of this kind of analysis in order to make the difference between traditional analysis and multivariate analysis clearer.

The second part deals with multivariate pseudo three-way analysis, i.e. two-way analysis of two-way and unfolded three-way NMR data. These methods are included, since they may offer an alternative choice for analysing three-way NMR data matrices and, furthermore, they are an important supplement to the real three-way methods described in the third part of the section. Here, application of three-way methods to three-way data is described and exemplified. The fourth part covers a short description of some related three-way methods primarily to inform about their existence and possible usage.

3.1. Traditional data analysis of 2D NMR experiments

Although all 2D NMR experiments are acquired as a collection of 1D spectra, there are still fundamental differences in the resulting data and the way in which they are traditionally pre-processed and analysed. In this paper, we therefore choose to divide 2D NMR data into two different groups which we call “real 2D” and “pseudo 2D” NMR data in order to be able in a simple way to highlight and keep track of this difference.

In our definition, real 2D NMR data are either homo- or hetero-nuclear data, where Fourier transformation is performed in both directions and a “chemical shift map” is created, as seen in COSY, TOCSY, NOESY, J-RES, HSQC, etc. In the case of HSQC, a short delay is being incremented during which the signals in the 1D spectrum are being coded with the frequency of the corresponding hetero-nucleus and 2D Fourier transformation is employed to create the frequency map. An example of a real 2D NMR spectrum can be seen in [Fig. 3A](#). With homo-nuclear data a similar picture is obtained, but the plot is symmetrical on the diagonal axis.

Real 2D NMR data are commonly used in relation to structural elucidation or molecular identification. Typically, several different 2D experiments are used, each providing complementary information, and structural information is extracted by using specific rules inferred by the design of the pulse sequence and the experimental parameters. Thus, a peak in an HSQC spectrum where magnetisation is transferred from a proton to a heteronucleus via a large one-bond coupling constant is in a straightforward manner structurally interpreted as a one-bond connection. And in a COSY experiment, off-diagonal cross-peaks commonly show proton couplings between protons that are two (geminal) or three (vicinal) bonds apart. No mathematical analysis is necessary, as the desired information is read directly from the 2D spectra (of the pure compound).

Pseudo 2D NMR data are generally characterised by the fact that Fourier transformation is only performed in one direction, whereas the other direction represents time of acquisition, varying gradient strength, different number of echoes, etc. It is thus apparent that the data matrix is a collection of 1D profiles. Examples could be monitoring reaction kinetics, diffusion-weighted data, 2D Carr-Purcell-Meiboom-Gill (CPMG) for T_2 measurements and 2D inversion recovery for T_1 measurements. An example of a pseudo 2D diffusion-weighted NMR spectrum can be seen in [Fig. 3B](#).

Examples of traditional analysis of pseudo 2D NMR data are the calculation of longitudinal relaxation times (T_1), transverse relaxation times (T_2) and diffusion coefficients (D). For longitudinal and transverse relaxation times, the intensity of a selected peak is plotted as a function of a

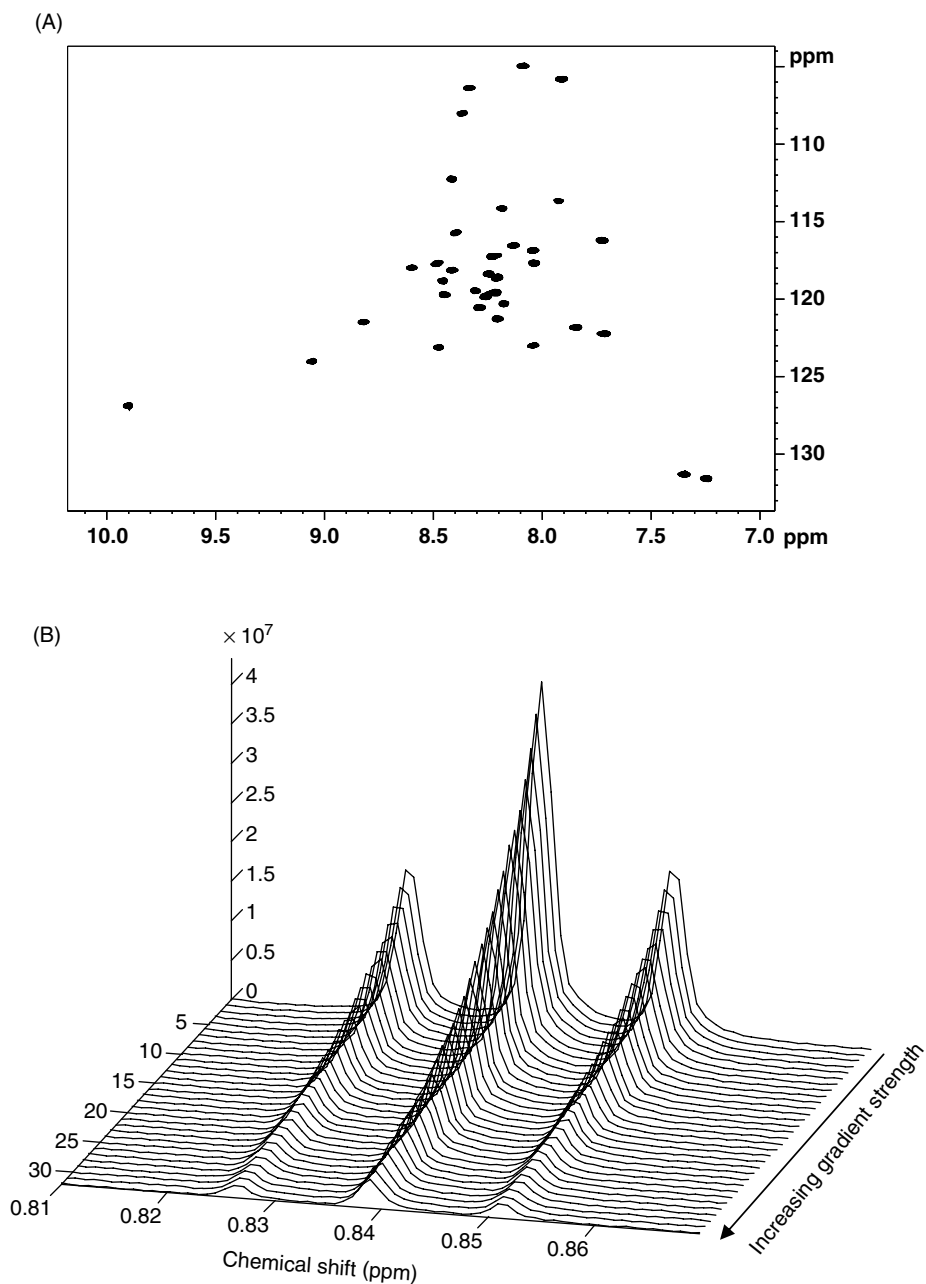


Fig. 3. (A) An example of “real” 2D NMR data being a part of a $[^1\text{H}-^{15}\text{N}]$ HSQC spectrum of a peptide and (B) “pseudo” 2D NMR data in the form of diffusion-weighted data.

delay. For diffusion-edited data, the intensity of a selected peak is plotted as a function of the applied (squared) gradient strength. In both cases, the change in peak intensity is fitted according to a known equation in order to obtain the T_1 , T_2 or D values. Common to this kind of analysis is that good results can only be achieved with well-separated peaks, and thus regions with overlapping peaks cannot be analysed if pure component estimates are desired. Furthermore, this kind of analysis is very sensitive to the noise level of the data, since as the signal intensity decrease the noise will increasingly dominate the signal. In order to get a more robust result, averaging of several peaks or several variables on a particular peak should be used.

In the case of 2D diffusion-weighted NMR spectra a transformation exists, which is able to transform the second dimension directly into the desired diffusion coefficient (D). In this form, the spectra are known as 2D DOSY and the diffusion coefficients can be extracted directly without using further mathematical analysis. However, this transformation – the inverse Laplace transform – is ill-posed, i.e. the solution can be highly inaccurate without adequate regularisation. A wiser choice may be to analyse the original diffusion-weighted data using three-way methods, as exemplified in Section 3.3.

With pseudo 2D NMR data consisting of a series of 1D profiles, analysis by multivariate techniques is obvious, since the large number of potentially overlapping variables makes visual analysis very difficult and improved methods of analysis are already called for. Analysis of real 2D NMR data by multivariate techniques is less obvious, since a lot of information can already be extracted from the 2D Fourier-transformed data. However, if real 2D NMR data from a series of samples needs to be compared, the application of multivariate techniques is an obvious possibility.

3.2. Two-way multivariate analysis

This section deals with the analysis of two- and three-way NMR data using two-way methods.

3.2.1. PCA theory

One of the most commonly used multivariate data analysis techniques employed for analysing two-way data tables is PCA.^{17,18} In PCA, the data matrix is commonly referred to as \mathbf{X} with size $I \times J$. Hence, the matrix has I rows (samples) and J columns (variables). The matrix is decomposed into F principal components (PCs) each represented by vectors \mathbf{t}_f and \mathbf{p}_f .

The mathematical expression of the PCA model is

$$\mathbf{X} = \mathbf{TP}' + \mathbf{E} \quad (1)$$

where \mathbf{P} is the loading matrix with columns \mathbf{p}_f (representing common underlying features or spectral profiles) of size $J \times F$, \mathbf{T} the score matrix with columns \mathbf{t}_f (representing amount of loadings) of size $I \times F$ and \mathbf{E} the residual matrix of size $I \times J$. Each individual PC is the outer product of the corresponding score (\mathbf{t}_f) and loading (\mathbf{p}_f) vectors as shown in Fig. 4. The different components (F in total) are forced to be orthogonal and the PCs are calculated so that the first PC explains the largest amount of variation, the second PC explains the second largest amount of variation and so forth until the systematic variation in the data set has been extracted. The first component (the product of the first score and loading vector) provides the best possible rank-one approximation of the data in an LS sense. The strength of PCA is that a high-dimensional data set can be compressed into a low-dimensional space, which can be interpreted visually by plotting \mathbf{T} and \mathbf{P} , and patterns in the samples and variables responsible for these patterns can be evaluated.

3.2.2. Applications of PCA

As previously mentioned, it is possible to unfold three-way data into two-way matrices and analyse these using ordinary two-way methods. Numerous examples can be found in the literature for many types of data, including NMR. An example of a recent application is the monitoring of equilibrium unfolding of the MerP protein by means of [^1H – ^{15}N] gradient-enhanced (ge) HSQC.¹⁹

An approach commonly known as “batch analysis” due to its origin in the field of analysing batch process data has become popular within the field of metabonomics when analysing NMR data collected over time in toxicity studies. In such cases, data can often be arranged in a three-way array consisting of *animals* \times *ppm* \times *time*, where *time* corresponds to multiple sample collections from each animal over time, e.g. after dosing of rats with a compound. Batch analysis is based on unfolding of the three-way array, splitting and compressing the variation into a time contribution and a sample

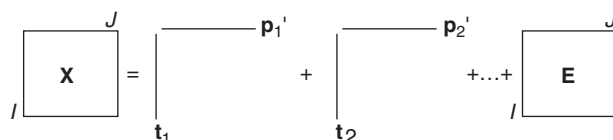


Fig. 4. Schematic representation of the decomposition of \mathbf{X} into scores (\mathbf{t}), loadings (\mathbf{p}) and a residual as performed in PCA.

(e.g. dose) contribution²⁰ by means of two-way methods. Though the three-way structure of the data is not preserved and some temporal information may be lost,²¹ batch analysis has been proven an efficient tool due to its ease of use and interpretation of the resulting model.

3.2.3. *MCR theory*

MCR²² was originally performed on a two-way array, but the method can also be applied to three-way arrays by unfolding the three-way array to a two-way array, as is conceptually depicted in Fig. 2. Trilinear data structure is not a requirement for MCR, and although data are unfolded before analysis, the unfolded factors may be refolded to factors that can be interpreted in relation to the original three-way data structure. Refolding is a general possibility but it should be kept in mind that there is no guarantee that the refolded factors are chemically meaningful.

MCR can be performed in a number of different ways, but only one approach will be described here. In this implementation, the decomposition is performed through an alternating least-squares (ALS) regression algorithm,⁷ using constraints as an integral part of the decomposition. The model can be written using an equation similar to the PCA decomposition model, but where orthogonality is inherent to the PCA model this is completely relaxed in the ALS decomposition. Owing to the unfolding of the three-way array, information in two of the modes are mixed and the calculated components have to be reconstructed to the size of the original three-way array before interpretation of the results.

3.2.4. *Applications of MCR*

Examples of the application of MCR to both 2D DOSY NMR data²³ and 3D [¹H–¹⁵N] HSQC NMR data²⁴ can be found. In the latter case, the reaction between ¹⁵N-labelled cisplatin and the amino acid–nucleotide hybrid (Phacmet-linker p^{5'}dG) is monitored and both analysis of the individual 2D HSQC spectra as well as the simultaneous analysis of all 2D HSQC spectra over time is performed in which case the kinetic reaction profiles can be obtained. The authors found that sub-structures involved in local unfolding as a consequence of the addition of denaturant could be identified, and that this would hardly have been possible without multivariate analysis of the data.

3.3. True multi-way analysis

This section deals with analysis of the three-way NMR data using true three-way methods.

3.3.1. PARAFAC theory

As early as 1970, Harshman²⁵ developed the parallel factor (PARAFAC) model. The model can be written in terms of the individual elements of the three-way array as

$$x_{ijk} = \sum_{f=1}^F a_{if} b_{jf} c_{kf} + e_{ijk} \quad (2)$$

where the information in the three-way array $\underline{\mathbf{X}}$ of size $I \times J \times K$ is modelled as a sum of F components. Ideally, each of the F components describes one underlying chemical component. Each component consists of one score vector, \mathbf{a}_f with I elements, and two loading vectors, \mathbf{b}_f with J elements and \mathbf{c}_f with K elements, where a_{if} is the i th element of \mathbf{a}_f . This decomposition is visualised in Fig. 5.

Given that the quality of the data is sufficiently high and data are low-rank trilinear, a meaningful unique solution can be calculated without imposing artificial constraints such as the orthogonality constraint imposed by PCA. In the PARAFAC case, the loadings should resemble the spectra of the pure chemical components and the individual compounds can be identified and quantified if the concentration in just one of the samples is known.

3.3.2. Applications of PARAFAC

Initially, two recent applications of PARAFAC to NMR data are presented followed by two older but somewhat more complex applications.

To illustrate the use of PARAFAC on three-way NMR data, an experimental design was used to create a set of only seven samples all containing glucose, lactose and isoleucine in various relative concentrations.²⁶ The corresponding full factorial design with three compounds at three concentration levels would require a total of 27 samples. On the basis of the diffusion-weighted pseudo 2D NMR data acquired for each sample, a three-way array was created. A typical example of the measurements of one sample is given in Fig. 6. The three compounds were selected in order to create a difficult example, because glucose and isoleucine show very similar diffusion rates and glucose and lactose show substantially overlapping spectra.

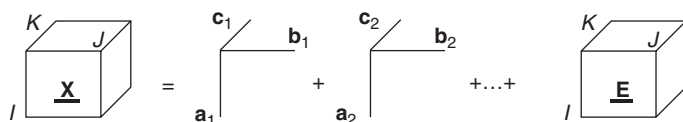


Fig. 5. Schematic representation of the decomposition of the three-way array $\underline{\mathbf{X}}$ into scores and loadings and a residual performed by PARAFAC.

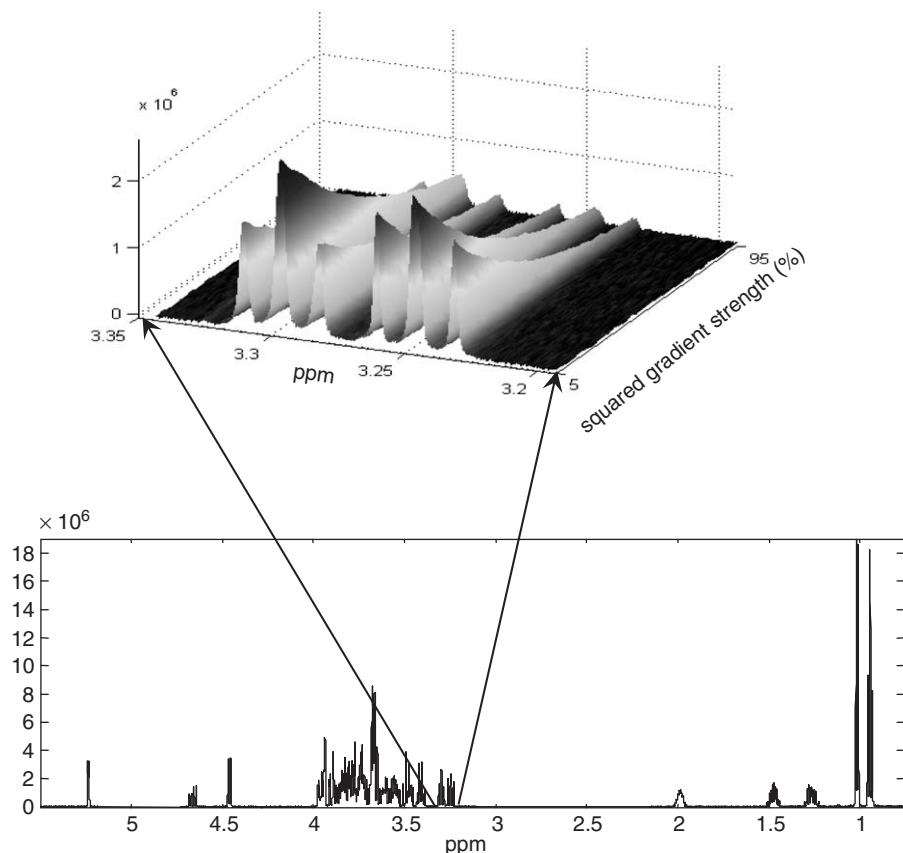


Fig. 6. Example of diffusion-weighted data. For clarity, the 1D spectrum corresponding to the first-gradient increment is pictured along with a 3D-plot of a subsection of the spectrum.

Since data can be assumed to be low-rank trilinear, the PARAFAC method was appropriate and performed very well. The PARAFAC loadings of the chemical shift mode provided estimates of the pure component spectra (Fig. 7A) and relative concentrations of these were found as the sample scores (not shown). Had the gradient system been calibrated, the diffusion coefficients could also have been calculated from the third mode loadings (Fig. 7B). An important point to note here is the ability to deconvolute substantially overlapping signals from only a small number of samples, something which cannot be expected to be accomplished using traditional methods of analysis. That the pure component spectra have in fact been deconvoluted by the PARAFAC model is evident from Fig. 8, where the pure component NMR spectra are shown along with the residual from the

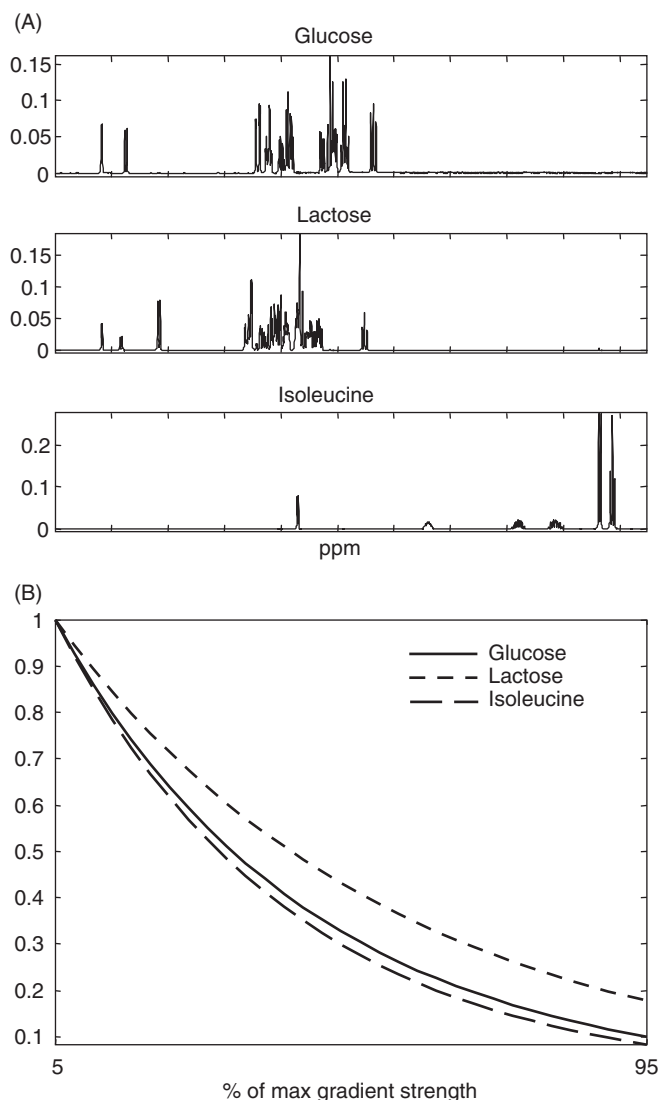


Fig. 7. (A) The spectral loadings calculated by PARAFAC and (B) diffusion attenuation profiles resulting from the PARAFAC model.

comparison of the acquired pure component NMR spectra and spectra calculated by PARAFAC. The residual resembles noise and it is clear that there is good agreement between the acquired and calculated spectra.

Dyrby *et al.*²⁷ demonstrated the use of PARAFAC to resolve approximately pure component spectra for the four lipoprotein main fractions in human plasma: VLDL, IDL, LDL and HDL. The study was a feasibility

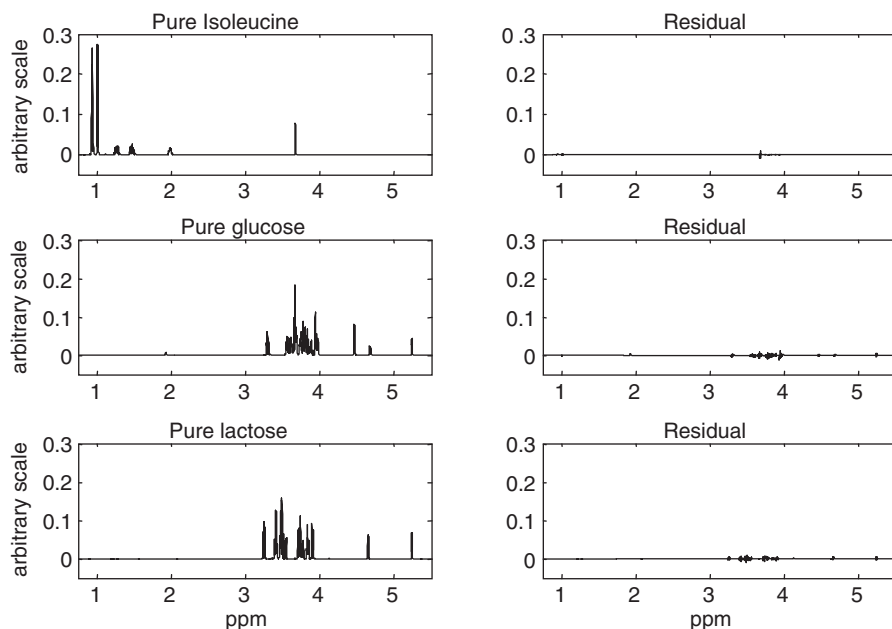


Fig. 8. On the left-hand side, the acquired pure component spectra as well as the residual spectra when comparing with the spectral loadings calculated by PARAFAC shown in Fig. 7.

study acquiring 2D diffusion-weighted NMR data for a number of samples and collecting these in a three-way array for subsequent analysis using PARAFAC. Although the system is expected to be trilinear, it is clearly not low rank, since all lipoprotein main fractions are distributions consisting of a sum of a large number of sub-fractions, which again are distributions. The distribution is related to lipoprotein particle size within each fraction. Despite the lack of low rank, the application of non-negativity constraints ensured an approximation with chemically meaningful spectra for all four components, giving confidence to the validity of the model.

The very first application of three-way analysis to 2D NMR data was performed in 1997 by Windig and Antalek²⁸ and was termed *Direct Exponential Curve Resolution Algorithm* (DECRA). Although the three-way analysis was straightforward, the generation of the three-way data analysed was rather special. A specific property of exponential data was utilised where pseudo 2D NMR data (1D NMR spectra collected over time) can be transformed into a three-way array. The purpose of the study was to monitor first-order reaction kinetics and calculate reaction rate constants. In a first-order reaction, reactants decrease exponentially and products increase exponentially; thus the underlying structures over time are

exponential, and due to the nature of the exponential function any sub-set of the data in the time direction will contain the same underlying exponential time constants, only in different quantities, as illustrated in Fig. 9. This means that based on a two-way data matrix, a three-way array can be created, as illustrated in Fig. 10, and subsequently analysed by three-way methods. In a recent paper, the effect of non- and multi-exponential decay behaviour on the performance on DECRA is investigated in relation to NMR.²⁹ The idea of generating a three-way array from a two-way array on a single sample was rather original, since it enabled application of the PARAFAC model and unique deconvolution of the pure profiles. Furthermore, the fact that only a single sample was analysed eliminated potential matrix effects and other artefacts. Since DECRA was initially published, the concept has been widely used with other kinds of spectroscopy and has also been developed for low-field NMR,^{30,31} where the resulting time domain relaxation data show multi-exponential behaviour directly.

In 2001, Orekhov *et al.*³² described a method that was called *MUlti-dimensional NMR spectra INterpretation* (MUNIN) for the analysis of 3D NMR data. The aim of MUNIN is to facilitate the analysis of the large amounts of data in 3D NMR experiments through the extraction of pure component spectra and in the original work the analysis of [^1H - ^{15}N]-NOESY-HSQC data is described. In essence, MUNIN is based on an initial data compression by Tucker3 (see Section 2.4) followed by three-way decomposition according to the PARAFAC model. A fairly large number of components are extracted in the PARAFAC model and because a larger number of components are calculated than what are directly supported by data a post-processing step called “de-mixing”, where mixed components (two-factor degeneracy) are resolved, has to be performed. Finally, the full-length pure components spectra are reconstructed and interpreted. In this paper, Orekhov *et al.*³² demonstrated one of the advantages of using three-way decomposition methods directly on the three-way array rather than unfolding data or analysing a 2D subsection. Rather than performing 3D Fourier transformation on the three-way array, the ^{15}N dimension is maintained in the time domain and it is shown that a random selection of only 20% of the 2D slabs in the ^{15}N direction provides close to identical deconvolution of the underlying components compared to the deconvolution of the entire three-way data set. In essence, this means that this data set could have been acquired in only 20% of the time, still providing meaningful results, which in the case of high-dimensional NMR data can mean a time-saving of days.

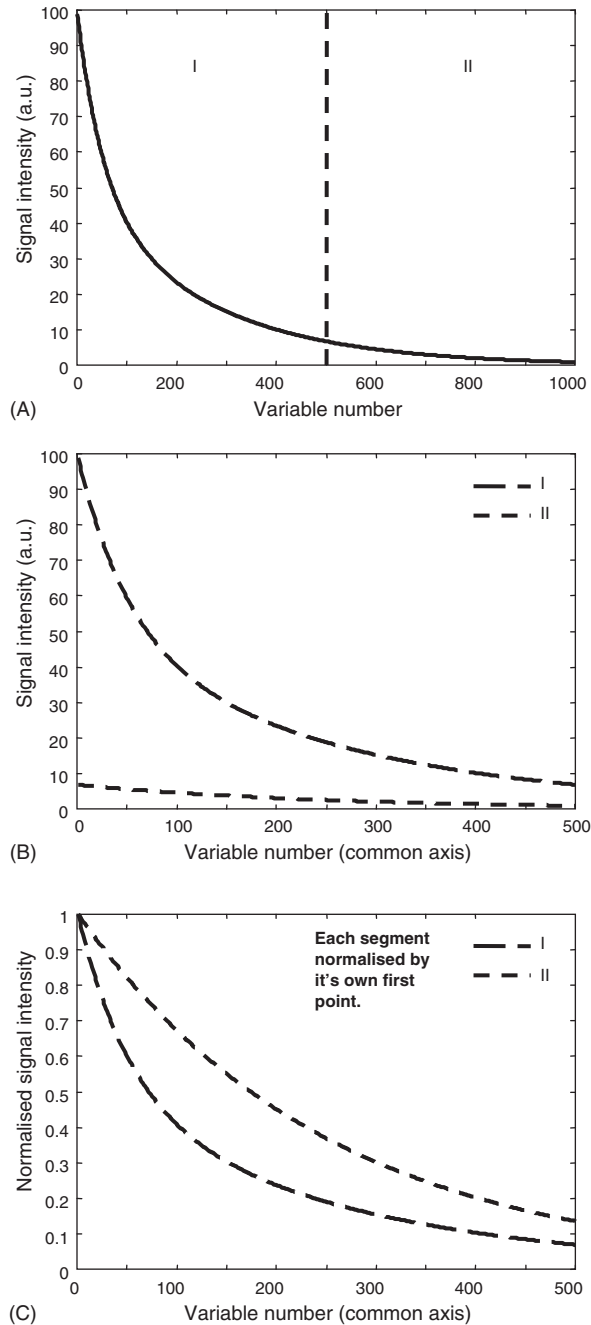


Fig. 9. (A) The nature of exponential data: a bi-exponential function is split into two halves, I and II. (B) I and II are arranged on a common axis. (C) I and II are normalised to maximum intensity equal to one. Bi-exponential fit of I and II will reveal identical decay constants only in different quantities.

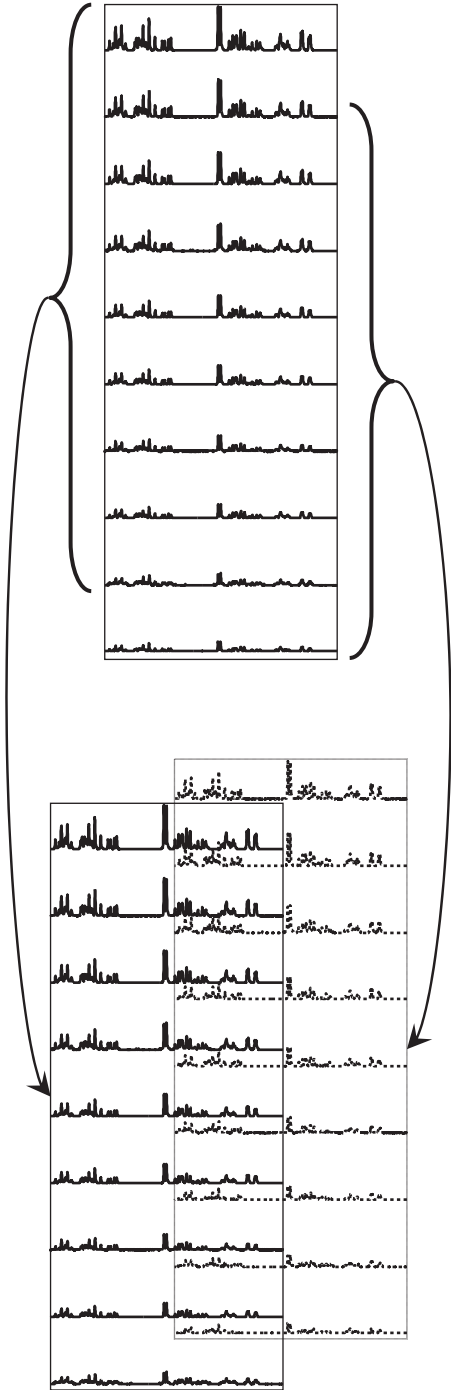


Fig. 10. Schematic representation of the concept in DECRA.

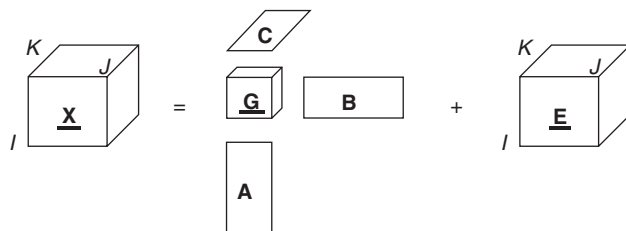


Fig. 11. Schematic representation of the Tucker3 model, which is a weighted sum of outer products between the components stored in the columns A–C. \mathbf{G} is called the core array.

3.3.3. Tucker3 theory

Tucker3 is a three-way model, which does not require low-rank trilinear data structure, nor does it provide pure component spectra from mixtures. A schematic representation of the Tucker3 model can be seen in Fig. 11.

A major difference between the Tucker3 model and the other models mentioned in this paper is the fact that in the Tucker3 model, different numbers of components can be used in the different modes such that if the size of the raw data matrix \mathbf{X} is $I \times J \times K$, then the size of decomposition matrices \mathbf{A} (first mode), \mathbf{B} (second mode) and \mathbf{C} (third mode) are: $\mathbf{A} = I \times P$, $\mathbf{B} = J \times Q$, $\mathbf{C} = K \times R$, where P , Q and R are the number of components in the three modes. Also the fact that scores and loadings from the different modes are allowed to interact is a special feature of the Tucker3 model. This interaction is accomplished through the core array, \mathbf{G} , the size of which is $P \times Q \times R$.

The interaction of the different components through the core array makes the interpretation of the Tucker3 model somewhat complicated and is probably a limitation to widespread use of the model.

3.3.4. Applications of Tucker3

In a paper by Dyrby *et al.*,²¹ three different data sets are analysed using Tucker3 in a study of metabolic response to toxins monitored by NMR. Owing to the different temporal response as well as differences in metabolic toxic response, these data are not expected to be low-rank trilinear. Furthermore, samples taken from living organisms may not be low rank due to the complexity of the metabonome.

The three toxins are hydrazine dihydrochloride, α -naphthyl-isothiocyanate (ANIT) and butylated hydroxytouluen (BHT), all of which are well-known and well-studied toxins. The same data have previously been analysed by Antti *et al.*²⁰ using batch analysis and the results obtained with the Tucker3 analysis are compared with the results of the batch analysis.

One of the resulting conclusions is that the interpretation of the Tucker3 model is clearly more difficult compared to the interpretation of the batch analysis model. This is primarily due to the interaction between components in the different modes in the Tucker3 model. However, changes in the metabolic state due to the toxin could be detected earlier from the Tucker3 model compared to the batch model.

3.4. Other two- and three-way methods

This section gives a short description of two- and three-way methods not described in the previous sections. These methods are included to allow the reader to recognise these as related methods when encountering them in scientific literature.

- Direct trilinear decomposition (DTLD) is a direct non-iterative and therefore fast algorithm for solving the PARAFAC model providing a non-LS solution. If data are low-rank trilinear, the solution produced by DTLD will be close to identical to that resulting from the PARAFAC algorithm.
- PARAFAC2 is a model, which can handle data of different length in one of the dimensions, but with the same underlying features as can be found in, for example, chromatographic data where the elution time may change with varying column conditions.
- Tucker1 can be seen as a special case of the Tucker3 model, but with the number of components so large in two modes that the variation in these dimensions is not reduced. It can be shown that this model is identical to PCA on unfolded data.
- Partial least-squares regression (PLS)³³ is a basic method in two-way multivariate data analysis. Where PCA is a method that only considers the structure of one matrix \mathbf{X} , PLS is a regression method where the variation contained in a \mathbf{X} matrix (typically the NMR data) is correlated to a known reference value typically referred to as \mathbf{Y} , which can be either a vector or a matrix. By simply acquiring the NMR spectrum of future samples, the concentration of the reference compound can be predicted using the previously calculated PLS model. This may be an advantage in terms of reduced cost and time of analysis compared to many traditionally more laborious chemical measurements. Furthermore, spectral data contaminated by interfering signals can be handled as long as the interfering signals are properly covered in the calibration model.
- N-PLS is the multi-way extension of the two-way PLS method. In the same way that it is possible to calculate a regression model between a two-dimensional \mathbf{X} matrix and a reference value (\mathbf{Y}) by means of PLS it

is possible to calculate a regression model between a three-way \mathbf{X} array and a reference value (\mathbf{Y}) using N-PLS.^{34,35} This does not normally result in significantly better predictions, but in line with the other three-way methods improved interpretation of the model is often an advantage. N-PLS has been applied to diffusion-weighted pseudo 2D NMR data with the contents of lipoprotein main fractions as the reference values (\mathbf{Y}).²⁷

4. CONCLUSIONS

During the last 2–3 years, the number of publications describing simultaneous analysis of a collection of 2D- or 3D NMR data directly by means of multi-way methods has increased substantially, although the overall number of applications is still rather low.

In the current literature, several examples are given where data analysis has been greatly simplified through the application of multi-way methods, and results are presented where conclusions based on multi-way analysis give greater insight into the problem being analysed. It has also been described how the time of acquisition of 3D NMR data can greatly be reduced, if the acquired data are analysed by three-way methods rather than traditional 3D Fourier transformation. Furthermore, problems, which can hardly be expected to be solved satisfyingly by traditional methods, are handled appropriately when the problem is turned into a multi-way problem and multi-way methods are applied.

All of the applications described so far in the literature deal with the analysis of hetero-nuclear 2D- and 3D NMR data, but analysis of symmetrical homo-nuclear NMR data should also be possible. In fact, in terms of validated data analysis this kind of data may present an added advantage, if data on one side of the diagonal is used for calibration and the other half on the other side of the diagonal is used for validation. This has yet to be tested, to see if it holds in practice.

It is foreseen that routine analysis of large amounts of NMR data can be greatly facilitated by means of multivariate techniques making multi-dimensional high-field NMR more interesting as a tool for routine analysis of complex samples, which will be unparalleled by most other instrumental techniques. This has yet to be proven, but promising signs of this are already appearing in published literature.

ACKNOWLEDGEMENTS

We thank Gilda Kischinovsky for helpful editing of the manuscript. Thanks are also given to Jens Breinholt for helpful comments on the traditional analysis of 2D NMR data.

REFERENCES

1. R. Bro, *Anal. Chim. Acta.*, 2003, **500**, 185.
2. H. Martens and T. Næs, *Multivariate Calibration*, Wiley, Chichester, 1989.
3. L. Munck, L. Norgaard, S. B. Engelsen, R. Bro and C. A. Andersson, *Chemometr. Intell. Lab. Syst.*, 1998, **44**, 31.
4. T. M. Alam and M. K. Alam, *Annual Reports on NMS Spectroscopy*, Elsevier, Oxford, 2005, p. 41.
5. M. Defernez and I. J. Colquhoun, *Phytochemistry.*, 2003, **62**, 1009.
6. R. Bro, *Multi-Way Analysis in the Food Industry. Models, Algorithms and Applications*, University of Amsterdam, The Netherlands, 1998.
7. A. de Juan and R. Tauler, *J. Chemometr.*, 2001, **15**, 749.
8. R. Bro, *Chemometr. Intell. Lab. Syst.*, 1997, **38**, 149.
9. R. Bro and C. A. Andersson, *Chemometr. Intell. Lab. Syst.*, 1998, **42**, 105.
10. B. K. Alsberg, E. Nodland and O. M. Kvalheim, *J. Chemometr.*, 1994, **8**, 127.
11. R. A. Harshman, *Research Methods for Multimode Data Analysis*, Praeger, New York, 1984, p. 566.
12. E. Comas, J. Ferre and F. X. Rius, *Anal. Chim. Acta.*, 2004, **515**, 23.
13. R. Bro and H. A. L. Kiers, *J. Chemometr.*, 2003, **17**, 274.
14. S. Wold, *Technometrics*, 1978, **20**, 397.
15. A. K. Smilde, R. Bro and P. Geladi, *Multi-Way Analysis. Applications in the Chemical Sciences*, Wiley, Chichester, 2004.
16. C. A. Andersson and R. Bro, *Chemometr. Intell. Lab. Syst.*, 2000, **52**, 1.
17. H. Hotelling, *J. Educ. Psychol.*, 1933, **24**, 417.
18. J. E. Jackson, *J. Qual. Technol.*, 1980, **12**, 201.
19. A. Berglund, A. C. Brorsson, B. H. Jonsson and I. Sethson, *J. Magn. Reson.*, 2005, **172**, 24.
20. H. Antti, M. E. Bollard, T. Ebbels, H. Keun, J. C. Lindon, J. K. Nicholson and E. Holmes, *J. Chemometr.*, 2002, **16**, 461.
21. M. Dyrby, D. Baunsgaard, R. Bro and S. B. Engelsen, *Chemometr. Intell. Lab. Syst.*, 2005, **76**, 79.
22. W. H. Lawton and E. A. Sylvestre, *Technometrics*, 1971, **13**, 617.
23. R. Huo, R. Wehrens and L. M. C. Buydens, *J. Magn. Reson.*, 2004, **169**, 257.
24. J. Jaumot, V. Marchan, R. Gargallo, A. Grandas and R. Tauler, *Anal. Chem.*, 2004, **76**, 7094.
25. R. A. Harshman, *UCLA Working Papers Phonet*, 1970, **16**, 1.
26. R. Bro, P. I. Hansen, N. Viereck, M. Dyrby, H. T. Pedersen and S. B. Engelsen, *Magnetic Resonance in Food Science – The Multivariate Challenge*, Royal Society of Chemistry, Cambridge, UK, 2005, p. 195.
27. M. Dyrby, M. Petersen, A. K. Whittaker, L. Lambert, L. Norgaard, R. Bro and S. B. Engelsen, *Anal. Chim. Acta.*, 2005, **531**, 209.
28. W. Windig and B. Antalek, *Chemometr. Intell. Lab. Syst.*, 1997, **37**, 241.
29. T. M. Alam and M. K. Alam, *J. Chemometr.*, 2003, **17**, 583.

30. H. T. Pedersen, R. Bro and S. B. Engelsen, *J. Magn. Reson.*, 2002, **157**, 141.
31. S. B. Engelsen and R. Bro, *J. Magn. Reson.*, 2003, **163**, 192.
32. V. Y. Orekhov, I. V. Ibraghimov and M. Billeter, *J. Biomol. NMR.*, 2001, **20**, 49.
33. S. Wold, H. Martens and H. Wold, *Lecture Notes in Mathematics*, Springer, Heidelberg, 1983, p. 286.
34. R. Bro, *J. Chemometr.*, 1996, **10**, 47.
35. R. Bro, A. K. Smilde and S. de Jong, *Chemometr. Intell. Lab. Syst.*, 2001, **58**, 3.

High-Resolution Protein Structure Determination by NMR

HIROYUKI TAKASHIMA

Novartis Institutes for BioMedical Research, Ohkubo 8, Tsukuba, Ibaraki 300-2611, Japan

1. Introduction	236
2. Statistics of protein structures solved by NMR on protein data bank	236
3. Critical factors for NMR structure qualities	238
4. High-performance computing	238
5. NMR structure determination process overview	240
6. Structure calculation	241
6.1. Algorithms	241
6.2. Metric matrix distance geometry	242
6.3. Torsion angle space minimization (variable target function method)	242
6.4. Molecular dynamics for NMR structure determination	243
6.5. NMR structure ensemble	245
6.6. Conformational sampling and refinement	245
7. High-performance computing implementation for structure determination	246
7.1. Verification of sampling scale	246
7.2. Comprehensive conformational space search for protein structure calculation	249
7.3. Distribution of local minima: ensemble size and its significance	254
8. Basic NMR-derived constraints for structure calculations	256
8.1. NOE intensities	256
8.2. Scalar coupling constants	258
8.3. Hydrogen bonds	258
9. Improve target function quality	259
9.1. Residual dipolar couplings	259
9.2. Database potentials	260
9.3. Backbone hydrogen bond topology	261
9.4. Other sources of conformational constraints	261
9.5. Resonance assignment precision: automated approaches	261
9.6. NOE validation	262
9.7. Improve force field	263
10. Dynamics	264
11. Quality check of the NMR ensemble	264

12. Protein sample preparations	265
13. NMR Experiments	266
13.1 Recent technological advances in equipment	266
13.2 Pulse sequence techniques and data acquisitions	266
13.3 Solid-state NMR	267
14. Concluding remarks	267
Acknowledgments	268
References	268

The quality of the three-dimensional structure of proteins determined by nmr is influenced by many factors. The factors are reviewed by focusing on structure calculation problems. High-performance computing implementations are introduced to improve the conformational sampling of the calculations. The quality and improvements of the nmr-derived structural information are also discussed.

1. INTRODUCTION

Drug discovery is often based on three-dimensional protein structures, which are mainly determined by X-ray diffraction crystallography or NMR spectrometry. To utilize the structures for the drug design in a chemical space,¹ atomic resolution is a crucial factor, because the atom is a common language between proteins (described by coordinates) and chemical compounds (described by structural formula). The atomic resolution protein structure determination therefore is an important subject. Furthermore, recent advance in genomics increases relevance of structural biology. Many pilot projects, e.g., Protein 3000 (by Riken Genome Sciences Center),² are determining the protein structure, and they are recently focusing on therapeutically relevant protein targets. These will be accomplished by characterization of the structural properties for biochemical functions. This review focuses on re-examining problems of protein structure quality by NMR and on introducing solutions and proposals. The central focus will concern high-resolution structure calculation by a comprehensive conformational space search (Section 7).

2. STATISTICS OF PROTEIN STRUCTURES SOLVED BY NMR ON PROTEIN DATA BANK

The importance of NMR in biological macromolecular structures is illustrated by the number of coordinate files that are deposited in the Protein

Data Bank (PDB, url: <http://www.rcsb.org/pdb>) (Table 1). As of January 2006, there are a total of 5,182 entries available in the PDB. This accounts for 15% of the total structures; the percentage was almost constant for the last decade, although the number of X-ray structures is drastically increasing. NMR plays a role complementary to the structure determination with X-ray. Many of the NMR structures in the PDB do not have corresponding crystal structures, and most of these proteins simply do not provide diffraction quality crystals. The size distribution of the PDB coordinate entries, shown in Fig. 1, indicates that the large majority of the structures for

Table 1. PDB statistics summary of released entries as of January 2006

Experimental method	NMR	X-ray	EM	Other	Total
Proteins	4,380	26,990	74	67	31,511
Protein/nucleic acids complexes	116	1,258	27	3	1,404
Nucleic acids	669	804	9	4	1,486
Other	17	85	0	0	102
Total	5,182	29,137	110	74	34,503

EM = Electron microscope.

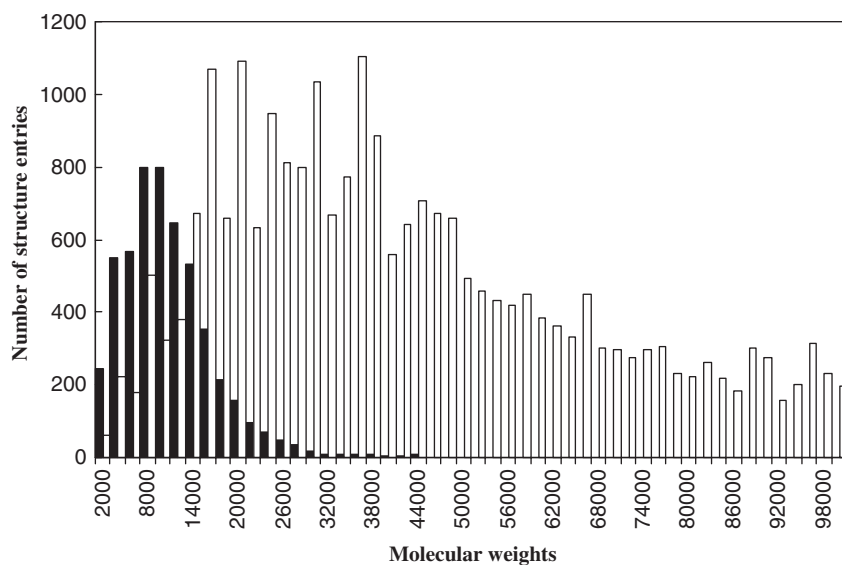


Fig. 1. A histogram of number of PDB entries as of January 2006 plotted against molecular weights. Closed bars, NMR structures; open bars, X-ray structure. The number of structure entries count up to 100 kDa, increasing by 2 kDa.

small proteins (up to 12 kDa) were determined by NMR. The proteins with a molecular weight below 20 kDa are solved regularly, whereas structure determinations for proteins above 25 kDa are still rare.

In the PDB, it is strongly encouraged that the depositors also submit files containing experimental data that were used in the structure calculation. These files include the distance and torsion angle constraints used in the structure calculations. These data are essential to judge the quality of a structure determined by NMR, and will be useful to reproduce the coordinates in other laboratories as structure calculation methods advance. Because of the different approaches for structure determinations by different depositors, it is, usually, difficult to compare and assess the quality of coordinates in the PDB.

3. CRITICAL FACTORS FOR NMR STRUCTURE QUALITIES

The accuracy of protein structures determined by NMR is very dependent on the quantity and quality of data that can be obtained. It has been known that the highest quality NMR structures have accuracies comparable to the medium-resolution X-ray structures (2.0–2.5 Å) for protein backbone atomic coordinates.³ To improve the structural qualities and utilize them for biological system studies, it is important to re-emphasize factors having a critical impact on quality as summarized below.

1. Protein sample preparations
2. Precision of information (e.g., NOE-derived distance prediction quality)
3. Structure calculations
4. Dynamics and relaxation

Factors 2 (see Sections 8 and 9) and 3 (see Sections 6 and 7) above are controllable, and are the main subject of this review. Factor 1 is partially controllable and is discussed in Section 12. Factor 4 is not essentially controllable. However, the dynamics occupy a fundamental role for understanding the biological system, which is discussed in Section 10.

4. HIGH-PERFORMANCE COMPUTING

Computing power is not a fundamental factor to determine the high-resolution NMR structure. However, it is true that NMR data analysis techniques have been advanced with computing power, which is growing faster and faster. In the 1960s, pioneering work for two-dimensional NMR

Fourier transform by Ernst *et al.*⁴ was strongly promoted by the computing power. Now, a desktop personal computer (PC) is far superior to a room-sized computer used for the first two-dimensional data processing. Actually, three- or four-dimensional NMR data analysis is routinely performed by PCs in laboratories. In the 1980s, distance geometry calculations (Section 6.2) were usually performed by super computer, now, far more resource-consuming molecular dynamics calculations are available on single CPU PCs that are also used for E-mail and word-processing. The highly advanced computing power has not been sufficient yet for practical protein structure calculations, thus techniques to compensate for the limitation of computational resources have been a main challenge of protein structure calculations (see Section 6). Conventionally, the obstacle is circumvented by a reduction of degrees of freedom by force fields and/or algorithms (i.e., artificial restriction of conformational space extent, see Section 6). Because the computing power is not a fundamental problem for the structure quality, the limitation imposed by computing power should be kept to the minimum. Therefore, a solution that relies on advanced computing power is better than that of the algorithm-dependent method. In other words, the computing algorithm dependency (Section 6) can be eliminated. This is feasible, and the computing power will keep advancing faster than expected. The perspective view of high-performance computing is presented below.

Recently, a distributed computing technique is building popularity in high-performance scientific calculations.⁵⁻¹⁰ This is an array of PCs or workstations connected by the Internet or an Intranet. It is classified as GRID computing and PC cluster, for instance. The computing power can be easily amplified by increasing the number of connected computers that are usually connected in the network. Recently, a distributed computing system composed of thousands or even tens of thousands of machines is available and utilized in some institutes. Protein structure calculations by NMR are also a promising subject for the distributed computing⁷ (see Section 7).

PC cluster (or parallel computing) uses multi-CPU as a virtual single CPU by parallel computing module (such as LAM-MPI, url: <http://www.lam-mpi.org>); therefore, it is possible to speed up a long calculation. This can be used for a heavy calculation of molecular dynamics simulation (nanoseconds to microseconds) starting from a single conformer. In contrast, GRID computing just administrates the CPUs by a scheduler (sometimes called GRID engine, e.g., SUN GRID engine that is provided by SUN Microsystems, url: <http://www.sun.com>). Usually, the two methods are used on a case-by-case basis with a distributed computing package (such as ROCKS cluster, url: <http://www.rockclusters.org>).

In general, parallel computing needs a program source modification to optimize the performance. Still now, just a minority of programs has the

standard parallel computing modules, and their availability is mostly unknown. However, the distributed calculations can be easily paralleled without modification of the programs by the GRID engine. Recently, examples of the GRID-computing implementation for NMR structure determination were reported by Takashima *et al.*^{7,11} Twenty PCs were used for the calculations by a non-paralleled program, XPLOR-NIH.¹² The results demonstrated that problems in conventional structure calculation can be solved by the high-performance computing, resulting in drastic increase of structural quality as extensively discussed in Section 7. To reconfirm the problem in structure calculation, the NMR structure determination process (Section 5) and the calculation algorithms (Section 6) are briefly reviewed below.

5. NMR STRUCTURE DETERMINATION PROCESS OVERVIEW

NMR structure determination is a complex process. It has steadily progressed as shown in many extensive reviews.^{13–23} A brief step-wise summary of the process is presented below.

1. Protein sample preparation including possible isotopic labeling.
2. Data collection by a set of multidimensional NMR experiments.
3. Assignment of the chemical shifts of the nuclear spins by sequential assignment technique developed by Wüthrich.¹³ In statistics of the assignment table deposited in a Biological Magnetic Resonance Data Bank (url: <http://www.bmrb.wisc.edu>), nearly complete assignments for backbone and side chain are presented for almost all proteins smaller than 15 kDa, while many of the proteins bigger than 20 kDa just have backbone assignments and very partial side chain assignments (e.g., for part of methyl protons only) due to resonance complexities and isotope labeling.
4. Assignment of NMR-derived experimental information, such as nuclear Overhauser effect (NOE) and scalar coupling constants. The information is converted into approximate NMR-derived structural constraints (Section 8). Some of the NOEs could remain unassigned because of spectral complexities. If stereospecific assignment is not possible, NOEs of stereochemical protons in prochiral groups are assigned to a pseudo-atom with correction for the derived distances (pseudo-atom correction).¹³ Unresolved NOEs for ring protons and methyl protons are also treated by pseudo-atoms.
5. Preliminary structure calculations in order to verify the consistency of NOE-derived distance constraints. Some of the remaining NOEs are

assigned in this process. The preliminary calculations are generally repeated until most of the constraints are in agreement with the calculated structures.²³ Sometimes, a constraint refinement against NOE peak intensities (back-calculations)²⁴ is carried out to improve the approximation quality.

6. Structure calculations (or refinements, in the case of using preliminary calculated structures as starting structures).

This review focuses on Steps 5 and 6 hereafter. The NMR-derived structural information quality and its problem are discussed in Sections 8 and 9.

6. STRUCTURE CALCULATION

NMR structure determination can be viewed as a global optimization problem for a target function in the conformational space to determine three-dimensional coordinates. The target function is normally a hybrid potential between the NMR-derived structural information and empirical steric conditions. The conformational space means the total degrees of freedom for the atomic positions, typically more than a thousand. The conformational space search for the highly complicated system has been a challenging computational target.

6.1. Algorithms

Historically, there are many calculation algorithms for the NMR structure determination. These are roughly classified into three categories as listed below.

1. Metric matrix distance geometry
2. Torsion angle space minimization (variable target function method)
3. Molecular dynamics

The computational challenge has mainly focused on effective CPU usage by algorithms that are artificial restrictions of the conformational space. The restrictions are mainly achieved by constraints of atomic bond lengths and angles, which are not essential subjects for NMR-derived structural information. Torsion angle space with fixed length and angle constants is used for some programs. In the metric matrix distance geometry, a distance space is used instead of real spaces. Even in molecular dynamics, usually a simplified empirical force field is applied for NMR structure calculations.

In practice, more computational resources are required for the more recently developed algorithms. The molecular dynamics calculation is the

latest, and became feasible by the highly advanced computing power. These algorithms have been often combined to use computational resources more effectively, i.e., preliminary structure calculations and refinements (see Sections 5 and 6.6). The effective CPU usage is often a work-around solution for limited computational resources as discussed in Section 4. The cost of the work-around solution by means of the structural quality has not been fully discussed. A brief historical overview and update focused on the resulting structure quality are presented below. Subsequently, NMR structure convergences (Section 6.5) and conformational samplings (Section 6.6) are discussed. Solutions for the problems are discussed in Section 7 with the high-performance computing implementation.

6.2. Metric matrix distance geometry

Distance geometry based on the metric matrix was the first and epoch-making method for the protein structure determination by NMR data.^{25,26} Because of the great contribution for the development of NMR structure, NMR structure calculations are often termed ‘distance geometry calculations,’ regardless of the different algorithms used. The metric matrix-based distance geometry relies on the fact that the chemical topology of an atomic position can be represented as distance constraints as well as NOE-derived distances. This is the distance space, and it can be converted into Cartesian coordinates by a mathematical theorem ‘distance geometry’ using three-dimensional Euclidean space. Because of the simple algorithm and relatively small number of degrees of freedom (small conformational space), metric matrix distance geometry had an advantage when computational resources were limited. On the other hand, the algorithm required a complete distance matrix for all atoms involved, which is not obtained by NMR and has to be predicted over the geometries. This may cause unignorable structural bias. The distance space, however, has a different potentiality compared to real space algorithms. This method was extensively reviewed by Brünger and Nilges,²⁴ and recently summarized by Havel.²⁷ Programs DISGEO,²⁸ DG-II,²⁹ EMBOSS,³⁰ and TINKER³¹ have been used for this type of calculation.

6.3. Torsion angle space minimization (variable target function method)

The second method developed is the torsion angle space minimization algorithm.³² This is a method to optimize the target function in the torsion angle space. The degrees of freedom are the torsion angles. Basically, the

target function of this algorithm is a summation of penalty function for NOE-derived distances and repulsions by van der Waals radii. The initial Cartesian coordinate (initial structure) that consists of randomly generated torsion angles is subjected to the target function optimization. Because of the steric repulsion, it is difficult to correct inappropriately folded structures. Therefore, the target function is *variable* for step-wise calculations, starting from the intra-residual target function with and without van der Waals repulsion, then including a next-neighbor residue, and so on, step by step up to the length of the complete polypeptide chain. It is easily understood that the step-wise schedule has to be modified one-by-one for proteins. For instance, disulfide bond, helices, and β -sheet should be independently considered to improve the hit rate of the folding. This made the method hard to automate, and tends to cause incompatibilities for calculated structure qualities in different laboratories.³³

Usually, a hundred random initial structures are calculated to explore the conformational space and to eliminate the initial structure dependency. Subsequently, the final structures that equally satisfy the NMR data are selected (in most of the cases, by the target function) to compose an NMR structure ensemble (see Section 6.5). Actually, the number of initial structures and the size of ensemble had not been systematically determined or validated, but had been just limited by computational resources. A systematic validation for the number and size is discussed in Section 7.

To increase the hit rate for structural folding with limited computational resources, statistics for torsion angle in the set of calculated local structures was included as a new torsion angle constraint in the step-wise iteration at some programs, e.g., DIANA.³⁴ This algorithm could effectively reduce a structural convergence for the NMR ensemble. Therefore, the convergences of NMR structure ensembles in the 1990s were often strongly dependent on the algorithm.

This method was also extensively reviewed by Brünger and Nilges²⁴ and Güntert.³⁵ Programs like DISMAN,³² DADAS,³⁶ DIANA³⁴ have been used for instance.

6.4. Molecular dynamics for NMR structure determination

Molecular dynamics calculation is solving Newton's equation of motion using a hybrid target function between empirical force fields and experimental data. The degrees of freedom are the Cartesian coordinates of the atoms. The dynamics aim to cross potential barriers caused by inappropriately folded structures. This can reduce the problem of being trapped in local minima more than the torsion angle space minimization. Usually, a

simulated annealing method³⁷ is applied with a simplified force field without non-bonded interactions in a vacuum. In a typical simulated annealing protocol of program XPLOR,³⁸ the simulated annealing is performed for a few picoseconds at a high temperature, e.g., $T = 2,000$ K, starting with a very small weight for the steric repulsion that allows atoms to penetrate each other. Subsequently, the system is cooled down slowly with increasing strength of the steric repulsion for picoseconds or tens of picoseconds. The coordinate of the final trajectory is subjected to energy minimization in order to create a final structure. This process is repeated for each of the initial structures independently to compose an NMR structure ensemble (Section 6.5).

The initial structures for the molecular dynamics are generated by various procedures. For instance, the torsion angle space minimization (as of preliminary calculations), a molecular modeling using a resembling protein or a so-called ‘random array.’³⁹ A random array is a set of atoms that has randomly distributed Cartesian coordinates (typically in the range from 0 to 20 Å) without any steric information. Subsequently, energy is minimized to achieve a randomly generated molecule. The random array is easy to create even for tens of thousands of initial structures, which are randomly distributed in the conformational space.

The differences of the initial structure generation procedure will influence the quality of NMR structures, because of the initial structure dependency of the calculations. The ability to cross the potential barrier (i.e., conformational space exploration efficiency) definitely depends on the molecular dynamics conditions (typically simulation time). The conditions, however, are usually not validated, because of limitations by computational resources. The computing power required is linearly dependent on the simulation time, and thus has been a strong limitation of the calculations. Furthermore, temperature and steric repulsion weighing schedules as well as the force field will influence the structural quality.

To use computational resources effectively, a new method was developed by Güntert *et al.*⁴⁰ He combined torsion angle optimization and molecular dynamics into a so-called ‘torsion angle dynamics.’ The program CYANA⁴¹ is an example and is used in many laboratories. Because the torsion angle dynamics has features similar to the torsion angle space minimization (Section 6.3), it also has a similar structural bias for convergences.

The molecular dynamics for NMR structure determination and the torsion angle dynamics were extensively reviewed by Güntert.³⁵ The method was also reviewed by Clore and Schwieters.²⁰ The molecular dynamics programs, e.g., CHARMM,⁴² AMBER,⁴³ and GROMACS⁴⁴ can be used for the structure determination. XPLOR,³⁸ its successor CNS,⁴⁵ and XPLOR-NIH¹²

are programs optimized for NMR- as well as X-ray-based structure determination.

6.5. NMR structure ensemble

Because the NMR-derived structural information, e.g., NOE, has unavoidable ambiguity (Section 8), the NMR structure is represented by a set of structures that equally satisfy the target function. The structures of the set are superimposed (usually onto averaged coordinates) to compose an NMR ensemble that is deposited in the PDB. The structural convergence is calculated for the ensemble, and is indicated by root mean square difference (rmsd). Usually, the rmsd value of backbone atoms is used to assess the NMR structure quality with a combination of statistics for satisfied constraints. Because a smaller rmsd value reflects a precise atomic position in the ensemble coordinates, the convergence is known as a measure for NMR structure precision.⁴⁶ This is, however, not a measure for structure resolution.^{24,46–50} This is because the conformational sampling by the ensemble is not validated, as mentioned above. Furthermore, the validation for a target function quality, that is mainly an NOE-derived distance prediction quality, also should be considered comprehensively. The structural convergence, the conformational sampling, and the target function quality are equally indispensable to assess the NMR structure resolution. The problem for the convergence and the conformational sampling can be overcome by high-performance computing and is discussed in Sections 7.1 and 7.2. On the basis of the discussions, the significance of the ensemble is revisited in Section 7.3. The validation for NOE is discussed in Section 9.6.

The rmsd value is elucidated in two different manners. A pair-wise-averaged rmsd is calculated by averaging for rmsd values among atomic positions in every pair of coordinates. A residue-averaged rmsd is calculated by rms deviations for all of the superimposed structures followed by averaging for residues. The residue-averaged rmsd is considerably smaller than the pair-wise-averaged rmsd; therefore, the manner should be notified. A pair-wise rmsd value is a distance between two conformers in the conformational space; thereby, it can be used as a measure for the conformational search extent (Section 7.2).

6.6. Conformational sampling and refinement

A fundamental problem for the structure determination algorithms has been an insufficient conformational sampling that causes the initial structure

dependency. To overcome the problem, many structure-refinement procedures were reported.^{51–55} The initial structure dependency is usually noticed as a bias toward particular conformations that may emphasize artificial structural precision (convergence in NMR ensemble). This is, however, just an aspect of the initial structure dependency. If the final structures in the NMR ensemble are trapped in local minima, which are most likely with insufficient conformational sampling, then the initial structure dependency results in critical loss of structural precision and quality.

Fig. 2 schematically represents the conformational sampling problem with an example of a structure-refinement procedure. Because the number of initial structures and the molecular dynamics conditions are not validated, it is very difficult to assess whether the conformational sampling is sufficient or not. If the number of initial structures is too small and the conformational space exploration ability of molecular dynamics is limited (by computational resources), the definitive global minimum structure cannot be obtained. Furthermore, the apparent convergence for the refined ensemble will be increased by the extent of the conformational space exploration ability (Figs. 2A and B). This is most likely true for many of the reported NMR structures. It should be noted that the initial structure dependency occurs for all structure-determination algorithms including structure-refinement process itself. If the number of initial structures is larger and the refinement schedule is efficient, the global minimum structure can be searched by chance (Fig. 2C). The refined structures, however, may just be searched on conformational sampling biased by the preliminary calculation algorithm or the starting structures modeled by resembling protein coordinates such as X-ray structures.

The simplest way to overcome the problem is a comprehensive search with a sufficiently large number of randomized (i.e., completely distributed in conformational space) starting structures. The high-performance computing strategy (Section 4) can be applied (Section 7).

7. HIGH-PERFORMANCE COMPUTING IMPLEMENTATION FOR STRUCTURE DETERMINATION

7.1. Verification of sampling scale

The conformational space drastically increases with the size of proteins. Conventionally, the computational resource limitation restricts the amount of calculations, and less than 200 of the initial structures have been used. There was no clear understanding for how many initial structures are needed to determine the protein structure by the calculations. Takashima *et al.*⁵⁶

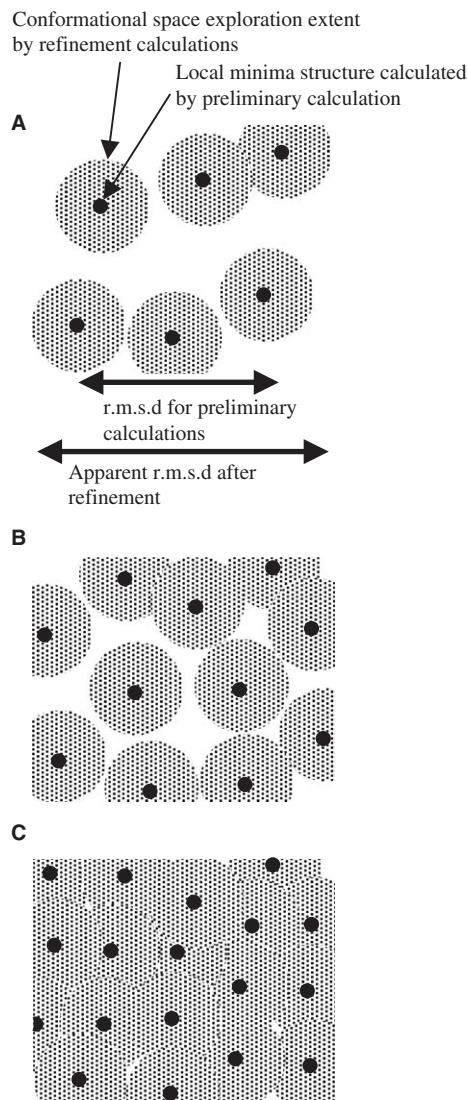


Fig. 2. Schematic representation of conformational space exploration efficiencies and their dependency for the different sampling scale with, insufficient (A), nearly sufficient (B), and almost sufficient (C) number of initial structures. In this example, preliminary calculations are distance geometry or torsion angle space algorithms, and refinement is restraint molecular dynamics with same set of NMR-derived structural information. The exploration extents of the refinements are assumed to be similar for selected preliminary calculation's results (i.e., initial structures of the refinement calculations).

used distributed computing with the SUN GRID engine (Section 4) to verify the sampling scale for the 21 amino acids peptide, endothelin-1, as described below.

The molecular dynamics algorithm was used with initial structures generated by random array (Section 6.4). Simulated annealing at a high initial temperature, 5,000 K, followed by 80 ps cooling step was performed using XPLOR-NIH.¹² The total number of initial structures was increased to 32,000, and the 20 final structures with the lowest energies of the target function were selected to elucidate rmsd values. To investigate the effect of the sampling scale based on the number of initial structures, the rmsd values were compared between smaller and larger subsets of simulated annealing structures from 50 to 32,000 (Fig. 3). There was a clear dependency of the rmsd on the number of initial structures, even for thousands and tens of thousands of structures. The rmsd and target function energies decreased exponentially with an increase of initial structures up to 16,000 and after that they were almost constant to 32,000, resulting in well-converged structures (PDB ID: 1V6R). These numbers are 100 times larger than those used conventionally for structure determination.

This small peptide is a suitable model system of protein folding, composed of secondary structural elements, α -helix and β -turn. The folding is stabilized by two disulfide bonds in the N-terminal region, whereas the C-terminal

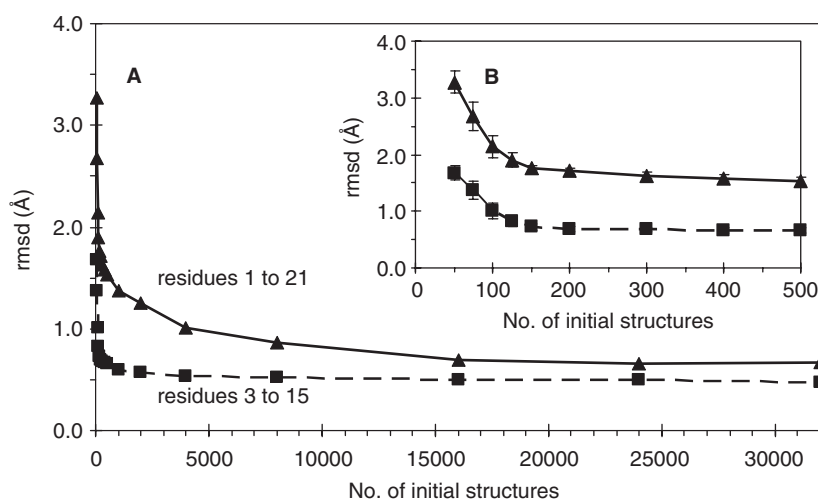


Fig. 3. (A) The pair-wise-averaged rmsd values of all backbone atoms of endothelin-1 (21 residues) have been elucidated for 20 minimum energy structures out of various numbers of calculated structures with 80 ps simulated annealing at initial temperature 5,000 K. (▲) Overlay for all residues from 1 to 21. (■) Overlay for residues from 3 to 15. (B) The same plot as panel (A), expanding the horizontal axis.

region was dispersed in the previously reported NMR ensemble.^{57,58} The rmsd for all residues, 1–21, exhibits a double exponential decay as shown in Fig. 3. It is obvious that the faster decay is caused by the local folding of the N-terminal region. A second very slow decay is presumably caused by the overall folding including the C-terminal region. With the use of a small number of initial structures, i.e., less than 500, the structure determinations will be very likely trapped in the localized folding, and it will bias the overall convergences. That is the reason why previously reported NMR structures of endothelin-1 had missed the convergence in the C-terminal region. One hundred initial structures with this simulated annealing condition are sufficient to search a local conformational space strongly restricted by disulfide bonds, but not sufficient for the larger space, i.e., the overall folding of the 21 amino acids peptide.

Takashima *et al.*⁵⁹ confirmed the C-terminal folding that is a hydrophobic core around a tyrosine ring by another NMR technique, photo-chemically induced dynamic nuclear polarization, accompanied by mass spectroscopy, matrix-assisted laser desorption/ionization time of flight mass spectrometry. This folding is not consistent with the X-ray structure (PDB ID: 1EDN),⁶⁰ which has an α -helix in the C-terminal region, but is in good agreement with experimental NMR parameters (3J -coupling and sequential NOEs).^{57,58} The discrepancy was caused by the inter-molecular hydrogen bond in a dimer-like formation of crystalline endothelin-1 that the tyrosine ring involved.

7.2. Comprehensive conformational space search for protein structure calculation

In general, the conformational space of proteins is much larger than that of endothelin-1, and the number of initial structures needed to explore them comprehensively from the random array (see Section 6.4) with tens of picoseconds simulated annealing is definitely greater than tens of thousands. A longer molecular dynamics, e.g., nanoseconds, microseconds or more, may search global minimum structure by chance, but is not feasible yet. Furthermore, generally, there is no standard criterion to assess the completion for target function optimization. The initial temperature of simulated annealing also influences the conformational search extent. The higher initial temperature resulted in a larger extent and a rougher search in the conformational space.

Takashima *et al.*¹¹ designed a multiplied simulated annealing procedure (Fig. 4) to implement distributed computing for protein structure determination, and applied it to a β -sheet-rich protein neocarzinostatin (113 amino acids + chromophore). The procedure consists of the higher and lower initial

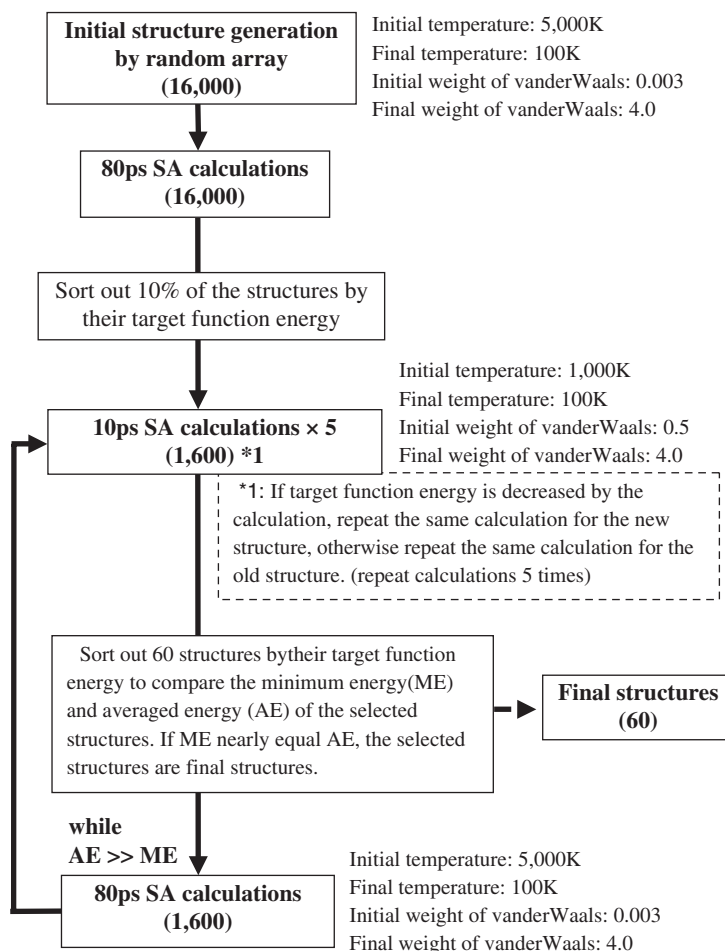


Fig. 4. Calculation regimen of a multiplied simulated annealing procedure. The number of structures is indicated by parenthesis. All simulated annealing (SA) were restrained by NMR-derived information.

temperatures simulated annealing in an iterative manner with a newly introduced completion criterion, that is ‘averaged target function energy (AE)–minimum target function energy (ME) ≈ 0 ’ in the calculated structure ensemble. The procedure can easily be automated, and can use the distributed computing resources effectively.

The procedure also used random array initial structures for molecular dynamics algorithm using XPLOR-NIH.¹² Sixteen thousand initial structures were subjected to an initial simulated annealing (5,000 K, 80 ps). This means that the initial structures did not cover the entire conformational space, but were randomly distributed all over the space. The conformational

space exploration extent by the single simulated annealing (5,000 K, 80 ps) for neocarzinostatin was estimated to be $<2 \text{ \AA}$ by preliminary calculations. It was elucidated by the pair-wise rmsd for backbone atoms between before and after the simulated annealing. The folding hit rate of structure calculations generally depends on the structural topology, e.g., secondary structures. In practice, β -sheet-rich protein has the lowest hit rate because of the higher energy barriers for improperly folded structures. Usually, the hit rate is $<10\%$, and many algorithms have been straggled to improve the hit rate.^{24,35} To make the calculation strategy very simple, the procedure just cut-off 90% of structures from the results of initial simulated annealing sorted by target function energies (Fig. 4). Sixteen hundred potentially folded structures were obtained, and were subjects of iterative calculations. The calculations were repeated broad-range search (5,000 K, 80 ps simulated annealing) and fine search (1,000 K, 50 ps simulated annealing) alternatively until the AE-ME ≈ 0 for the structure ensemble selected by target function energies (Fig. 4).

At the ending stage of the iteration, the pair-wise-averaged rmsd values for calculated structures (1,600) became $<2 \text{ \AA}$, meaning that the conformational exploration extent of the simulated annealing was extensive enough for the (sampled) calculated structures. Therefore, the problems of convergence and conformational sampling (Section 6.5) can be extensively solved by the comprehensive conformational space search implemented by high-performance computing. The remaining problem is the quality of the target function (Sections 8 and 9), i.e., empirical force field and NMR-derived information precision.

In general NMR studies, loop regions frequently show poor convergence, to be often assumed as high internal motion in solution. Some of them are correlated with dynamic structure and function, such as a hinge region, by NMR relaxation studies,⁶¹ but there are others waiting for structural clarification. Neocarzinostatin was a typical example. It has a seven-stranded anti-parallel β -barrel folding.^{62,63} The many loops of the protein had poor convergences in previously reported PDB coordinates (PDB ID: 1J5H, 1J5I).⁶⁴ The proposed procedure (Fig. 4) drastically improved the convergence (Fig. 5A), resulting in a pair-wise-averaged rmsd of backbone atoms = $0.32 \pm 0.07 \text{ \AA}$ for 60 ensemble (PDB ID: 1O5P)¹¹ and good agreement with X-ray structure (PDB ID: 1NCO).⁶² The good convergence was confirmed by order parameters (Section 10) determined by ^{13}C -NMR methine relaxation experiment.¹¹ The steric repulsion by the complicated β -sheet topology could be a reason for poor convergence in previously reported structures obtained with conventional conformational sampling.

Neocarzinostatin is a complex protein carrying the anti-tumor active enediyne ring chromophore. Because of the labile chromophore reflecting its

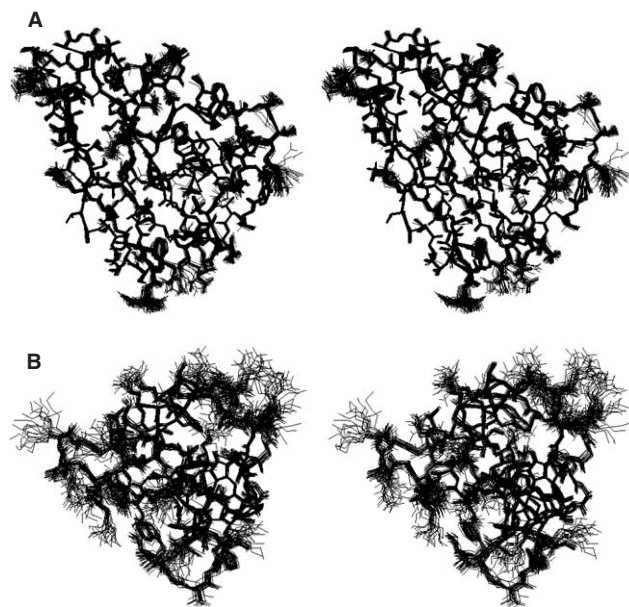


Fig. 5. NMR structure ensemble examples calculated by distributed computing with procedure described in Fig. 4. All heavy atoms are displayed. (A) Neocarzinostatin (PDB ID: 1O5P) 60 conformers, (B) cytochrome c552 (PDB ID: 2AI5) 20 conformers. Because cytochrome c552 contains many α -helices, the calculation completed very much faster (within a few days) than all β -protein neocarzinostatin (weeks) using the same calculation conditions (except for the number of final structures).

extremely strong DNA cleavage activity and complete stabilization in the complex, neocarzinostatin has attracted much attention in clinical use as well as for drug delivery systems.^{64,65} The order parameters also showed that the chromophore displayed an internal motion similar to that of the protein moiety. This agreed with the good convergence of the chromophore in the ensemble (rmsd for all heavy atoms = 0.26 Å). The atomic positions of the chromophore enediyne ring were typically in good agreement with that of the X-ray structure (an rmsd for all heavy atoms in the comparison = 0.15 Å). X-ray B-value of the chromophore atoms also had values similar to those of the protein moiety. It was therefore suggested that the NMR solution structure has atomic resolution comparable with the X-ray neocarzinostatin coordinates (1.8 Å).

The chromophore-stabilizing mechanism of neocarzinostatin had been discussed mainly based on a hydrophobic interaction of the highly hydrophobic chromophore molecule in its binding site.⁶² On the basis of the new findings of the solution structure, a new mechanism in addition to the hydrophobic

core was proposed. This is a freezing mechanism by the protein scaffold. The compound, like the chromophore (MW 657), has high mobility in aqueous solution. The mobility was strongly restricted by the protein scaffold as indicated by the solution structure ensemble and the order parameters that are comparable to those of the protein. The restriction corresponds to a freezing temperature for the chromophore. Because of the strong binding (the dissociation constant is about 10^{-10} M), the protein scaffold is considered to act as a molecular deep freezer in a cell to carry the highly reactive compound.

In contrast to the chromophore and the global protein structure, the loop region of neocarzinostatin has a characteristic topology difference between NMR and X-ray. On the basis of the three-dimensional structure, the chromophore-releasing mechanism by a three-state equilibrium was proposed. It consists of open, close, and free state of neocarzinostatin. These states sufficiently describe both the strong binding and the prompt releasing of the chromophore.¹¹ In this proposed mechanism, X-ray structure was considered to be an intermediate (open state) corresponding to the crystallization condition that was the chromophore dissociation condition.

The calculation for neocarzinostatin took about a month with 20 of 1.6 GHz Pentium 4 CPUs scheduled by SUN GRID engine. The computation time can be easily reduced by advanced CPUs and an increased number of GRID computing nodes. In the near future, the computation time for this size of calculations will be days or hours, and can become a routine process with full automation. If the calculation becomes a routine, there will be no need to care about differences in calculation qualities of the PDB coordinates (Section 2). By distance constraint files, the structures can be easily reproduced with equal calculation qualities. For this purpose, the deposition of the constraints file in the PDB is very important. The constraints file and order parameters (if available in the Biological Magnetic Resonance Data Bank) will be able to describe a unique NMR structural potentiality with dynamics as discussed in Section 10.

It is noteworthy that the comprehensive conformational search depends on the structural distribution in the space and does not depend on individual calculated conformers. The possible drop out of structures in the calculation does not have an impact on the result ensemble, as far as the drop out occurs randomly and the number of drop outs is ignorable compared to the total number of random structures. This means very small systematic bias compared to the effect of the conventional number of initial structures (typically about 100, see Section 6.3). This approach thus requires a great number of independent calculations that are easily performed by the GRID computing.

7.3. Distribution of local minima: ensemble size and its significance

Using a huge number of initial structures leaves one question. How many conformers should be selected to compose the ensemble? The answer has been simple: any feasible number to utilize the ensemble.³⁵ Normally, the ensemble contained tens of conformers deposited in the PDB. In the case of neocarzinostatin, 60 conformers were deposited. The number just depends on handling of the coordinate file to deposit or superimposing of structures displayed in graphic programs. When 600 conformers out of 1,600 calculated structures were used, any graphic programs could no longer display the superimposed structures, and the rmsd calculation would last 1 day by a single CPU (for 1,600 conformers it took a week). However, one criticism could arise, whether tens of conformers out of 1,600 (or 16,000) can reliably sample the calculation result. To revisit the question, and to discuss the size of the ensemble, a verification calculation was achieved for neocarzinostatin as shown in Fig. 6. Four thousand random initial structures were subjected to the simulated annealing (5,000 K, 80 ps) twice under the same condition with the procedure in Fig. 4. The results were plotted by histograms between target function energy and number of structures. It is clearly shown that there are distributed peaks in the histogram apparently caused by inappropriately folded conformers. A similar result was reported by Güntert³⁵ using 2,000 conformers of cyclophilin A. Because of a hit rate of the folding, it is obvious that some of the conformers should be selected for the ensemble. The question here is a criterion of the selection.

The distributions are schematically represented in Fig. 6. With the iteration of the simulated annealing as described in Fig. 4, the distributions shifted toward the lower target function energy. This is a result of the conformational space search. The lowest energy peak moved faster, because of the nearly appropriate folding and likely smoother potential energy landscape. Therefore, the cut-off at the first simulated annealing in Fig. 4 is a reasonable solution for the hit-rate problem. There is no need to increase the hit rate by algorithms. As long as completely random initial structures are used, we can cut-off at any target function value. The distributions are shifted by the optimization because they consist of many local minima. Thus, peaks of apparently misfolded conformers (Fig. 6A, right side) are not shifted but just decreased by the iterations (jump up to more appropriate folding). The final structures of Fig. 4 show Gaussian-like distribution as schematically represented in Fig. 6C. This likely means separation of local minima peaks by differences of shifting speeds (on the potential energy landscape), and is a result of the comprehensive conformational space search. Therefore, the stop motion of the peaks can be a new criterion of the structural calculation to assess its completeness, and the lowest energy

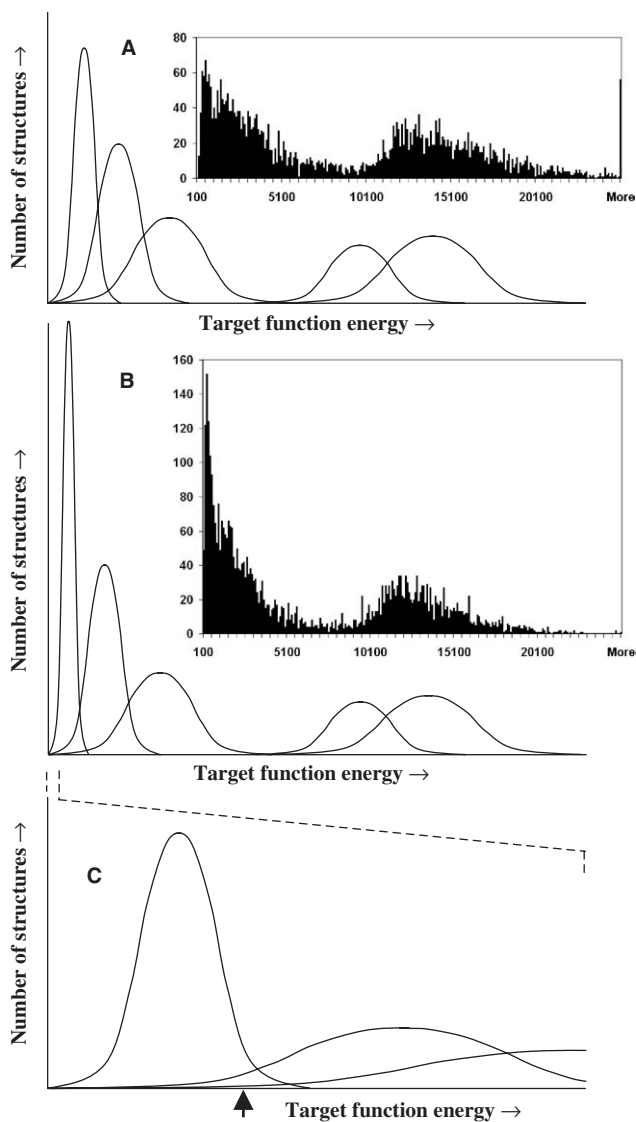


Fig. 6. Histogram of number of structures vs. target function energy calculated for neocarzinostatin using 4,000 initial structures, and schematic representation of probable distribution of local minima. (A) Result of first round of SA (see Fig. 4), (B) result of second round of SA, (C) schematic representation of structure distribution of final result with expanded horizontal scale. Arrow indicates a probable cut-off target function value for final structure ensemble.

distribution indicates the global minimum structure *determined by the target function*. The distribution can be derived from the intrinsic dynamics (Section 10) as long as the target function is validated (see Sections 8 and 9). In this regard, the members of ensemble are statistically equivalent conformers. Thus, any randomly selected structures in the distribution (defined by 90% confident upper limit, see arrow in Fig. 6C) or any statistically sufficient number of structures sorted out from the distribution can be used as NMR structure ensemble. The ensemble size is independent of the number of random initial structures or the folding hit rate. Because of the Gaussian-like distributions of local minima (see Fig. 6C, right side), any structures in the NMR ensemble have a probability of being a local minimum. Therefore, a large number of calculated structures are necessary to compose the ensemble and to assess the structural quality. The lowest energy structure has a meaning of the lowest probability of being the local minimum, but not a single representative of the global minimum.

The distribution properties shown in Fig. 6 strongly depend on protein folding (dependence of hit rates). In practice, α -helix-rich protein has a smoother distribution. This is because of the smaller potential energy barrier of steric repulsion, which results in faster conformational space search (Fig. 5B). The procedure of Fig. 4 can be applied to the proteins with relatively few iterations and short calculation time.^{66,67}

8. BASIC NMR-DERIVED CONSTRAINTS FOR STRUCTURE CALCULATIONS

Once the conformational sampling problem is solved (Section 7), the controllable factors of high-resolution NMR structure (Section 3) are dominated by a quality of target function, which consists of NMR-derived information and empirical force field (Section 9.7). NOE, scalar coupling, and hydrogen bond are widely used as sources of structural constraints. In this section, problems of the constraints are revisited with brief reviews.

8.1. NOE intensities

The solution NMR structure determination strongly relies on NOE, because inter-atomic distances can be predicted by it. Spatially adjacent hydrogen atoms are coupled by dipole–dipole through space magnetization transfers, and cause the distance-dependent NOE. The dependency is approximated by a rigid two-spin system hypothesis stating that the intensity of the NOE is correlated with r^{-6} (crude first-order approximation), where r is the distance

between the two spins. Because of the relation, direct magnetization transfers among a pair of atoms occur by a short-range interaction (less than ~ 5 Å). This can define specific inter-atomic distances in the secondary and tertiary structure of the protein. However, protein is not a simple two-spin system, and it is not rigid in solution. This causes systematic errors in the NOE-derived distance prediction derived from spin diffusion and internal motion.^{4,13}

The transfer is caused not only directly but also by spin diffusion, i.e., indirectly via other spins in the environment.^{68,69} Spin diffusion depends on the duration of the magnetization transfer, so-called 'mixing time' in the NOESY experiment. Shorter mixing time gives a better prediction of the distance,. However the mixing time cannot be made arbitrarily short, because the intensity of NOE is, also, strongly dependent on the mixing time.⁷⁰ The shorter mixing time results in a poorer S/N ratio of the spectra. A compromise has to be made between the suppression of spin diffusion and the S/N ratio. In some cases, NOE build-up rate analysis is effective to determine an optimal mixing time. The sensitivity enhancement of NMR equipment (Section 13.1) can shorten the mixing time, resulting in better distance prediction qualities.

The established procedure to tolerate the effects of spin diffusion and protein motion is a crude classification of NOE intensities into strong, medium, and weak.¹³ A strong NOE is typically assigned to an inter-proton distance below 2.7 Å, a medium NOE to a distance below 3.3 Å, and weak NOE to a distance below 5.0 Å. The NOE-derived distances can also be calibrated by the approximation of the r^{-6} with a known r , such as average distance for sequential NOEs, e.g., distance between H^α and next-neighbor H^N , for regular secondary structures, i.e., α -helix and β -sheet. For this purpose, the secondary structures have to be preliminarily identified by using the sequential NOE patterns,¹³ scalar couplings (Section 8.2), and hydrogen exchange measurements (Section 8.3). The calibrated distances with a *proper* error margin will result in a quality of three-dimensional structures similar to the crude classification. The advantage of this procedure is easy automation of peak picking and intensity integrations with less handling, while the disadvantage is the difficulty to validate the margins. The different processes and the margins of the NOE conversion will result in a different structural convergence (Section 6.5) for the final three-dimensional structure, and will often make it difficult to assess the structural qualities.

In many laboratories, the NOE cross peaks are automatically integrated into the volume by using programs such as NMRPipe and Pipp.⁷¹ The programs are extensively reviewed by Baran *et al.*²³ Since the line-widths can vary remarkably for different resonances, the integration is mandatory. The programs are also effective for the deconvolution of overlapping peaks, and

for the identification of possibly hidden overlapping peaks with a complete resonance assignment table. In this regard, the complete assignment is also mandatory for high-quality distance predictions. In case of a partial assignment, which is often caused by resonance complexity especially for larger proteins, the peaks from non-assigned resonance regions should be eliminated from the structure calculations or analyzed very carefully to eliminate the cross peak assignment ambiguity using a preliminary calculated structure model.³⁵ The resonance complexity often makes NOE-derived constraints poorly comprehensive.

8.2. Scalar coupling constants

Torsion angles are related to vicinal coupling constants through the Karplus equation. Since the equation allows several torsion angles for a given coupling constant, it is difficult to define specific conformational constraints. The coupling constants are usually converted into allowed torsion angle ranges. The scalar coupling constants are typically important to define the regular secondary structures together with the sequential and medium range NOEs as well as hydrogen bonds.¹³ For instance, typical $^3J_{\text{HN}^{\alpha}\text{H}}$ values for a regular α -helix and a β -sheet are 4 and 9 Hz, respectively. The differences cause characteristic cross peaks in the amide proton region that is easily identified. If the secondary structures are defined, the regular torsion angle constrains (that are consistent with the Ramachandran plot) can be used for the backbone φ and ψ angles.

In contrast to NOEs, scalar coupling relies on localized direct interaction. They have therefore potentiality to define precise local structure information. They can also be used to obtain stereospecific assignments (e.g., for C^{β} methylene protons) in combination with intra-residual and sequential NOEs.⁷²

8.3. Hydrogen bonds

Measurement of the exchange rate of amide hydrogens in D_2O plays an important role in the assignment of hydrogen bonds. Slowly exchanging hydrogens are more likely to be involved in a hydrogen bond than faster exchanging hydrogens. These can be measured by simple two- or three-dimensional spectra recorded immediately after solvating in D_2O . Because of the resonance simplification in the amide proton region, the spectra are also useful to isolate the overlapping resonances. Therefore, full sets of NMR experiments are often performed in D_2O solution as well. Usually the

lifetime of slowly exchanging proton in the regular secondary structures is days or months for medium size globular proteins, and there is enough time for the measurements. Because the acceptor oxygen or nitrogen atom cannot be identified directly by normal NMR experiments, the assignment of the corresponding backbone hydrogen bond is made on the basis of assumptions about the regular secondary structure. This should be verified by the typical sequential NOE pattern and the scalar coupling. A through-hydrogen bond scalar coupling^{73,74} can directly assign them, but it is normally difficult to detect in protein.

Hydrogen bond constraints are introduced into the structure calculation as distance constraints, typically by confining the acceptor hydrogen distance to the range 1.8–2.0 Å and the distance between the acceptor and the atom to which the hydrogen atom is covalently bound to 2.7–3.0 Å. Because these are based on empirical values, the distance constraints have a much smaller error margin (usually, ± 0.1 Å) compared to NOEs. Therefore, it has to be noticed that the hydrogen bond constraints have a strong impact for the structure determination.

9. IMPROVE TARGET FUNCTION QUALITY

The quality of NMR-derived information has been exclusively dependent on NOE. To compensate the prediction ambiguity of NOE (Section 8.1), many experimental methods have been studied as introduced below. Furthermore, to be applicable for large protein systems with a specific isotope label or a selective deuteration (see Section 12) that results in a remarkable loss of NOE quantities, minimal NOE-based methods are also required.^{75,76}

9.1. Residual dipolar couplings

Residual dipolar couplings (RDCs) are the most widely used method to refine (if possible) the NOE-based structure calculations.^{77–80} RDCs are physical values originating from a through-space dipole–dipole coupling mainly studied by solid-state NMR. RDCs were first introduced for protein structure investigation in liquid crystals, and are applied for aqueous solution by addition of alignment media that causes partial order in magnetic fields. RDCs were developed in line with the dissemination of multinuclear NMR techniques in the late 1990s. The dipolar coupling among spins (e.g., ^{15}N – $^{13}\text{C}^\alpha$) is usually averaged out by Brownian motion in solution. If there is an anisotropy of the local magnetization induced by a small degree of molecular alignment (partial restriction for Brownian motion), RDC is

observed.^{78–80} RDCs provide information useful for structure determination on angles between covalent bonds and global axes in a protein. Bicelles that have a diameter comparable with a protein and rod-shaped virus are widely used as the alignment media. The conventional ^1H scalar coupling (Section 8.2) is strong and many spins involved result in spectral complexity and subsequent low S/N ratios. In contrast, the coupling of RDCs is much weaker and involved spins are fewer than the scalar coupling and can consequently provide precise structural information.

Clare *et al.*⁸¹ calculated a structure of the B1 domain of the streptococcal protein G (56 residues) by RDCs (for $^{15}\text{N}\text{--}\text{H}^{\text{N}}$, $^{15}\text{N}\text{--}^{13}\text{C}'$, and $\text{H}_\text{N}\text{--}^{13}\text{C}'$) and 32 backbone hydrogen bond constraints (Section 8.3) without NOE-derived distances. They compared structural convergences for their calculations using 152 RDCs measured in tobacco mosaic virus, 150 RDCs measured in DMPC/DHPC (3:1) bicelles, and without RDCs. The rmsd values with RDCs were both improved significantly (four-fold). A further improvement was observed for calculations using the two sets of the constraints simultaneously by 20–30%. This indicated that the alignment mechanisms are different and complementary to the two medias.

Ding and Gronenborn⁸² measured RDCs for $^{15}\text{N}\text{--}^{13}\text{C}^\alpha$ and $^1\text{H}\text{--}^{13}\text{C}^\alpha$ for the same B1 domain, and indicated that backbone ϕ torsion angles can be predicted with Karplus equation. The predicted values were in good agreement with the PDB coordinates, demonstrating the precision of RDCs as of the structural constraints in target function.

The RDCs are useful for large proteins that have poorly comprehensive NOEs.⁸³ The NOE free structure determination by RDCs in combination with other NMR-derived information, such as chemical shift perturbations⁸⁴ and side chain rotamer prediction⁸⁵ also demonstrated the usefulness of the methods.

9.2. Database potentials

Chemical shifts have been recognized as a potential source for target function. In particular, $^{13}\text{C}^\alpha$ and $^{13}\text{C}^\beta$ shifts have been used for the secondary structure prediction and to elucidate the backbone torsion angles.^{86–88}

An approach to elucidate new empirical restraints from PDB coordinates and chemical shift in the Biological Magnetic Resonance Data Bank was applied by Kuszewski *et al.*^{89,90} for a structure determination automation program. The relation between the chemical shift and coordinates can be used for an NMR assignment validation.⁹¹ The torsion angle ranges of ϕ and ψ that are favorable in Ramachandran plot and their mean values in PDB are also useful as pseudo-potentials.^{92,93}

9.3. Backbone hydrogen bond topology

A method using empirical hydrogen bond topology has been presented by Grishaev and Bax.⁹⁴ Usually, the hydrogen bonds are used just as distance constraints (Section 8.3). Grishaev and Bax⁹⁴ extracted the topologies of backbone hydrogen bonds and statistically analyzed them. They found that the angle between donor group (NH) and acceptor group (carbonyl) has Gaussian distribution. They thereby assumed that the angle has harmonic potential, and included the new empirical structural restraint in their protein structure determination. Ten proteins that were already determined by X-ray and NMR, e.g., BPTI, were subjected to the new structure determination. The results were statistically analyzed, and the assumption of the harmonic potential was verified. Empirical topologies like this can be useful for general structure determination.

9.4. Other sources of conformational constraints

Unlike the NOE and coupling that are localized information, some physical values obtained by NMR provide global structural information of a protein. The radius of gyration (R_{gyr}) is one of these values and can be used as a pseudo-potential of target function restricting the crude shape of the protein.⁹⁵ R_{gyr} is particularly profitable for proteins consisting of domains connected by a flexible hinge, or proteins having subunit–subunit interactions. Similar to RDCs there are some other useful physical values introduced from solid-state NMR, such as a chemical shift anisotropy.⁷⁹

There are many other methods to provide the conformational constraints, such as paramagnetic relaxation enhancement,⁹⁶ disulfide bridge topology using ambiguous inter-sulfur restraints,⁹⁷ and time-averaged J -coupling.⁹⁸ Additional structure information can increase the structure quality with fewer amounts of NOEs.

9.5. Resonance assignment precision: automated approaches

With the dissemination of multinuclear multidimensional NMR experiments, the automated NMR resonance assignment became feasible and indispensable, simultaneously.^{23,35,41,99} Typically, 10–20 individual multidimensional NMR spectra are measured for a large protein. The NMR-derived information quality definitely relies on the resonance assignment. The precious assignment has been based on and assessed by the sequential NOE continuity on the peptide sequence and consistency with the amino acid spin

systems.¹³ For three- or four-dimensional spectra of large protein, the continuities and the consistencies extended across tens of spectra cannot be traced without the aids of the computer programs. The resonance assignments followed by (or simultaneously in case) NOE peak picking and the volume integrations (Section 8.1) are automated by some programs.^{35,41,71} If the assignment result can be validated, then the structure calculation can also be automated (Section 7). The automations can decrease a probability of human error, and can result in high-quality protein structures. Currently, the assignment validation is a milestone for the automation.

Recently, relational databases are used to manage the vast amount of data set in some laboratories.^{100–102} The multidimensional NMR spectra files are huge, and their administration and backup are also resource-consuming tasks. If there are storage servers for the NMR spectra files connected by metropolitan networks in regions or countries (just like mirror servers of PDB), NMR laboratories can easily secure their files. The access privilege of the files can be confident until when they are released by the owners. Using GRID storage servers, hundreds of terabytes of storage is practically available, and is already utilized for MRI images. With the open replicated storage server and released spectra (after publications or grant requirements), the data processing precision and structure calculation quality can be assessed by many other laboratories in the future.

9.6. NOE validation

Challenges for NOE-derived data precision have been studied as well. NOE intensities and a complete relaxation matrix-based¹⁰³ structure calculation can eliminate the unexpected effect of spin diffusion by simulating the complete direct and indirect relaxation (see Section 8.1). The method, however, has not been applied to general protein NMR because of the difficulty to predict the complete relaxation with molecular motion. The NOE intensity-based refinement was extensively reviewed by Brünger and Nilges.²⁴ Recently, Linge *et al.*¹⁰⁴ included the relaxation matrix into their automated assignment program. This approach will reduce the ambiguities of NOE volume integrations.

Another historical method is the NOE cross-validation.⁴⁷ This is performed by a partial elimination of NOEs from a full set of NOEs. The elimination is random. Calculated structures from the different sets of partially eliminated NOEs are statistically analyzed in comparison with the structure calculated from the full set of NOEs. The predictability of the eliminated NOEs from remaining NOEs is assessed as structural consistency (and therefore high quality) of the eliminated NOEs. With increased computing power, the statistical analysis will be feasible to determine high-resolution protein structure.

Two randomly separated sets of NOEs (that is half the number of NOEs) were used for structure calculations of neocarzinostatin (see Section 7.2, verified calculation of ref. 11, unpublished data) to compare the subset of structures and confirmed that there was no structural bias detected by the randomly selected NOEs. With more advanced computing power, the systematic statistical analysis may become a standard procedure in the future.

On the other hand, the approach to increase the error tolerance (instead of increase the NOE precision) by a calculation algorithm was studied by Kuszewski *et al.*⁹⁰ Usually, the experimental error and peak detection error (due to resonance overlap) are uniformly treated by the margin of error (Section 8.1). The method to separate the two types of errors by statistical analysis may become mandatory in the future.

A relative ratio of intra-residual NOE intensities strongly depends on side chain conformations and global folding by the spin diffusion. The dependency makes the intra-residual NOE difficult to use for structure calculations. Changing the disadvantage into an advantage, the dependency can also be utilized for a new pseudo-potential of the side chain conformation. This will create a database of mixing time build-up curves for structure-resolved proteins in the future.

9.7. Improve force field

The empirical force field of molecular dynamics is also a key player of high-quality structure determination by NMR. The use of generalized Born (GB) solvent (implicit solvent) or explicit solvent can greatly improve the calculated structure quality of molecular dynamics.^{53,55,105,106} The calculation time of GB model is about 10 times longer than conventional simulated annealing of simplified force field (Section 6.4), and that of explicit solvent is longer than the GB model. In the near future, however, the advanced computing power can cover the calculation time, and the solvent models will be standard for NMR protein structure calculations. In program AMBER,⁴³ the explicit solvent model can be calculated with parallel computing module (e.g., LAM-MPI, see Section 4), but the GB model cannot. It means that the explicit solvent model calculation can be further sped up by PC cluster (Section 4). By the calculation overhead, however, the speed up ratio of molecular modeling of protein by PC cluster is not linearly increased with the number of CPUs. Therefore, currently, the GB solvent model with GRID computing is more feasible for the NMR structure calculations than the explicit solvent model. It was reported that the GB solvent model improves the structural quality with less information on NMR-derived structure.^{53,55} Because of the computational resource limitation, currently, the solvent models are usually used just

for the structure refinement for a few conformers that likely cause the conformational sampling problem (see Section 6.6).

10. DYNAMICS

NMR structure calculation alone cannot describe the dynamic structure of protein. If structure calculations (Section 6) and NMR-derived information (Sections 8 and 9) are reliable enough, a poor convergence (if it remains in the NMR ensemble) likely arises from the internal mobility of atoms. The molecular motion is usually confirmed by order parameters of spins derived from relaxation time experiments.^{107–109}

Recently, Lindorff-Larsen *et al.*¹¹⁰ included the order parameter (S^2) in the target function, and refined an ubiquitin X-ray structure by restrained molecular dynamics (Section 6.4) to obtain an NMR structure ensemble (Section 6.5) from the trajectories. They simulated the values of RDCs (Section 9.1) and side chain scalar coupling from the calculated ensemble to confirm that the method can determine the protein three-dimensional structure and dynamic structure simultaneously. The simulated values were in good agreement with the corresponding measurement data. The simulation accuracy was improved from the preliminary calculated structure without the order parameters. The approach is typically important, because they tried to link the ensemble with a dynamic structure directly.

On the other hand, the extraction of the structural ensemble from the molecular dynamics trajectories likely generates a fluctuation along the starting structure unless the conformational sampling is assessed correctly. In the case of ubiquitin, the X-ray structure could be a good approximation of a global minimum of the solution structure.

Lindorff-Larsen *et al.*¹¹⁰ analyzed the NMR structure ensemble by a generalized Lindemann criterion¹¹¹ to define the mobility of side chain atoms. The result suggested that the side chain atoms have liquid-like mobility even in the core of protein, whereas the backbone atoms uniformly have a solid-like rigidity. As they proposed, the addition of thermodynamic properties for target function of structure calculation can increase the quality and usefulness of NMR structures.

11. QUALITY CHECK OF THE NMR ENSEMBLE

The physical meaning of the NMR structure ensemble normally has not been discussed, and often has been ignored. The rmsd elucidated from

the ensemble has been used as structure precision criteria (Section 6.5). However, there is no consensus whether it can represent the structural quality. This is partially due to the NOE prediction ambiguity (Section 8.1) and the convergence problem of structure calculation algorithms as discussed in Section 6. Recently, the development of much useful NMR-derived structural information other than NOE (as discussed in Section 9) is likely awakening the discussion of structural precision and convergences.

Side chain atom packing of amino acid residues has been an important structural quality measure in X-ray.^{112,113} The structural quality criteria are also introduced for NMR structure quality checks.^{50,114} However, almost all NMR structures deposited in PDB uniformly have poor scores for the side chain packing. There is no consensus whether X-ray packing-derived structural criteria can be used for NMR quality check. Some checking programs are available in PDB, e.g., PROCHECK,¹¹⁵ PROCHECK-NMR,¹¹⁶ and WHAT-CHECK.¹¹⁷

As discussed in Section 10, the side chain atoms presumably have high mobility even in protein core.¹¹⁰ In the near future, the quality check criteria for NMR structures will be developed including the dynamic properties.

An NMR *R*-value (analogous to the X-ray *R*-value) was proposed by Brünger and Nilges²⁴ using back-calculated NOE intensities by complete relaxation matrix (Section 9.6). The improved approaches were proposed¹¹⁸ to eliminate unnecessary simulations. Statistical quality scores, *F*-measure scores, are also used to assess the NMR structure quality.¹¹⁹ The approaches are used for the structure quality assessment by some automation programs.

12. PROTEIN SAMPLE PREPARATIONS

Sometimes it is said that ‘sample preparation is everything.’ Recently, the importance is increasing because of the extended difficulty to handle a protein solution in high concentration (typically about 0.5–1 mM). Because of the intrinsic insensitivity of NMR experiments, this high concentration is required. Many of the biologically significant proteins, e.g., membrane proteins, cannot easily be solved in this high concentration. If a protein can be solved and has a folding structure, dispersed cross peaks can be observed in ¹⁵N- or ¹³C-edited HSQC spectra. This dispersion can be used as a sensitive indicator of protein foldedness. The solubility is a prerequisite of a high-quality protein structure determination.^{21,120} If specific protein has poor solubility, there are some approaches to resolve the problem, as briefly summarized below.

1. Peptide chain truncation to a soluble domain. If the domain still has poor solubility, further truncation, e.g., flexible region cut-off, can be performed.
2. Peptide sequence modification or addition of a tag region, e.g., a His tag, to reduce the flexibility and/or to increase stability.
3. Screening of solvent conditions, e.g., pH or salt. This is a historical method and is still important.

Protein NMR has advanced with the help of stable isotope labeling techniques, which allowed to obtain multinuclear multidimensional spectra. To apply the NMR for large proteins, the control of relaxation time is also important.^{21,120} For instance, a deuteration for non-exchangeable protons significantly attenuates the relaxation rates. In this case, the amount of NOEs also reduced depending on the deuteration. Therefore, other complementary NMR-derived information will be required (Section 9).

Kainosho *et al.*¹²¹ proposed a method termed ‘Stereo-Array Isotope Labeling (SAIL).’ They used stereochemically and/or optimally enriched amino acids^{23,120} to label the protein. The method can decrease the resonance complexity and relaxation rate, and can increase the stereospecific assignment quality significantly.

13. NMR EXPERIMENTS

13.1. Recent technological advances in equipment

The NMR data acquisition sensitivity depends on the NMR probe performance. Recently, a remarkable sensitivity enhancement was achieved by a cryogenic probe.¹²² This technology reduces the thermal noise of the NMR signal by cooling the device by liquid helium. In practice, the enhancement strongly depends on the sample condition. Usually, the S/N ratio increases by factors from two to four for protein solution.

13.2. Pulse sequence techniques and data acquisitions

The advance of multidimensional NMR started from a product operator established by Ernst *et al.*⁴ and Kessler *et al.*¹²³ The product operator is composed of matrices (operators of spin rotation correspond to the NMR pulse), which are combined by a ‘product of matrix’ based on quantum mechanics with just a simple ‘high-temperature approximation.’ The approximation quality is excellent. This is a great advantage of the NMR method compared to other spectroscopic methods, such as the Raman spectrum.

The product operator can clearly describe the spin behavior, and is the base of many multinuclear multidimensional NMR pulse sequences.^{14,16,20} The pulse sequence is a technique to visualize the invisible phenomena by rotation in complex space. This technique has much potential.

The most important recent advance of the solution NMR pulse sequence methodology is transverse relaxation optimized spectroscopy (TROSY) due to its significant sensitivity enhancement for large proteins by increasing the lifetimes of NMR signals.^{17,120,124–126}

Data acquisition of free induction decay (FID) also has room for sensitivity improvement. Recently, there are many approaches for speeding up of FID acquisition aiming at high-throughput data capturing.^{127–132} They are mainly utilized to shorten the acquisition time, but can also improve the S/N ratio with increasing the data scan time. A typical example is a randomized non-linear sampling with maximum entropy method. This shortens the FID acquisition time by non-uniformly incremented evolution period (for F_2 , F_3 , or F_4 FID axis), complementing the decreased frequency resolution by maximum entropy method. Because this causes loss of peak volume precision, the availability and compensation with the S/N ratio should be considered.

13.3. Solid-state NMR

Another recent advance for biomacromolecular NMR was achieved by solid-state magic-angle-spinning NMR (MAS-NMR).^{133–136} The biggest advantage of the MAS-NMR compared to solution NMR is a high-quality distance prediction, e.g., by REDOR. The confidence of the prediction can be increased up to 0.05–0.1 Å, whereas that of solution NMR NOEs is about 1 Å (Section 8.1). This can be a dramatic increase of the quality of target function. On the other hand, a disadvantage is intrinsically small numbers of information.

As discussed in Section 9, there are approaches to use fewer NOEs for large protein complemented by other more reliable information. The solid-state NMR and solution NMR can be complementary.^{137,138} A large number of poorly precious information can be a trade off with a small number of highly precious information in the high-performance conformational space search (Section 7).

14. CONCLUDING REMARKS

The high-resolution protein structure determination by NMR is possible and becomes more and more feasible. There are many obstacles, but there

are many approaches to overcome them. The target function quality is key; it contains NMR-derived structural information precision and empirical force field quality. The information precision relies on experiments and data processing. The processing quality can be improved by the relational database of spectra and notations, such as resonance assignment table. The force field quality can be improved by useful knowledge extractions from many structural databases, such as the PDB. The structure calculations should only depend on the validated target function. The calculation algorithm dependency can be eliminated by the high-performance computing. In this regards, the structure calculation should be independent from the preliminary structure calculations, which are performed to assess the data-processing quality. The quality of the NMR-derived structural information includes dynamic properties and can be a main output from NMR laboratories, instead of the rmsd for calculated ensemble. The advanced computing power in the future will focus on more precious modeling of protein, such as solvated models with validated conformational sampling and conformational space exploration extent. As a result, there can be animated protein structures utilized for biochemical and biophysical studies globally.

ACKNOWLEDGMENTS

I thank Prof. Yuji Kobayashi, Prof. Robert Hof, Prof. Manuel Peitsch, Dr. Norio Mimura, Dr. Takanori Kanazawa, Dr. Takuya Yoshida, Prof. Tadayasu Ohkubo, and Prof. Yoshimasa Kyogoku for their generous support and discussions.

REFERENCES

1. C. M. Dobson, *Nature*, 2004, **432**, 824–828.
2. S. Yokoyama, H. Hirota, T. Kigawa, T. Yabuki, M. Shirouzu, T. Terada, Y. Ito, Y. Matsuo, Y. Kuroda, Y. Nishimura, Y. Kyogoku, K. Miki, R. Masui and S. Kuramitsu, *Nat. Struct. Biol.*, 2000, **7(Suppl)**, 943–945.
3. M. Billeter, *Quart. Rev. Biophys.*, 1992, **25**, 325–377.
4. R. R. Ernst, G. Bodenhausen and A. Wokaun, *The Principles of Nuclear Magnetic Resonance in One and Two Dimensions*, Clarendon Press, Oxford, 1987.
5. C. D. Snow, H. Nguyen, V. S. Pande and M. Gruebele, *Nature*, 2002, **420**, 102–106.
6. A. Fersht, *Proc. Natl. Acad. Sci. USA.*, 2002, **99**, 14122–14125.
7. H. Takashima, N. Mimura, T. Ohkubo, T. Yoshida, H. Tamaoki and Y. Kobayashi, *J. Am. Chem. Soc.*, 2004, **126**, 4504–4505.

8. M. Ota, M. Ikeguchi and A. Kidera, *Proc. Natl. Acad. Sci. USA.*, 2004, **101**, 17658–17663.
9. P. Bradley, K. M. Misura and D. Baker, *Science*, 2005, 1868–1871.
10. O. Schueler-Furman, C. Wang, P. Bradley, K. Misura and D. Baker, *Science*, 2005, **310**, 638–642.
11. H. Takashima, T. Yoshida, T. Ishino, K. Hasuda, T. Ohkubo and Y. Kobayashi, *J. Biol. Chem.*, 2005, **280**, 11340–11346.
12. C. D. Schwieters, J. J. Kuszewski, N. Tjandra and G. M. Clore, *J. Magn. Res.*, 2003, **160**, 65–73.
13. K. Wüthrich, *NMR of Proteins and Nucleic Acids*, Wiley, New York, 1986.
14. G. M. Clore and A. M. Gronenborn, *Science*, 1991, **252**, 1390–1399.
15. K. H. Gardner and L. E. Kay, *Annu. Rev. Biophys. Biomol. Struct.*, 1998, **27**, 357–406.
16. G. M. Clore and A. M. Gronenborn, *Curr. Opin. Chem. Biol.*, 1998, **2**, 564–570.
17. G. Wider and K. Wüthrich, *Curr. Opin. Struct. Biol.*, 1999, **9**, 594–601.
18. G. T. Montelione, D. Zheng, Y. J. Huang, K. C. Gunsalus and T. Szyperski, *Nat. Struct. Biol.*, 2000, **7(Suppl)**, 982–985.
19. V. Kanelis, J. D. Forman-Kay and L. E. Kay, *IUBMB Life*, 2001, **52**, 291–302.
20. G. M. Clore and C. D. Schwieters, *Curr. Opin. Struct. Biol.*, 2002, **12**, 146–153.
21. J. L. Markley, E. L. Ulrich, W. M. Westler and B. F. Volkman, *Meth. Biochem. Anal.*, 2003, **44**, 89–113.
22. S. W. Homans, *Angew. Chem. Int. Ed. Engl.*, 2004, **43**, 290–300.
23. M. C. Baran, Y. J. Huang, H. N. B. Moseley and G. T. Montelione, *Chem. Rev.*, 2004, **104**, 3555.
24. A. T. Brünger and M. Nilges, *Quart. Rev. Biophys.*, 1993, **26**, 49–125.
25. W. Braun, C. Boesch, L. R. Brown, N. Go and K. Wüthrich, *Biochim. Biophys. Acta.*, 1981, **667**, 377–396.
26. T. F. Havel and K. Wüthrich, *J. Mol. Biol.*, 1985, **182**, 281–294.
27. T. F. Havel, *Magn. Reson. Chem.*, 2003, **41**, S37–S50.
28. T. F. Havel and K. Wüthrich, *Bull. Math. Biol.*, 1984, **46**, 673–698.
29. T. F. Havel, *Prog. Biophys. Mol. Biol.*, 1991, **56**, 43–78.
30. T. Nakai, A. Kidera and H. Nakamura, *J. Biomol. NMR.*, 1993, **10**, 351–362.
31. M. E. Hodsdon, J. W. Ponder and D. P. Cistola, *J. Mol. Biol.*, 1996, **264**, 585–602.
32. W. Braun and N. Go, *J. Mol. Biol.*, 1985, **186**, 611–626.
33. Y. Kobayashi, H. Takashima, H. Tamaoki, Y. Kyogoku, P. Lambert, H. Kuroda, N. Chino, T. X. Watanabe, T. Kimura, S. Sakakibara and L. Moroder, *Biopolymers*, 31, 1991, 1213–1220.
34. P. Güntert and K. Wüthrich, *J. Biomol. NMR.*, 1991, **1**, 447–456.
35. P. Güntert, *Quart. Rev. Biophys.*, 1998, **31**, 145–237.
36. T. Ohkubo, Y. Kobayashi, Y. Shimonishi, Y. Kyogoku, W. Braun and N. Go, *Biopolymers*, 1986, **25**, 123–134.
37. A. T. Brünger, P. D. Adams and L. M. Rice, *Structure*, 1997, **5**, 325–336.
38. A. T. Brünger, *X-PLOR, Version 3.1. A System for X-ray Crystallography and NMR*, Yale University Press, New Haven, 1992.

39. M. Nilges, G. M. Clore and A. M. Gronenborn, *FEBS Lett*, 1988, **239**, 129–136.
40. P. Güntert, C. Mumenthaler and K. Wüthrich, *J. Mol. Biol.*, 1997, **273**, 283–298.
41. P. Güntert, *Meth. Mol. Biol.*, 2004, **278**, 353–378.
42. B. R. Brooks, R. E. Brucoleri, B. D. Olafson, D. J. States, S. Swaminathan and M. Karplus, *J. Comput. Chem.*, 1983, **4**, 187–217.
43. D. A. Case, T. E. I. Cheatham, T. Darden, H. Gohlke, R. Luo, K. M. Merz Jr, A. Onufriev, C. Simmerling, B. Wang and R. Woods, *J. Comput. Chem.*, 2005, **26**, 1668–1688.
44. E. Lindahl, B. Hess and D. van der Spoel, *J. Mol. Mod.*, 2001, **7**, 306–317.
45. A. T. Brünger, P. D. Adams, G. M. Clore, W. L. DeLano, P. Gros, R. W. Grosse-Kunstleve, J. -S. Jiang, J. Kuszewski, M. Nilges, N. S. Pannu, R. J. Read, L. M. Rice, T. Simonson and G. L. Warren, *Acta Cryst. D*, 1998, **54**, 905–921.
46. G. M. Clore, M. A. Robien and A. M. Gronenborn, *J. Mol. Biol.*, 1993, **231**, 82–102.
47. A. T. Brünger, G. M. Clore, A. M. Gronenborn, R. Saffrich and M. Nilges, *Science*, 1993, **261**, 328–331.
48. D. Zhao and O. Jardetzky, *J. Mol. Biol.*, 1994, **239**, 601–607.
49. F. R. Chalaoux, S. I. O'Donoghue and M. Nilges, *Proteins*, 1999, **34**, 453–463.
50. C. A. E. M. Spronk, S. B. Nabuurs, A. M. J. J. Bonvin, E. Krieger, G. W. Vuister and G. Vriend, *J. Biomol. NMR*, 2003, **25**, 225–234.
51. G. M. Clore and A. M. Gronenborn, *Proc. Natl. Acad. Sci. USA.*, 1998, **95**, 5891–5898.
52. C. A. Spronk, J. P. Linge, C. W. Hilbers and G. W. Vuister, *J. Biomol. NMR*, 2002, **22**, 281–289.
53. B. Xia, V. Tsui, D. A. Case, H. J. Dyson and P. E. Wright, *J. Biomol. NMR*, 2002, **22**, 317–331.
54. J. P. Linge, M. A. Williams, C. A. E. M. Spronk, A. M. J. J. Bonvin and M. Nilges, *Proteins*, 2003, **50**, 496–506.
55. J. Chen, W. Im and C. L. Brooks III, *J. Am. Chem. Soc.*, 2004, **126**, 16038–16047.
56. H. Takashima, N. Mimura, T. Ohkubo, T. Yoshida, H. Tamaoki and Y. Kobayashi, *J. Am. Chem. Soc.*, 2004, **126**, 4504–4505.
57. H. Tamaoki, Y. Kobayashi, S. Nishimura, T. Ohkubo, Y. Kyogoku, K. Nakajima, S. Kumagaye, T. Kimura and S. Sakakibara, *Protein Eng*, 1991, **4**, 509–518.
58. B. A. Wallace, R. W. Janes, D. A. Bassolino and S. R. Krystek Jr, *Protein Sci*, 1995, **4**, 75–83.
59. H. Takashima, H. Tamaoki, N. Teno, Y. Nishi, S. Uchiyama, K. Fukui and Y. Kobayashi, *Biochemistry*, 2004, **43**, 13932–13936.
60. R. W. Janes, D. H. Peapus and B. A. Wallace, *Nat. Struct. Biol.*, 1994, **1**, 311–319.
61. T. Yoshida, S. Oka, S. Uchiyama, H. Nakano, T. Kawasaki, T. Ohkubo and Y. Kobayashi, *Biochemistry*, 2003, **42**, 4101–4107.
62. K. H. Kim, B. M. Kwon, A. G. Myers and D. C. Rees, *Science*, 1993, **262**, 1043–1046.
63. H. Takashima, S. Amiya and Y. Kobayashi, *J. Biochem.*, 1991, **109**, 807–810.
64. M. D. Urbaniak, F. W. Muskett, M. D. Finucane, S. Caddick and D. N. Woolfson, *Biochemistry*, 2002, **41**, 11731–11739.
65. M. D. Urbaniak, J. P. Bingham, J. A. Hartley, D. N. Woolfson and S. Caddick, *J. Med. Chem.*, 2004, **47**, 4710–4715.

66. K. Ogawa, S. Nishimura, M. Doi, H. Takashima, Y. Nishi, T. Yoshida, T. Ohkubo and Y. Kobayashi, *J. Pept. Sci.*, 2006, **12**, 51–57.
67. S. Nakamura, S. Ichiki, H. Takashima, S. Uchiyama, J. Hasegawa, Y. Kobayashi, Y. Sambongi and T. Ohkubo, *Biochemistry*, 2006, **45**, 6115–6123.
68. A. Kalk and H. J. C. Berendsen, *J. Magn. Res.*, 1976, **24**, 343–366.
69. S. Macura and R. R. Ernst, *Mol. Phys.*, 1980, **41**, 95–117.
70. A. Kumar, R. R. Ernst and K. Wüthrich, *Biochem. Biophys. Res. Commun.*, 1980, **95**, 1–6.
71. F. Delaglio, S. Grzesiek, G. W. Vuister, G. Zhu, J. Pfeifer and A. Bax, *J. Biomol. NMR.*, 1995, **6**, 277–293.
72. P. Güntert, W. Braun, M. Billeter and K. Wüthrich, *J. Am. Chem. Soc.*, 1989, **111**, 3997–4004.
73. F. Cordier and S. Grzesiek, *J. Am. Chem. Soc.*, 1999, **121**, 1601–1602.
74. G. Bouvignies, P. Bernado, S. Meier, K. Cho, S. Grzesiek, R. Bruschweiler and M. Blackledge, *Proc. Natl. Acad. Sci. USA.*, 2005, **102**, 13885–13890.
75. X. Huang, F. Moy and R. Powers, *Biochemistry*, 2000, **39**, 13365–13375.
76. S. B. Nabuurs, C. A. Spronk, E. Krieger, H. Maassen, G. Vriend and G. W. Vuister, *J. Am. Chem. Soc.*, 2003, **125**, 12026–12034.
77. G. M. Clore, A. M. Gronenborn and N. Tjandra, *J. Magn. Reson.*, 1998, **131**, 159–162.
78. J. H. Prestegard, *Nat. Struct. Biol.*, 1998, **5(Suppl)**, 517–522.
79. J. H. Prestegard, C. M. Bougault and A. I. Kishore, *Chem. Rev.*, 2004, **104**, 3519–3540.
80. R. S. Lipsitz and N. Tjandra, *Annu. Rev. Biophys. Biomol. Struct.*, 2004, **33**, 387–413.
81. G. M. Clore, M. R. Starich and C. A. Bewley, *J. Am. Chem. Soc.*, 1999, **121**, 6513–6514.
82. K. Ding and A. M. Gronenborn, *J. Am. Chem. Soc.*, 2004, **126**, 6232–6233.
83. G. A. Mueller, W. Y. Choy, D. Yang, J. D. Forman-Kay, R. A. Venters and L. E. Kay, *J. Mol. Biol.*, 2000, **300**, 197–212.
84. M. A. McCoy and D. F. Wyss, *J. Am. Chem. Soc.*, 2002, **124**, 2104–2105.
85. M. Andrec, Y. Harano, M. P. Jacobson, R. A. Friesner and R. M. Levy, *J. Struct. Funct. Genom.*, 2002, **2**, 103–111.
86. S. Spera and A. Bax, *J. Am. Chem. Soc.*, 1991, **113**, 5490–5492.
87. D. S. Wishart and B. D. Sykes, *J. Biomol. NMR.*, 1994, **4**, 171–180.
88. G. Cornilescu, F. Delaglio and A. D. Bax, *J. Biomol. NMR.*, 1999, **13**, 289–302.
89. J. Kuszewski, A. M. Gronenborn and G. M. Clore, *Protein Sci.*, 1996, **5**, 1067–1080.
90. J. Kuszewski, C. D. Schwieters, D. S. Garrett, A. Byrd, N. Tjandra and M. Glöre, *J. Am. Chem. Soc.*, 2004, **126**, 6258–6273.
91. J. Meiler, *J. Biomol. NMR.*, 2003, **26**, 25–37.
92. J. Kuszewski and G. M. Clore, *J. Magn. Res.*, 2000, **146**, 249–254.
93. I. Bertini, G. Cavallaro, C. Luchinat and I. Poli, *J. Biomol. NMR.*, 2003, **26**, 355–366.
94. A. Grishaev and A. Bax, *J. Am. Chem. Soc.*, 2004, **126**, 7281–7292.
95. J. Kuszewski, A. M. Gronenborn and G. M. Clore, *J. Am. Chem. Soc.*, 1999, **121**, 2337–2338.
96. J. Iwahara, C. D. Schwieters and G. M. Clore, *J. Am. Chem. Soc.*, 2004, **126**, 5879–5896.

97. J. Boisbouvier, M. Blackledge, A. Sollier and D. Marion, *J. Biomol. NMR.*, 2000, **16**, 197–208.
98. A. E. Torda, R. M. Brunne, T. Huber, H. Kessle and W. F. Van Gunsteren, *J. Biomol. NMR.*, 1993, **3**, 55–66.
99. A. S. Altieri and R. A. Byrd, *Curr. Opin. Struct. Biol.*, 2004, **14**, 547–553.
100. M. C. Baran, H. N. Moseley, G. Sahota and G. T. Montelione, *J. Biomol. NMR.*, 2002, **24**, 113–121.
101. Z. Zolnai, P. T. Lee, J. Li, M. R. Chapman, C. S. Newman, G. N. Phillips Jr., I. Rayment, E. L. Ulrich, B. F. Volkman and J. L. Markley, *J. Struct. Funct. Genom.*, 2003, **4**, 11–23.
102. M. C. Baran, H. N. Moseley, J. M. Aramini, M. J. Bayro, D. Monleon, J. Y. Locke and G. T. Montelione, *Proteins*, 2006, **62**, 843–851.
103. J. E. Mertz, P. Güntert, K. Wüthrich and W. Braun, *J. Biomol. NMR.*, 1991, **1**, 257–269.
104. J. P. Linge, M. Habeck, W. Rieping and M. Nilges, *J. Magn. Reson.*, 2004, **167**, 334–342.
105. R. Zhou, *Proteins*, 2003, **53**, 148–161.
106. J. Chen, H. Won, W. Im, H. Dyson and C. L. Brooks III, *J. Biomol. NMR.*, 2005, **31**, 59–64.
107. K. T. Dayie, G. Wagner and J. F. Lefevre, *Annu. Rev. Phys. Chem.*, 1996, **47**, 243–282.
108. R. Bruschweiler, *Curr. Opin. Struct. Biol.*, 2003, **13**, 175–183.
109. J. G. Kempf and J. P. Loria, *Cell Biochem. Biophys.*, 2003, **37**, 187–211.
110. K. Lindorff-Larsen, R. B. Best, M. A. DePristo, C. M. Dobson and M. Vendruscolo, *Nature*, 2005, **433**, 128–132.
111. Y. Zhou, D. Vitkup and M. Karplus, *J. Mol. Biol.*, 1999, **285**, 1371–1375.
112. F. M. Richards, *J. Mol. Biol.*, 1974, **82**, 1–14.
113. J. Pontius, J. Richelle and S. J. Wodak, *J. Mol. Biol.*, 1996, **264**, 121–136.
114. R. W. W. Hooft, G. Vriend, C. Sander and E. E. Abola, *Nature*, 1996, **381**, 272.
115. R. A. Laskowski, M. W. MacArthur, D. S. Moss and J. M. Thornton, *J. Appl. Cryst.*, 1993, **26**, 283–291.
116. R. A. Laskowski, J. Antoon, C. Rullmann, M. W. Macarthur, R. Kaptein and J. M. Thornton, *J. Biomol. NMR.*, 1996, **8**, 477–486.
117. R. W. W. Hooft, G. Vriend, C. Sander and E. E. Abola, *Nature*, 1996, **381**, 272.
118. W. Gronwald, R. Kirchhofer, A. Gorler, W. Kremer, B. Ganslmeier, K. P. Neidig and H. R. Kalbitzer, *J. Biomol. NMR.*, 2000, **17**, 137–151.
119. Y. J. Huang, R. Powers and G. T. Montelione, *J. Am. Chem. Soc.*, 2005, **127**, 1665–1674.
120. V. Tugarinov, P. M. Hwang and L. E. Kay, *Annu. Rev. Biochem.*, 2004, **73**, 107–146.
121. M. Kainosho, T. Torizawa, Y. Iwashita, T. Terauchi, A. M. Ono and P. Güntert, *Nature*, 2006, **440**, 52–57.
122. D. Monleon, K. Colson, H. N. B. Moseley, C. Anklin, R. Oswald, T. Szyperski and G. T. Montelione, *J. Struct. Funct. Genom.*, 2002, **2**, 93–101.
123. H. Kessler, M. Gehrke and C. Griesinger, *Angew. Chem. Int. Ed. Engl.*, 1988, **27**, 490–536.

124. K. Per Vushin, R. Riek, G. Wider and K. Wüthrich, *Proc. Natl. Acad. Sci. USA.*, 1997, **94**, 12366–12371.
125. K. Wüthrich, *Nat. Struct. Biol.*, 1998, **5(Suppl)**, 492–495.
126. C. Fernandez and G. Wider, *Curr. Opin. Struct. Biol.*, 2003, **13**, 570–580.
127. A. S. Stern, K. B. Li and J. C. Hoch, *J. Am. Chem. Soc.*, 2002, **124**, 1982–1993.
128. S. Kim and T. Szyperski, *J. Am. Chem. Soc.*, 2003, **125**, 1385–1393.
129. E. Kupce and R. Freeman, *J. Am. Chem. Soc.*, 2004, **126**, 6429–6440.
130. D. Rovnyak, J. C. Hoch, A. S. Stern and G. Wagner, *J. Biomol. NMR.*, 2004, **30**, 1–10.
131. D. Rovnyak, D. P. Frueh, M. Sastry, Z. Y. Sun, A. S. Stern, J. C. Hoch and G. Wagner, *J. Magn. Reson.*, 2004, **170**, 15–21.
132. M. Mishkovsky and L. Frydman, *J. Magn. Reson.*, 2005, **173**, 344–350.
133. F. Castellani, B. van Rossum, A. Diehl, M. Schubert, K. Rehbein and H. Oschkinat, *Nature*, 2005, **420**, 98–102.
134. A. Drechsler and F. Separovic, *IUBMB Life*, 2003, **55**, 515–523.
135. C. P. Jaroniec, C. E. MacPhee, V. S. Bajaj, M. T. McMahon, C. M. Dobson and R. G. Griffin, *Proc. Natl. Acad. Sci. USA.*, 2004, **101**, 711–716.
136. S. K. Straus, *Philos. Trans. Royal Soc. London B Biol. Sci.*, 2004, **359**, 997–1008.
137. R. Bertram, J. R. Quine, M. S. Chapman and T. A. Cross, *J. Magn. Reson.*, 2000, **147**, 9–16.
138. R. Bertram, T. Asbury, F. Fabiola, J. R. Quine, T. A. Cross and M. S. Chapman, *J. Magn. Res.*, 2003, **163**, 300–309.

Index

- 1,10-decanedicarboxylic acids, phase transitions of 183
- 1,2,3-trichloro-4,5,6-trimethylbenzene (TCTMB) 179–181
- 2,3-dimethylnaphthalene, polar–alignment disorder measurement in 179
- 2D NMR data, multi-way analysis application to 207–231
 - 2D and 3D NMR data analysis 216–231, *see also under* pseudo 2D NMR data; real 2D NMR data
 - compression of data 214–215
 - constraints 214
 - DECRA method 225–226
 - model characteristics, comparison 213
 - multivariate data analysis 210–211
 - multi-way data analysis 211–213
 - MUNIN method 226
 - software 216
 - theory 210–216
 - three-way array into a two-way array, unfolding scheme for 212–213
 - three-way array, representation 209
 - true multi-way analysis 221–230, *see also under* true multi-way analysis
 - two-way multivariate analysis 219–221
 - validation 215–216
- 3-chloriodobenzene
 - ¹H multiple quantum spectra 13
 - 3Q ¹H NMR spectrum 12
 - MQNMR spectrum 8–9
- 3-phenyl-1-propyne, MQNMR 34
- 4-chlorotoluene 15
 - 6Q spectrum 21
 - MQ spectrum 16
- 4-cyano-40-pentylbiphenyl, MQNMR 34
- ab initio* chemical shift calculations 54–55, 118, 120, 124, 161, 166, 168, 193
- activation enthalpies 140–141, 143–144, 146, 152–154, 161–162, 179
- activation volume 140–141, 144, 159
- aligned molecules study, by MQNMR 30–36
- alternating least-squares (ALS) 221
- anisotropic media
 - diffusion measurement using MQNMR 25–27
 - MQ relaxation in 28–29
- anisotropic relaxation 78
- anisotropy lineshape analysis 53–56
- antiferroelectric phase transitions 157–158, 165–166
- Arrhenius formula 141, 143
- autocorrelation function 86
- average Hamiltonian theory 8
- averaged frequency 147
- averaged tensor 147, 181
- Avrami–Erofe’ev rate law 174
- azulene, polar–alignment disorder measurement in 179
- barium titanate BaTiO₃ 156, 167–168
- ‘batch analysis’ 220
- Bayer model 129
- benzene, diffusion measurements 27
- benzyl bromide
 - 1Q spectrum 17
 - MQNMR 32
- bio-fluid 208, 211
- Biological Magnetic Resonance Data Bank 240, 253, 260
- biphenyl, MQNMR 36
- biphenylene, MQNMR 34
- Bloch–McConnell equations 77
- broadening
 - homogeneous/inhomogeneous 138, 175–177, 183–187
 - inhomogeneous critical 134, 137–138, 176–177, 183–186
 - NMR/NQR 186–188
 - pretransitional 122, 154, 168, 177, 183
- butane, MQNMR 35
- butylated hydroxytoluen (BHT) 229

- chemical shielding 130
- chemical shift anisotropy (CSA) 49, 53–56
- chemical shift refocusing 20–21
- chemical-shielding tensor 53–54
- chlorotoluene, MQNMR 33
- Clausius–Clapeyron equation 127
- CODEX pulse sequence 103–106
- coexistence, hysteresis and kinetics, NMR studies 169–174
 - time-resolved NMR, kinetics 173–174
- coherence transfer echos 14
- compression of data 214–215
- computing technique, for protein structure determination by NMR 239
- conformational sampling 245–246
- conformational space 241–244, 245–246
- constraints 256–259, *see also under* high-resolution protein structure determination
- correlation function 79–80, 84, 86, 91, 142–143
- correlation spectroscopy (COSY) 208, 217
- correlation times 40–45, 59, 70, 74–77, 86, 91, 93, 97–99, 101–103
 - and relaxation and phase transitions 141–145
 - physical content of 140–141
- critical behavior 138, 150, 153–154, 166, 183
- cross-relaxation 144, 176
- cryogenic probe 266
- CuAlCl₄, phase transitions studies in 173
 - using PXRD experiments 173
- cyclohexane/thiourea-inclusion compound 185
- cyclooctatetraene 28
 - MQNMR 34
- cytochrome c552, NMR structure ensemble 251–252

- DANTE-type frequency-selective pulses 10
- decomposition methods 213, 220–222, 226, 229
- DECRA, *see* Direct Exponential Curve Resolution Algorithm
- density functional theory 53
- deuteration 18
- deuterium spectroscopy 70–77
- diffraction and NMR 122–125
- diffusion coefficient 27, 77, 194, 217, 219, 223
- diffusion ordered spectroscopy (DOSY) 208, 219, 221
- dipolar coupling 2, 59, 64, 111, 130
 - dipolar coupling constants (D_{ij}) 3, 19
 - dipolar coupling lineshapes 57–70
- Direct Exponential Curve Resolution Algorithm (DECRA) 225–226, 228
- direct trilinear decomposition (DTLD) method 230
- disorder
 - dynamical 122, 140, 149–151, 153, 161–162, 179, 191–192
 - intrinsic 175–177, 186
 - orientational 119, 134, 148, 155, 158, 161, 173, 176–183
 - polar or alignment disorder 177–181
- distance geometry 239, 241–242, 247
 - metric matrix distance geometry 242
- distance space 241–242
- distributed computing 239, 248–252
- double quantum-filtered COSY spectra 18
- double-quantum (DQ) coherence 64
 - DQ off-angle spinning (OMAS) experiment 71–73
 - DQ–DQ correlation spectroscopy 111–113
- dynamical disorder 122, 140, 149–151, 153, 161–162, 179, 191–192

- echo pulse sequence 70, 74, 87, 91, 94, 97
- Ehrenfest relationship 127
- exchange experiments/spectroscopy 98–114
 - 1D exchange spectroscopy and selective excitation 177
 - basics 98–101
 - CODEX pulse sequence 103–106
 - exchange-induced sideband methods (EIS) 101
 - one-dimensional experiments 101–106, 111
 - pure-exchange spectra 106–111
 - three- (or higher) dimensional exchange spectra 100
 - total suppression of spinning sidebands (TOSS) pulse sequence 101
 - two-dimensional experiment for ¹³C in DMS 109
 - two-dimensional experiment 98

- exchange-induced sideband methods (EIS) 101–102
- exchanging systems, MQNMR of 28
- explicit solvent 263
- fast-motion limit 45–46, 50
- ferroelastics, site multiplicity and NQR 187–188
- ferroelectric phase transitions, H-bonded systems 154–169
 - displacive ferroelectric phase transition, model 155
 - ferroelectricity, mechanisms of 154–157
 - hybrid organic–inorganic compounds 157–163
 - order–disorder phase transition model 155, 163–169
- F-measure scores 265
- free induction decay (FID) 267
- generalized Born (GB) solvent 263–264
- GRID computing, for protein structure determination by NMR 239–240
- half-integer spin spectroscopy 77–81
- Hamiltonian interaction 129
- Hartman–Hahn cross polarization 57, 68
- H-bonded systems, ferroelectric phase transitions in 154–169, *see also under* ferroelectric phase transitions
- heteronuclear multiple-quantum spectroscopy (HMQC) 24–25, 208
- heteronuclear single-quantum spectroscopy (HSQC) 208, 217–221, 226
- hexabenzocoronene 66
- high-resolution protein structure determination, by NMR 235–268
 - ‘torsion angle dynamics’ method 244
 - algorithms 241–242
 - backbone hydrogen bond topology 261
 - basic NMR-derived constraints for 256–259
 - comprehensive conformational space search 249–253
 - conformational sampling and refinement 245–246
 - critical factors 238
 - database potentials 260
 - dynamics 264
 - ensemble size and its significance 254–256
 - force field 263–264
 - high-performance computing implementation for structure determination 246–256
 - high-performance computing 238–240
 - hydrogen bonds, as constraints 258–259
 - metric matrix distance geometry 242
 - molecular dynamics for 243–245
 - NMR ensemble, quality check of 264–265
 - NMR experiments 266–268, *see also under* NMR experiments
 - NMR on protein data bank, statistics 236–238
 - NMR structure determination 240–241
 - NMR structure ensemble 245
 - NOE intensities, as constraints 256–258
 - NOE validation 262–263
 - protein sample preparations 265–266
 - resonance assignment precision, automated approaches 261–262
 - sampling scale, verification 246–249
 - scalar coupling constants, as constraints 258
 - structure calculation 241–246
 - target function quality 259–264
 - torsion angle space minimization 242–243
 - ‘hole-burning’ experiment 176, 183
- host/guest structure 181
- hybrid organic–inorganic compounds, phase transitions in 157–163, *see also* pyridinium salt compounds
- hydrazine dihydrochloride 229
- hydrogen carbonate family XHCO₃ polymorphism, using NMR 149–151
- hydrogen sulfides of alkali metals (MHS) polymorphism, using NMR 151–152
- hydrogen-bonded systems hydrostatic pressure 149, 154–169
- hysteresis 169–174
- INADEQUATE spectra 18
- incoherent quasielastic neutron scattering (IQNS) NMR 121, 141, 146, 153, 159, 182
 - hydrogen carbonate family XHCO₃ 149–151
 - hydrogen sulfides of alkali metals 151–152
- indene 6, 22–23, 35

- intrinsic disorder 175–177, 186
isotropic solution, NMR in 2–3
- Johnson–Mehl–Avrami–Kolmogorov model 170–171
- J-WISE experiment 59, 61–62
J-WISE experiment to L-alanine 63
- Landau theory, of phase transitions 125–127
- least-squares (LS) algorithms, for multiway method 215
- Lee–Goldburg CP (LG-CP) pulse sequence 57–60
- lineshape analysis 44–81
powder lineshapes, resolving 45–53
- lineshape and motion 145–147
- Liouville–von Neumann equation 39, 70, 79
- lipoprotein 224–225, 231
- liquid crystals as solvents for NMR 2–3, 10–11, 16–30, 189–191, 193–194, 259
- loadings 215, 220–225, 229
- low-field NMR 226
- magic-angle spinning (MAS) spectrum 63–65, 134–136, 267
and exchange experiments 98–111
and high fields 133–138
and quadrupole coupling lineshapes 70, 74–75
and single crystal 164, 165
and WISE experiment 61
hydrostatic pressure cells and pressure gradients in MAS probes 139–140
hydrostatic pressure cells and pressure gradients in 139–140
in resolving powder lineshapes 45–53
MQMAS NMR method 137–138
of naphthylphenylsulphoxide 56
temperature and pressure in static and MAS probes 138–140
temperature and pressure in static and MAS probes 138–140
temperature gradients 138–139
- magic-angle turning (MAT) 45–49
- magnetic field gradient 11–14
- Markov model for the motion 74–75
- McConnell's semi-classical exchange formalism 81
- mesophase 2–3, 193–194
- mixing time 43, 98–107, 112, 114, 176, 257, 263
- molecular crystals, polar and alignment disorder in 177–181
- molecular motion/dynamics, solid-state NMR studies 41–114
as incoherent processes 86
exchange experiments 98–114, *see also under* exchange experiments/spectroscopy
motionally averaged interactions, *see under* motionally averaged interactions
relaxation time measurements 81–98, *see also under* relaxation time measurements
- motionally averaged interactions, lineshape analysis and measurement 44–81
basics 44–45
chemical shift anisotropy lineshapes 53–56
dipolar coupling lineshapes 57–70
half-integer spin spectroscopy 77–81
powder lineshapes, resolving 45–53
quadrupole coupling lineshapes 70–81, *see also under* quadrupole coupling lineshapes
- MQNMR, *see* multiple quantum NMR
- Multidimensional NMR spectra INterpretation (MUNIN) 226
- multiple quantum coherence (MQCs) 6–17
coherence transfer echos 14
excitation and detection 6–17
non-selective excitation/detection 7–9
selective detection 10–14, *see also under* selective detection of MQC
selective excitation of 9–10
- multiple quantum NMR (MQNMR), *see also* multiple quantum coherence
1,1,1,6,6,6-hexadeuterohexane 33
1,3-dichloro-2-ethylbenzene 32
1-bromonaphthalene 33
2-chlorotoluene 33
3-chlorotoluene 33
3-phenyl-1-propyne 34
4-chlorotoluene 33
4-cyano-40-pentylbiphenyl 34
aligned molecules study by 30–36
analysis and simulation 19–24
and spectral simplification 4–6

- anisotropic media, diffusion measurement using 25–27
- applications 221
- basic 3–pulse sequence for generating 7
- benzyl bromide 32
- biphenyl 36
- biphenylene 34
- butane 35
- chemical shift refocusing 20–21
- counting spins in clusters 29–30
- cyclooctatetraene 34
- heteronuclear MQNMR 24–25
- indene 35
- MQ filters to simplify 1Q spectra 15–17
- MQ relaxation in anisotropic media 28–29
- naphthoquinone 32
- of 3-chloriodobenzene 8–9
- of exchanging systems 28
- of partially aligned molecules 1–36
- order parameters estimation by 21–24
- phenylacetylene 32
- p*-xylene 35
- theory 221
- to simplify the complex NMR spectra 18
- toluene 33
- versus conventional single quantum NMR 5
- Multivariate Curve Resolution Alternating Least Squares (MCR-ALS) 216
- multivariate data analysis 209–211
- multi-way analysis application, to 2D NMR data, *see under* 2D NMR data
- naphthoquinone, MQNMR 32
- naphthylphenylsulphoxide 56
- neocarzinostatin, NMR structure ensemble 251–252
 - chromophore-stabilizing mechanism 252–253
- n*-hexane, MQ spectra 19
- NMR experiments 266–268, *see also individual entries*
 - advances in equipment 266
 - for protein structure determination, *see* high-resolution protein structure determination
 - pulse sequence techniques and data acquisitions 266–267
 - solid-state NMR 267
 - nonadecane, phase transitions of 183–184
 - nonzero averaging of dipolar couplings 3
 - N-PLS method 230–231
 - NQR and phase transitions, *see* pure NQR and phase transitions
 - nuclear Overhauser spectroscopy (NOESY) 208, 217, 226
 - nucleation 169–170, 173–174
 - number of transitions 4
 - ODESSA experiment 104
 - o*-dichlorotetramethylbenzene (DCTMB) 179–181
 - order parameters 3, 122, 125–128, 148, 150, 155–156, 174, 184, 264
 - order–disorder/displacive phase transitions 154–156, 163–169
 - ammonium chloride in 156
 - Barium titanate BaTiO₃ 156, 167
 - displacive component in order–disorder phase transition (H-bonded compounds) 164–166
 - order–disorder component in displacive phase transition (perovskites) 166–169
 - order-selective detection 11
 - using 3D NMR 14–15
 - orientational disorder 134, 155, 158, 177, 179, 183
 - PARAFAC three-way method 213, 215, 222
 - applications 222–229
 - PARAFAC2 model 230
 - spectral loadings calculation by 224
 - theory 222
 - parallel linear channels-inclusion compounds 181–185
 - partial least-squares regression (PLS) 230
 - partially aligned molecules, NMR 1–36, *see also under* multiple quantum coherence (MQCs); multiple quantum NMR (MQNMR)
 - pattern recognition 208
 - PC cluster, for protein structure determination by NMR 239–240
 - perovskites, phase transitions in 166–169
 - phase cycling 10–11
 - limitation 11

- phase transitions, NMR studies 117–194, *see also under* polymorphic solid–solid phase transitions
- ‘first-order’ phase transitions 125
- ‘second-order’ phase transitions 125
- coexistence, hysteresis and kinetics 169–174, *see also under* coexistence, hysteresis and kinetics
- continuous- or discontinuous-phase transitions 125
- diffraction and NMR 122–125
- ferroelectric phase transitions, H-bonded systems 154–169, *see also under* ferroelectric phase transitions, H-bonded systems
- generalities and static contribution 122–140
- incoherent quasielastic neutron scattering (IQNS) and NMR 148–152, *see also under* incoherent quasielastic neutron scattering
- lineshape and motion 145–147
- MAS NMR, sensitivity and low- γ nuclei 134–136
- mean interaction tensor in the fast-motion regime 147–148
- phase transitions and NMR, motions 140–154
- phenomenology 122–124, 125–128
- physical content of correlation times 140–141
- pseudocritical features near a transition 152–154
- pure NQR and phase transitions 185–188, *see also under* pure NQR and phase transitions
- relaxation, correlation times and phase transitions 141–144
- single-crystal phase transition studies 174–185, *see also under* single-crystal phase transition studies
- thermodynamical classification 125
- phenylacetylene, MQNMR 32
- polar–alignment disorder measurement 177–181
- polymorphic solid–solid phase transitions, NMR studies 117–194, *see also under* phase transitions, NMR studies
- chemical shielding 130
- dipolar coupling 130
- lineshape and relaxation 128–130
- MAS NMR, sensitivity and low- γ nuclei 134–136, *see also under* magic-angle spinning (MAS) spectrum
- NMR interactions and symmetry 130–133
- quadrupolar interaction 130
- quadrupolar nuclei and high-field NMR 136–138
- sensitivity and resolution, MAS and high fields 133–138
- site symmetry 131–132
- space group validation or invalidation 132–133
- powder sample 44, 46, 53, 131, 134, 147, 186
- pressure hydrostatic, hydrogen-bonded systems 149, 154–169
- pretransitional effects 122, 154, 168, 177, 183
- principal component analysis (PCA)-based approach 214–218
- application 220–221
- theory 219–220
- probability 141, 148, 178, 181, 183, 256, 262
- product operator 266–267
- Protein Data Bank (PDB) 236–238
- protein structure determination by NMR, *see* high-resolution protein structure determination
- pseudo 2D NMR data 217
- diffusion coefficients (D) calculation 217–218
- longitudinal relaxation times (T1) calculation 217–218
- transverse relaxation times (T2) 217
- pulse sequence 10, 25, 51
- amide 1H T2-relaxation time constants 96–97
- for a three-dimensional exchange experiment 100
- for measuring relaxation times 88–89
- pure NQR and phase transitions 185–188
- ferroelastics, site multiplicity and NQR 187–188
- NQR features 186–187
- pure-exchange spectra 106–111
- PUREX spectra 106
- p*-xylene 35

- pyridinium salt compounds, phase transitions in 157–163
dynamic disorder in 161
microscopic mechanisms 161
properties 158
- quadrupolar interaction 130
- quadrupolar nuclei and high-field NMR 136–138
- quadrupole coupling lineshapes 70–81
deuterium spectroscopy 70–77
- radius of gyration 261
- random array 244, 248–250
- real 2D NMR data
definition 217
in structural elucidation and molecular identification 217
- recoupling strategies 52–53
- REDOR pulse sequence 50–51
rotor-encoded REDOR 65
- relaxation matrix 262, 265
- relaxation quantum mechanic treatment 79
- relaxation time measurements 81–98,
see also under phase transitions,
NMR studies
examples 90–97
experiments 87–90
in polymer work 93
pulse sequences for 88–89
theory 81–87
- REPT–HDOR experiment 65–66
- REREDOR pulse sequence 65, 68
- residual dipolar couplings (RDCs) 259–260
- root mean square difference (rmsd) 245
- rotor-encoding effect 64–65, 111
- R-value 265
- SANS (small-angle neutron scattering) 174
- Saupe order parameters, 3, 22
- scores 220–223, 229, 265
- second moment 145–146, 152–153, 157,
159–163, 167–168, 184, 192
- second-order data 210–211
- selective detection of MQC 10–14
magnetic field gradients 11–14
phase cycling 10–11
- selective deuteration to simplify spectral analysis 17–19
- selective excitation
and 1D exchange spectroscopy 177
of multiple quantum coherence 9
- selective saturation 176, 179
- sidebands 61–67, 71–73, 101–105, 111–114,
135–136, 139
- simulated annealing 244, 248–251, 254, 263
- single-crystal phase transition studies 174–185
parallel linear channels-inclusion compounds 181–185
site selectivity, intrinsic disorder and slow motions 175–177
- Smoluchowski model for motion 77
- solid-state NMR studies 267
for phase transitions, difficulties 191
molecular motion 41–114, *see also under*
molecular motion/dynamics
- space group validation or invalidation 132–133
- spectral densities 28, 80, 84–85, 142–143,
146, 153
- spin diffusion 257, 262–263
- spin-echo measurements 25
- spin-lattice relaxation 43–44, 87–88
- Stejskal–Tanner equation 25
- Stereo-Array Isotope Labeling (SAIL) 266
- symmetry
group validation/invalidation 121,
132–133
group/subgroup 125
Point group and NMR interaction 131,
184
symmetry breaking parameter 109, 119,
123, 156, 167–168, 180, 184
- temperature and pressure in static and MAS probes 138–140
- temperature gradients 10, 138–139
- time proportional phase incrementation (TPPI) 14
and order selective detection using 3D NMR 14–15
- time-resolved NMR, kinetics 173–174
- time-reversed ODESSA (trODESSA) experiment 104–105
- toluene, MQNMR 33
- ‘torsion angle dynamics’ method 244
- torsion angle space 242–243, 244, 247

- total correlation spectroscopy (TOCSY) 208, 217
- total suppression of spinning sidebands (TOSS) pulse sequence 101
- toxicity studies 220
- transverse relaxation optimized spectroscopy (TROSY) 267
- trioxane 28–29
- true multi-way analysis 221–230
 - PARAFAC, applications 222–229
 - parallel factor (PARAFAC) theory 222
- Tucker1 model 230
- Tucker3 three-way method/model 213–215, 226, 229
 - applications 229–230
 - theory 229
- two-dimensional nuclear magnetic resonance, *see under* 2D NMR data
- two-way multivariate analysis 219–221
 - MCR theory 221
 - MCR, applications 221
 - PCA theory 219–220
- WISE experiment 59–61, *see also* J-WISE experiment
- X-ray diffraction 133, 140, 151, 155, 171–173, 177–179, 181–182, 184, 188
- xylene, MQNMR 35
- Zeeman interaction 82–83, 129
- Zeeman quantum number (M), 19